Electronic Properties of

Doped-Nanoscale Diamonds

Abdulkareem Afandi

This thesis is submitted for the degree of Doctor of Philosophy

Department of Electronic and Electrical Engineering

University College London

March 2018

Declaration

‘I, Abdulkareem Afandi confirm that the work presented in this thesis is my own. Where information has been derived from other sources, I confirm that this has been indicated in the thesis.'

Acknowledgments

To my dear Mother and Father, to my grandmother Naima and aunt Kawthar, to my sisters and brothers. I can't thank you enough for your constant encouragement and support. To my beloved wife Salma; you were always there for me, understanding, selfless, and put our small family first. To my little ones, the joy of my life, Ibrahim and Layla. I love you all, and I dedicate this thesis to you.

I'd like to acknowledge the endless support and guidance from my supervisor Professor Richard Jackman. I've learned a lot from you, and I hope to learn more in the future. Many thanks to you for four years full of hard work and fun. Thanks to present and former members of the Diamond Electronics Group. Special thanks go to Robert Edgington, Fang Zhao and Thuong Thuong Nguyen for supervision during my early days as a member of the DEG and for lots of advice. I also want to thank Joe Welch, our very capable postdoc and lab manager. I know I've bothered you endless times, so thank you for being very patient. Thanks to Alice Taylor and Alexander Pakpour-Tabrizi for always being there for advice, and thanks to Suguru Amakubo, Mohammad Golsharifi, Ralph Moors, Marie-Laure Hicks (especially for valuable AFM expertise), Will Parfitt, Steven Evans, Terry Kang, Des Paschou, Maeve McLaughlin, and finally Max Ramsay. You are all one great team.

Many thanks to the LCN cleanroom team, Steve Etienne, Vijay Krishnan, and Lorella Rossi, and to the EE Nanolab manager, Steve Hudziak.

I also want to thank Dr Olga Shenderova of AdamasNano (adamasnano.com) and Dr Igor Vlasov of the National Research Nuclear University MEPhI and

the General Physics Institute (Moscow) for providing valuable samples, without which this thesis wouldn’t have been possible.

Abstract

Nanodiamonds (ND) have been the subject of intense research in recent years, for they have unique physical properties normally associated with diamond, in addition to their rich surface chemistry and bio-compatibility. In this thesis, the electronic properties of intentionally boron-doped nanodiamond materials are studied. In chapter 5, the possibility of substitutional doping of NDs is investigated. The properties of boron-doped, detonation nanodiamonds (B-DND) are studied using electrical impedance measurements and spectral analysis, and are compared to un-doped detonation-NDs (DND). Activation energies from variable-temperature impedance spectroscopy are found to be lower in comparison to intrinsic NDs. Chapter 6 discusses the nucleation of high-pressure, high-temperature (HPHT) boron-NDs, as well as B-DNDs on silicon. By combining pH titration and ultra-sonication from solution, nucleation densities are measured using atomic force microscopy (AFM). It is found that for most samples, highly acidic solutions (pH~2) are ideal for high surface coverage. Chapter 7 describes the electrical properties and activation energies of boron-doped HPHT and detonation nanodiamonds. Thin films are aggregated on conductive silicon substrates, and are subjected to electrical impedance measurements in vacuum. Following vacuum annealing, electrical measurements showed activation energies comparable to highly boron-doped PE-CVD thin film diamond. Electrical conductivity and resistivity are also compared to literature. In chapter 8, aluminium-diamond Schottky-barrier diodes (SBD) are fabricated. HPHT nanodiamond films were used as both Ohmic contacts and

as a source of dopant (boron), where aggregated nanodiamonds were subjected to PE-CVD film growth. Electrical (I-V) and capacitance-voltage (C-V) measurements are performed to study conduction mechanisms in fabricated devices. Resulting devices are found to have low carrier densities in the grown active layer (~10^{15} cm^{-3}), which is desirable for SBDs. This is the first account of using doped-NDs as the source of low boron-doping in PE-CVD diamond films, paving the way for potentially economical nanoscale diamond electronic devices.

Impact Statement

In this thesis, the first account confirming the existence of substitutional boron dopants in sub-10 nm diamond particles is presented. This finding enables their use in electronic applications, as well as in nanomedicine. Larger NDs with heavier doping levels have also been studied, and have shown great potential for electronics applications, manifested in their use to fabricate diamond-based Schottky barrier diodes (chapter 8). The electrical properties detailing mechanisms of conductivity (chapter 7) and surface adhesion/nucleation (chapter 6) have also been reported for the first time, allowing further research into this interesting class of materials. Boron-NDs have already been shown to be a suitable candidate for applications in nanomedicine, such as localised hyperthermia treatments,[58] which may enable their use in targeted cancer treatments via diamond-based nano-agents. High-power electronics can also benefit from heavily doped boron-NDs, by using them as a low-level doping source (chapter 8) during plasma-enhanced CVD growth. This can help reduce the economic and environmental costs that arise from needing a separate CVD growth chamber for boron doping. In addition, patterning of such conductive materials on substrates at micro or nano-scales can make them useful in 2D or 3D structures, such as electrodes in diamond-based sensors[136] and emitters for secondary electron emission sources.[205]

Table of Contents

List of Abbreviations

A*	Modified Richardson's constant
AC	Alternating current
AFM	Atomic force microscopy
APD	Avalanche photodiode detector
ATR	Attenuated total reflectance
ATR-FTIR	Attenuated total reflectance Fourier transform infrared spectroscopy
B	Boron
B-DND	Boron doped detonation nano-diamond
B-NCD	Boron doped nano-crystalline diamond
B-ND	Boron doped nano-diamond
BNC	Bayonet Neill–Concelman connector
C	Capacitor/capacitance
C-V	Capacitance-voltage
CL	Cathodoluminescence
CPE	Constant phase element
CVD	Chemical vapour deposition
CVU	Capacitance-voltage unit
DB	Diamond blend
DC	Direct current
DFT	Density functional theory
DI	De-ionised
DLS	Dynamic light scattering
DND	Detonation nano-diamond
E_a	Activation energy
EELS	Electron energy loss spectroscopy
E_F	Fermi energy level
E_g	Band gap
EIS	Electrical impedance spectroscopy
E_M	Avalanche breakdown field
E_V	Valence energy level

FT-IR	Fourier transform infrared spectroscopy
G-V	Conductance-voltage
H-ND	Hydrogen terminated nano-diamond
HMX	High melting explosive
HPHT	High-pressure high-temperature
HR-TEM	High-resolution transmission electron microscopy
I-V	Current-voltage
IEP	Iso-electric point
IR	Infrared
IS	Impedance spectroscopy
k	Boltzmann's constant
LCN	London Centre for Nanotechnology
MCP	Micro-channel plate
MIGS	Metal induced gap states
MP-CVD	Microwave plasma chemical vapour deposition
n	ideality factor
N-V	Nitrogen-vacancy
N_A	Acceptor concentration
NCD	Nano crystalline diamond
ND	Nano-diamond
N_d or N_D	Donor concentration
NEXAFS	Near edge X-ray absorption fine structure
N_F	Fermi level
$Ø_b$	Schottky barrier height
$Ø_b^0$	Intrinsic Schottky barrier height
PDDAC	Poly(diallyldimethylammonium chloride)
PE-CVD	Plasma enhanced chemical vapour deposition
pH	Potential of hydrogen
PL	Photoluminescence
R	Resistance
RC	Resistor-capacitor
RCF	Relative centrifugal force

RDX	Research department explosive (cyclotrimethylenetrinitramine)
R_S	Series resistance
SBD	Schottky barrier diode
SBH	Schottky barrier height
SCS	Semiconductor characterisation system
SEE	Secondary electron emission
STM	Scanning tunnelling microscope
T	Absolute temperature
T_C	Critical temperature
TCSPC	Time-correlated single photon counting
TEM	Transmission electron microscopy
TFE	Thermionic field emission
TMAH	Tetramethylammonium hydroxide
TNT	Trinitrotoluene
UNCD	Ultra-nano crystalline diamond
UV	Ultraviolet
V_{bi}	Built-in potential
V_R	Applied bias
V_{TH}	Voltage threshold
XANES	X-ray absorption near edge structure
XPS	X-ray photoelectron spectroscopy
Z_W	Warburg element
ϵ_r	Relative permittivity
ζ	Zeta potential
σ	Mobility
Φ_M	Metal work function
χ	Electron affinity
9BBN	9-Borabicyclo[3.3.1]nonane dimer

List of Figures and Tables

1. Introduction

Nanoscale Diamonds (ND) are among the first discovered nanoparticles. The history of NDs began following their synthesis in detonation chambers in the USSR around 1963,[1] and were labelled detonation nano-diamonds (DND). Nanodiamonds have a unique set of properties that make them usable in many environments; they are very hard,[2] chemically stable, possess a rich, accessible surface chemistry, and are bio-compatible.[3] The ability to introduce substitutional dopants to NDs would make them interesting for electronic and opto-electronic applications.[4] In recent years, computational studies into the feasibility of modifying the band-gap of nanodiamond via surface chemistry[5] or substitutional boron-doping in few-nm particles had mixed results, at times suggesting boron atoms would end up on the surface of an ND, while others suggested boron atoms favour being at the centre.[6,7] To the time of writing this thesis, no experimental accounts were published confirming or disproving the existence substitutional boron-dopants in sub-10nm NDs. In this thesis, boron-doped ND materials of several origins (detonation, milled micron-scale HPHT, and nanoscale HPHT) are studied, with emphasis on spectroscopic and electronic properties for applications in diamond electronics. Chapter 2 introduces diamond and the carbon-carbon bond, orbital hybridization in carbon, and the several methods of diamond synthesis. Following that, substitutional doping in diamond is discussed, in addition to the effects of doping on diamond and nanodiamond (as compared with intrinsic diamond). Chapter 3 introduces Schottky barrier diodes (SBD), with a brief look at their history followed by a discussion of the theory explaining their behaviour.

Applications of Schottky diodes in high-power applications leads to the inevitability of using diamond as a material for SBDs. Chapter 4 describes the experimental methods used in this thesis; surface treatment and de-agglomeration of DND aggregates using acid cleaning and solution preparation are detailed. Moreover, imaging techniques (HR-TEM, AFM) and spectroscopic measurements (Raman spectroscopy, Photoluminescence, FT-IR and ATR-FTIR) are described. This is then followed by an explanation of impedance spectroscopy methods, and the details of SBD fabrication. In chapter 5, spectroscopic and electronic properties of aggregated, detonation boron-NDs are studied and discussed. Combining electrical impedance results with spectroscopic results (PL, FT-IR and ATR-FTIR), it is shown that substitutional boron exists in 4-5nm detonation boron-NDs. Activation energies from electrical measurements suggest this material is semiconducting, with more than one path of conductivity.

Chapter 6 explores introduces additional boron-ND samples produced using the high-pressure, high-temperature (HPHT) method. In this chapter, surface properties are studied using XPS, Zeta-potential measurements and particle size analysis via dynamic light scattering (DLS). Zeta-potentials and DLS are studied as a function of solution pH, and the dynamics of ND nucleation on silicon substrates using ultra-sonication from solution are discussed. It is found that heavily doped boron-NDs behave differently to undoped NDs, and resemble the behaviour of boron-carbide surfaces. It is found that the highest coverage is achieved at a pH~2.

In chapter 7 the electrical properties of different boron-ND samples are studied using variable temperature impedance spectroscopy in vacuum. For

this chapter, a vacuum chamber is specifically modified to allow for low-noise measurements in an inert environment (using argon purging). Aggregated ND films on conductive silicon substrates in a sandwich configuration (silicon-NDs-silicon) are used to perform measurements. Results show conductivity values similar to moderately-to-highly doped CVD films, in absence of surface conductivity. Such results encourage the use of ND films in many applications that do not necessarily require high crystalline quality, but still require diamond-grade properties.

Chapter 8 concludes experimental chapters, and is the first report of diamond-based Schottky barrier diodes fabricated from boron-NDs. Synthesis of the active layer using PE-CVD is described, followed by characterisation using electrical I-V and frequency dependant C-V measurements. I-V results show diode behaviour with ideality factors as low as ~5.5 without annealing, and also confirm the contribution of the Poole-Frenkel current limiting mechanism above ~1V, as expected. Carrier concentrations from C-V results confirm low-level doping is present, making this the first account of low-level doping in PE-CVD diamond from a doped-ND source.

Chapter 9 summarises the results of the thesis as a whole, followed by future work in chapter 10, and the impact of attained results in chapter 11.

Publications

The publication below has resulted from work presented in this thesis:

Afandi, A.; Howkins, A.; Boyd, I. W.; Jackman, R. B. Nanodiamonds for Device Applications: An Investigation of the Properties of Boron-Doped Detonation Nanodiamonds. *Sci. Rep.* **2018**, *8*, 3270.[8]

2. Diamond

Nanoscale diamonds (NDs) are finding an increasing number of applications[9] in fields as diverse as electronics,[10] spintronics,[11] electrochemistry,[12] biotechnology[13] and medicine,[14] as well as being used as 'seeds' enabling the chemical vapour deposition (CVD) of diamond films.[15] Diamond can be considered as a wide band gap semiconductor (E_g ~ 5.5 eV), which behaves as a dielectric unless purposefully doped. The preeminent technique for the production of NDs is a detonation process[16] that typically involves detonating a mixture of TNT and hexogen in an oxygen-deficient environment,[17] which is important to avoid early oxidation of carbons.[18] The reaction conditions result in the formation of micron-sized aggregates of nanometre scale diamonds; techniques have been developed[19] that enable de-aggregation resulting in individual NDs in the size range 3-10 nm. The surface of detonation synthesised nanodiamonds (DNDs) host a wide range of oxygen and hydrogen based moieties, and can be functionalised with a wide range of chemical groups.[13] Plasma-enhanced CVD grown diamond is often doped with boron, by the inclusion of boron containing gases to the growth plasma; boron imparts electrical conductivity from p-type character through to semi-metallic behaviour at high concentrations,[20] and is also associated with superconductivity within diamond films.[21] Boron-doped NDs (B-NDs) would be an attractive material for many applications including high surface area electrodes for electrochemistry, electrode material within supercapacitors, electro-catalytic material within fuel cells and for nm-scale diamond electronic devices and sensors. Boron also increases the oxidation resistance of carbon-

based materials. Moreover, the widespread use of undoped DNDs as seeds for the subsequent growth of boron-doped diamond films leads to the inevitable introduction of a highly resistive layer between the doped film and the substrate that is deleterious for many applications.[22]

Attempts to generate boron-doped NDs to date have relied on either the growth of a boron-doped layer over undoped NDs[23] or by solid-state diffusion,[24] but the remaining insulating diamond core leads to a high over all resistivity for the doped material. Heavily boron doped NDs have been produced using a milling process to crush boron-doped CVD grown diamond,[25] yielding NDs in the size range 10-60 nm. There are currently no reports of the properties of boron doped DNDs, whose ~5 nm size is essential for several applications. Recently, for example, boron-doped diamond has been studied as a potential electrode material for brain computer-interfaces,[26] and single-digit Boron-NDs can be potentially useful as conductive, biocompatible nano-electrode. Boron-DNDs are a boron-containing diamond material where boron has been purposefully added to the synthesis environment. A process for doing this has been proposed in a patent by Shenderova.[27] One method involves the introduction of boron containing graphite or boron carbide powders to the combustion mixture prior to detonation. Theoretical predictions for the properties of boron containing NDs with dimensions typical for DNDs are widely varied. Barnard & Sternberg (2006) suggest that the elemental boron will primarily be located at the surface,[6] the same authors also predict the boron to be metastable within the ND core and therefore unstable[7] and Wang *et al.*. propose that the boron is in a stable substitutional state within the ND core.[28] This chapter reports an

experimental investigation into the properties of boron-doped DNDs giving evidence for substitutional doping, supporting the theoretical predictions of Wang *et al.*

2.1 Diamond Bonding

2.1.1 The Carbon-Carbon Bond

Diamond is known to be one of the hardest materials with many other extraordinary properties, and it owes its properties to the tetrahedral carbon-carbon bond.[29] Other carbon systems such as graphite have weaker bonds, even though they too are entirely composed of carbon. In nanodiamond, properties such as toughness and conduction are greatly affected by the ratio of diamond-like carbon bonds to non-diamond phases of carbon, such as graphitic shells or carbon-based polymers. The covalent carbon-carbon bond is one of nature's strongest in terms of binding energy[29] (on the order of ~5 eV), and when compared to carbon-silicon bonds for example, it is seen that they are very close in terms of binding energies; however, binding energy is only one of many contributory factors resulting in the superior properties carbon possesses. The orbital configuration of diamond is:

$$[1s^2]\ 2s^2\ 2p^2$$

When this configuration is compared to other group IV elements on the periodic table, it is clearly seen that carbon is the only element having exclusively spherically symmetric *1s* core orbitals. The orbital hybridisation of the outer *2s* and *2p* orbitals are discussed next.

2.1.2 Orbital Hybridization in Diamond

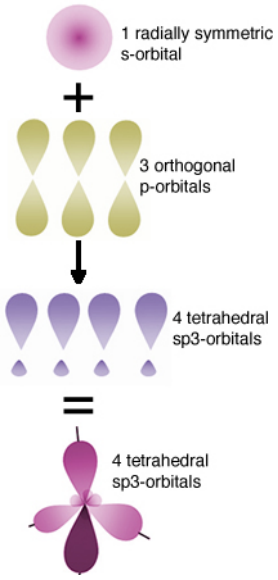

Figure 2-1 - Orbital hybridisation in diamond. Figure taken from http://virtuallaboratory.colorado.edu[30]

The carbon atom's ground state has one *2s* and three *2p* orbitals occupied in the outer shell. This is the lowest energy configuration when carbon is not bonded, however carbon allotropes have different hybridizations of orbitals, giving each allotrope its distinct behaviour in physical and electrical properties. When forming bonds, orbitals can be reconfigured in space, and energy is released in the process. In diamond, the four orbitals (one *s* and three *p* orbitals) hybridize to form an sp^3 system, which is energetically favourable, and hence has a stronger bond with surrounding atoms.[31] In the sp^3 system, one electron of the doubly occupied *2s* orbital is excited to the empty *2p* orbital, hence forming four symmetric tetrahedral sigma (σ) bonds (figure 2–1). Hybridization is a form of quantum mechanical superposition that mixes the properties of different orbitals, such as *s* and *p*, into combined states.[31] In addition to sp^3 hybrid orbitals, planar sp^2 and linear *sp* orbitals also form in carbon systems, and can co-exist in systems like nano-diamond and

amorphous carbons. This hybridisation is not unique to carbon systems, and crystalline silicon for example forms sp^3 orbitals very similar to those of diamond; however, silicon, unlike carbon, is unable to naturally form sp^2 orbitals. This is due to the larger size of *3p* orbitals (compared to carbon's *2p*), making, meaning the overlap between *s* and *p* orbital wave-functions is smaller than in carbon, and the hybrid orbital has a lower *p* contribution.[31]

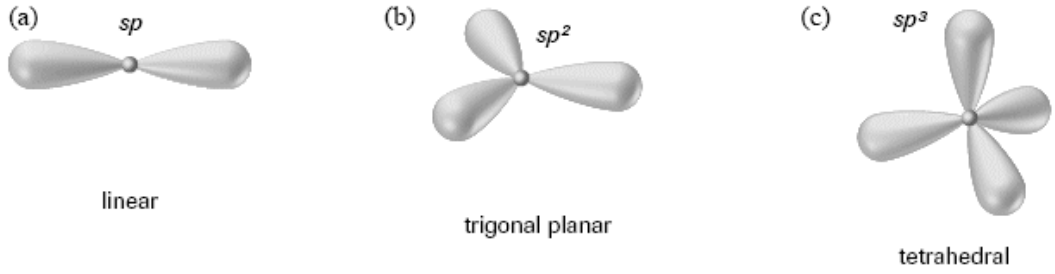

Figure 2-2 - Spatial configurations of orbital hybridisations. Figure taken from http://rjwarren0.tripod.com[32]

2.2 Diamond Synthesis

2.2.1 Plasma Enhanced Chemical Vapour Deposition (PE-CVD)

Diamond can be grown synthetically from carbon precursors via Microwave-plasma enhanced chemical vapour deposition (MP-CVD) and High Pressure High Temperature (HPHT). MP-CVD is a type of plasma-enhanced chemical vapour deposition (PE-CVD) which employs CVD. CVD involves gas-phase chemical reactions, which result in deposition of thin films onto the chosen substrate, when optimal growth conditions are met. Although this process can be very slow, it gives a level of control that is hard to match in other growth techniques.[33] In PE-CVD growth, a carbon precursor gas, such as (but not limited to) methane, is used as the source of atomic carbon. This method

usually involves using other gases to control the seeding, growth, etching and re-growth of diamond films and other structures. Conditions such as plasma frequency, energy, growth temperature, gas purity and pressure all play a role in determining the dynamics of the process. PE-CVD allows high levels of control over inclusions and substitutional dopants in grown diamond.[33] Gases or solid sources containing Nitrogen, Boron, Phosphorous and other elements are used to control impurities and concentrations of dopants selectively introduced to the system.[33] Growth of diamond films by chemical vapour deposition (CVD) is the most common route for obtaining synthetic diamond.[33] For diamond, the source of carbon is usually methane or another hydrocarbon; however, the most important component for a successful growth process is atomic hydrogen or oxygen. When present during a growth process, atomic hydrogen will act as an agent, which ensures graphitic carbons do not grow. This happens because hydrogen or oxygen terminates dangling carbon bonds, in addition to preferentially etching sp^2 phases of carbon much faster than sp^3 phases, allowing diamond to grow.

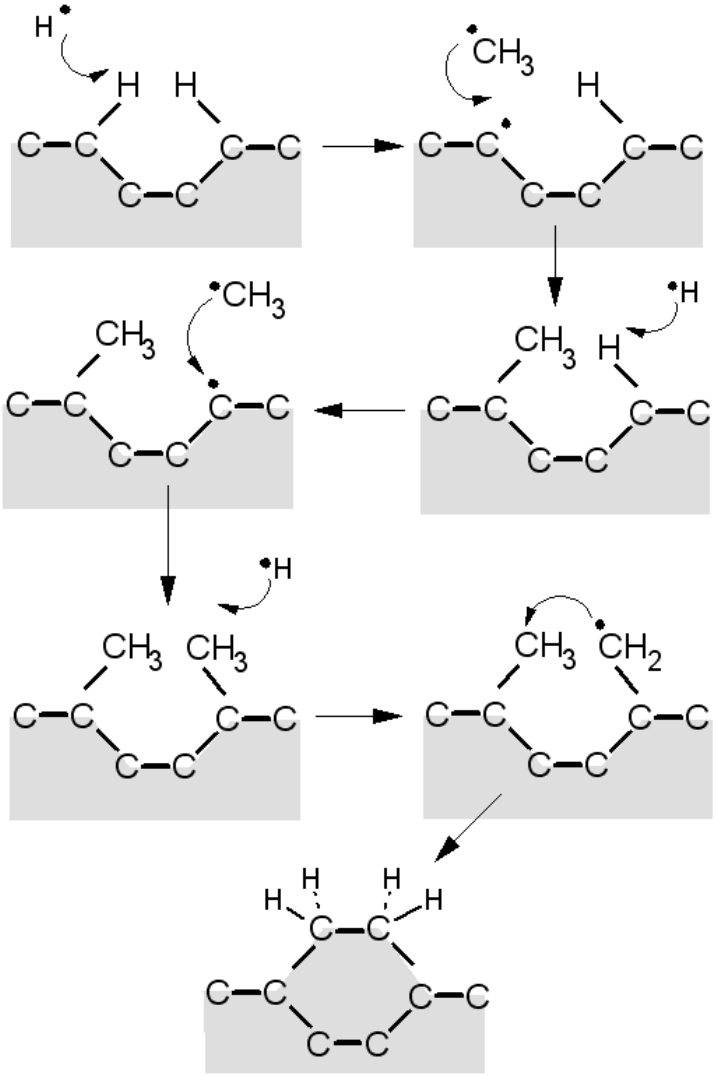

Figure 2-3 - Schematic of simplified CVD diamond growth process from methane. Figure taken from May, P.W. [2000][34]

Oxygen is also known to perform the same role. The ratios of C/H/O in the CVD gas mixture are selected carefully to control the quality of the growth. Bachmann *et al.*[35] collected data from over 70 deposition experiments, and plots the results in a diagram of elemental gas ratios (figure 2–4). In addition, atomic hydrogen facilitates the creation of carbon radicals, which are more reactive than carbon feedstock. Substrate temperatures in the range of 1000 and 1400 K are known to work, however growth at much lower temperatures has been reported.[33]

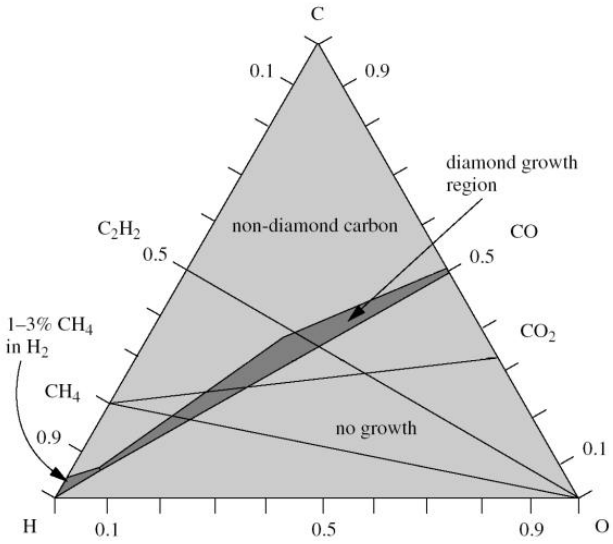

Figure 2-4 - CVD gas mixture ratio diagram for diamond growth. Figure taken from May, P.W. [2000][34]

In addition, the choice of energy supply plays a significant role. Plasma sources such as microwave, radio frequency, hot filament, direct current, laser induced or chemical activation can be used. Depending on the energy activation method, parameters of the growth process have to be adjusted, since distributions of temperature, pressure, gas mole-fractions would be different. Seeding also significantly affects the growth of diamond, silicon is often used as a substrate for CVD diamond growth, and monolayer seeding with few-nm nanodiamonds greatly improves the growth rate, but also affects the quality of the film and the density of diamond grains in the grown film.[34] Homoepitaxial growth of diamond results in the new diamond growth following the crystalline structure of a pre-existent substrate.

2.2.2 High-Pressure High-Temperature (HPHT)

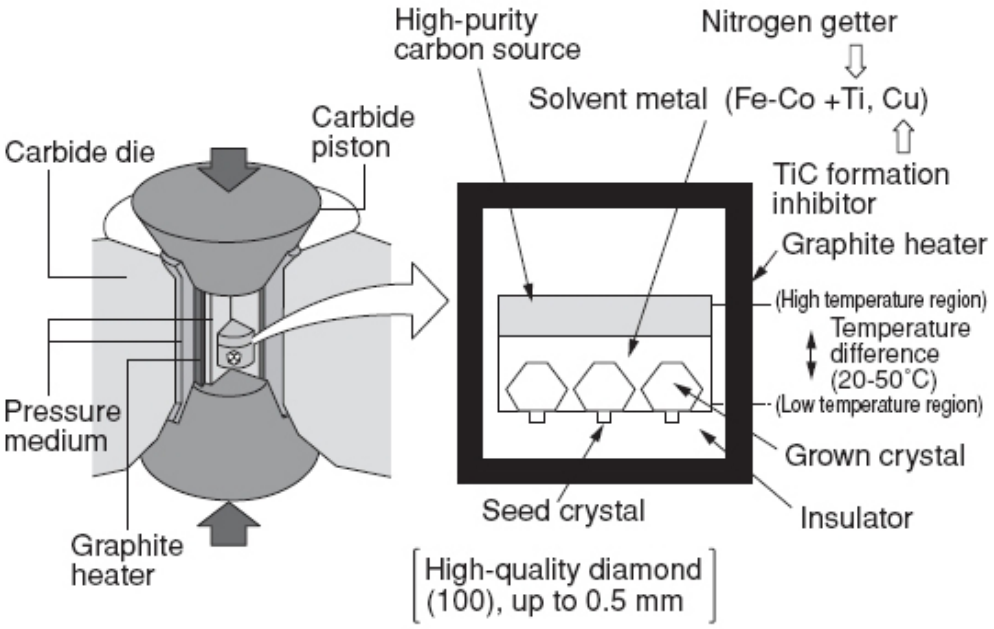

Figure 2-5 - HPHT diamond growth apparatus. Figure taken from http://diamondabrasives.eu [36]

Using a combination of high pressure and high temperature (3000 °C and 150 kBar), Bundy *et al.*[37] succeeded in converting graphite into diamond. Previous attempts using high temperature or high temperature, but not both, were unsuccessful, since the energy barrier between the two allotropes becomes larger with increased pressure.[37] Later attempts were successful at obtaining diamond at lower temperatures and pressure by using transition metal catalysts. HPHT treatments are also used to change the properties of natural gem diamonds.[38] Successful growth of few-nm nanodiamond powder using the HPHT method has been first reported in 2013 by Fang *et al.*[39] In their work, they used graphitic carbon nitride (C_3N_4) as a source, under a pressure of 22 GPa, and in a temperature range between 1400-1600 °C, to produce nanodiamond particles of high purity and very low sp^2 content.

2.2.3 Detonation Nanodiamond (DND)

Nanodiamond produced in a detonation chamber, usually a few nm in diameter, were first synthesized in 1963 in the USSR.[40] The process involving a mixture of explosives in a detonation chamber provides the right pressure-temperature combination for diamond to form. Since the conditions to form diamond exist very briefly in the detonation shockwave (less than 1 microsecond), diamonds form in few nm diameters. The process most commonly involves a mixture of TNT with RDX or HMX, where most of the diamond content comes from the TNT. This confirmed by using C^{13} and C^{14} isotopes to identify the source of the diamond content.[40] The explosive mixture is oxygen deficient, and the explosion medium is non-oxidising.[40] The exact theory as to why nanodiamonds form via this method is still unknown, however one suggested mechanism of production is via formation of amorphous carbon from atomic carbon, which goes through a phase transition as the mixture cools down. The temperature range required to form DNDs is thought to be between 3500-4500 K, in a pressure range of 18-35 GPa.[17,40] Of particular note is the propagation of the shock wave within the detonation chamber following the explosive ignition. It has been calculated that carbonaceous material within the chamber experience the required conditions for diamond formation for around 1 μs as the shock wave propagates.[40] This is sufficient time to assemble a nanodiamond ~5 nm is size, and all detonation derived nanodiamonds lie within the size range 3-5 nm.[1,40,41] Moreover, as the conditions for formation of the diamond phase of carbon subside, but before the nanodiamond is 'cold' it is thought an amorphous type sp^2 carbon coating results on much of the surface of the nanodiamond.[1,16] Finally, due to

the strength of van der Waals forces on these nm-scale particles they tend to aggregate into near-μm clusters.[42] The fact that many species other than carbon exist within the detonation chamber the surface of the nanodiamonds often play host to a mixture of C-H, C-OOH and C-OH species, as illustrated in Figure 2–6, taken from Krueger *et al.*[43] Further, the presence of metals at the grain boundaries of the aggregates is often observed, due to metal contaminants within the detonation chamber.[44]

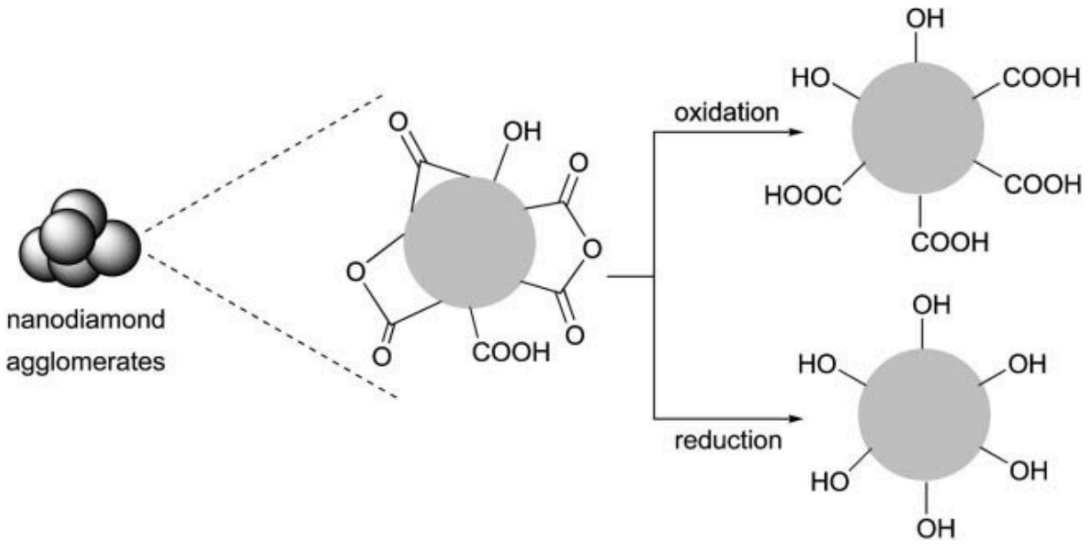

Figure 2-6 – Surface functional groups that may be present on surfaces of detonation NDs, and potential modifications via oxidation or reduction reactions. Figure taken from Kruger et al. [2006][43]

2.2.4 Cleaning and De-aggregation of DND

DND yield varies significantly depending on many factors, including the explosive mixture and additives. Data from several sources suggest ND content between a few per cent up to 80% of the diamond blend (DB).[40] The DB is a mixture of nanodiamonds with other non-diamond carbons, in addition to other materials involved in the synthesis process. DND producers have to purify the mixture to extract a maximum yield of diamond matter, and this usually involves a several steps, which include oxidation of non-diamond

content. Nitric and/or sulphuric acids at high concentrations and high temperatures are used to remove graphitic carbon, as well as metals and metal compounds. This is followed by filtration and subsequent rinsed with de-ionised water to minimize metal contents.[45] The purity of used materials in the cleaning process is essential to avoid agglomeration of nanodiamond products. Aleksenskiy *et al.*[44] suggest that heavy metal ion impurities present in water, such as iron, can facilitate the formation of bridges between carboxylic groups attached to DNDs, hence allowing large and stable aggregates to form. The process of obtaining mono-dispersed DNDs in aqueous solutions involves many steps, beginning with purification from heavy metals and non-sp^3 carbon phases. Other steps include breaking sp^2 shells that enclose diamond cores and prevent dispersion. This is usually achieved by a combination both of gas and mechanical treatments such as annealing in air, centrifugation, ball milling and ultra-sonication.[19,25,46]

2.3 Substitutional Doping in Diamond

2.3.1 Substitutional Doping

Doping in diamond occurs naturally in gems, where boron and nitrogen were the only dopants known to influence the conductivity of diamond crystals, until doping with phosphorus was achieved.[47,48] Purposeful doping of diamond is controllable in growth processes such as PE-CVD and HPHT, and these materials can be 'crushed' to form doped nanodiamonds. However this limits the minimum size of NDs produced to significantly above 10 nm,[7] hence the interest in boron-doping DNDs for applications requiring smaller NDs. As suggested by Shenderova,[27] this can be done by introducing boron containing

solid carbon sources, such as boron-containing graphite, during the detonation process. This however does not guarantee, at least in theory, the inclusion of substitutional boron within diamond cores, especially when considering that the detonation production of nanodiamond isn't well understood. The concentration of boron within diamond crystals defines their electrical conductivity, which can range from insulating at very low concentrations, to metallic at high concentrations (above ~10^{20} cm^{-3}).[49] Boron-doped diamond can act as a p-type semiconductor, revealing valance-band conduction with high mobility values, in intermediate concentrations, but displays quasi-metallic conduction (with the commensurate lower mobility values) associated with 'hopping' conduction. In the latter case the activation energy for the conduction process is as low as the meV range, due to the formation of an impurity band which merges with the valance band edge. In the former case, the activation energy is measured as 0.37 eV, subsequently decaying to meV as concentrations increase. This is illustrated in figure 2–7 which shows the effect of boron concentration on activation energy as measured by Borst and Weis.[20]

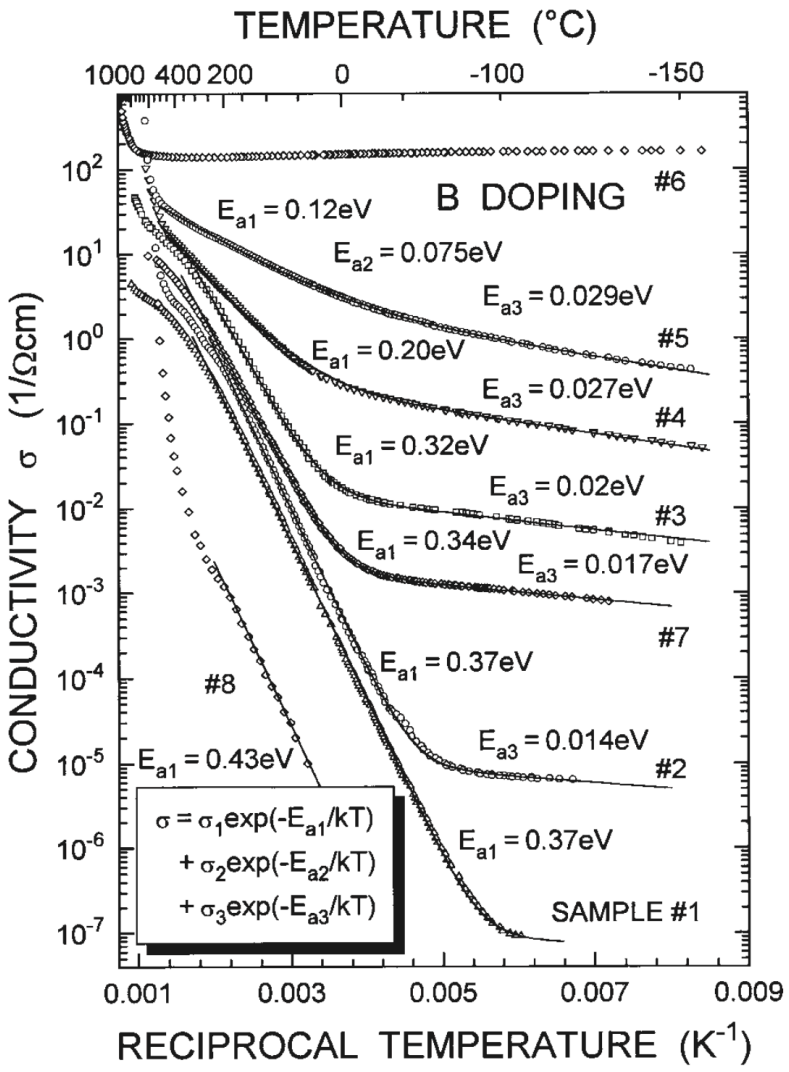

Figure 2-7 – Conductivity as a function of reciprocal temperature for Homoepitaxial boron-doped diamond Hall bars, grown by Borst and Weis.[20,50] Samples have different levels of boron compensation (from SIMS): sample #1: 7–15 × 10^{17} cm^{-3}, #3: 1.2 × 10^{19} cm^{-3}, #4: 4–5 × 10^{19} cm^{-3}, #5: 1.2 × 10^{20} cm^{-3}, #6: 3 × 10^{20} cm^{-3}, #7: 3–9 × 10^{18} cm^{-3}. Figure taken from Borst & Weis [1996][19]

Stable n-type doping in diamond is proving to be challenging due to stability issues of larger nitrogen atoms within diamond crystal structures, as well as the fact that nitrogen is considered a deep donor with a high activation energy, in both diamond and silicon[47,48]. Phosphorus is currently considered an acceptable method to achieve n-type doping in diamond, since it has a

much lower activation energy (~0.57 eV) when compared to nitrogen (~1.7 eV).[48]

2.3.2 Substitutional Boron Stability in Nanodiamond

Until recently, there were no reports or claims of substitutional doping in detonation nanodiamond (DND). The production of boron-doped nanodiamond from crushed or ball-milled PE-CVD or HPHT crystals has been reported,[25] however this limits the size of the final product to above ~10 nm, due to the nature of the milling process. The motivation of boron doping in DND is hence justified by the size of a DND, normally between 3 and 5 nm. For many applications, the size of a DND is ideal, such as seeding for subsequent growth of thin, doped diamond films. The stability of boron inclusions in nanodiamonds has been the subject of many studies. Barnard & Sternberg (2006)[6] concluded in their computational study that boron tends to be unstable within the bulk of nanodiamond and bucky-diamond. The study used DFT tight-binding simulations, and predicted that boron is more likely to be located near or at the grain boundaries in diamond films. While it is energetically preferable for boron to be in close proximity to the grain boundaries or edges, especially near {111}/{111} edges, it is more likely for nitrogen to be present at the edges and grain boundaries. In another DFTB study, Barnard & Sternberg (2007)[7] have found that neither boron nor nitrogen can be stable within nanodiamonds and bucky-diamonds. They suggest that they can be present as impurities, but not as stable substitutions, unless the diamond is large. Wang *et al.*[28] found in their computer simulations that the most energetically stable location for a boron atom in a nanodiamond is in the middle of the particle, while nitrogen will be more stable on the

surface. They conclude in their study that boron can be present as a substitutional atom, and they discuss its electronic properties within the nanodiamond. Since different computational studies show conflicting results concerning the stability of substitutional boron in nanodiamond, experimental validation becomes necessary. Several experimental techniques can be used to detect substitutions and impurities in nanodiamonds, which are discussed in more detail in this thesis, chapter 5.

2.3.3 Substitutional Doping in PE-CVD Diamond Films

Substitutional doping of diamond using boron (p-type) and phosphorus (n-type) enables semiconductor device fabrication. Methods to achieve substitutional doping include, but are not limited to, PE-CVD, HPHT and high-energy ion-implantation.[48]

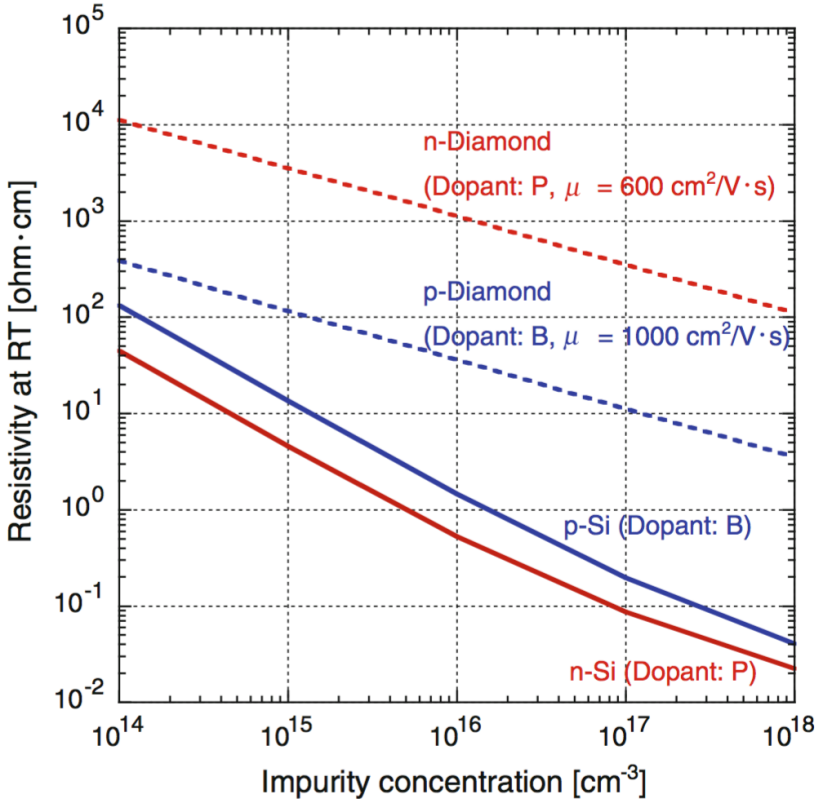

Figure 2-8 - Resistivity of diamond and silicon at room temperature as a function of impurity concentration. Figure taken from Arnault, J.C. [2015] [48]

Among the three methods, PE-CVD provides the highest level of doping control. Being a slow growth process by design, PE-CVD growth of doped diamond films is realized by introducing a boron-containing gas (e.g. diborane) or a phosphorus containing gas (e.g. phosphine) during the growth process. Epitaxial growth of diamond films, where growth is done layer by layer as time progresses, allows the growth of p-n junctions, for example, by introducing different gases at different stages of the growth, allowing high levels of control over the thickness, dopant concentration and overall quality of films.[48]

2.4 Conductivity in Diamond

2.4.1 Conductivity in the Bulk of Diamond

As a wide band-gap semiconductor, diamond can be thought of as the ideal material for electronic devices in hostile environments. Its chemical and physical stability, in addition to exceptional mechanical properties and thermal conductivity, make it a good candidate in the harshest conditions.[47] Many diamond-based electronic devices have been demonstrated since the synthesis of artificial diamond,[47] and since then the electronic properties had to be studied in depth. Massarani[51] discusses the hopping conduction mechanisms in boron-doped semiconducting diamond. Without donors or acceptors, diamond has a band-gap of ~5.5 eV, and when mildly doped with substitutional boron (concentration well below 10^{20} cm^{-3}), single-boron states form deep acceptors with energy E_a~0.37 eV above the valence band.[51] It is found that conduction takes place as expected for doped semiconductors, and that the hopping mechanism is temperature dependent below 200 °C.[51] As

the boron acceptor locations act like holes in the diamond lattice, they can be thought of as forming hydrogen-like systems around the boron atom, and hence a Bohr radius of ~3.5 Å. If hopping between dislocations is the only mechanism of conduction, then it can be assumed that boron concentrations higher than 10^{20} cm^{-3} are required to show semi-metallic behaviour, where there is enough overlap of wave-functions.[51] However when approaching this concentration an impurity band forms, allowing hopping between nearest neighbours, as well as beyond nearest neighbours at higher temperatures. The conductivity is thought to be dependent on the temperature in the hopping system, since the occupancies of boron impurities, as well as compensators, are temperature dependant.[51]

In the low temperature regime (below 150 K), the conductivity is described by:

$$\sigma = \sigma_0 \, e^{-\frac{\varepsilon_1}{kT}} \qquad \textit{Eqn. 2–1}$$

This is ascribed to nearest neighbour hopping, and the term ε_1 is the activation energy, dependant on the level of compensation, and can be found from experimental results[51]. At higher temperatures, Mott's law describes conductivity as:

$$\sigma = \sigma_0 \, e^{-A/T^{\frac{1}{4}}} \qquad \textit{Eqn. 2–2}$$

Here variable range hopping (VRH) starts to take place, and the term A is proportional to N_f^4, where here N_f is the Fermi level. Note that the critical temperature T_c at which the hopping mechanism changes, varies with boron and compensator concentrations.[51]

Other dopants, such as nitrogen, aluminium or phosphorus, can also be used as dopants to induce n-type behaviour in diamond, however; only boron is

known to form p-type acceptors in diamond. Being the only group-IIV element smaller than carbon, in addition to being comparable in size, makes it the most convenient p-type substitution. Recently, however, aluminium doping of diamond films has been reported.[52] Both nitrogen and phosphorus are larger than carbon, hence they are more likely to form systems containing more than an atom (and/or vacancy) to fit within the diamond lattice.[48]

2.4.2 Surface Conductivity

The surface of diamond has been known to conduct electronically when hydrogen terminated, however the mechanism was not well understood.[53] Electrical measurements of this surface suggested[53] that p-type carriers of densities around 10^{13} cm^{-2} are responsible for conductivity, and that they have a Hall mobility in the range of 30-70 cm^2 V^{-1} s^{-1}, and a corresponding carrier density of ~10^{12} cm^{-2}. The mobilities above are very close to what's measured for boron doped diamond.[53] Conductivity values reported in literature are between 10^{-4} and 10^{-5} Ω^{-1}. The exact mechanism of conduction was yet to be determined, with opinions suggesting it can be present on the surface, or tens of nanometres deep within the diamond bulk. Maier *et al.*[53] have found that hydrogen is necessary to form surface conductivity in diamond, however, they also found that surface adsorbates originating from the atmosphere are also necessary to form an accumulation layer with accepting nature. Williams *et al.*[54] have studied surface conductivity of the hydrogen terminated CVD diamond surface at different temperatures and ambient conditions, using electrical conductivity and Hall measurements. Their results agreed with those previously reported, however they concluded that the presence of an adsorbed water layer is necessary, and that proton screening in this layer acts

as the main electron sink. Williams *et al.* measured resistivity values ranging between ~10^3 and ~10^6 Ω/sq between 300 and 550 K. Multiple device types have been reported utilising surface conductivity in hydrogen terminated diamond, however, according to Williams *et al.*, caution must be exercised since conductivity is dependent on ambient conditions.[54]

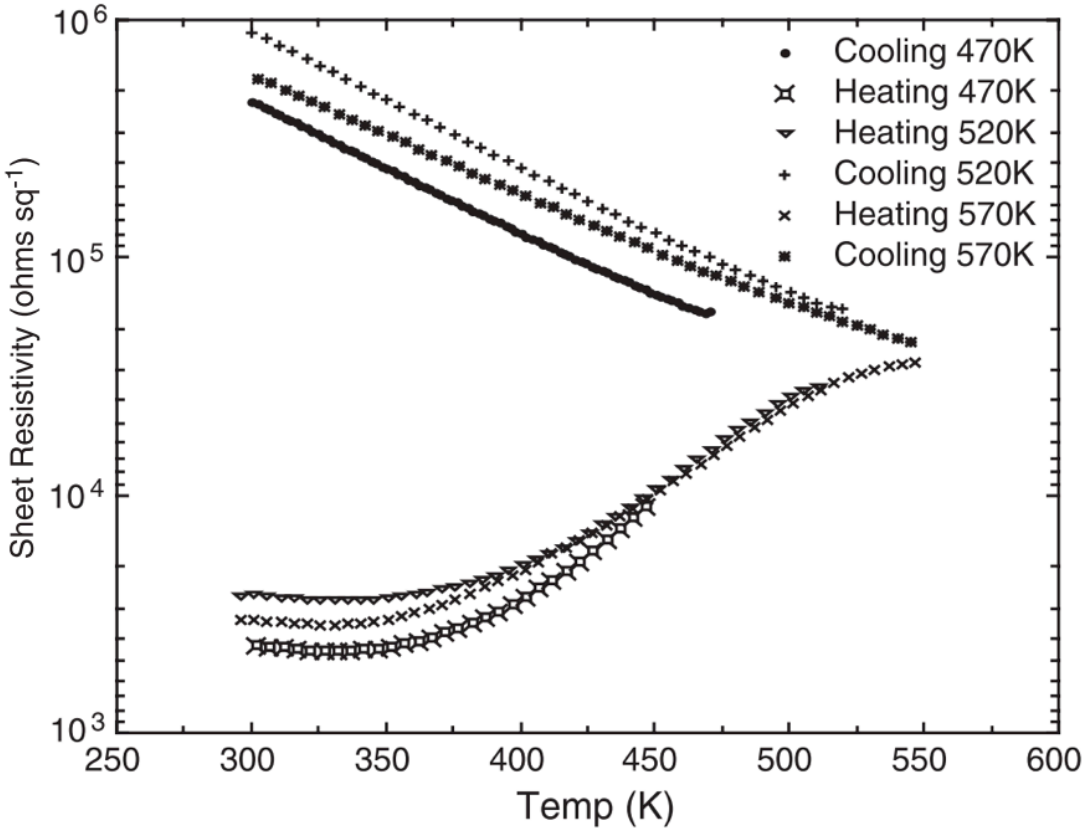

Figure 2-9 - Conductivity as a function of temperature in hydrogen terminated CVD diamond films. Figure adapted from Williams & Jackman [2003][54]

Figure 2–10 shows a band diagram to illustrate the so-called 'transfer doping model' for surface conductivity in diamond. Here, surface C–H bonds set up a surface dipole and the presence of adsorbates encourage sufficient additional band-bending to cause the Fermi level to enter the valance band at the surface. This results in a p-type (hole conduction) surface.[55]

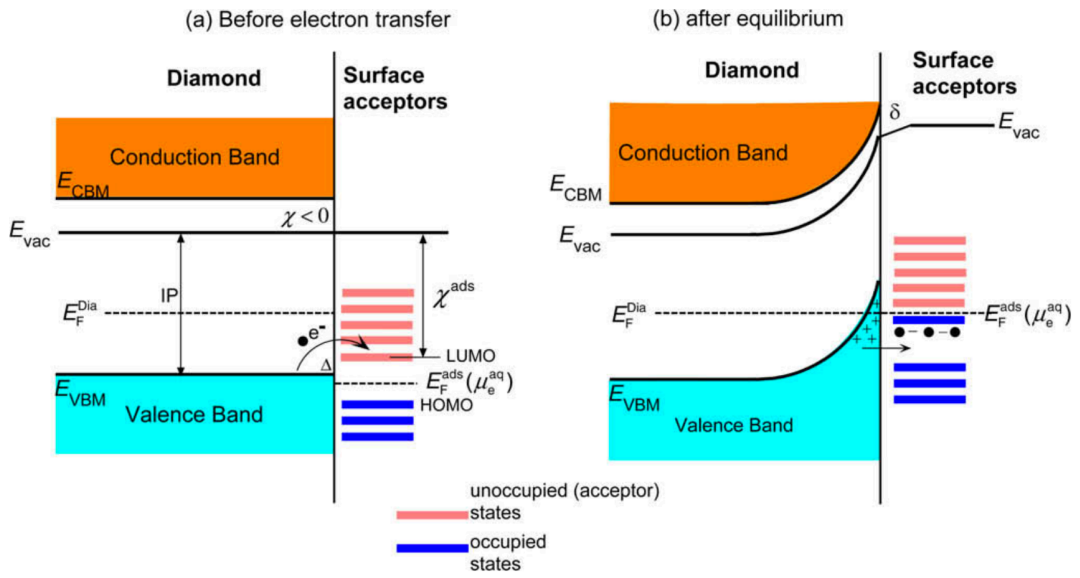

Figure 2-10 – Band diagram of diamond and surface acceptors before (a) and after (b) electron transfer. Band bending causes the Fermi energy to cross the valence band at the surface causing p-type conductivity. Figure taken from Chen et al. [2009][55]

2.5 Nanodiamond

Nanodiamond (ND) materials were produced for the first time during the 1960's in the Soviet Union, however they were only researched from the 1990's.[16] Initially, they were synthesised in aggregate form during detonation experiments in closed chambers, but further research into their properties and potential applications suggested they'd be more useful in single-digit (3-9 nm) colloidal solutions.[16] Ozawa *et al.*[56] have reported the separation of single-digit (4-5 nm) nanodiamonds for the first time in 2007. NDs have since found many applications, due to many unique properties. Being chemically inert meant they could be used for drug delivery and medical imaging,[14,57,58] and having a rich and accessible surface chemistry meant they were of great potential. Other types of NDs have also been synthesised. Ball milling of CVD or HPHT diamond also yields NDs, however they tend to be larger than

Detonation NDs (DND) due to limitations of the milling process.[25] Recently, Ekimov *et al.* have reported synthesis of HPHT NDs as small as 10 nm. Their process limits the growth of crystals by varying the temperature during growth, however their material is heavily boron-doped.[59]

2.5.1 Substitutional Doping in Nanodiamond

In 2008, Ay *et al.*[60] reported on the properties ND powders coated with a boron-doped layer. In their work, insulating ND powders were subjected to CVD growth in presence of diborane and argon; they reported on the electrochemical properties of insulating NDs with a conductive, boron-doped diamond coating. More recently, in 2014, Heyer *et al.*[25] described for the first time the synthesis of boron-doped NDs (10-60 nm) by milling of CVD grown films (boron content ~10^{21} cm^{-3}). In 2015, Ekimov *et al.* have achieved the first direct route for the production of 10 nm, highly doped HPHT boron-NDs. Starting from 9BBN crystals (9-borabicyclo [3,3,1] nonane dimer, $C_{16}H_{30}B_2$) (figure 2–11), and applying a pressure between 8-9 GPa at a temperature of 1550K, diamond crystals were grown to self-limiting ~10 nm crystals in aggregate form.[59] A subsequent acid cleaning process followed the growth to isolate NDs. Boron content of up to 1 at% is estimated from the diamond-peak shift in Raman spectra.

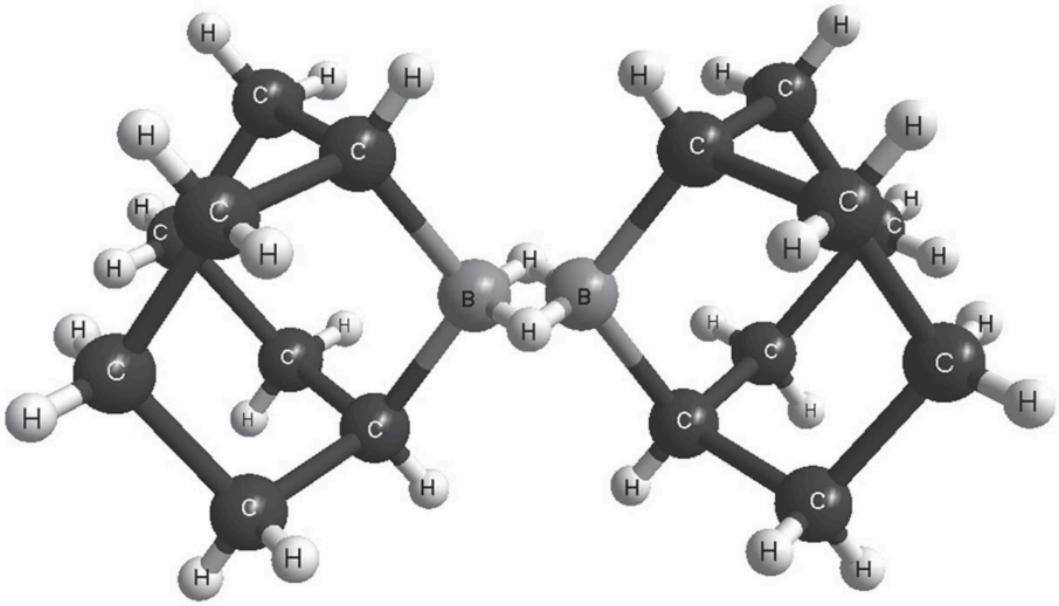

Figure 2-11 - 9BBN precursor molecule used for the direct synthesis of HPHT boron-doped NDs. Figure taken from Ekimov et al. [2015][59]

To date, only p-type doping using boron has been reported in ND materials, with no reports of n-type substitutional doping. Electrical properties of conductive, boron-doped NDs have not been reported, with the exception of insulating NDs coated with boron-doped CVD layers reported by Ay *et al.*[60] In chapter 5, the properties of boron-DNDs, including electrical properties, are discussed. Boron-DNDs are synthesised via the detonation route, by including boron-containing carbons in the detonation chamber.[27] Furthermore, chapter 7 discusses electrical properties of B-DNDs as well as multiple HPHT boron-NDs using electrical impedance spectroscopy (IS) measurements at varying temperatures.

2.5.2 CVD Film Growth from Diamond Seeds

Diamond films can be grown by method of chemical vapour deposition (CVD) on different substrate types, as discussed in section 2.2.1. Such films can be used for electronic applications, ranging from high-power circuits to sensors and detectors, to name a few. In order to grow diamond films efficiently, diamond 'seeds' are used to speed up the process of CVD growth. Epitaxial growth on existing diamond substrates is easily achievable, since CVD growth using methane and hydrogen facilitates growth on top of the existing crystal lattice. However, when growing diamond on other substrates, most commonly silicon or silicon dioxide, diamond seeds are necessary. As discussed before (2.2.1), the nucleation density of diamond seeds on growth substrates, in addition to initial crystal size and gas mixture, play a decisive role in the quality of the resulting films. Williams *et al.* (2008)[61] have studied the effects

of varying the methane/hydrogen ratio in the growth chamber on film quality. As this ratio increases (99% Argon, 1% methane, no hydrogen),[61] the rate of re-nucleation of sp^3 phase carbon increases, resulting in very small crystals (3-5 nm), and hence a high ratio of sp^2 content due to the existence of many grain boundaries. These types of film, usually having grains smaller than 10nm, are named ultra-nanocrystalline diamond (UNCD); they have grain sizes independent of film thickness.[61,62] They can be made conductive by increasing sp^2 content, however this makes them less transparent.[61,62] On the other hand, a hydrogen gas content below 3% results in little or no re-nucleation of sp^3 carbon, thus maintaining growth on existing lattices, in the Van der Drift regime. In this regime, film thickness determines grain size, with thicker films having larger grains. Several environmental factors play a role in determining which crystal facets proceed to grown and which stop growing, as first described by van der Drift in 1967.[63] Films of grains up to 100nm are named nano-crystalline diamond (NCD);[62,64] continued growth yields thicker films with larger grains. In chapter 8, film growth using boron-doped diamond seeds on Si/SiO_2 surfaces is described. In chapter 6, the nucleation process of boron-doped nanodiamonds from DI water colloids is discussed.

3. Schottky Barrier Diodes (SBD)

3.1 Brief History of Metal-Semiconductor Barriers

Ferdinand Braun has first discovered potential barriers at metal-semiconductor interfaces, now known as Schottky barriers, in 1874,[65] for which he was awarded the Nobel prize in Physics in 1909. In 1939 Mott described the behaviour of drift and diffusion through the barrier while at the University of Bristol. Prior to Mott, several researchers[66,67,68] have attempted to explain the behaviour of the interface via a tunnelling mechanism through a barrier formed between a metal and a semiconductor. Mott later described the behaviour of conduction through such barriers as the result of thermal excitation of electrons over the barrier.[69] This was later known as the Mott barrier,[69] correctly describing for the first time the direction of rectification observed experimentally, which wasn't explained in earlier research. Later Spenke and Schottky expanded Mott's model to correct for the profile of the electric field, initially assumed by Mott to be constant with depth, and thus introducing the depletion layer model into the argument.[70] In addition, Schottky and Spenke inferred that the barrier height is equal to the difference between the metal's work function and the semiconductor's electron affinity.[70]

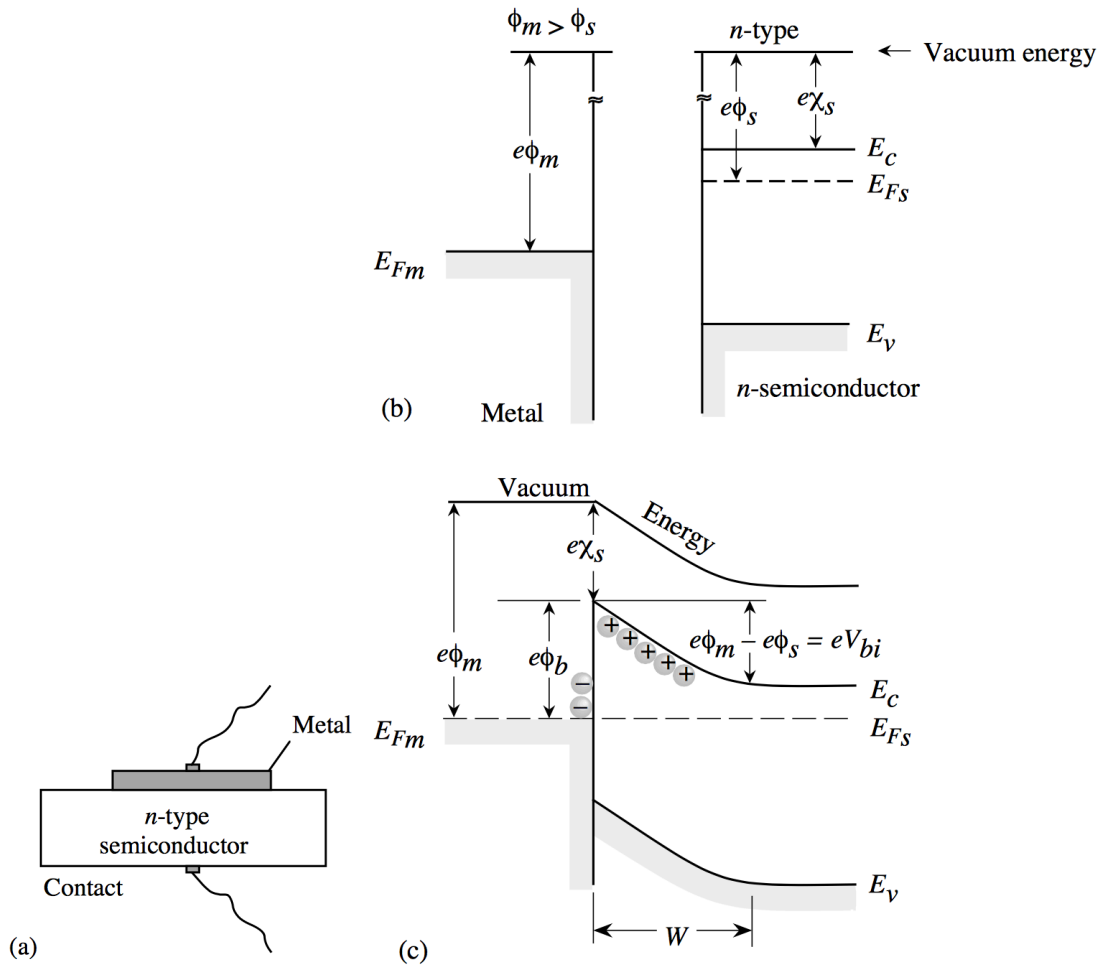

Figure 3-1 - (a) A schematic of a metal on n-type semiconductor junction with top and bottom Ohmic contacts, (b) band structures of separated metal and n-type semiconductor, (c) band structure of the interface between a metal and n-type semiconductor, namely a Schottky barrier, at equilibrium. Figure taken from Singh, J. [2001][71]

Experimental results, however, did not match well with Schottky and Spenke's barrier height argument. In 1947, John Bardeen attempted to explain the deviation as a product of electronic interfacial states, however Heine asserted in 1965 that such localised states cannot exist in junctions of this type.[72] Heine instead proposed that the tails of metal wave functions behave in a similar fashion to resonant or virtual surface states, mimicking the behaviour of surface states initially proposed by Schottky and Spenke.[72]

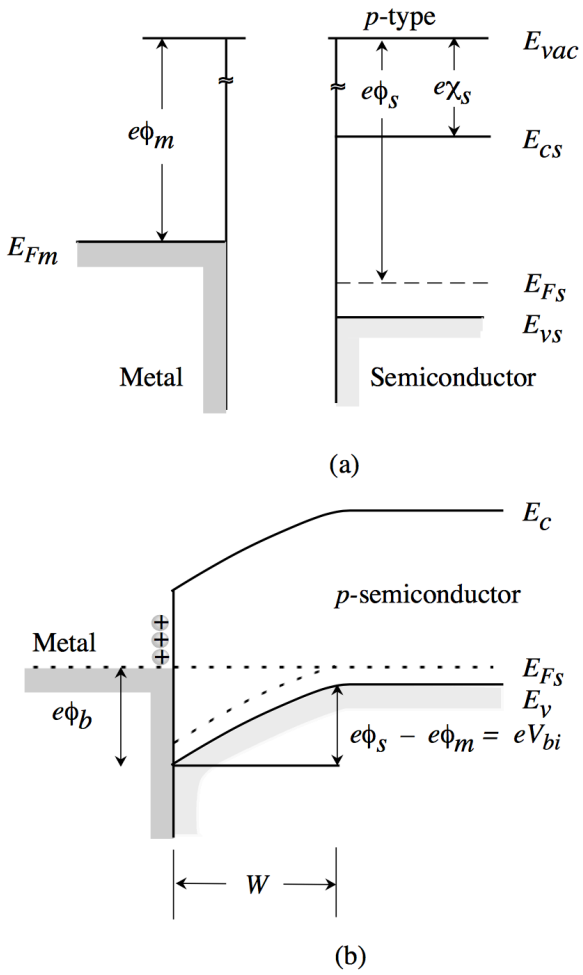

Figure 3-2 – (a) Band structures of separated metal and a p-type semiconductor, (b) band structure of the interface between a metal and a p-type semiconductor, namely a Schottky barrier, at equilibrium. Figure taken from Singh, J. [2001][71]

3.2 Theory of Schottky Barriers

3.2.1 Ideal Schottky-Barrier Interfaces

The theory describing ideal SBDs with high semiconductor mobility, such as Si, GaAs and diamond, postulates the current is due to thermionic emission over the Schottky barrier.[73] Current-voltage (I-V) measurements are modelled by the equation

$$I = I_0 \left[\exp\left(\frac{qV}{nkT}\right) - 1 \right] \qquad \textit{Eqn. 3–1}$$

Here *n* is the ideality factor of the junction, *k* is Boltzmann's constant, *T* is the absolute temperature, and *q* is the elementary charge, while I_0 is expressed as

$$I_0 = SA^*T^2e^{\left(-\phi_B/kT\right)} \qquad \textit{Eqn. 3–2}$$

In this equation S is the diode's area, A* is the semiconductor's modified Richardson constant, and ϕ_B is the barrier height. Performing I-V measurements, the barrier height ϕ_B can be deduced. For n-type semiconductors

$$\phi_B = \Phi_M - \chi \qquad \textit{Eqn. 3–3}$$

Whereas for p-type it is

$$\phi_B = \frac{E_g}{q} - \Phi_M + \chi \qquad \textit{Eqn. 3–4}$$

Where χ is the electron affinity of the semiconductor and Φ_M is the metal's work function, and E_g is the band gap. Capacitance-voltage (C-V) measurements of SBDs can reveal valuable information about their characteistics.[73] In reverse bias mode and while applying a small AC voltage, capacitance *C* of the depletion region is given by

$$C = S\left[\frac{\epsilon_s q N_d}{2(V_{bi} + V_R - kT/q)}\right]^{1/2} \qquad \textit{Eqn. 3–5}$$

Again, here *S* is the diode's area, ϵ_s is the semiconductor's permittivity, N_d is the donor concentration in n-type devices, V_{bi} is the built-in potential and V_R is the applied bias. Plotting the applied voltage against the inverse square capacitance $(1/C^2)$ should give a linear region in the depletion area. The slope of this linear region is $2/S^2\epsilon_s q N_d$, which can be directly used to determine the donor concentration.

When an external bias is applied to the diode, the metal-to-semiconductor barrier height remains the same, however, the semiconductor-to-metal barrier increases in height under reverse bias, and decreases under forward bias.

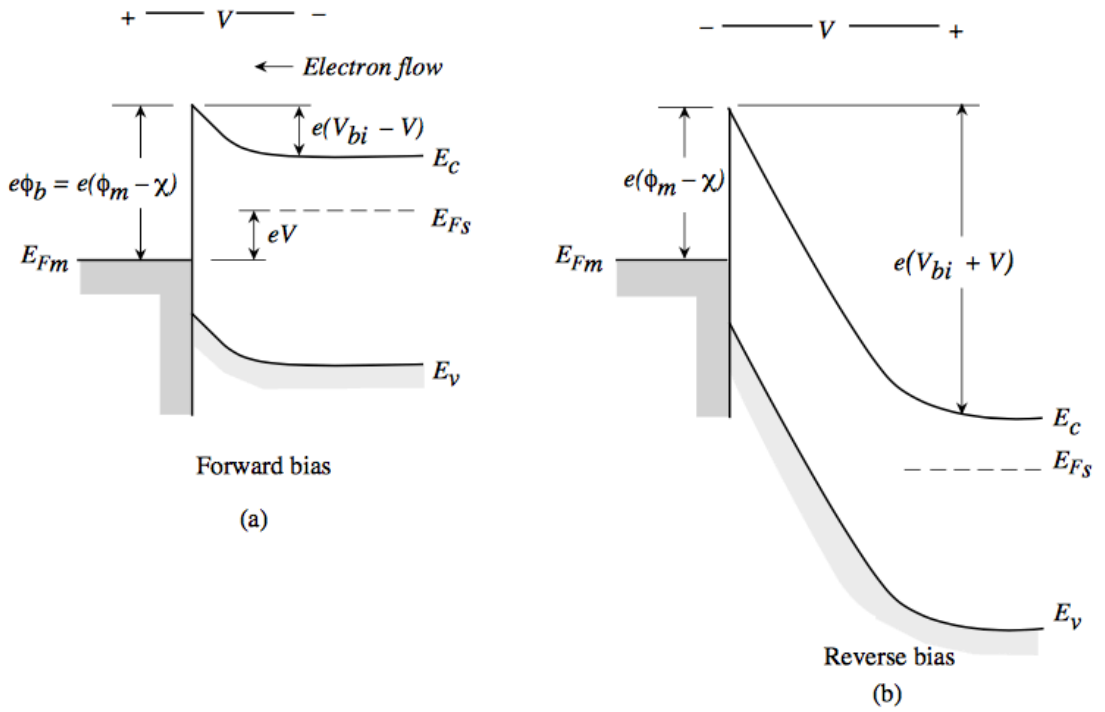

Figure 3-3 – Band diagram of an n-type SBD under (a) forward bias and (b) reverse bias. The metal to semiconductor barrier remains of the same height regardless of bias, while the semiconductor to metal electron flow is affected by the direction of bias. Figure taken from Singh, J. [2001][71]

3.2.2 Modifications to Schottky-Barrier Interfaces

Experimentally, SBD behaviour can deviate from ideal behaviour described in section 3.2.1, and such deviations necessitate modifications to accommodate empirical findings. One of the deviations found empirically are the relation between barrier heights ϕ_B and metal work functions Φ_M. Equations 3–3 and 3–4 above apply well to ionic semiconductors, however the linear relation does not hold well for covalent semiconductors such as GaAs, silicon and diamond.[73] At the boundary of a covalent semiconductor, dangling bonds are present, and thus surface states arise according to Bardeen's theory.[73,74]

Such states give rise to a work function ϕ_0 for surface states. This work function effectively changes the built in potential, such that $V_{bi} = \Phi_M - \phi_0$ for n-type, and $V_{bi} = \phi_0 - \Phi_M$ for p-type semiconductors.[73,74] Surface states are localised according to Bardeen, however, as mentioned in 3.1, Heine modified this theory to properly explain the origin of such states.[72] Surface states affect the barrier height by influencing the charge formed in the depletion area.[73] If the density of surface states is very high, on the order of number of surface atoms at the interface, the barrier height becomes independent of the metal's work function Φ_M and the barrier height is described as being 'pinned' by the surface charge, according to

$$\phi_B = E_g - \phi_0 \qquad \textit{Eqn. 3–6}$$

Mead proposed an empirical term in the relation, suggested further modifications to Bardeen's theory.[73]

3.2.3 Metal-Semiconductor Interfaces

Interfaces between metals and non-metals (insulating or semiconducting) are generally classified depending on the nature of chemical bonding at the interface:[73]

1. A metal is physisorbed on the non-metal's surface,
2. A metal bonds weakly (non-reactive bonding) with a highly polarizable semiconductor (e.g. silicon), forming a compound,
3. A metal bonds chemically to a highly polarizable non-metal,
4. A thin insulating layer, such as an oxide, is formed on the non-metal, stopping the formation of direct bonding between the metal and the non-metal. This is referred to as an interfacial layer.

In type 1, a Schottky barrier is expected to form, with a barrier height directly dependent on the metal's work function. In type 2, surface states play a role in the height of the barrier according to theories such as Bardeen's and Heine's, where the barrier height is less dependent on the metal's work function. Type 3 is the case in which the chemical nature of the bonding decides whether or not a barrier is formed. Type 4 is the case that is most frequently encountered in experiment, thus it is discussed below.[73]

3.2.4 Interfacial Layers between Metals and Semiconductors

The existence of an oxide layer on semiconductor surfaces is almost unavoidable, depending on cleaning and preparation methods prior to device fabrication. Native oxides, or interfacial layers in general, must not exceed 20 Å in thickness for Schottky contacts to form. This is usually the case for silicon, where a native oxide layer between 1-2 nm forms following chemical cleaning.

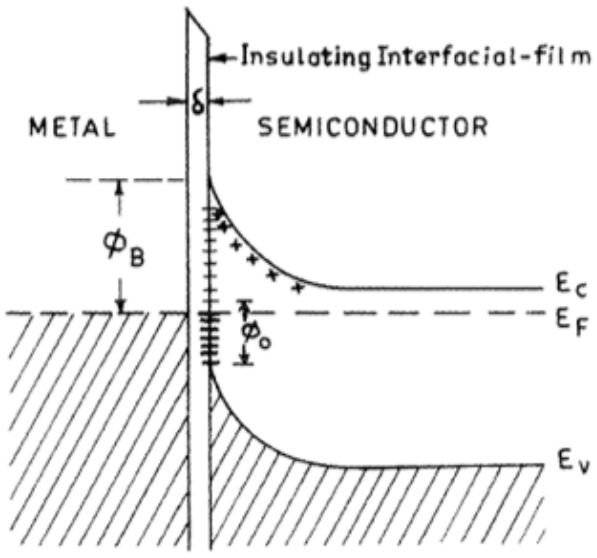

Figure 3-4 – Band diagram of a metal-semiconductor interface with an insulating interfacial layer. Surface states are also shown. The potential is shown to drop

linearly assuming the interfacial layer is a perfect insulator. Figure taken from Tyagi, M. S. [1984][73]

If the interfacial later is assumed to be perfectly insulating, a linear potential drop across the layer may be assumed. This potential drop is very small if the layer does not exceed about 2 nm in thickness, and its effect on the built in potential and barrier height are insignificant and can be ignored.[73] Such contacts effectively separate the metal from the semiconductor into two independent systems, making them easier to study theoretically.[73]

3.3 Applications in High-Power Electronics

Silicon is considered the cornerstone of modern electronics, however the need for large band-gap semiconductor devices is becoming noticeable in fields such as high-power electronics, and in environments where large thermal efficiency is a requirement. Large band-gap semiconductors have higher breakdown fields, and can function well in relatively high-temperature environments due to their low intrinsic carrier density, whereas silicon can only operate up to 200 °C due to having a relatively high intrinsic carrier density.[75] This leads to high leakage currents in silicon in the off-state, a problem that is solved by using large bang-gap materials. Large band-gap materials include Silicon Carbide (SiC) and Gallium Nitride (GaN). Gallium Nitride has been shown to be a suitable material for several types of devices, such as Schottky diodes, and it has the benefit of being easy to grow epitaxially on silicon substrates.[75] This however limits its use in high power electronics since silicon substrates become a limiting factor, however it still has the commercial advantage of being more affordable than SiC. One major drawback of GaN is the difficulty of attaining p-type doping, ruling out

development of bipolar device applications.[75] Silicon carbide, on the other hand, has the advantage of being more developed than GaN and diamond in industry. SiC brings significant gains in efficiency for high-power systems, however it remains prohibitively expensive compared to other materials.[75,76] Such gains in efficiency promoted other materials, such as diamond, for being of greatest performance, hence driving research and development into this promising material.[76] Diamond is arguably the ultimate semiconductor material, however many technical challenges had to be overcome before making it a suitable candidate. The most challenging hurdle to overcome was obtaining n-type doping in diamond. Both nitrogen and phosphorus can be used to achieve n-type substitutional doping diamond, however nitrogen is considered a 'deep' donor with large activation energy (~1.7 eV), making it unsuitable for switching devices. Phosphorus on the other hand has a lower ionization energy (0.58 eV), however until recently,[77,78] it has proven hard to incorporate in high concentration during CVD growth.[78]

3.4 Diamond SBDs

3.4.1 Unipolar and Dipolar Diamond SBDs

Unipolar Schottky diodes are a popular choice in power electronics as they have several advantages over other switching methods. Compared to p-n and p-i-n configurations, unipolar Schottky diodes have much faster switching capabilities and lower recovery times. Quick recovery times in SDBs compared to bipolar devices is caused by the fact that current in SBDs are carried by majority carriers, but is carried by minority carrier injection in bipolar devices.[75,76] In addition, SBDs have low forward voltage drops. Silicon SBDs

for example have a voltage drop range between 0.15 and 0.45 V, whereas that for p-n diodes ranges between 0.6 to 1.7 V. Diamond SBDs has been reported to have breakdown voltages as high as 12 kV, and have the highest mobility values among large band-gap semiconductors.[79] Figure 3–5 compares physical properties of silicon, diamond and other large band-gap semiconductors.

Property	[unit]	Si	4H-SiC	GaN	Diamond
Band gap	E_G [eV]	1.1 i	3.23 i	3.45 d	5.45 i
Dielectric constant	ϵ_r	11.8	9.8	9	5.5
Breakdown Field	F_B [MV/cm]	0.3	2	3 - 4	10
Thermal conductivity	λ [W/cm.K]	1.5	5	1.5	22
Sat. drift velocity e^-	v_s [10^7 cm/s]	1.0	2.0	2.2	2.7
Sat. drift velocity h^+	v_s [10^7 cm/s]	1.0			1.1
Electrons mobility	μ_e [cm^2/V.s]	1500	1000	1250	1000
Holes mobility	μ_h [cm^2/V.s]	480	100	200	2000

Figure 3-5 – A comparison of electrical properties of silicon, SiC, GaN and diamond at room temperature. Figure taken from Traore, A. [2014][76]

Properties of SBDs are dictated by the properties of the semiconductor, as well as the properties of the metal semiconductor interface. The blocking voltage as well as the series resistance is decided by the semiconductor and its properties, such as crystal quality, while leakage current and voltage drop are decided by the interface and its properties.[75,76] Interfacial layers, oxides, chemical bonding between metal and semiconductor, as well as the surface geometry at the interface, are all of significance to device operation.

3.4.2 Diamond SBD Configuration

The geometry of a device also has major effects on electrical and thermal properties.[79] In figure 3–6, the two most common configurations for diamond SBDs are compared. On the left, a vertical setup is shown where a p- layer is grown on top of a p+ layer. Ohmic and Schottky contacts are on opposite

sides of the diamond bulk. The pseudo-vertical setup on the right of the figure shows a thin p+ layer grown on top of an intrinsic diamond layer. A p- layer is grown on top of the p+ layer, and Ohmic contacts are deposited on the p+ layer after etching through the p- layer. Schottky electrodes are deposited directly on top of the p- layer. Generally, p- layers are lightly boron-doped, with B content around ~10^{15} cm^{-3}. On the other hand, p+ layers are metallic with B content at or exceeding 10^{21} cm^{-3}.

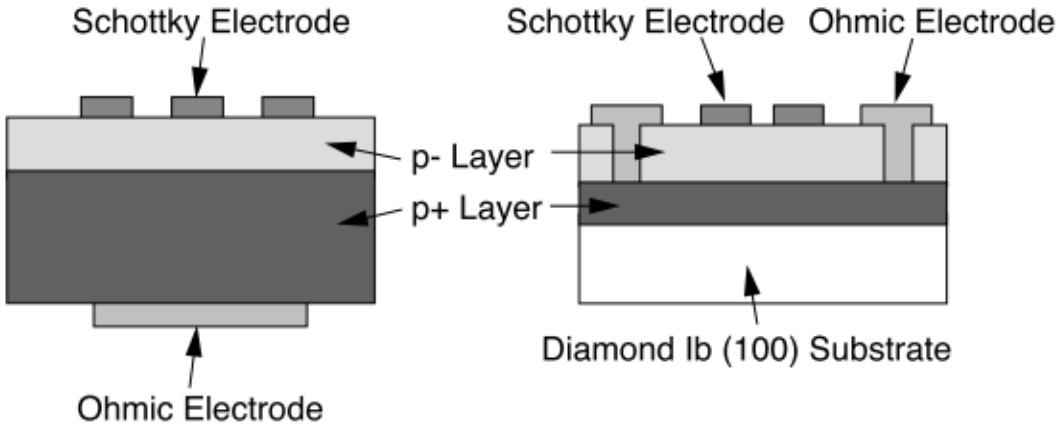

Figure 3-6 – Configurations of diamond Schottky barrier diodes, showing the vertical configuration (left) and the pseudo vertical configuration. Notice the lack of intrinsic substrate in the vertical configuration. Figure taken from Tatsumi et al. [2009][80]

The vertical configuration diamond SBD is the most promising candidate to replace other large bang-gap devices.[75,76,79] This configuration allows for very low series resistance (R_s) value compared to other structures. The breakdown voltage in this configuration is defined as

$$BV = E_M W - qNW^2/(2\epsilon_r) \qquad \textit{Eqn. 3–7}$$

While the specific resistance is defined as

$$R{\times}S = \frac{W}{\sigma} + R_{sub}{\times}S + R_C{\times}S) \qquad \textit{Eqn. 3–8}$$

In the above equations *S* is the diode area, *q* the elementary charge, E_M is the avalanche breakdown field, *W* is the drift layer thickness, ϵ_r is the dielectric constant of diamond, *N* is the dopant concentration, *p* is the drift layer conductivity, σ is the carrier mobility, $R_{sub}\times S$ is the specific resistance of the metallic layer, and $R_C\times S$ is the specific resistance of the Ohmic contact(s).[76] To maintain low series resistance, specific resistance of the Ohmic contacts as well as the metallic layer have to be insignificant, a requirement easily achieved in the vertical configuration by ensuring the use of a degenerate semiconductor (metallic) substrate. When it comes to optimising the breakdown voltage, ensuring a thin drift layer improves performance. A high dopant concentration N reduces the breakdown voltage, thus low doping is also a requirement in the active layer. In pseudo vertical configuration, series resistance values as low as $R_S = 1\ \Omega$ were reported.[79] However, planar device configurations remain superior when it comes to breakdown voltage values; and the high series resistance resulting from low doping in the p- remains a limiting factor for vertical and pseudo vertical diamond SBDs.[79]

4. Experimental Methods

4.1 DND Surface Termination

Diamond materials, in general, accept a wide range of chemical groups on their surfaces. This however is only achievable at harsh conditions, due to the low reactivity of diamond. Bulk diamond, for example, starts oxidising at or above 1000 °C, whereas detonation nanodiamond of few-nanometres starts combusting around 425 °C. Nanodiamonds, generally speaking, are more reactive than bulk diamond, due to different surface energies and electronic levels. Applying treatments in gas phase or in plasma can modify surface terminations of NDs. Nanodiamond synthesis and subsequent cleaning with harsh chemicals results in a mixture of oxygen-containing surface groups which can be further modified.[46]

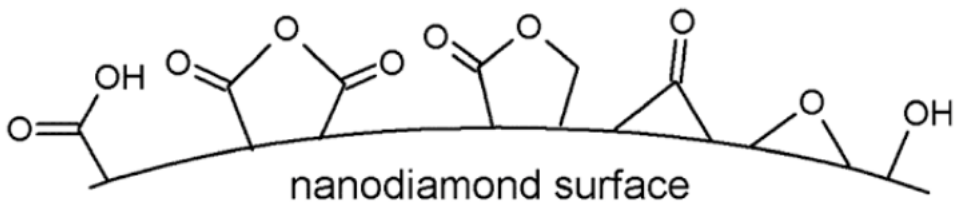

Figure 4-1 - Nanodiamond surface terminations following chemical cleaning. Figure taken from Williams et al [2014] [46]

4.1.1 Hydrogen Termination

Hydrogen termination of NDs is widely used to change their surface groups and overall surface charge. H-NDs are known to be hydrophobic with a positive zeta potential, which is ideal for solution stability and nucleation on silicon dioxide (negative zeta potential). This termination can be achieved using hydrogen plasma (for bulk and thin film diamond), or in gas phase by

annealing nanodiamond powders using molecular hydrogen. The process used in our work is an annealing step in hydrogen gas, at 700 °C for 5 hours and a pressure of 10 mBar. Elemental hydrogen is necessary to achieve complete C−H termination, however terminations at higher temperatures yield hydrophobic particles with positive zeta potentials, with a mixture of C−H and CCOH terminations.[46]

4.1.2 Ozone (Carboxylated-ND) Termination

There are several treatments that can be applied to oxidise NDs, among which are the Carbonyl (C=O) and Carboxyl (COOH). Where the carbonyl group leaves one free carbon bond, carboxylic termination leaves no such free bond and is connected to the ND by a single C−C bond. This termination therefore has multiple uses, and is considered a higher state of oxidation. This termination can be achieved by using mixtures of acids, or can also be performed in the gas phase using ozone as a highly oxidising agent.[46] In this work, we use ozone generated from oxygen gas using a UV light source, and the conditions required to achieve the termination are annealing in 50 mBar of ozone for 5 hours, at a temperature of 700 °C.

4.2 DND De-agglomeration

4.2.1 Agglomerate Separation and Mono-Dispersion

Nanodiamonds can be obtained commercially from many suppliers, and can be sold as powders, hydrogels, or solutions in water or other polar solvents. Following the detonation process, a soot containing DNDs is collected and is processed to remove most of the non-diamond products.

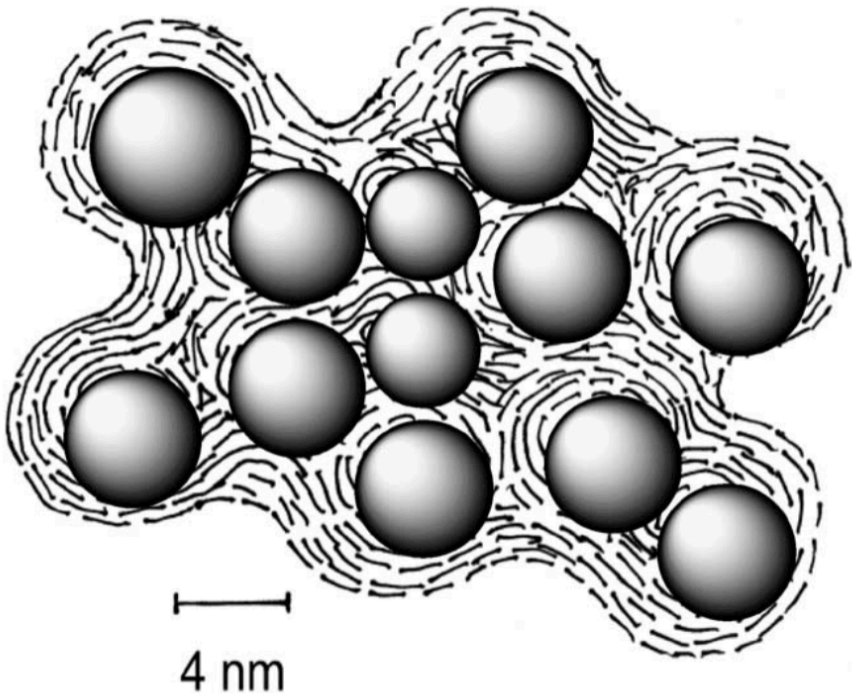

Figure 4-2 - Nanodiamond cores (round) surrounded by aggregate structure. Figure taken from Kruger et al. [2005][19]

Non-sp^3 carbon phases are known to form on diamond grain surfaces,[44] among other elements and compounds that can be present in the detonation chamber. The cleaning steps following detonation will affect the resulting DND product, depending on the nature of the cleaning agents, as well as their quality and purity. Separation of single-digit DNDs is very attractive for nanotechnology applications; however, after careful dynamic light scattering (DLS) experiments, commercially available solutions have been found to be one to two orders of magnitude larger than advertised.[44] This may be due to re-agglomeration of single DNDs, due to instability of single DNDs in solutions. Vul *et al.* (2009)[81] found that the pH level of the DND solution affects the stability of single particles, and that inadequate pH levels can cause DNDs to re-agglomerate. Sub-micron sized DND agglomerates are very stable structures, which are very strong at the core and become more

porous near their surface.[44] Many attempts have been made to reduce the size of these structures, such as ultra-sonication, shock-wave treatment, and bead milling.[19,82] Ceramic bead milling was found to be especially effective at dispersing agglomerates to below 10 nm, however this process is known to cause graphitisation of DND surfaces caused by local heating.[44] As mentioned earlier, Aleksenskiy & Vul[44] have found that metals such as iron, found in cleaning water used to process DND soot, can facilitate the re-agglomeration of DNDs by forming bridge bonds with carboxylic surface groups. For this reason, the authors suggest a cleaning process that includes the use of hydrochloric acid to remove iron and other metals that may be present in water.

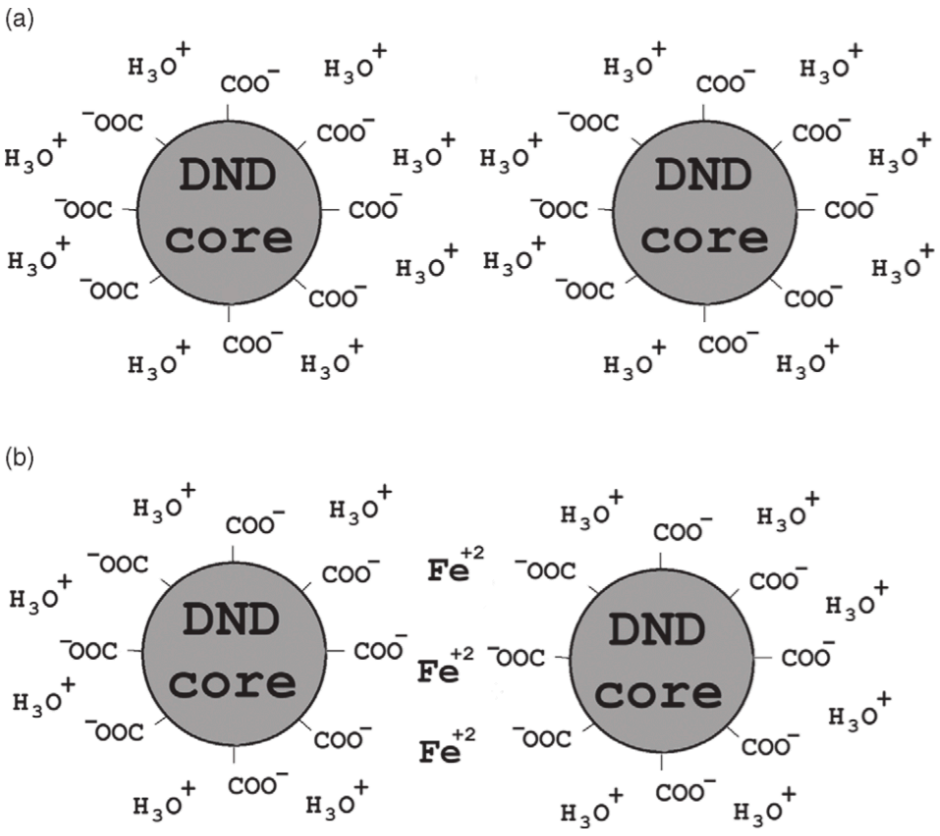

Figure 4-3 - DND particles separated by a double electric layer (a) compared with iron bridge-bonded DNDs (b). Figure taken from Aleksenskiy et al. [2011] [44]

4.2.2 Concentrated Acid Cleaning

Acid-cleaning methods were used in this work to remove sp^2 shells from B-DND agglomerates. To successfully de-agglomerate B-DNDs, subsequent processes were applied. First of all, a boiling step in hydrochloric acid is necessary to remove iron ions. This was done by mixing 250 mg of as-received B-DND powder in 30 ml of hydrochloric acid (37%) and keeping the mixture at a temperature of 80 °C for 15 hours. The next step was to remove sp^2 envelopes[44] and free diamond cores. Boiling B-DNDs in a mixture of concentrated sulphuric and nitric acids achieves this. The process requires the starting material to be free of water as much as possible; therefore, the B-DND sludge following hydrochloric acid treatment was washed in distilled water a few times, then dried in air, and was washed with ethanol a few times. Each washing step comprised of dilution in ethanol or DI, brief ultra-sonication, centrifugation at ~1100 G-RCF and then drying on a hotplate just below the boiling temperature where ethanol was used. This ensures that only atmospheric water levels can remain within the B-DNDs, and the more volatile ethanol would be mostly evaporated. Once the product is dried, it is mixed with a mixture of 10:1 mixture of concentrated sulfuric acid (Alfa-Aesar, ACS, 95-98%) to nitric acid (Alfa-Aesar, ACS, 68-70%) at 80 °C. This treatment was performed twice, once for 18 hours (sample 18H), and the other time for 70 Hours (sample 70H). After each acid treatment, solutions are centrifuged (5 minutes, ~1100 RCF) and supernatants are replaced with DI. This is repeated at least 3 times to ensure only trace amounts of the acids remain. Solutions are prepared in DI water at desired concentration (0.05 g/L), and solutions are

ultra-sonicated for 10 hours at 500 W power and a maximum temperature of 30°C.

4.3 Solution Stability and Nucleation on Substrates

4.3.1 Water-Based Colloidal Stability

One of the main reasons for achieving mono-dispersion in nanodiamond solutions, including DNDs, is to be able to coat surfaces and substrates with monolayers. In order to grow diamond thin films, for example, the seeding coverage on substrates like silicon (with SiO_2 native oxide layers) is required to be as high as possible. For this to be achieved, stable solutions with mono-dispersed NDs and appropriate electrostatic properties are desired. Hees *et al.*[83] have performed air-annealing and hydrogen surface treatments on DNDs, and have prepared solutions of the products in a range of pH levels. They have found that the choice of surface group termination and pH level of a solution are essential for high nucleation densities on SiO_2 surfaces. The zeta potential is defined as the charge of the electric double layer surrounding particles in solution,[84] and for optimum nucleation of particles on surfaces, a maximal zeta-potential separation between them (one positive, the other negative) ensures maximal electrostatic attraction. Silicon dioxide is known to have a negative zeta potential above pH≈4, therefore a strongly positive zeta potential in the same pH range would significantly improve the seeding process.[83] Hees *et al.* performed hydrogen termination of DNDs by annealing powders in a hydrogen atmosphere at a pressure of 10 mBar, and a temperature of 500 °C. This was followed by ultra-sonication in DI water for several hours, then centrifugation at 40,000 RCF for two hours.

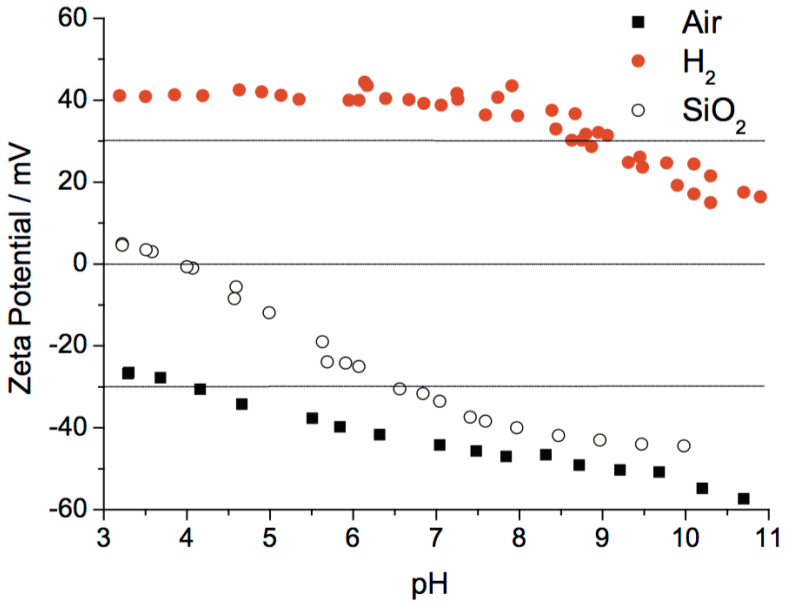

Figure 4-4 - Zeta potentials at different pH levels for air-annealed DNDs, hydrogen annealed DNDs, and Silicon dioxide. Figure taken from Hees & Williams [2011][83]

4.3.2 Ultra-sonic Nucleation from Aqueous ND Solutions

Nanoparticles such as NDs can be very useful when coated on surfaces. For diamond electronics applications, for example, nucleation or 'seeding' of NDs on Si/SiO_2 substrates enables them to be used as the starting point for CVD diamond growth.[85] Many methods can be used to seed nanodiamonds onto flat substrates, such as ND grit abrasion, bias-enhanced nucleation, and spin coating of ND containing photoresists. While the methods above can yield high nucleation densities (up to 10^{12} cm^{-2}), they only apply to flat surfaces.[85] Using ultra-sonication, substrates submerged in ND solutions can be easily and quickly coated with nanodiamonds, and the properties of the resulting layer depend on factors such as frequency and energy of ultra-sonication. 3D structures as well as flat surfaces can be coated alike, enabling CVD diamond growth on arbitrary substrates.[85] In this work, we use a bench-top 120 W, 40 KHz ultra-sonic bath for nanodiamond seeding.

4.3.3 Salt Concentration Variation

Yoshikawa's[86] work suggests a KCl concentration between 10^{-2} M and 1 M suppresses the potential energy (repulsive) between NDs, which isn't good for seeding. On the other hand, deionized water (~10^{-7} M) water results in very long range potentials (~100s of nm), keeping in mind average spacing for ~4 nm single NDs in solution (0.05 g/l approx.) is ~100 nm. Hence it is best to have positive potentials, which are short range, on the order of 10s of nm, therefore keeping single NDs comfortably distant from neighbors compared to just DI water. This is done using a KCl concentration between 10^{-5} and 10^{-3} M in the colloidal solution. KCl (~3 M, Sigma Aldrich) is first diluted in DI water for added control over the amount added, and is then added to the DI water solution using a micropipette. Solution is then ultra-sonicated for 10 minutes. It is important to also note that when interfacing with a seeding substrate (SiO_2), attractive forces from negative-Z-potential SiO_2 are much stronger than repulsive force between NDs, hence forcing them to be in close proximity of each other on the surface. This results in instability when the repulsive forces are long range, so they're more likely to form surface aggregates. On the other hand, if the repulsive forces are short ranged, NDs will be more comfortable forming thin layers without being forced to form agglomerates.

4.3.4 Variation of Solution pH level

Titration of pH is performed to test the effect of pH titration on the seeding density of boron-doped NDs. Starting from 10 ml DI water solutions of ND concentrations between 0.05 and 0.1 g/L, each sample's pH was measured prior to testing using a Mettler Toledo MP220 pH probe. The samples were then split to appropriate portions to allow processing of the acidic and alkali

sides of the titration on fresh samples. For example, where the starting pH was 2, 2 ml was sampled to perform the pH 1-2 titration and the remaining 8ml was used for the 2-12 pH titration. The pH titration was performed manually following these steps:

- A portion of sample was placed into a glass vial with a small magnetic flee on a stirrer plate whilst continually measuring the pH.
- Drops of 0.01 M or 0.1 M of HCl (hydrochloric acid) were used to reduce the pH until it reached the desired pH.
- Drops of 0.01 M or 0.1 M of NaOH (sodium hydroxide) were added to increase the pH to reach the desired pH.

Once the pH reached the desired point 0.5 ml of the sample was removed to measure the zeta potential using the dip cell. Once this measurement was completed a second portion of 0.5ml was added to the cell to measure the particle size. Due to the limited sample volumes, once the analysis was completed, the sample was recombined with the bulk and the pH adjusted again for the next pH point. The samples were measured in ~1 pH point increments at room temperature.

4.3.5 Zeta Potential Measurement

Dispersions in solutions acquire a surface charge due to interactions with ions. The electric double layer that forms around a particle in solution can be thought of as two separate layers; the Stern layer, representing ions with strong adhesion to the particle, and a diffuse layer.[84,87] A slipping plane is

thought to form inside the diffuse layer, in close proximity to the Stern layer. The surface potential surrounding the particle becomes of less significance in solution, due to the formation of the double layer, and the potential at the slipping plane, known as the Zeta (ζ) potential, gains more significance.[87]

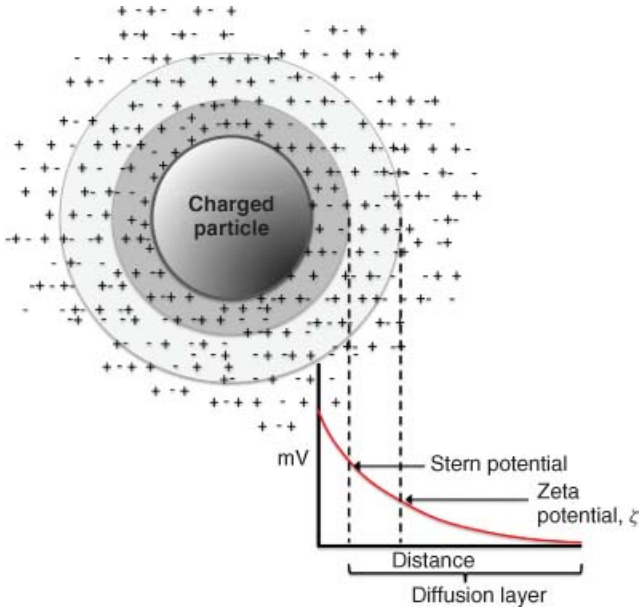

Figure 4-5 – A particle in solution showing the Stern layer, the diffuse layer and potential as a function of distance from the particle edge. Figure taken from Fernandez et al. [2010][88]

The Zeta potential is then the acquired charge in solution, and is affected by the particle's surface charge, ionic formulation and concentration of the solution. Choosing the right charge and concentration of ions will therefore strongly affect the stability and dispersion of particles in the medium, deciding whether particles attract or repel each other. This gives the pH level of a solution great significance when considering colloidal stability or interfacing with surfaces.[87] The Zeta potential cannot be measured directly, and instead other methods can be used. One method, which is used in this work, is measuring particle velocities in solution due to electrophoresis. When a bias is applied, charged particles will be attracted or repelled from an electrode, and

the velocity at which they travel will be proportional to their charge and the strength of the applied field. The laser Doppler effect is used to measure particle velocities, and one of multiple theories can be used to better estimate the Zeta potential from particle velocities. Here the Smoluchowski coagulation model is used with the F(*ka*) parameter set to 1.5, where *k* is the inverse Debye length and *a* is the particle diameter.[89]

4.4 Particle Size Analysis using Dynamic Light Scattering (DLS)

Dynamic light scattering (DLS) is a technique for particle size analysis, based on the dynamics of Brownian motion of colloids and nanoparticles. Particles in solution move around affected by random thermal fluctuations; and the speeds at which they move are directly related to their size distributions.[87] Larger particles move slower than smaller ones, and the temperature is also a determining factor in Brownian motion. To measure particle size, a laser irradiates the solution, and a dotted pattern emerges.[87] The intensity of the pattern at a certain angle varies with time, and an avalanche photodiode detector (APD) is used to detect it. A correlation function relating to the dimensional distribution is formed, giving detailed information about particles' size.[87]

4.5 FT-IR and ATR-FTIR

Fourier-transform infrared spectroscopy (FT-IR) is a characterisation technique that is highly sensitive to molecular vibrational modes in gases, liquids and solids.[90] In the 1960's, FT-IR was mostly used to reveal the structures of organic compounds, and since then it has evolved to become a very capable analytical technique.[90] Even though FT-IR spectrometry is very

revealing, it is usually used as a complimentary analytical method, and is rarely used alone to study the structure of a material. This is due to the principals of infrared absorption in molecules. Molecular vibrations aren't always active in the infrared region, depending on whether or not the dipole moment of the vibrational mode changes.[90] In the mid-infrared region, IR absorption between 400 and 4000 cm^{-1} is usually measured, in resolutions of about ~4 cm^{-1}. Higher resolution of between 1-2 cm^{-1} can also be achieved.[90] A prism is usually used to achieve high resolutions, but it means only a very small part of the spectrum is measure at one instance, and long measurements (~15 minutes) are necessary to cover the full spectrum between 400 and 4000 cm^{-1}. [90] Certain molecules, such as water, have very strong, dominant absorption spectra, and are routinely avoided when making FT-IR measurements.[90] To achieve this, purging the chamber containing the apparatus and sample with nitrogen is desirable. Since not all molecules (or molecular groups) are IR active, FT-IR spectra can only be used for partial identification, and is almost always accompanied by other techniques such as Raman spectroscopy.[90]

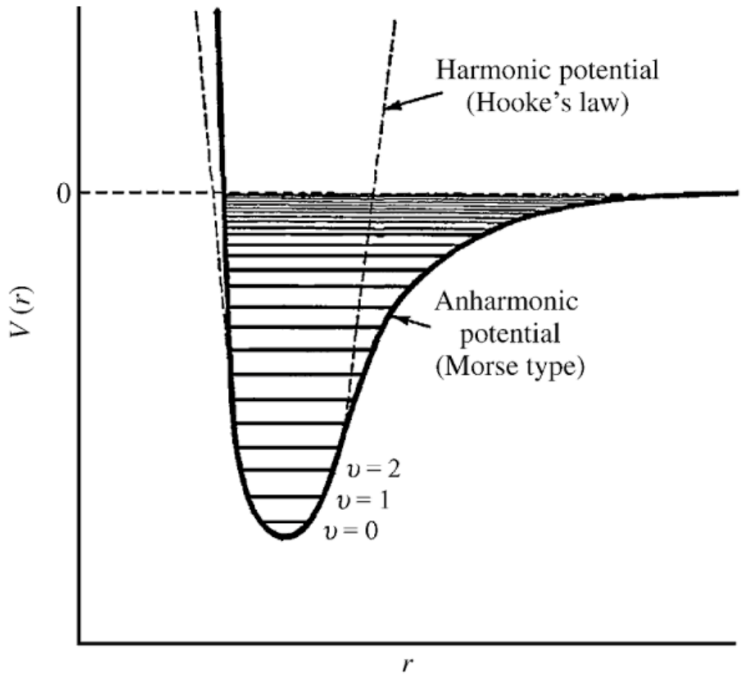

Figure 4-6 - Potential energy of a diatomic molecule as a function of displacement during a harmonic vibration (dashed) and anharmonic vibration (solid). Figure taken from Griffith & Haseth [2007][90]

Vibrational modes, when quantised, result in discrete energy levels, and when transitions between energy levels take place, absorption and emission in the infrared take place. The number of vibrational modes for a molecule with N atoms is 3N, three of which represent rotational modes, and three represent translational motion, therefore leaving 3N−6 modes in which they can vibrate. For linear molecules, however, symmetry about one axis means that some modes are degenerate, leaving 3N−5 unique vibrational modes. For this reason, diatomic molecules have only a single fundamental vibrational mode, making them very identifiable using FT-IR. In this work, FT-IR spectra were measured using KBr pellets, prepared by mixing KBr salt with nanodiamond powder and applying 10 tonnes of pressure in a mechanical press.

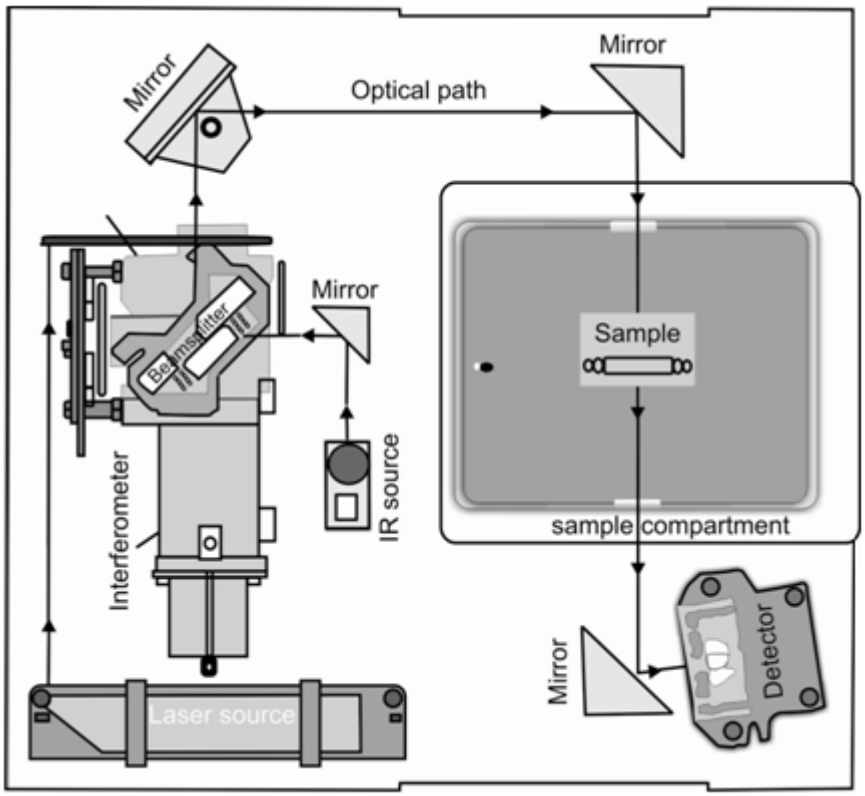

Figure 4-7 – Example of FT-IR apparatus in transmission mode. Figure taken from http://www.expertsmind.com[91]

Transmission through the pellets is then measured, and the thickness of the pellets is kept between 1-2 mm for optimal results. In addition to the above, ATR (attenuated total internal reflection) FT-IR was also used in this work, to obtain reflectance spectra directly from powders. Although this method allows direct measurement of samples by placing them on the ATR crystal, results weren't comparable in quality to transmission FT-IR. This was mainly due to the strong absorption of water in nanodiamond powders, which dominates the spectrum. Another method for transmission measurements from aqueous solutions is to use calcium fluoride (CaF_2) windows, which can be drop coated with nanodiamond solutions and annealed on a hotplate to obtain thin films. This has to be done slowly and carefully to avoid damaging the CaF_2 windows, which are very sensitive to heat. In nanodiamond, FT-IR and ATR

are especially useful to detect CH_x, C=O, C=C and O−H groups, among others, which are useful in determining the surface terminations present.

4.6 Raman Spectroscopy

As is the case for FT-IR spectroscopy, Raman spectroscopy is an analytical method that is sensitive to vibrational modes.[92] However, the main difference between the two methods is that in Raman spectroscopy, the process of scattering involves two-photons, whereas in IR spectroscopy, the resonance process only involves one photon.[92] In a Raman scattering process, a change in the polarizability of the molecule takes place as a result of molecular vibration, which then interacts with incoming radiation; this interaction creates the induced, or virtual, dipole moment, which radiates the observed photon.[92]

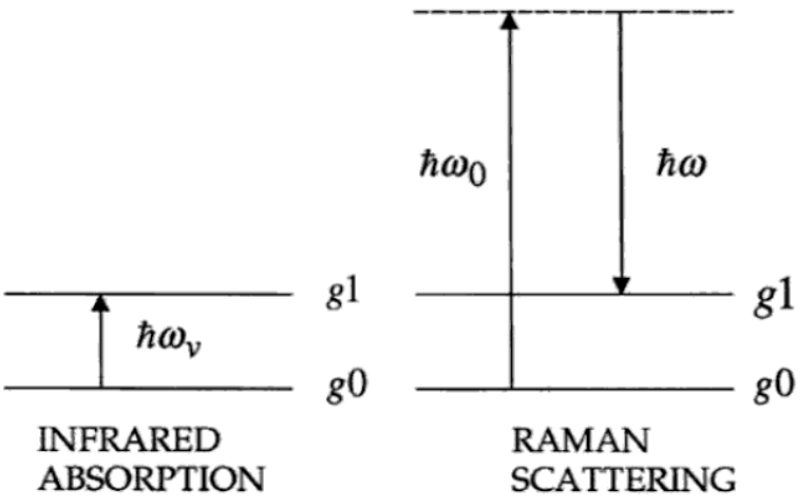

Figure 4-8 - Energy diagram comparing IR and Raman scattering. The dashed line represents the virtual energy state. Figure taken from Lewis & Edwards [2001][92]

The induced state can be one of many allowed vibrational states, and in theory, Raman spectroscopy is sensitive to all allowed modes.[92] When the

vibrational energy of the molecule is increased, it is a Stokes-Raman process, however if the vibrational energy is decreased, it is considered an anti-Stokes-Raman process. Generally speaking, Stokes-Raman modes have stronger emissions than anti-Stokes modes, however modifications to the apparatus can allow accurate measurement of anti-Stokes Raman modes.[92]

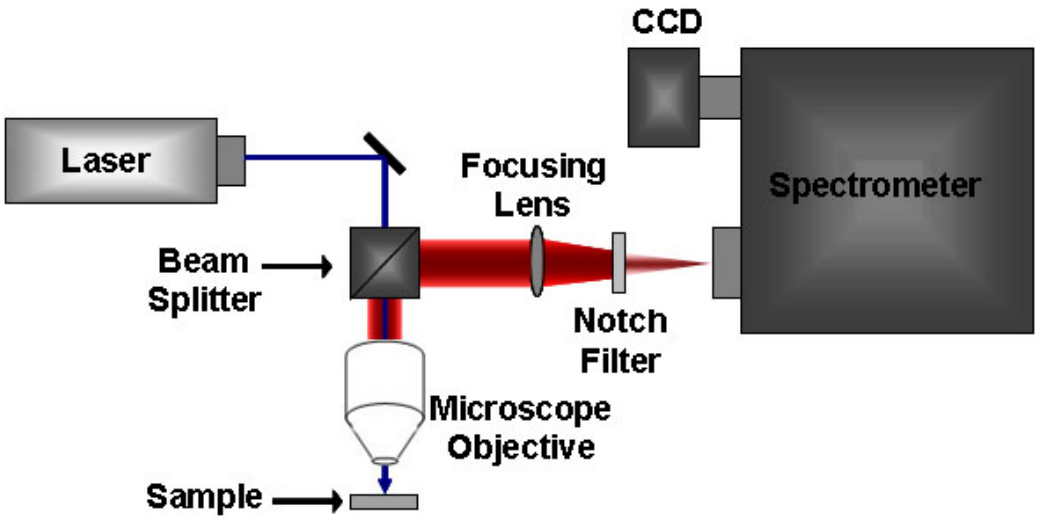

Figure 4-9 - Schematic of micro-Raman apparatus. Figure taken from http://archive.cnx.com[93]

According to Ferrari and Robertson[94], nanodiamond materials have a main diamond feature at ~1332 cm^{-1}, in addition to four additional features at ~1150 cm^{-1}, ~1350 cm^{-1}, ~1480 cm^{-1} and ~1550 cm^{-1}. The main peak at ~1332 cm^{-1} is the first order Raman peak observed in tetrahedral, sp^3 C–C phases, and intensifies with reduced excitation wavelength. The location and width of this feature is sensitive to grain size in the single-nm range, due to phonon confinement.[94] The feature at 1150 cm^{-1} is attributed to trans-polyacetylene, along with its companion feature at 1480 cm^{-1}. The peak at 1350 cm^{-1} is assigned to the D peak of amorphous carbon, while the 1550 cm^{-1} one is the

G peak, also of amorphous carbon. The D peak is generally due to breathing in sp^2 carbon rings, while the G peak originates from bond stretching in sp^2 phases.[94] Nanodiamond spectra are normally dominated by features representing sp^2 phases, except in UV excitation, where the first order Raman peak becomes intense. The G peak is known to be linearly dispersive in disordered carbon, where dispersion is dependent on excitation wavelength, while the D peak is normally linearly dispersive with excitation energy.[94] In this work, micro-Raman spectrometers from Renishaw are used, which have Nd:YAG, frequency-doubled 532 nm green laser sources. The wavelength of excitation affects the outcome of Raman measurements, with some features, or peaks, being more or less sensitive depending on the excitation. In diamond, the first order Raman excitation at ~1332 cm^{-1} is considered the main identifier, and it's intensity depends on the exciting radiation. When excited with UV radiation, the first order Raman is most intense, and its intensity is reduced as the wavelength of excitation increases. A 532 nm excitation is normally sufficient to detect the first order Raman feature in most diamond samples, including nanodiamond powders or films, however, when the diamond cores are embedded within sp^2 structures, for example, UV excitation may be necessary to observe the first order Raman feature. Other features in nanodiamond are also measured using Raman spectroscopy, including sp^2 carbon phases, boron impurities (in concentrations above 10^{20} cm^{-3}), among others.[95,49] All nanodiamond Raman spectra presented in this thesis were taken after depositing NDs by drop-coating on silicon surfaces. Drop-coated films exceed 0.5 μm in thickness to minimise the silicon background. A 20x objective lens is used at a working distance of ~8.8 mm.

The laser spot size is estimated to be ~3.75 μm and the penetration depth is 0.7 μm for a 532 nm wavelength excitation. This objective ensures the laser spot is large enough to measure hundreds to thousands on NDs at a time, depending on average ND diameter. Scans are performed at multiple locations per sample (centre, edges of drop-coated film) to find the spectrum with the smallest silicon background, requiring no further silicon background subtraction. When exposed at 50-100% laser power (150 mW maximum laser power), small variations of the D/G peak ratios are measured due to sample overheating and graphitisation, on the order of a few percent. This is avoided by changing scan settings in the Renishaw WiRE control software to low laser power (1-5% of maximum power) for extended periods of time (30 second exposure time per scan), while averaging over 20 scans per sample.

4.7 Atomic Force Microscopy (AFM)

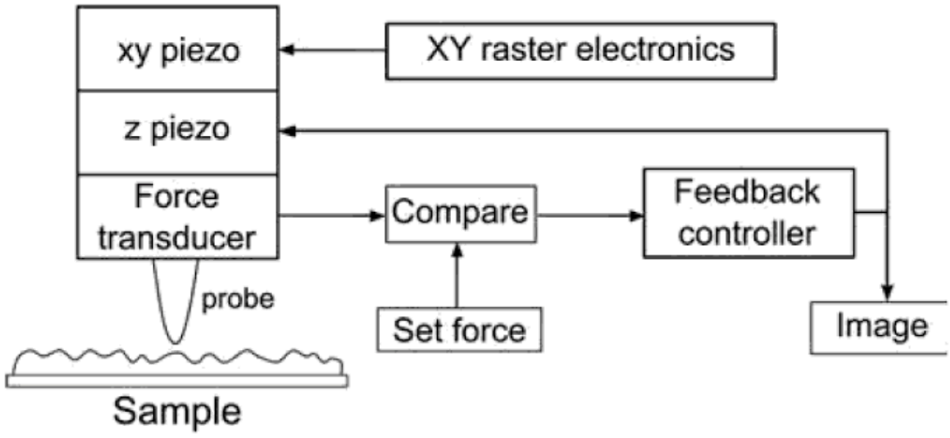

Figure 4-10 - Schematic of an atomic force microscope setup. Figure taken from Eaton & West [2010][96]

Atomic force microscopy is used in this work to check the seeding of nanodiamonds from colloidal solution onto silicon substrates. The principle

behind AFM technology is a scanning probe that is kept close to the scanned surface by maintaining a feedback loop.[96] There are several modes of operation for AFM, which work for different types of sample, such as tapping mode and contact mode. A cantilever with a tip on one end is excited near its resonant frequency by a laser beam, which is reflected off the cantilever surface onto an optical detector.[96] Using a combination of force transducers, piezoelectric transducers (with sub-nanometre movement range) and feedback controllers, the AFM instrument (figure 4–10) is able to reliably maintain a constant distance from the measured surface (in non-contact mode) and feel the surface topography at the same time.[96] This allows sub-nanometre topography to be measured, and in controlled conditions, AFM can even be used to image single atoms.[96] To be able to image diamond surfaces, or silicon substrates seeded with nanodiamond layers, special AFM tips of increased hardness are sometimes necessary. In addition, to be able to scan surfaces of single nanodiamonds below 100 nm in diameter, narrower tips, sometimes of few-nanometre dimensions are used.

4.8 Impedance Spectroscopy

Impedance spectroscopy (IS) is a relatively new and very capable technique that allows the study of electrical and electrochemical properties of materials and interfaces, as a function of frequency.[97] Different conduction processes in one material, with different dipole responses, react differently to induced potentials, and reveal information about conduction processes and energy storage in a material.[97] Many dielectric processes, generally divided between resonances and relaxations, are in the range of frequencies studied by IS, typically between 1 mHz and 10 MHz.[97] Since diamond is considered a

dielectric material, the dielectric interface between electrodes and the dielectric can be studied using IS, and the response can be fitted to known equivalent circuits, such as the parallel R-C element, or the constant phase element.[97] In most common, commercially available IS instruments, impedance is measured at a constant frequency after applying an alternating potential, and the current and phase are then measured.[97] This is repeated for a range of frequencies, and is commonly represented by plotting the resulting real and imaginary impedance components against each other (known as a Nyquist diagram).[97] The impedance of a capacitive component is:

$$Z_c(\omega) = \frac{1}{j\omega C} \qquad \textit{Eqn. 4–1}$$

Whereas a resistive component has:

$$Z_R = R \qquad \textit{Eqn. 4–2}$$

Therefore, a combination of the two components in parallel gives:

$$\frac{1}{Z_{RC}} = \frac{1}{R} + j\omega C \qquad \textit{Eqn. 4–3}$$

And the amplitude of Z_{RC} is:

$$|Z_{RC}| = \frac{1}{\sqrt{\left(\frac{1}{R}\right)^2 + (\omega C)^2}} \qquad \textit{Eqn. 4–4}$$

And finally, the phase between the applied and measured currents is:

$$\phi_{RC} = \tan^{-1}(-\omega RC) \qquad \textit{Eqn. 4–5}$$

The R and C components in parallel have a Nyquist diagram, which is best described as a semicircle (see figure 5–1 for example). The equivalent circuit model ascribed to a materials response is not unique, and different combinations of components, which have the same response over the frequency range, can sometimes be found. When studying samples with large

degrees of structural inhomogeneity, such as nanodiamond materials, equivalent circuits containing CPEs are usually the closest fit, and information about resistance and capacitance values can be obtained.[97] When this is repeated for a range of temperatures, the Arrhenius relation can be used to obtain information on activation energies of conduction paths. Nanodiamonds can behave similar to nano-crystalline diamond films, which are diamond grains separated be grain boundaries, and conduction can happen through the crystals, or bypassing them altogether through grain boundaries. This kind of behaviour has been studied by Ye *et al.,*[98] and similar methodology in this work, keeping in mind the additional conduction mechanisms that may be introduced by boron doping.

4.9 Transmission Electron Microscopy (TEM)

Transmission electron microscopy is an imaging technique that uses accelerated electrons to look at samples with sub-nanometre resolutions.[99] Electrons are accelerated in an electric field to between 100-200 kV after being emitted from an electron gun, and magnetic lensing 'condensers' are utilized to guide accelerated electrons.[99] Further lensing is applied once electrons have passed through the specimen, and they're guided to an image sensor.[99] Both elastic and inelastic processes take place between accelerated electrons and samples, therefore samples have to have thicknesses between few nanometres and 100 nm, depending on their composition.[99]

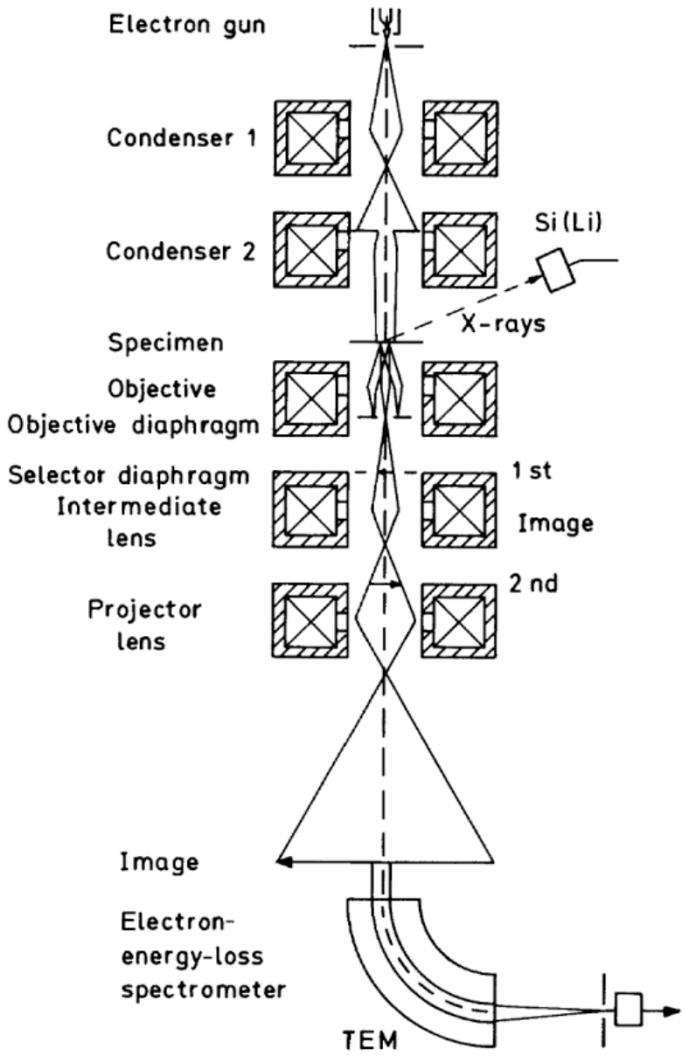

Figure 4-11 - Schematic of a TEM equipped with additional X-ray and EELS modules. Figure taken from Reimer & Kohl [2008][99]

High-resolution TEM (HR-TEM) was used in this work to image single nanodiamonds and ND agglomerates. Resolutions of 0.2 nm were obtained when resolving diamond lattice lines. This was performed in collaboration with the Experimental Techniques Centre at Brunel University, using a Jeol 2100F FEG 200 kV HR-TEM. Samples were briefly prepared in Argon plasma after being deposited onto a carbon-film on copper grid specimen supports.

4.10 Photoluminescence (PL)

Photoluminescence spectroscopy is the technique of exciting electronic levels of materials, such as crystals, using photons of known energy, and measuring the resulting photonic emissions. The energies and time delays of emissions depend on the relaxation processes involved, and can be used to identify inclusions, dopants and defects in crystals and semiconductors.[100,101] In semiconductors, strong absorption is expected at or above the bang-gap energy (~5.5 eV, corresponds to ~225 nm photons in diamond). Dopants and inclusions known to have photonic emissions in diamond include nitrogen, boron, nickel, silicon[101] and aluminium,[52] in addition to PL from radiation damage and dislocations.[101] In this work, a time-correlated single-photon counting instrument (TCSPC) from Edinburgh Instruments (Lifespec-PS with 405 nm pulsed laser) is used. It is equipped with a standard MCP detector. All samples are deposited on silicon substrates from aqueous solutions prior to measurement.

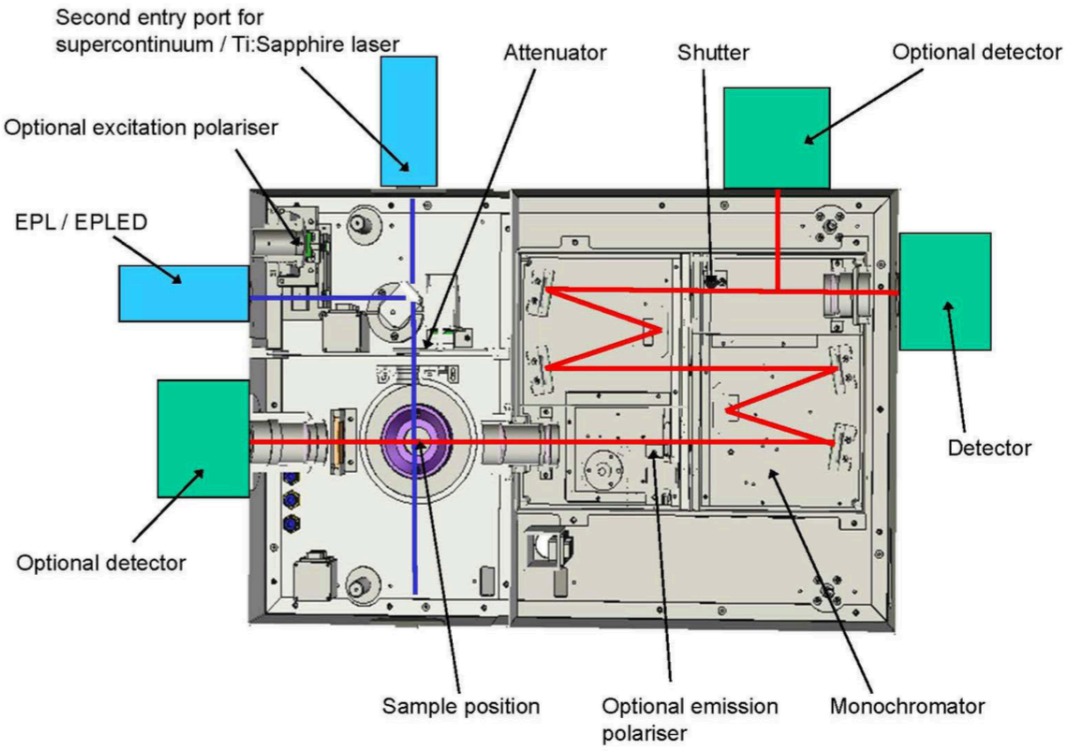

Figure 4-12 - Schematic of Edinburgh Instruments Lifespec TCSPC. Figure taken from http://www.edinst.com[102]

4.11 Impedance Measurement Setup

4.11.1 Apparatus and Connections

Impedance measurements presented in chapter 7 were performed in a specially modified vacuum chamber. The need for performing this experiment in a vacuum chamber originated from the desire to avoid making surface measurements. Some surface terminations, such as hydrogenation) can cause surface conductivity, so can sp^2 carbon phases. To ensure minimal surface conductivity measurement, the need to anneal samples at high temperature in presence of an inert gas (Argon in this case) meant a vacuum chamber is required. High purity Argon has been used to purge the chamber after reaching base pressure, then an annealing process is performed at 10 mBar Argon pressure (200 °C) for 30 minutes. This ensured desorbed water

vapour is evaporated. The low-pressure cylindrical cold wall (water cooled) chamber is capable of reaching pressures as low as 1×10^{-7} mBar. Pumping down is done using an Edwards E28 rotary oil sealed pump, assisted by a Leybold Oerlikon TurboVac 50 turbo pump. Inside the chamber, a ceramic vacuum heater capable of reaching 500 °C is placed on top of ceramic beads for better thermal insulation. The heater is driven by a programmable TENMA 72-2550 voltage source, capable of 60 V and 3 A currents. Maximum current is limited to 0.6 A to avoid damaging the heater. A C-type thermocouple is built into the heating element, which is connected to a K-MAX6675 thermocouple readout, sampled every second by an Arduino Mega 2560.

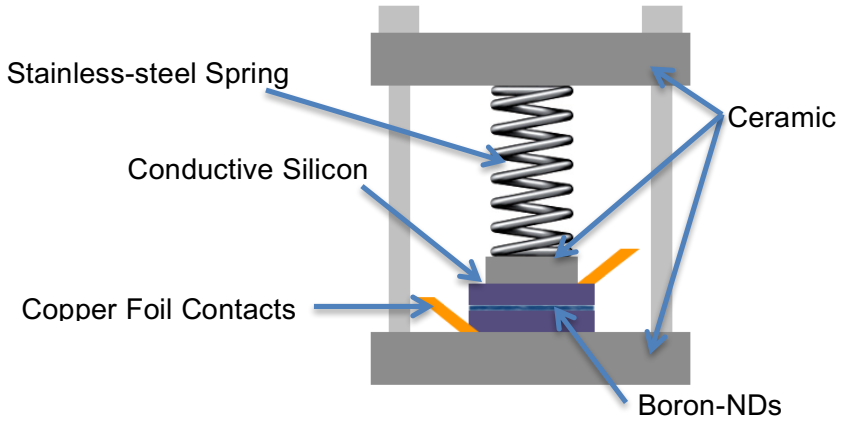

Figure 4-13 – Schematic of the sample holder used during impedance spectroscopy measurements. Two ceramic plates (top and bottom) are held together by stainless steel bolts and nuts. Two conductive silicon substrates enclose the nanodiamond layer being measured. A ceramic spacer is placed on top of the top silicon substrate, so that even pressure is applied using a stainless steel spring. Copper foil Ohmic contacts are also shown.

Copper wires are used to connect the sample inside the chamber to BNC coaxial cables (also copper) outside the chamber, through a BNC vacuum feed through. A Solartron 1260A Impedance Gain-Phase Analyser, equipped with a high impedance input Solartron 1296 Dielectric Interface, with the

optional reference module, is used to perform impedance measurements. The 1260 impedance analyser is capable of measuring impedances of up to 100 MΩ, however, the addition of the high impedance dielectric interface enables accurate impedance measurements of up to 10^{14} Ω. Accuracy of impedance measurements is <0.2% for impedances between 100 KΩ and 100 TΩ (10^{14} Ω) and a frequency range between 0.1 Hz and 1 MHz (figure 4–14). All connections between the heating element and power supply, as well as the thermocouple and readout, go through a vacuum feed through. In case of the power supply, feed throughs are copper based, while thermocouple feed throughs are Chromel and Alumel. SMaRT Impedance readout software is used for measurements, and is interfaced with a Python script that monitors and controls the temperature. A sample holder (figure 4–13) specifically designed for this type of measurement, is placed on top of the ceramic heating element.

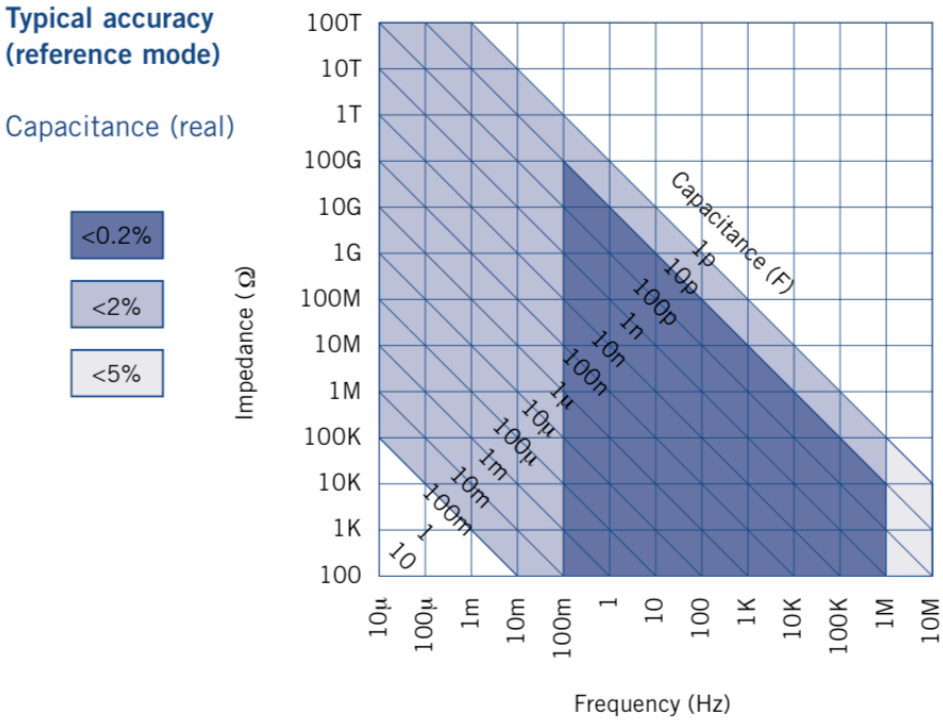

Figure 4-14 – Impedance measurement range, as a function of frequency, for the Solartron 1260 impedance interface equipped with a Solartron 1296 dielectric interface in reference mode. Figure adapted from http://www.ameteksi.com[103]

4.11.2 Noise Reduction

To achieve an acceptable signal-to-noise ratio, several modifications had to be made to the apparatus. First, inside the vacuum chamber, Kapton insulated, vacuum approved coaxial cables (LewVac Kapton insulated wires) were used instead of copper wires. This minimised noise to an acceptable level, and ensured very minimal noise from other equipment in our laboratory. Even though the chamber is expected to act as a Faraday cage, some radiation might still find its way through the quartz viewport. In addition, the Python automation script used ensured a long enough time (at least 10 minutes) is applied after reaching the measurement temperature for better thermal equilibrium. This was also found to improve signal to noise ratios in measured data. In addition to the above, it was important to ensure results

were reproducible, and one source of data variation was uneven applied pressure between top and bottom silicon substrates. To ensure equal and even pressure is applied for every measurement, a ceramic plate is placed on top of the upper silicon substrate, and two stainless steel springs were used to apply a known pressure to the substrates under measurement (figure 4–13).

4.11.3 Data Analysis and Model Fitting

Acquired data is processed using the ZView 2.0 software package. Impedance gain, phase and amplitude data analysis, including fitting to equivalent circuits, is provided by the software package.

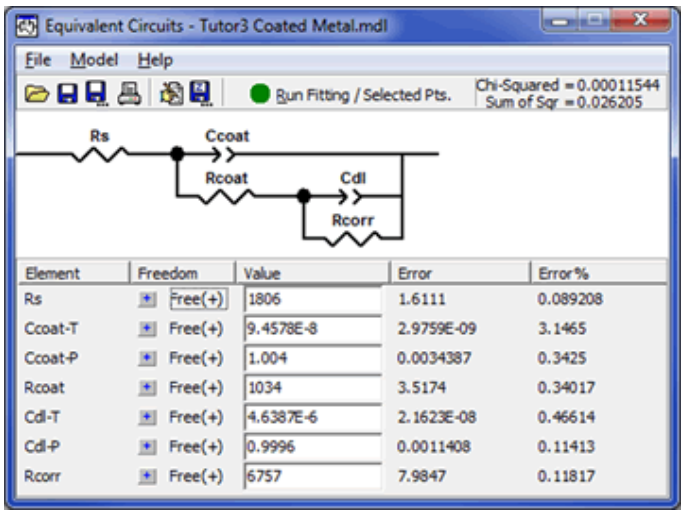

Figure 4-15 – ZView 2.0 software package equivalent circuit fitting screen. Figure taken from http://www.scribner.com

When equivalent circuits are fitted according to a model, values for resistance, capacitance, and CPE elements are fitted with errors. Error values are an important measure when attempting to reduce signal noise (see 4.11.2). Initial values for fitted parameters are first provided, then the software attempts to fit values to the data provided. Fitting is run in the software's 'fitting' mode, and the frequency range is obtained from the data. Maximum iterations are set to

500, optimization iterations set to 200, type of fitting is ‘Complex’ and type of data weighting is ‘Calc-Modulus’.

4.11.4 Measurement Error

For impedance measurements using the setup described in 4.11.1, four main sources of random error are identified:

- Apparatus measurement error, between 0.2% and 2% (relative), as shown in figure 4–14. This is taken to be 0.2% for the measurement range used, except for the narrow range between 1 MHz and 10 MHz, where it rises to a maximum of 2%.
- Aggregated ND layer thickness, which is taken to be 0.5 μm on average, varies with location, and was determined to have a relative error of 8.9%. This was determined using height profile analysis in AFM data using the NanoScope analysis software package, averaged for 10 height profiles per AFM image, and a total of 4 AFM images.
- Fitting error for semi-circles in Nyquist plots, ranging between ~0.1% and ~4.5% for fitted resistance values.
- Temperature measurements from thermocouple, accurate to within 0.25 °C, are averaged for a total of 1200 seconds before measurement (1 reading per second). A temperature gradient is expected, however a small separation between heating element and sample (4 mm) and good isolation in vacuum mean this is negligible.

Overall, error is dominated by layer thickness error, and following error propagation analysis, relative error is between 8.9% and 10.2%. In Arrhenius plots, logarithmic resistance is plotted within 1-2 orders of magnitude, which makes errors in this range too large to plot. Relative errors are, however,

included in linear fitting analysis, and have a small yet measurable effect on activation energies E_a due to comparable weights. Activation energies are quoted with corresponding errors.

4.12 Schottky diode fabrication

4.12.1 Coating Substrate with NDs

Ralchenko *et al.*[85] have described several methods of detonation ND adhesion to flat surfaces, including ND grit abrasion and ultra-sonication in ND solution. In practice, ultra-sonication of intrinsic, undoped NDs on Si/SiO_2 substrates is straightforward and can yield monolayers of full surface coverage.[83] However, when considering boron-doped NDs, whether of detonation or HPHT origin, surface adhesion using ultra-sonication is very poor. Improving surface adhesion of boron-NDs using ultra-sonication is the topic of chapter 6. However, for the purpose of fabricating Schottky diodes, thicker ND layers are required (few hundred nanometres or more), requiring the use of drop-coating on a hot plate (~90 °C).

Figure 4-16 – Nanodiamond drop-coating on a 1 × 1cm Si/SiO_2 substrate. Coverage is limited compared to ultra-sonication nucleation techniques.

Drop coating of NDs on a hotplate, however, yields small regions of coverage, as seen in figure 4–16. To achieve full surface coverage and the desired thickness, 'confinement' of ND solution was performed prior to drop coating. In this technique, a drop of ND solution (a few μL) is deposited on the polished side of the silicon substrate, and is then 'sandwiched' between it and a second polished silicon surface. Mild pressure is applied by hand (using tweezers), and the two substrates are rubbed together until the drop dries. This is repeated several times. The substrate is then washed using DI water, and then drop coating is performed, ensuring the ND solution fully covers the substrate. It is noticed that following the solution 'confinement' step, the contact angle of the solution with the substrate is significantly reduced, and as the solution dries, the whole substrate is left covered with a thick layer of NDs.

4.12.2 Aluminium Contact Evaporation

Aluminium evaporation is carried out in an Edwards 306A Bell jar kit inside a cleanroom environment (London Centre for Nanotechnology). Using a tungsten spiral, 1cm of high purity aluminium filament (GoodFellow©, 2 mm thick, 99.999% purity) was placed inside the chamber and connected to the electrodes. The base pressure was 2×10^{-6} mBar, and the evaporation rate kept under 0.2 nm/second. Thickness was measured using a quartz crystal monitor. A shadow mask with 2mm diameter holes was used to deposit Al contacts on devices. A glass slide was also exposed to evaporation so it can be used to confirm total thickness using the DekTak profilometer, also in the LCN cleanroom.

Figure 4-17 – Edwards 306A Bell jar metal evaporation kit at the cleanroom of the London Centre for Nanotechnology. Image taken from http://www.london-nano.com

4.12.3 Probe Station

To perform electrical measurements on devices, an Everbeing© EB-8 Multi probe station was used. Equipped with tungsten probes of 15 μm tip diameter, electrical I-V and C-V measurements were performed.

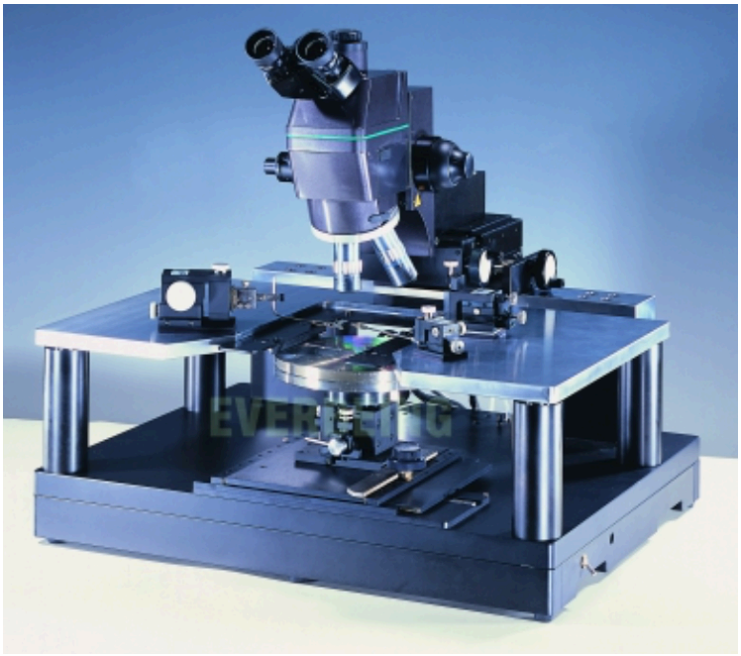

Figure 4-18 – The Everbeing© EB-8 Multi probe station used when performing electrical measurements, here shown equipped with an optical microscope.

The probe station is housed in a Faraday cage metal housing to reduce noise and interference with mains and other electrical equipment. Tri-axial connections are used to connect the probes to measurement equipment, for robust noise reduction. All measurements are performed at room temperature, and electrical insulation between the sample holder and sample under measurement is always ensured.

4.12.4 Electrical I-V and C-V Measurements

Electrical measurements performed on Schottky diode devices (chapter 8) were performed using a Keithley 4200 Semiconductor Characterisation System (SCS). The 4200-SCS was equipped with a Capacitance-Voltage Unit (CVU), enabling C-V measurements at frequencies between 1 kHZ and 10MHz. The AC bias can be between 10 and 100mV RMS, under a DC bias between -30 and 30 V. For C-V measurements, two modes are available, the series mode, and the parallel measurement mode, where the device under

testing (DUT) is made of a resistor and a capacitor connected in series or in parallel, respectively. Other than temperature variation (<0.37%), factors affecting measurement results include contamination (e.g. humidity), electrostatic interference, leakage currents, generated currents (such as piezoelectric effects) and source impedance. The 4200-SCS has a current measurement tolerance limit of 105 mA at 1 μA resolution, and a current source limit of 105 mA at 5 μA resolution. The voltage source range is ± 210 V Volts with 5 mV resolution, and voltage measurement range of ± 210 V Volts with 1 mV resolution. Within the voltage measurement range used in chapter 8 (–5 to +5 V) error contributions for measurement from the Keithley 4200 unit are <0.05% for current and <0.01% for voltage, while sourcing errors are <0.05% for current and <0.02% for voltage. Connections between the probe station and the 4200-SCS are via coaxial BNC cables, and to the CVU module are through tri-axial BNC cables. All I-V measurements are performed in 'quiet' mode to improve signal quality. A metal box shielded the probe station during measurement. Good quality insulation (Kapton® polyimide tape) was used to insulate devices from probe station sample holder. A dehumidifier was used in the lab to reduce humidity and keep it within the operational limit of the measurement apparatus. Measurements for devices under testing were repeated 5 times each with no apparent difference in results. For consistency, results were reported for measurements performed at 27±1 °C. The measurement apparatus was allowed to warm up for 30 minutes before commencing with measurement.

5. Characterization of Boron-Doped Detonation Nanodiamonds (B-DND)

5.1 Impedance Spectroscopy

B-DNDs were investigated using AC impedance spectroscopy (IS), which can give insight into the differing electrical conduction processes that are present.[97] Here the NDs were compacted and IS measurements taken in a 'sandwich' configuration. Figure 5–1(a) shows the real vs. imaginary components plotted against each other as a function of measurement frequency – plots at several temperatures are included. These so-called 'Cole-Cole' plots should reveal a semicircular response for a given conduction path, which can be modelled as an RC circuit component[97]. It is clear from figure 5–1 that no single semicircular response is apparent. Using established methods for IS curve fitting[97] individual semicircular responses can be determined from this data, as shown in figure 5–1(b) for a given temperature. Two distinct semicircular responses can be proposed, one at higher measurement frequencies than the other. R and C values can be determined from the fitted plots assuming two RC circuits exist (one per conduction path) in series. Arrhenius style plots of the value of R as a function of temperature allows the determination of thermal activation energy for each suggested conduction path, as shown in figure 5–2. For each of the two semicircles (large and small), two plateaus can be observed, each associated with a conduction path. This suggests the two different activation energies for the conduction processes are apparent; a higher activation

energy of E_a~0.8 eV at temperatures between 300 °C and 450 °C, and a much lower activation energy E_b= ~0.02 eV below 200 °C. Following acid-cleaning steps (see experimental methods), activation energies around E_a= 0.4 eV were measured between 230 °C and 400 °C. This result may indicate the successful removal of sp^2 shells, which would reduce the average distance between ND grains, and therefore improve wave-function overlap. The improved wave-function overlap would result in lower hopping energies and a lower overall activation energy. Activation energies of 0.39 eV are very close to the theoretical activation energy of p-type, semi-conducting boron-doped diamond of ~0.37 eV.

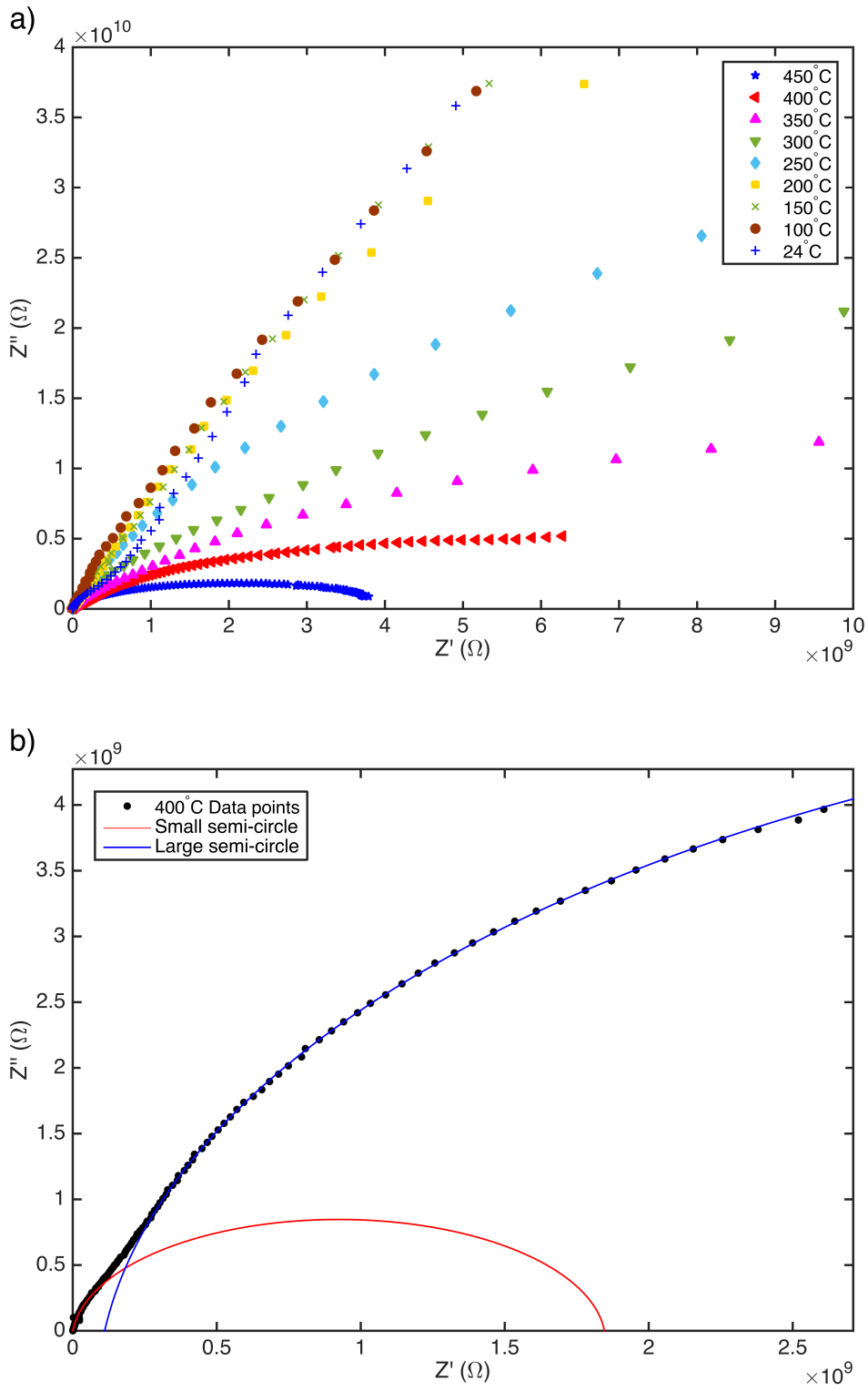

Figure 5-1 - a) Cole-Cole plot of impedance measurements between 50 °C and 450 °C, and b) Two semi-circles fitted to Cole-Cole data at 400 °C

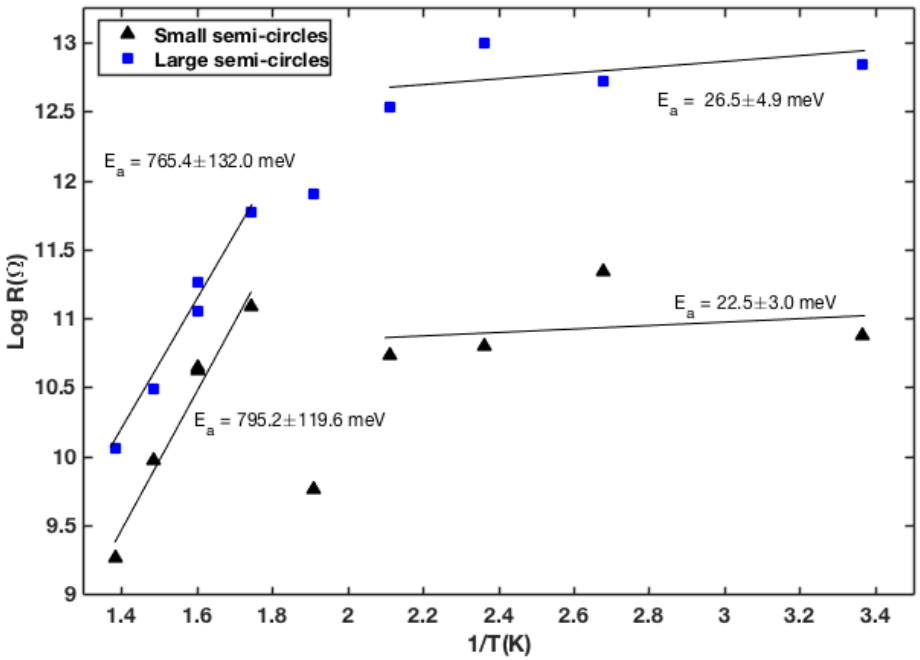

Figure 5-2 - Arrhenius plot of as-received Boron-DND with linear fitting, and corresponding activation energies from impedance measurements at different temperatures

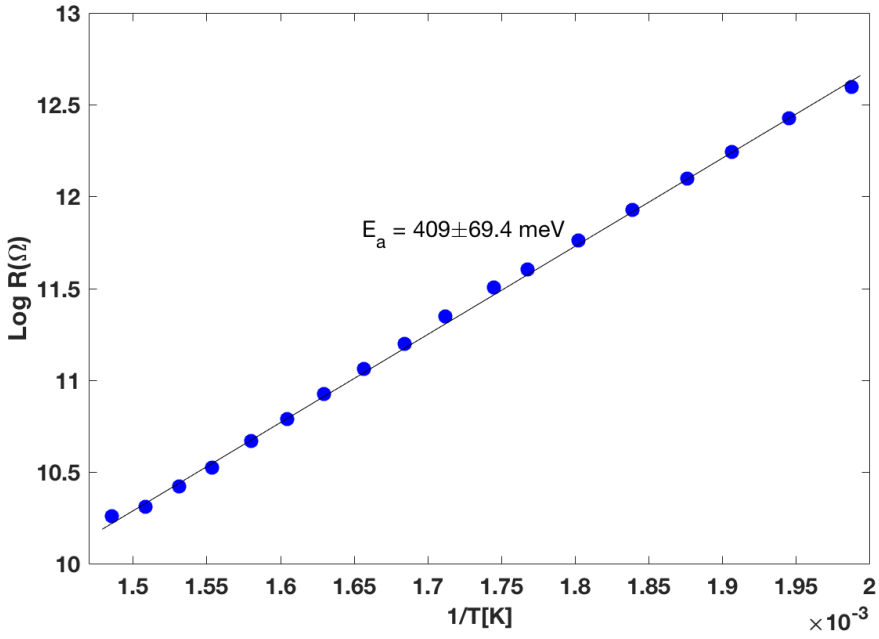

Figure 5-3 - Arrhenius plot of acid-cleaned Boron-DNDs between 230 °C and 400 °C, obtained using R-values from large semi-circles

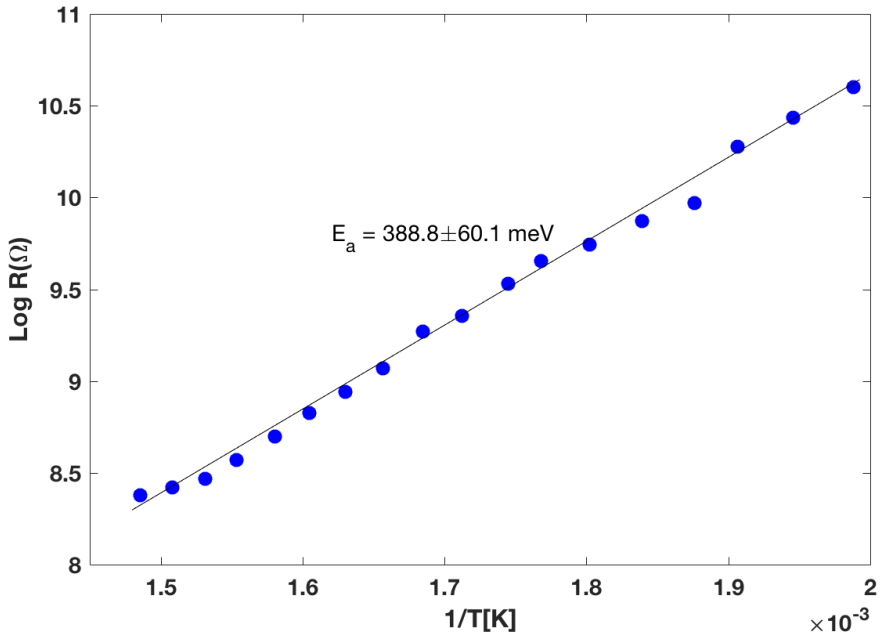

Figure 5-4 - Arrhenius plot of acid-cleaned Boron-DNDs between 230 °C and 400 °C, obtained using R-values from small semi-circles

5.2 AFM of Ultra-Sonication Seeded B-DNDs

Atomic force microscopy (Bruker Dimension Icon AFM, tapping mode) was used to identify the average grain size of the DNDs. Using AFM in tapping mode, a laser excites the cantilever near its resonant frequency, and the tip will resonate. Depending on the atomic forces close to the surface, the cantilever's oscillations will be affected by the van-der-Waals forces, which are dominant up to a few nanometres from the surface. A feedback system keeps the oscillations constant by varying the distance from the surface, hence allowing topographic imaging with sub-nanometre accuracy. This method should allow accurate measurements of heights of single DNDs, but not of their widths parallel to the substrate's surface. However, given that DNDs are generally symmetric in shape (confirmed using HR-TEM, see

below), height measurements should be sufficient to verify their average size. A typical AFM image of DND aggregates deposited onto a SiO_2-Si substrate (ultra-sonication from an aqueous solution) is shown in figure 5–5. In addition, figure 5–6 shows single-digit nanodiamonds following ultra-sonic nucleation on silicon, following acid treatments to break aggregates (see experimental methods). Prolonged concentrated acid treatment (section 4.2.2) can, in addition to etching sp^2 carbon shells, etch diamond cores, resulting in reduced ND diameters. AFM imaging of ultra-sonicated NDs immediately following acid treatment shows features at or below 4 nm, with a background of features <2 nm, as seen in the three-dimensional image in figure 5–6. Stored NDs will soon aggregate in solution, with diameters reaching 100s of nanometres or even micrometres.

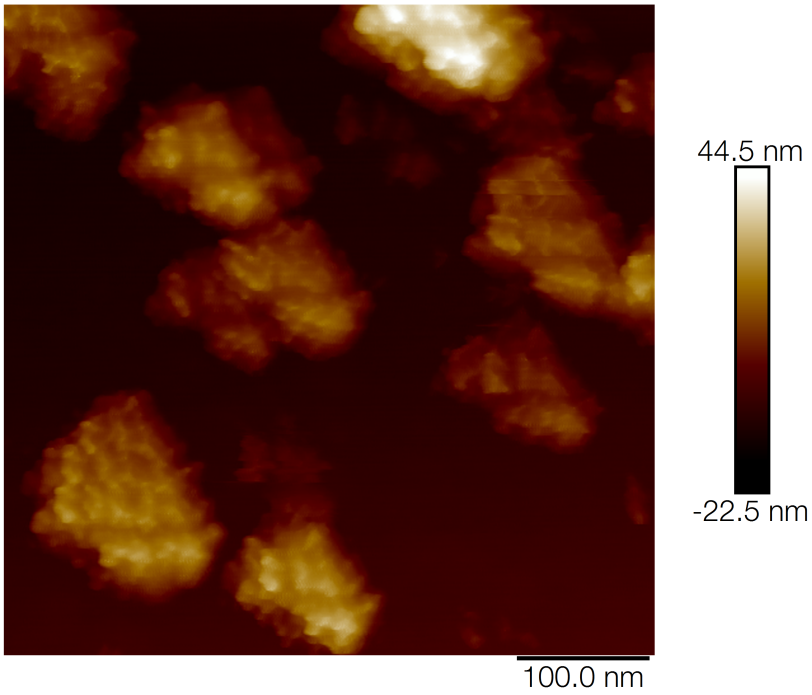

Figure 5-5 - AFM imaging of few-hundred nanometre Boron-DND aggregates nucleated on SiO_2.

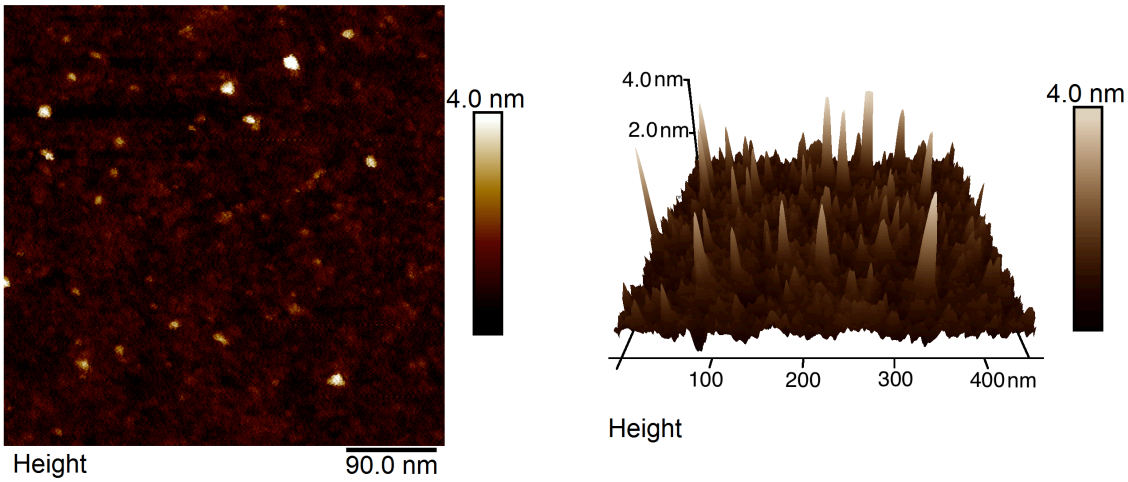

Figure 5-6 - AFM imaging of acid-cleaned, dispersed Boron-DNDs nucleated on SiO_2, shown in 2D (left) and in 3D (right).

5.3 HR-TEM Imaging

To verify the atomic structure of the DNDs, High resolution-transmission electron microscopy (HR-TEM) was used (refer to experimental methods). HR-TEM images of the B-DNDs confirm the crystalline structure of the nanodiamonds, and clearly show diamond cores surrounded by sp^2 carbon structures around the cores (figure 5–7). The presence of NDs is clear from the lattice spacing of (111) diamond faces (0.206 nm), shown by the arrow in the figure. Overlapping of DND crystal lattices can also be seen clearly. The lattice spacing increased to 0.213 nm in other locations, possibly indicating the presence of dopants such as Nitrogen and Boron.

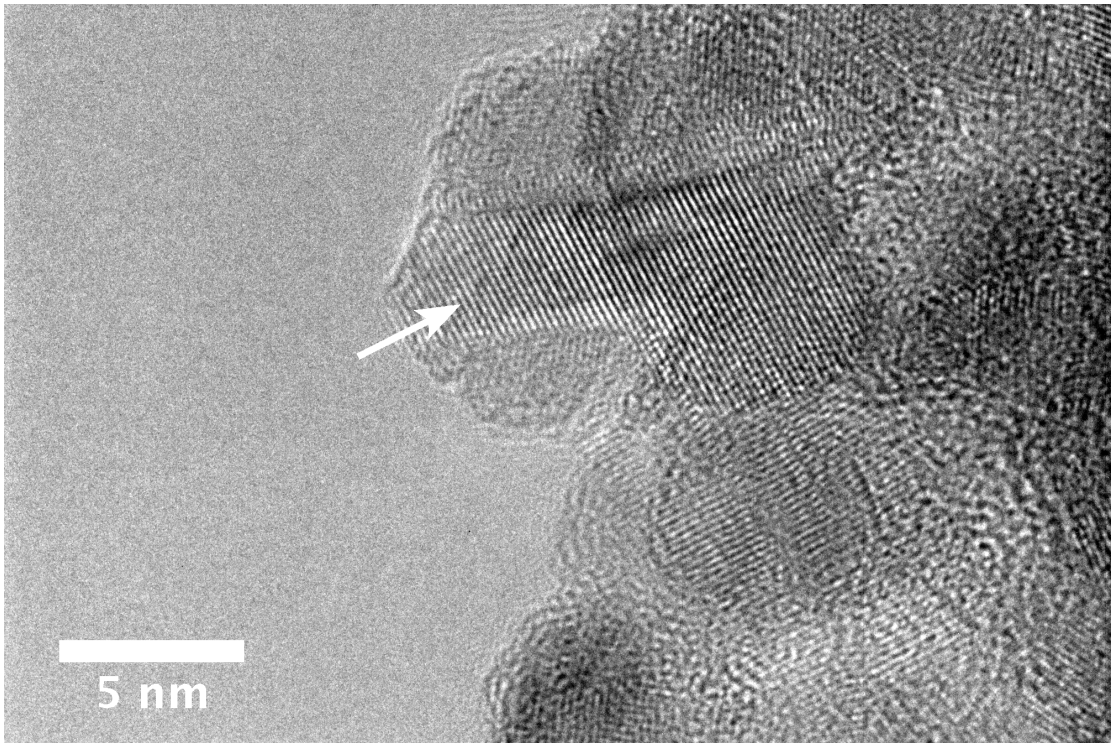

Figure 5-7 - HR-TEM image of Boron-DNDs. The arrow points to the (111) diamond lattice lines.

5.4 Raman Spectroscopy

Raman spectroscopy is a non-destructive method, which can be used to detect carbon crystal structures and obtain information about their quality and composition, where vibrational modes in Raman active molecules scatter light. Using an excitation wavelength of 532 nm, the obtained spectra are composed of modes corresponding to sp^3 and sp^2 bonded structures. Typical results are shown in figure 5–8, following fitting and photoluminescence background subtraction.[104,105] Boron-DNDs show prominent features at Raman shifts of 1332 cm^{-1}, and 1586 cm^{-1}; the peaks correspond to the sp^3 diamond peak, and the sp^2 carbon G peak respectively.[106,94] The diamond peak expected at ~1332 cm^{-1} in bulk material is expected to be upshifted and broadened for nm-scale diamond.[104] The undoped samples also show similar

features, however the diamond peak is narrower, and is centred at 1322 cm^{-1}, whereas the G peak is at 1599 cm^{-1}. Other Raman peaks may also be present in highly Boron-doped DNDs, such as the ~1200 cm^{-1} peak, usually present in highly Boron-doped diamond films, which is usually accompanied by a 500 cm^{-1} peak, where the peaks centred around 500 cm^{-1} can be used to estimate the substitutional Boron concentration in diamond thin films.[107,105] The strong background luminescence from substrates, however, prevented proper observation of features below 1100 cm^{-1}.

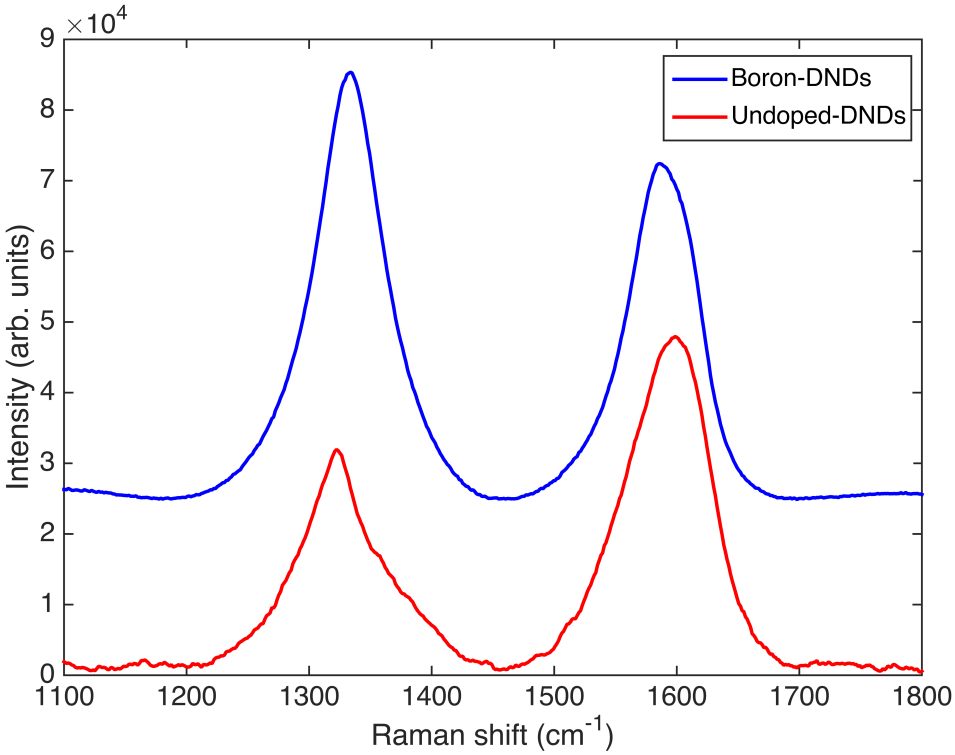

Figure 5-8 - Raman spectra of Boron-DNDs (top) and undoped-DNDs (bottom).

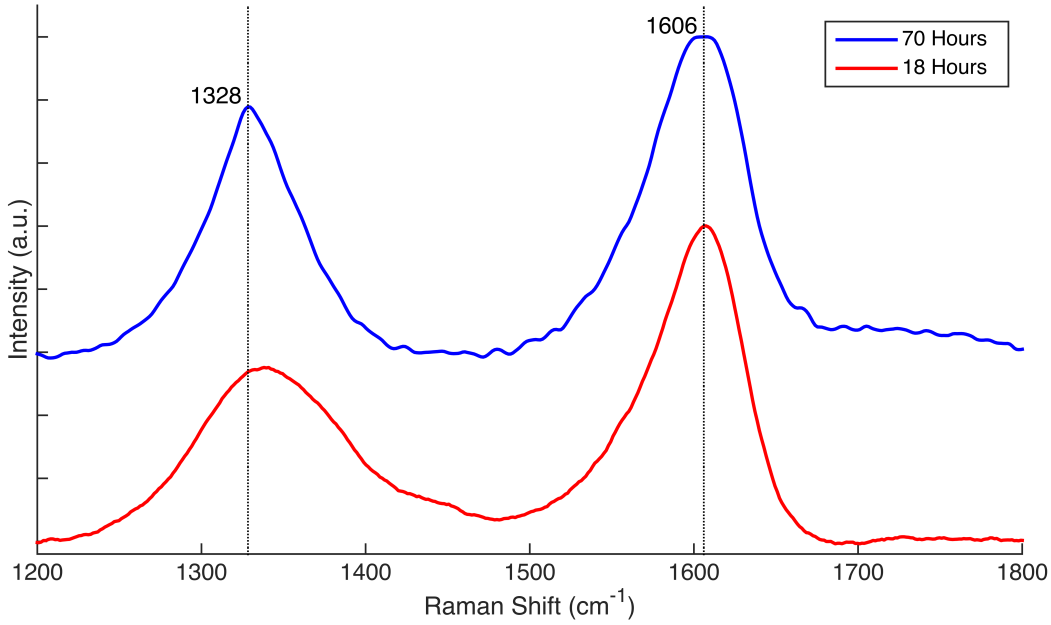

Figure 5-9 - Raman spectra of acid-treated B-DNDs, after 18 hours of treatment (bottom) and 70 hours (top).

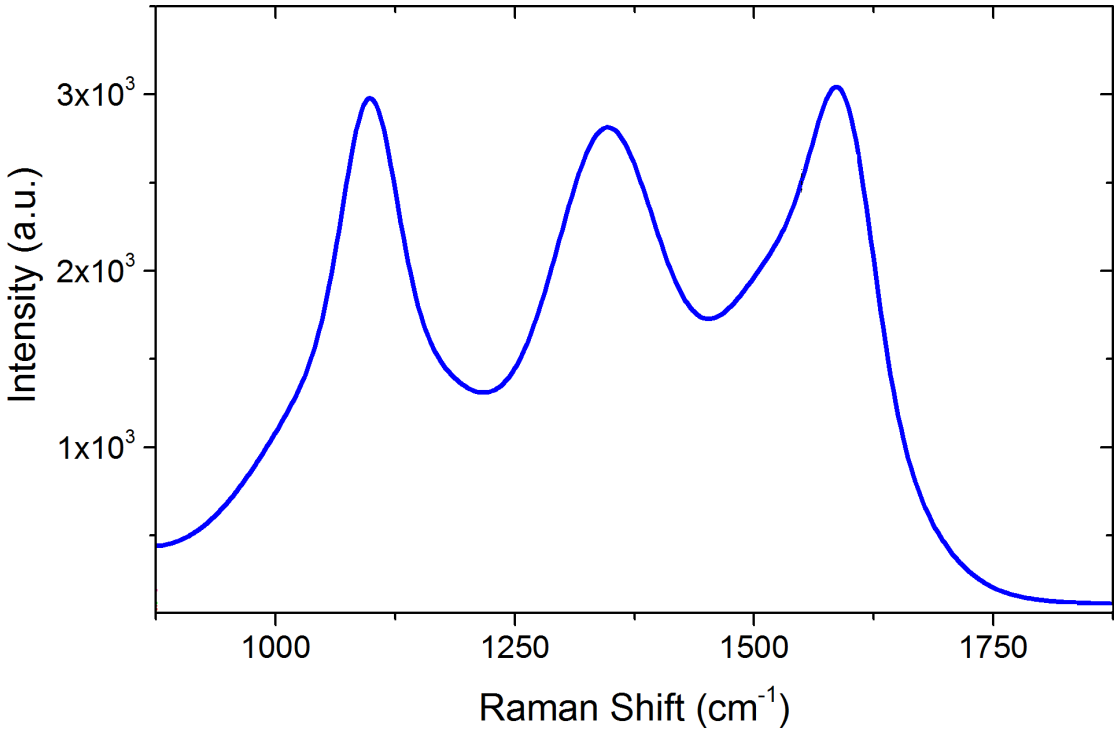

Figure 5-10 - Raman spectrum of ozone treated Boron-DNDs.

5.5 Infrared Spectroscopy (FT-IR, ATR-FTIR)

To obtain information on the surface composition of our DND samples, ATR and FT-IR spectroscopy, which can measure absorption of infrared light passing through vibrating molecules on the surface were performed. FT-IR measurements used DNDs mixed into KBr pellets, while ATR measurements were made by directly pressing DND powder on top of the ATR crystal. ATR measurements of the as-received DND powder show an abundance of organic groups on the surface (figure 5–11), including a probable signature of boric acid.[108] This is likely due to surface groups left from the detonation method used to produce the DNDs, and the subsequent (acid based) treatments typically used to purify the material recovered from the detonation chamber.[40] Prominent features in the FT-IR spectrum, shown in figure 5–12, are a peak at 1630 cm^{-1} on top of a 1550-1700 cm^{-1} broad feature, representing the C=C bond stretch, while a smaller feature from ~2850 to about 3000 cm^{-1} can be attributed to the C–H stretch. A large feature between 3000 and 3650 cm^{-1} is for the O–H stretch. The ATR spectrum looks similar to the FT-IR spectrum above ~1250 cm^{-1}, but also includes a ~1050-1150 cm^{-1} C–O stretch peak on top of a broad feature, extending from between 1000 and 1500 cm^{-1}, which could also include the signature for –C–H bending.[109]

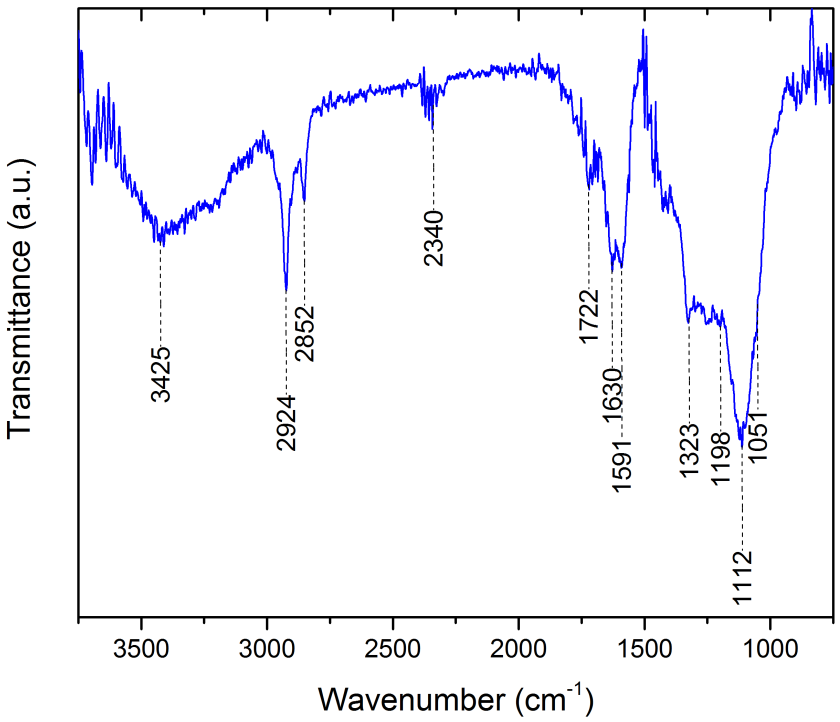

Figure 5-11 - ATR-FTIR spectrum of as-received Boron-DND powder.

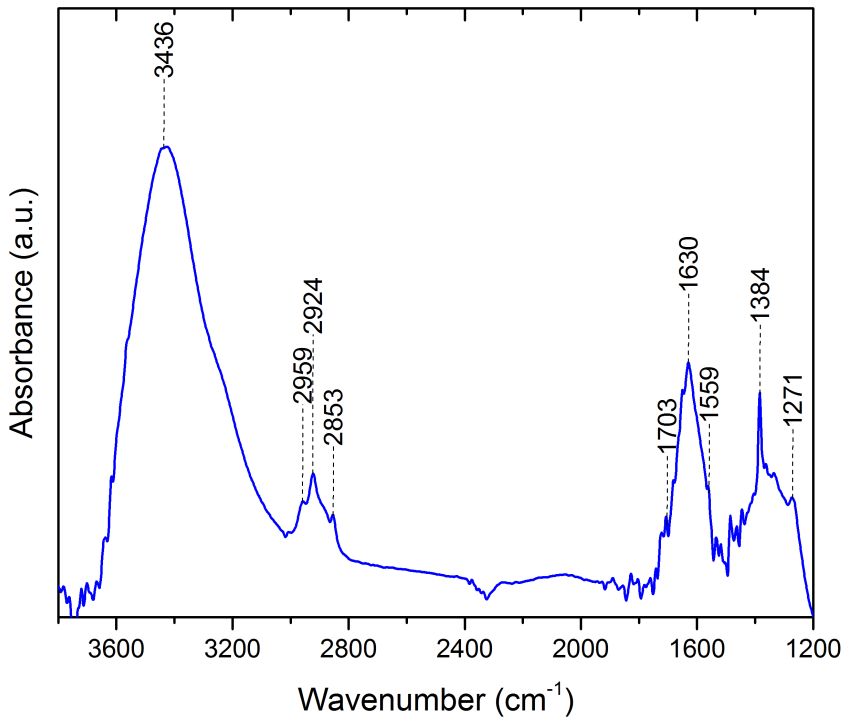

Figure 5-12 - FT-IR absorption spectrum of Boron-DNDs embedded in a KBr pellet, obtained in a nitrogen atmosphere.

5.6 Photoluminescence

The PL spectra obtained using a 405 nm laser shows the presence of three prominent peaks at 435, 469 and 522 nm in both Boron-DNDs and undoped DNDs, as shown in figure 5–13. The peak at 522 nm corresponds to energy of 2.39 eV. The feature at 435 nm corresponds to the first order Raman feature of diamond, and the 520-530 nm feature is measurable when excited with shorter wavelengths. Both features above, and is attributed (530 nm) to N-V^0 defect centres.[110] Both features are accompanied by the presence of peaks around 575 and 636 nm, attributed to N-V centres. That these peaks are not seen in the Boron-DNDs spectrum here could indicate that a significant

amount of substitutional boron is present, filling up vacancies, thus preventing significant N-V centre formation.[105] Alternatively, boron could be acting as a compensator to electrons from N-V centres. The undoped DNDs on the other hand clearly have a feature at 636 nm ($N\text{-}V^-$), and a possibly suppressed feature at 575 nm ($N\text{-}V^0$), indicating the presence of N-V centres as expected. The peak at 469 nm may be explained by the existence of N4 nitrogen centres, which are composed of four substitutional nitrogen atoms surrounding a single vacancy.[101]

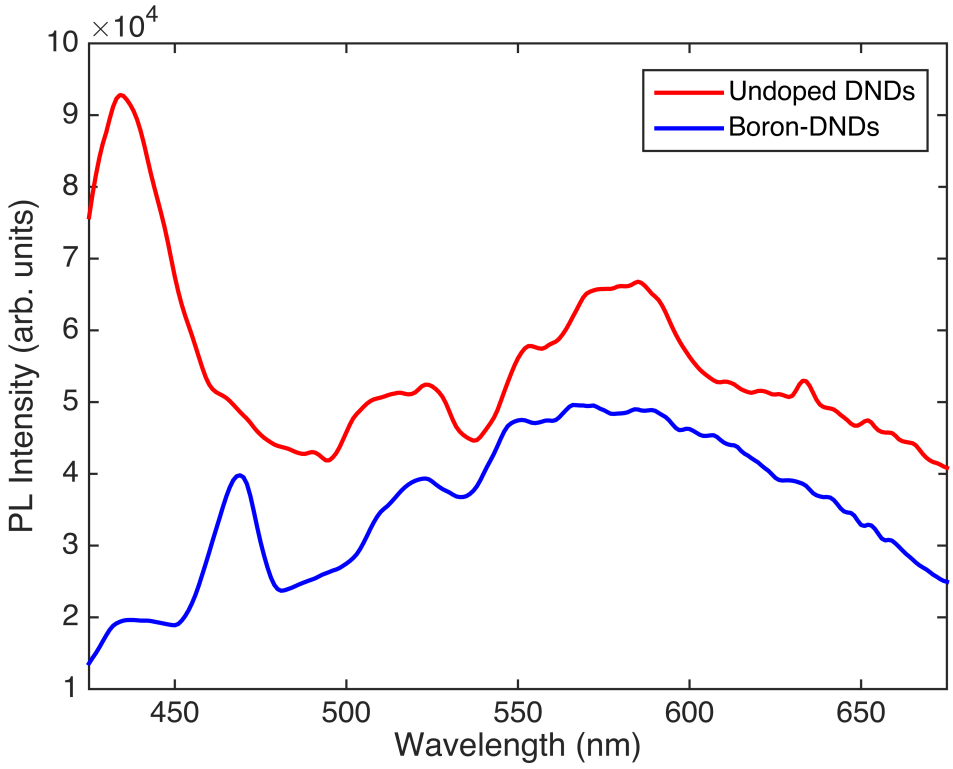

Figure 5-13 - Photoluminescence spectrum of Boron-DNDs (top) and undoped-DNDs (bottom), both nucleated on silicon substrates.

5.7 Discussion

The photoluminescence (PL) feature with the peak at 469 nm may be explained by the existence of N4 nitrogen centres, which are composed of four substitutional nitrogen atoms surrounding a vacancy.[101] According to Collins, there is no evidence that this form of nitrogen impurity behaves as a donor in diamond. The 435 nm peak is assigned to the first order (Raman) peak in PL. In lightly boron doped diamond, the first-order Raman peak is usually accompanied by an N-V centre luminescence peak at 636 nm. The presence of this 636 nm peak in the undoped-DNDs PL spectrum, but their absence in Boron-DNDs, has previously been attributed to an increase of boron in the diamond lattice, potentially acting as acceptors that can strip N-V centers of their electrons.[111] The 575 nm N-V centre peak is also missing from the B-DND PL spectra recorded here. N-V– vibrational side bands are expected to have strong, broad luminescence between 630–800 nm, which is not seen here, however the substrate effect has been shown to affect the intensity of this feature, especially when SiO_2/Si substrates are used to study NDs.[112] The evidence from PL alone, however, does not confirm the presence of boron in B-DND powder samples, and only suggests the possibility of boron doping. Further investigation into B-DND luminescence is therefore essential, such as spectroscopic cathodoluminescence, or higher resolution photoluminescence while considering the type of substrate used.

The Raman spectrum obtained from B-DND powder confirms the presence of detonation nanodiamonds,[94] although the peak associated with bulk diamond (1332 cm^{-1}) was broadened. According to a number of authors, the 1332 cm^{-1} diamond Raman peak shouldn't be detected for NDs smaller than 5

nm.[94,113,114] The other main feature in the spectrum is at 1586 cm^{-1}, corresponding to carbon sp^2 bonds in the form of the G peak.[94] The near equivalence of the intensity of the two main peaks suggests an sp^2 content of between ~1-2% of total bonds. This is due to the fact that sp^2 carbon bonds have a significantly higher Raman efficiency when compared to sp^3.[115] Small features between 1040 cm^{-1} and 1100 cm^{-1} are observed in both spectra, but are comparable in size to background features; The latter can shift depending on exciting wavelength, and is around 1100 for a 514 nm laser.[94] According to Ferrari, the ~1100cm^{-1} peak is due to trans-polyacetylene at grain boundary, while the ~1040 cm^{-1} feature is seen in amorphous carbon as well as nanodiamonds.[106,94] The ~1100 peak has increased significantly in intensity following Ozone treatment of the Boron-DND powder (figure 5–10). The broadened diamond peak in the B-DND spectrum may include a component of the ~1345 cm^{-1} Raman peak attributed to both sp^2 and amorphous carbon (D peak).[104] A diamond peak can become broad due to the presence of impurities, in addition to strong phonon scattering from NDs.[28] Using visible excitation, the ~500 and ~1220 cm^{-1} features are detected in highly boron doped diamond films.[105] In this case, the ~500 cm-1 feature, however, may be the result of substrate background subtraction, and is not necessarily part of the DND spectrum. Figure 5–9 compares Raman spectra of acid-treated B-DNDs, and shows a narrowing diamond peak at 1328 cm^{-1} following 70 hours of concentrated acid treatment. This suggests reduced amounts of sp^2 carbon are present in treated samples.

The presence of Boron and other dopants in ND cores of some of the nanodiamonds is inferred from the longer C-C bond spacing seen in NDs,[116]

where the bond length increased by about 5 pm. This can also indicate other dopants (N being most likely candidate). Although nanodiamonds are clearly visible in HR-TEM imaging, the distribution of dopants cannot be directly inferred, due to its limited field of view. However, the fact that some regions display the expected longer C-C bond length supports the assertion that at least some of the NDs may have substitutional boron present. Shells surrounding NDs, composed of sp^2 structures, are also seen surrounding diamond cores in HR-TEM images.

In the case of IR spectroscopy, Jiang *et al.* argue that phonon confinement due to the size of individual NDs (<5 nm) hinder the two-phonon process in IR between 1900 and 2500 cm^{-1}. The same confinement effect is also partly responsible for the missing 1332 cm^{-1} Raman peak in small NDs.[113] FT-IR spectra of B-DNDs above 1500 cm^{-1} are nearly identical to spectra obtained from undoped NDs, suggesting similar surface terminations created by the detonation and subsequent cleaning process. The boron characteristic absorption IR line in diamond, at ~1290 cm^{-1}, can be used to estimate the boron content of diamond films.[117] For a 1 mm thick KBr pellet mixed with Boron DNDs (~10:1 by weight), absorbance of 3% suggests substitutional boron content of ~6×10^{17} cm^{-3}.

Impedance values obtained in figure 5–1, on the order of 10^8–10^{10} Ω, are in agreement with values obtained by Bevilacqua *et al.* for nanocrystalline diamond films with significant conductivity contribution from grain boundaries, where boron doping was found to reduce resistivity by 1-2 orders of magnitude.[118] In their work, Bevilacqua *et al.* used the same impedance measurement apparatus as the one used here (see section 4.11). In previous

work, aggregated detonation nanodiamonds, without boron doping, have been shown to display only a single semicircular response in Cole-Cole plots determined from impedance spectroscopy.[42] Indeed, the material showed near-to ideal dielectric behaviour. Similar measurements on mono-dispersed DNDs revealed similar properties.[119] Therefore, whilst the presence of two conduction paths, indicated from the two semicircular responses in the impedance spectroscopy data (figure 5–1) could be discussed in terms of diamond grain and diamond grain boundary conduction seen in intrinsic[98] and boron containing[118] nano-crystalline diamond films, this is not a likely explanation here. At low temperatures both conduction paths display low activation energies (20-30 meV); whilst moderate boron doping in thin film diamond is associated by an activation energy of 0.37 eV, this value decreases to meV values as the boron doping concentration increases.[20] Given the TEM observations (some grain doping, some grains with graphitic outer shells), with the suggestion from the Raman that at least some material is heavily doped and there is graphitic material present, then the most likely attribution for the two conduction paths at the lower temperatures is due to these two materials-phases in the un-treated samples. Given one of these is attributed to boron doped DNDs, the activation energy of ~22 meV translates to ~1×10^{20} cm^{-3} boron content when applying the formula developed by Borst and Weiss.[20] That PL suggest the presence of lower B-doping would be consistent with these particular grains contributing little to the conduction observed in IS due to their inherently higher activation energy. That the PL technique does not indicate heavily doped material is not surprising as at high boron levels, B no longer acts as a discrete centre but rather forms an

impurity band[20] which will not contribute to sharp features in these excitation measurements. The Arrhenius plots (figure 5–2) show that at higher temperatures an increased activation energy (~0.8 eV) is apparent; this has been previously observed in a number of diamond studies, and can be attributed to conduction from deep traps arising from defects within the diamond.[98] In addition, following a combination of hydrochloric acid treatment and a concentrated acid-treatment, impedance measurements between 230 °C and 400 °C (figures 5–3, 5–4) resulted in activation energies around 0.39 eV and 0.41 eV. This may suggest the reduced separation between ND cores resulted in improved hopping in this temperature range, therefore redirecting conduction from deep-traps to substitutional boron. This also supports inhomogeneous boron doping in Boron-DNDs, where a fraction may be semi-conducting, and another fraction metallic or semi-metallic. The reduction in sp^2 content following acid treatments also supports this argument (figure 5–9), where a diamond peak at 1328 cm^{-1} becomes clearly visible.

When the Raman, FTIR and IS observations are combined it can be inferred that the B-DNDs studied here comprise a mixture of grains with varying boron content. TEM observations of some grains indicated enlarged lattice spacing. This observation supports the theoretical predictions of Barnard and Sternberg[28], but disagree with some others. That a conduction path most likely attributed to a highly boron doped ND, suggest other grains display quasi-metallic behaviour typical of diamond with a boron impurity band,[20] which again supports the assertion that NDs with a size <5 nm are capable of supporting substitutional boron, rather than it forming clusters or simply existing on grain edges.[6,7] Finally, although PL suggests boron is present, it

does not directly contribute to the evidence supporting the case for boron doping in DNDs.

5.8 Conclusion

Nanodiamonds are an important class of nano-carbons for many applications, with NDs produced by a detonation process being unique in offering access to the sub-5nm particle size. The inclusion of boron within nanodiamonds to create semiconducting properties would create a new class of applications in the field of nanodiamond electronics, but to date examples of boron doped NDs are principally limited to 'crushed' and milled CVD diamond films[17], which do not offer sub-nm sizes and the properties that are associated with this scale. Theoretical studies have differed in their conclusions as to whether sub-5nm NDs would support a stable substitutional boron state, offering semiconducting properties, or whether such a state would be unstable, with boron instead aggregating or attaching to edge structures[18-20]. In the present study detonation-derived NDs with purposefully added boron during the detonation process have been studied with a wide range of experimental techniques. The individual DNDs are of ~4 nm in size, and have been studied with PL, Raman and IR spectroscopies, AFM and HR-TEM as well as electrically measured through the use of impedance spectroscopy. When the results from these differing techniques are combined, with the exception of PL, it can be predicted that semiconducting properties of B-DNDs studied here are potentially attributable to substitutional boron doping. With the above assumption, moderate doping levels are found (~10^{17} B cm^{-3}) alongside the observation that some particles are heavily doped (~10^{20} B cm^{-3}) and are likely to be quasi-metallic in character. Whilst further B-DND research is

required to generate a more homogeneous distribution of doping concentration, the current study has shown that substitutional boron doping in sub-nm NDs is likely conceivable. Further spectroscopic and electrical measurements are necessary, however, to reach a solid conclusion about substitutional doping in such materials, which can open up the path to a whole host of new applications for this interesting class of nano-particles. Applications include, but are not limited to: studies in spintronics, superconductivity, as well as nanomagnetometry and single photon emission.[59] They are also potentially useful as biosensors on the nanoscale.[59]

6. Nucleation of Boron-NDs on Si/SiO_2 Substrates

6.1 Introduction

Nanodiamond materials are the topic of active research due to many unique properties. Nanodiamonds have been shown to be sources for single photons, [120,121,122] and have notable luminescence and fluorescence properties.[123,111,124] In addition, their usability in nanoscale spin imaging has been shown.[125] Their use as bio-markers,[123] and as means for drug delivery have also been demonstrated,[57] due to their stability both physically and chemically, their low cytotoxicity,[126] as well as biocompatibility and appropriateness for use as bio-sensors.[43,127,128,129] Nanodiamonds are potentially usable for quantum computing and communications,[130] given that many of their luminescent and spin properties are accessible at ambient conditions,[131] and with relatively high yield.[132] Dopants, such as nitrogen and boron, are known to give diamond its luminescent properties, in addition to facilitating spin interactions at ambient temperature.[124] Specifically, boron is currently the only dopant known to give conductive properties to dispersed nanodiamonds,[59] although other dopants have been shown to induce conductivity in nano-crystalline thin films.[133] One way to harness the unique properties of nanodiamonds is to nucleate them onto substrates, such as silicon or quartz, which can then be used to perform measurements or detect emissions. Furthermore, monolayer and multilayer nanodiamond films of high surface coverage can be obtained by electrostatic self-assembly,[134,135] ultra-sonication from aqueous suspensions, micropipette patterning, among other methods;[85] such layers and patterns can be used for multiple applications,

especially those requiring well-defined shapes such as MEMS.[136] High-pressure high-temperature (HPHT) boron-doped nanodiamonds of single and double-digit nanometre diameters have been synthesised from boron-containing, organic molecules.[59] Ekimov *et al.*[59] have shown that highly doped nanodiamonds can be made into well dispersed, stable colloidal solutions. Such a material is very promising for diamond based electronics, especially so if they can be patterned or self-assembled at the micro and nano-scale. This class of material gains more significance for its ability to be used as the source for boron-doping in diamond film growth using PE-CVD, as discussed in detail in chapter 8. In this work, we study the electrostatic self-assembly of heavily and moderately boron-doped nanodiamonds, by method of pH controlled, ultra-sonication assisted nucleation onto Si/SiO_2 substrates with native oxide layers. Zeta potentials and average particle diameters in aqueous solutions are studied as a function of pH for part of the sample range. Additionally, AFM imaging is performed following ultra-sonic nucleation to measure surface coverage. As a result, it was found that most samples start nucleating at or below pH~3, potentially due to the positive Zeta potential acquired by SiO_2 at very low pH. At this low pH range, aggregation of nanodiamonds in solution starts to occur, affecting the quality of seeded layers. To explain the origin of this behaviour, XPS analysis was performed to compare the surface chemistry of boron-NDs to that of intrinsic NDs.

6.2 Electrostatic Properties of Silica Surfaces

In diamond electronics, silicon is often used as a substrate when seeding and growing PE-CVD films for many applications, such as secondary electron emission (SEE), diamond based sensors, and many more. In this thesis,

silicon is used exclusively as the substrate for nanodiamond nucleation, both as an electrode for impedance spectroscopy measurements (chapter 7), and as a substrate and Ohmic contact for Schottky-barrier diode devices (chapter 8). Detonation NDs are frequently seeded onto silicon by method of ultra-sonication from aqueous solutions, which was discussed earlier in 4.3.2. Silicon quickly forms a native oxide layer 1-2 nm in thickness following acid cleaning, starting with a monolayer within hours of exposure to ambient conditions, making silica the interface naturally encountered unless precautions are taken to avoid this. Silica is known to have a Zeta (ξ) potential that is dependant on pH when present in aqueous media.[137] In this chapter HCl and NaOH titration is used to modify pH, and subsequently enable the measurement of Zeta potentials and check corresponding nucleation densities. This dependence on pH denotes dependence on H^+ and OH^- concentrations in water, and when silica surfaces are hydrated, the solid's surface, interfacing with the solution as silanol (Si–OH), interacts as:[137]

$$Si–OH + H^+ \rightleftharpoons SiOH_2^+$$

$$Si–OH + OH^- \rightleftharpoons SiO^- + H_2O$$

The charged sites of silica interact with counter-ions introduces to modify pH, forming the following relations:

$$Si–OH_2^+ + Cl^- \rightleftharpoons SiOH_2^+ \ldots Cl^-$$

$$Si–O^- + Na^+ \rightleftharpoons SiO^- \ldots Na^+$$

The above relations dictate the surface charge of silica, and the distribution of charges surrounding the solid's surface determine the Zeta potential acquired.[137] When silica nanoparticles are subjected to pH titration, Zeta potential measurements indicate an iso-electric point near pH~2. According to

Bizi,[137] the IEP of silica is 1.47, and the IEP for quartz is 1.4. The iso-electric point (IEP) is the point at which the Zeta potential is zero.[137] At this point, silica nanoparticles do not possess enough electrostatic potential to oppose aggregation. When considering flat surfaces, as is the case with silicon substrates, this becomes of significance when considering nucleation of nanoparticles with particularly large (and negative) Zeta potentials. At low pH (1-6), Ohshima[138] predicted a linear relation between pH and Zeta potential (figure 6-1), which is in good agreement with literature.[137]

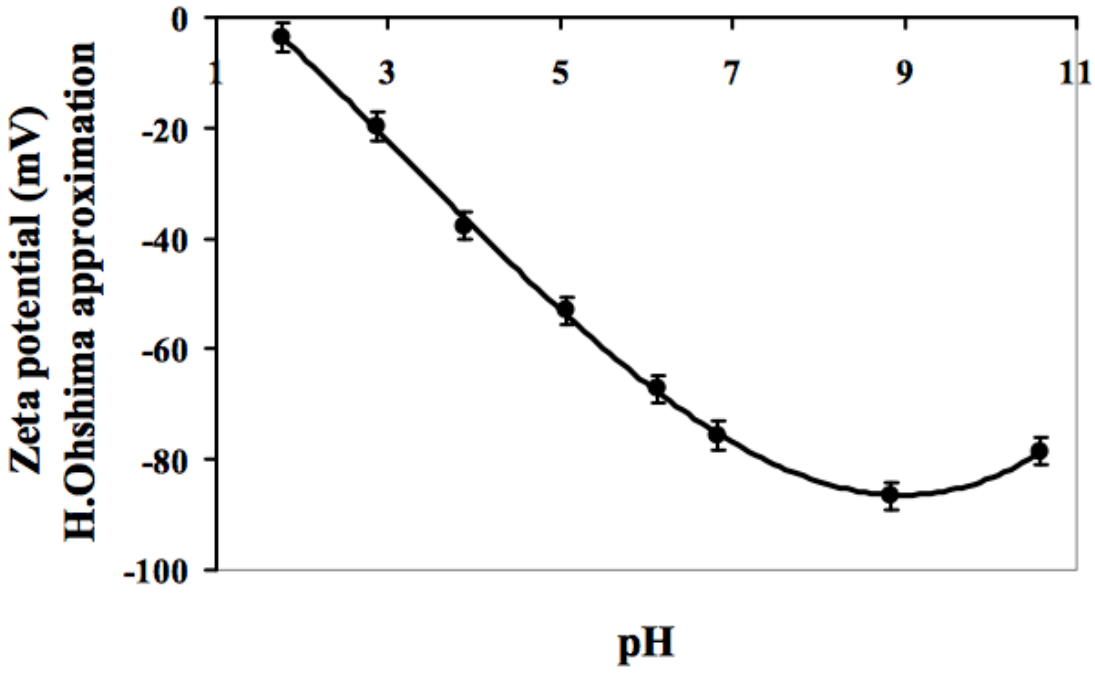

Figure 6-1 – Calculated relation between pH and Zeta potential of silica particles in water-based solutions. A linear region is predicted between pH 1-6, and the Zeta potential intersects the zero-point at pH~1.47. Figure taken from Ohshima, H. [1994][138]

6.3 The Surface of a Nanodiamond

As discussed in section 4.1, nanodiamonds have a rich surface chemistry. Most notably, when dealing with detonation NDs or HPHT NDs, carboxyl

(COOH) and carbonyl (C=O) surface groups result from acid cleaning steps. The Carboxyl group (containing a hydroxyl part) donates a proton to the solution, resulting in a negative Zeta potential that increases in intensity as pH increases.[83] Both surface groups interact with water based solutions. Carbonyl groups form a hydrate under acidic conditions, where excess H+ causes the protonation of the carbonyl group. Following this initial reaction, the hydration is completed by nucleophilic attack, turning the carbonyl into an alcohol group.[139] The initial reaction is, however, unlikely to happen,[139] thus suggesting the carbonyl group's effect on the Zeta potential is not affected by pH in the low pH range. The resulting alcohol group means it can behave as an acid or base, similar to water, again suggesting a weak effect of the group on Zeta potential. When the surface is hydrogenated, the electrons in diamond nanoparticles are expected to interact with hydronium in the solution, possibly due to the high electron density of states resulting from sp^2 carbon surrounding NDs.[83] Conductive highly-doped NDs would then be expected to have similar behaviour to hydrogenated NDs, assuming they have similar surface groups.

6.4 Experimental Methods

6.4.1 Sample definitions

Five sample types of boron-doped nanodiamond material are studied in this chapter for comparing nucleation on Si/SiO_2. Table 1 below summarises the techniques applied to each sample.

Table 6-1 – Summary of samples used and techniques applied.

Sample	Description	AFM	Zeta-potential	DLS	KCl	Titration starting pH
A	4-5nm DND	✔	✔	✔	–	8.20
B	10nm HPHT	✔	✔	✔	✔	2.96
C	20nm HPHT	✔	–	–	–	–
D	45nm HPHT	✔	–	–	–	–
E	100nm HPHT	✔	✔	✔	–	8.81

- Sample A is composed of 4-5nm boron-doped detonation nanodiamonds (B-DND), the same as the sample used in chapter 5. However, the sample was further purified and cleaned using a concentrated acid cleaning as described in 4.2.2. In addition, an air-annealing step was performed following a drying step by centrifugation in DI water at 1116 RCF (3 times). Dried DNDs were air-annealed in an oven at 425 °C for 120 minutes. Following this step, dry powder is weighed then mixed in DI water and ultra-sonicated for 10 hours (500 W, 20 kHz Sonics VCX 500) using a cup horn accessory. A concentration of 2.2 g/l is initially prepared, then diluted to 0.5 g/l in fresh batches before titration or nucleation. Sample A was estimated to have a boron concentration ranging from 10^{17} and 10^{20} cm^{-3} in chapter 5, and has a light grey colour in solution.
- Sample B, synthesised by a HPHT process from 9BBN crystals, was provided by Dr Igor Vlasov (National Research Nuclear University, Moscow). The sample is described in detail in their publication.[59] It has a solution concentration of 0.1 g/l, and an estimated boron

concentration of 1 at% calculated from the shift in the diamond Raman peak. This sample has a deep blue colour in DI water solution.

- Samples C, D and E were provided by Prof Olga Shenderova of Adamas Nano (adamasnano.com). Samples originate from HPHT micron sized diamond, heavily boron doped during growth (up to 800 ppm). Samples are then subjected to a novel milling process, reducing their size significantly. Sample D is different from samples C and E in that its surface was chemically reduced to further remove sp^2 carbon that may be present on the surface.
    - Sample C: original solution concentration of ~0.5% w/v. Solution has a light brown colour. Particles have average diameters of ~20 nm.
    - Sample D: original solution concentration of ~0.1% w/v. Solution has a dark brown colour. Particles have average diameters of ~45 nm.
    - Sample E: original solution concentration of ~2.5% w/v. Solution has an opaque grey colour. Particles have average diameters of ~100 nm.

6.4.2 AFM imaging

A Bruker Icon AFM was used in air-tapping mode to perform atomic force microscopy imaging. For surveying nucleation on silicon dioxide surfaces, silicon based AFM tips with a low spring constant (~48 N/m) and a radius below 10 nm were used. For higher resolution imaging, tips with radii below 5 nm were also used. Tips were changed frequently to avoid degradation of

image quality. 1x1 μm images at 512 lines per image were obtained, at a frequency of 1 Hz. In some cases, where the nucleation density was low, larger images (10x10 μm) were taken for better assessment of coverage. To measure surface coverage numerically, the threshold tool in the GIMP software package was used.

6.4.3 Zeta-Potential Measurement

Three 10 ml nanodiamond solutions each were prepared, at 5 nm (sample A), 10 nm (sample B) and 100 nm (sample E) for pH titration prior to measuring the zeta potential and particle size between the pH range 1-12, in increments of ~1 pH. More details about the titration process are given is section 4.3.3. To ensure adequate sample dispersion in solution before titration, all samples were measured as received and then subjected to increasing levels of ultra-sonication. Solutions were ultra-sonicated for 60 minutes using a UP200S Ultrasonic Processor. The samples were measured using the Malvern Zetasizer Nano ZS with the dip cell to determine the zeta potential at 25 °C. The Smoluchowski coagulation model was used,[89] and the F(ka) parameter was set to 1.5 for calculation of zeta potential. The number of sub runs per measurement was 200 runs. All measurements were run three times, and the average value reported.

6.4.4 Particle Size Analysis using Dynamic Light Scattering (DLS)

The samples were measured using the Malvern Zetasizer Nano ZS to determine the particle size at 25 °C using disposable cuvettes. All samples were run in triplicate and the average value reported. The particle refractive index and absorbance values used were those for diamond (2.42 and 1

respectively), and the dispersant refractive index and viscosity data used were based on water (1.33 and 0.8872 cP respectively).

6.4.5 Ultra-Sonication Nucleation

Nucleation of nanodiamonds onto silicon substrates with a native oxide was performed by ultra-sonication. Silicon substrates (1×1 cm) were de-greased in a clean-room environment by ultra-sonication in Acetone, followed by ultra-sonication in Isopropyl alcohol, and finally in DI water for 5 minutes each. Substrates are then dried using a nitrogen gun. Nanodiamond solutions in DI water (resistivity > 18 MOhm) have diamond concentrations of 0.1 g/l, and were ultra-sonicated (500 W, 120 KHz) for one hour (maximum temperature of 30 °C, 2 seconds on, 3 seconds off cycle). For nucleation, a silicon substrate was inserted into a vial containing 3ml of nanodiamond solution, with the polished side facing up. The vial was then subjected to ultra-sonication for 10 minutes. The substrate was then removed using metal tweezers and dried gently using a nitrogen gun. Samples were then stored before AFM imaging was performed.

6.5 Results

6.5.1 Zeta Potentials and DLS

The results of the pH titration measuring the Zeta-potential and particle size analysis at different pH points for sample A (initial pH=8.20), sample B (initial pH=2.96) and sample E (initial pH=8.81) are shown in figure 6-2. All measured samples (A, B and E) have negative potentials across the range. At higher pH, higher absolute values are recorded, indicating higher colloidal stability in water. At the lower end of the pH range, absolute potential values decrease, suggesting reduced colloidal stability and potentially aggregation of particles in solution. Figure 6-3 plots average particle diameters from DLS measurements of samples A, B and E. As predicted from Zeta-potential measurements, particles remain stable in the higher pH range, and begin to aggregate and increase in diameter as the pH falls below ~4. Note that for both figures (6-2 and 6-3), average values were reported after making 3 measurements for each data point. For DLS measurements, distributions with multiple features are normally measured, showing both single particle diameters and aggregate diameters, however results reported here are for the average diameter. Average diameters quoted in figure 6-3 represent the weighted average of all features measured in the size analysis distribution. For comparison, figure 11-7 (appendix) shows a single feature, which solely contributes to the average diameter, while appendix figures 11-5 and 11-6 have multiple peaks. Particularly, figure 11-7 shows a feature centered around 47.5 nm, another at 545 nm, and a much larger feature centered at 345 nm, which has the largest contribution to the average diameter (331 nm) at a pH of 2.8.

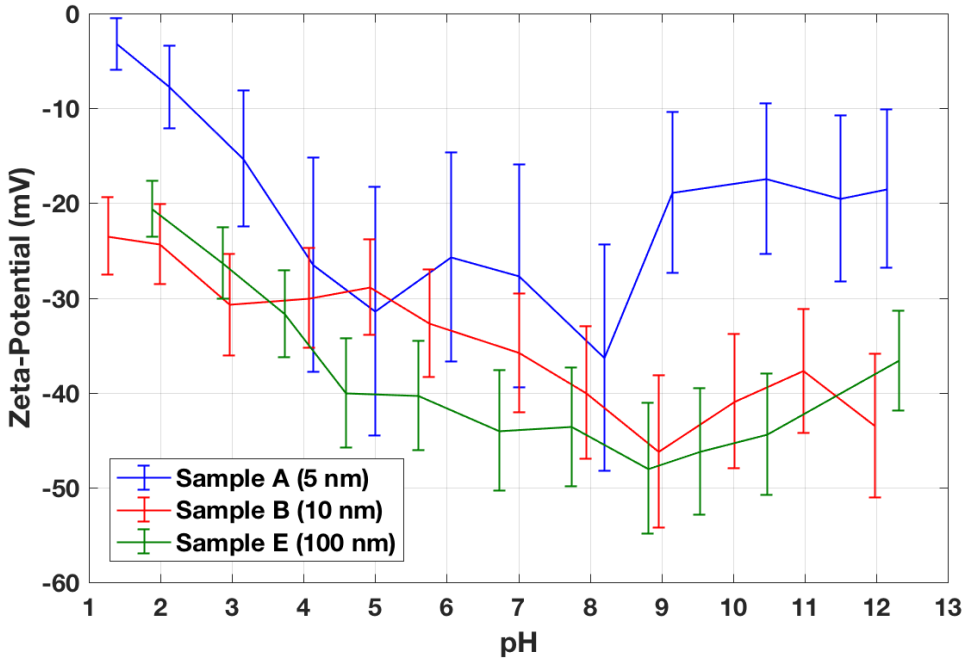

Figure 6-2 - Zeta potential plotted against pH for samples A, B and E. All samples have negative Zeta potential across the entire pH range. Error bars represent the average relative error at corresponding pH.

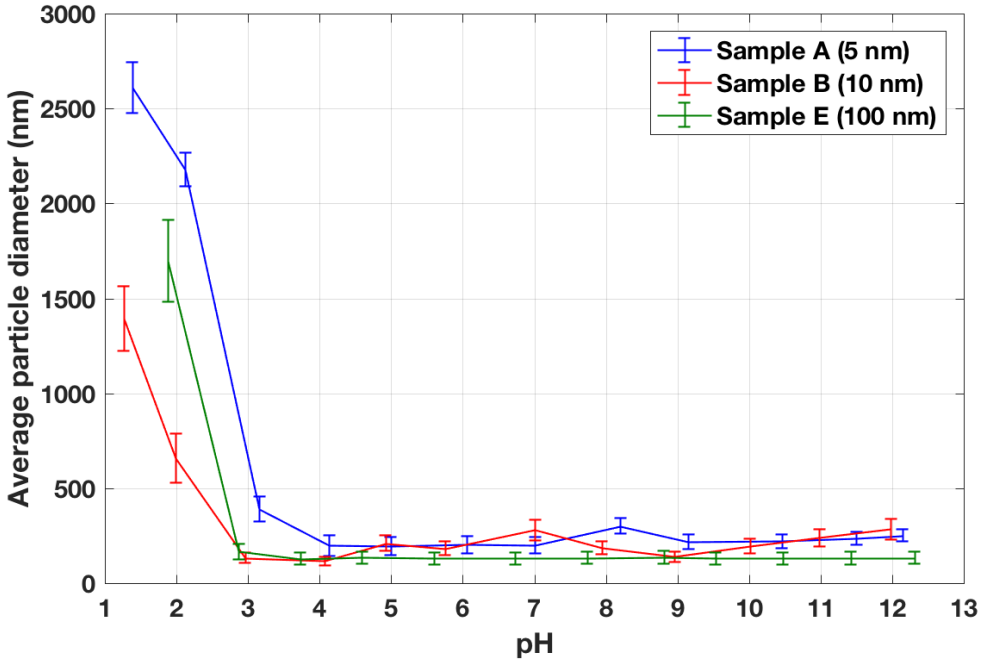

Figure 6-3 – DLS measurements showing average particle diameters as a function of pH for samples A, B and E. Diameters increase as pH drops below 4 and particles begin to aggregate, however they maintain the same diameter across pH range 4-12. Error bars represent the average relative error at corresponding pH.

6.5.2 AFM Imaging

Figures 6-4 to 6-6 show AFM imaging results for nucleation of sample B onto Si/SiO_2 substrates by method of ultra-sonication. All solutions used had the same nanodiamond density of 0.1 g/l at the time of ultra-sonic nucleation. The figures show the contrasting seeding densities as a function of pH at values of 1, 2 and 3. It is clearly seen that as the pH is lowered closer to 1, the nucleation density is significantly improved. Figures 6-8 to 6-10 show AFM images for samples C, D and E respectively; all nucleated at pH 1, 2 and 3. Samples C, D and E show a similar trend where the nucleation density reaches a maximal value between pH 1 and 3. The highest nucleation density among all samples was found at pH~1 for sample B; therefore, an attempt was made at varying the salt concentration of the solution. Potassium chloride solution (Sigma-Aldrich, ~3M in H_2O) was first diluted in DI water then added to increase the salt concentration to 1×10^{-1}, 1×10^{-2} and 1×10^{-3} in water-based solutions. Solutions were ultra-sonicated for one hour before ultra-sonic nucleation on Si/SiO_2 substrates was performed. Figure 6-7 shows a comparison between seeding densities of the three solutions, all having pH=1. It is seen that the concentration of potassium chloride can have a significant effect on the nucleation density and coagulation of nanodiamonds. A concentration of 1×10^{-3} results in the highest coverage among other salt-containing samples; resulting in a slight improvement (~50% coverage in one sample) over samples that didn't contain added salt. Sample A had the lowest nucleation density of all samples. Between pH 1-8, the seeding density was at best ~5%, which was recorded at pH=2 (figure 6-11). For this reason, reversal of the surface charge of silicon was attempted by attaching PDDAC

(Poly(diallyldimethylammonium chloride) solution, 20 wt.% in H_2O, Sigma-Aldrich) to the surface. This method, described by Girard *et al.*,[140] enabled full surface coverage (figure 6-12(a)). In figure 6-12(b), a larger area was imaged to check coverage, and a region was scratched using metal tweezers to check film thickness against the flat silicon background. Step profile measurement from AFM data yielded a layer thickness of 24 nm. This seeding method was also applied to other samples, with no improvement recorded at low or high pH. Figure 6-13 summarizes surface coverage results for pH titration of samples B, C, D and E, while figure 6-14 is a summary of surface coverage results of sample B as a function of salt concentration.

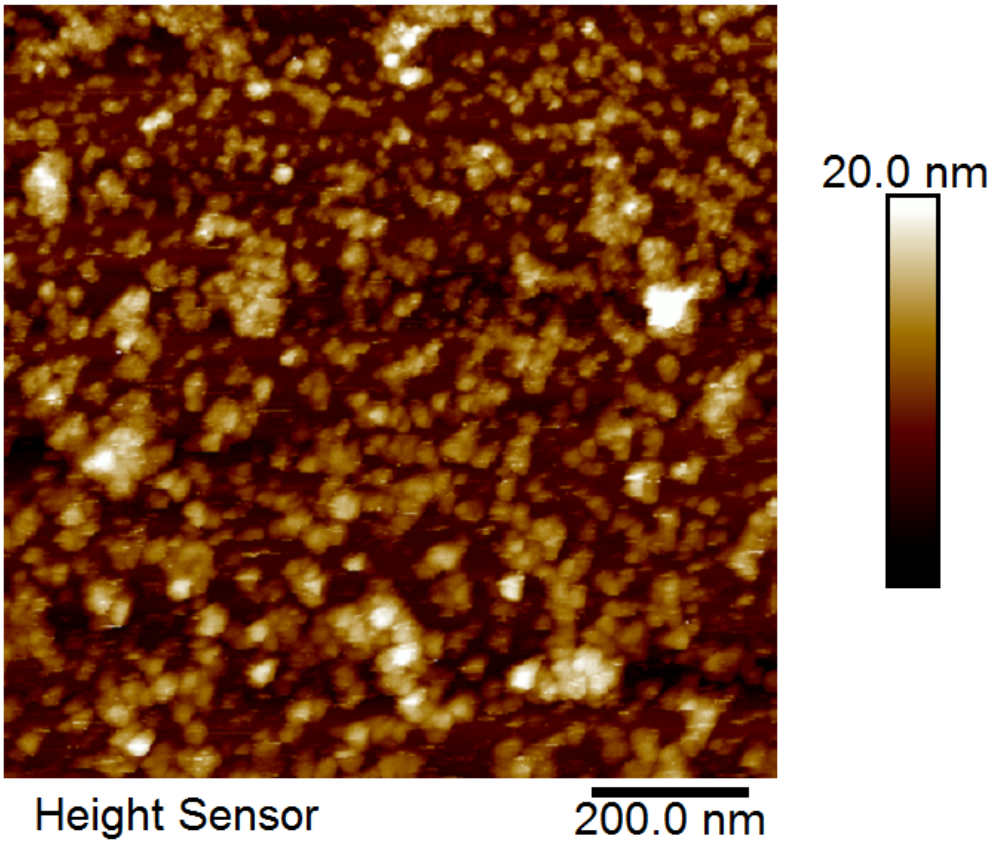

Figure 6-4 - AFM imaging of 10 nm HPHT BNDs seeded from pH=1 solution. The corresponding surface coverage is 45%, where few aggregates are seen.

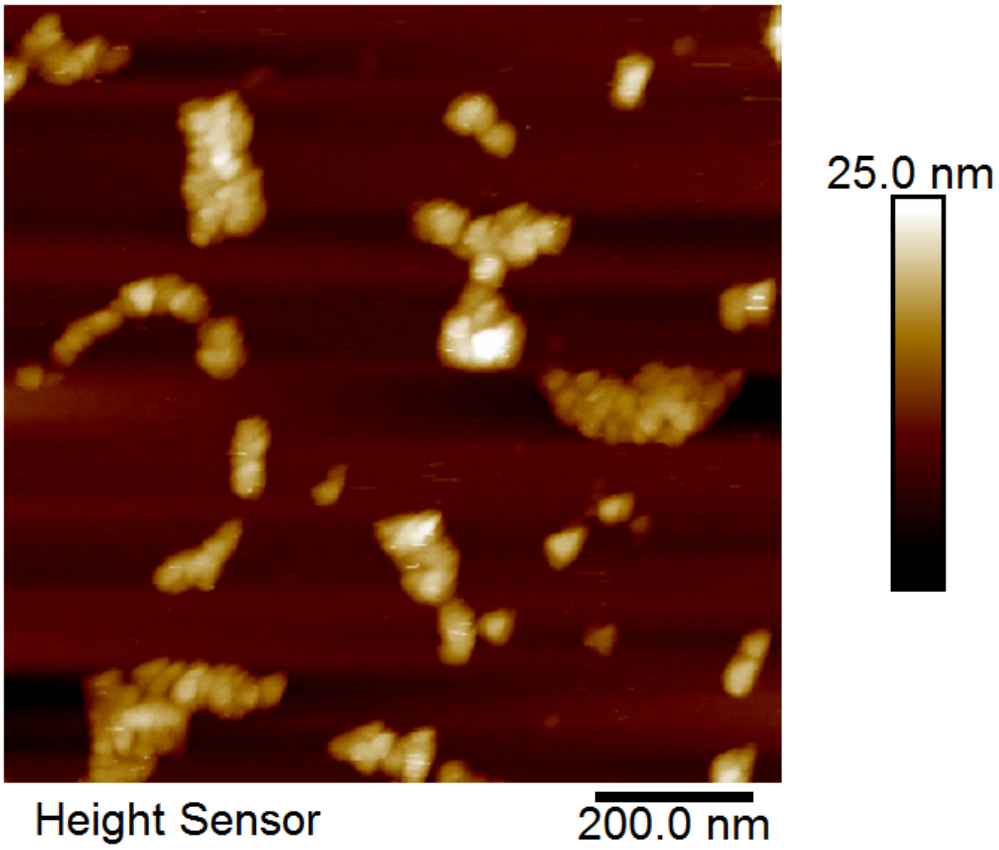

Figure 6-5 - AFM imaging of 10 nm HPHT BNDs seeded from pH=2 solution. The corresponding surface coverage is 25%, and nanoparticles are agglomerated.

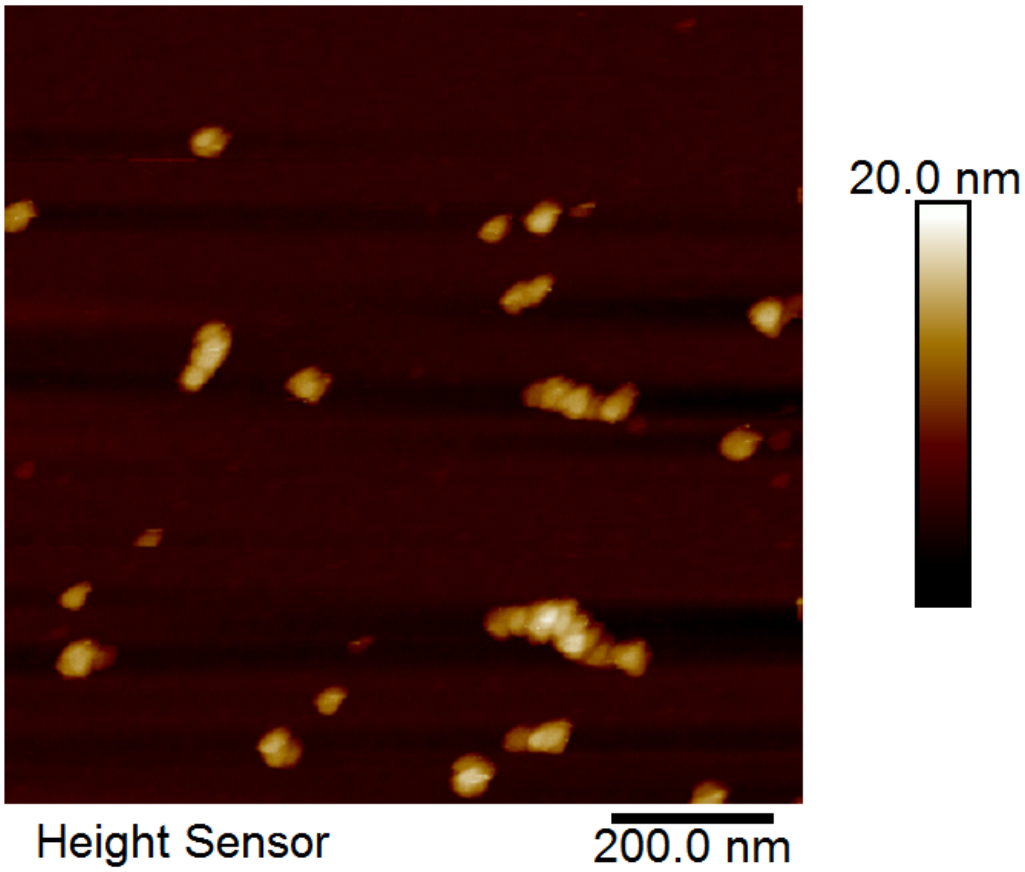

Figure 6-6 - AFM imaging of 10 nm HPHT BNDs seeded from pH=3 solution. The corresponding surface coverage is 6%. Nanoparticles forming small aggregates in line shapes are observed.

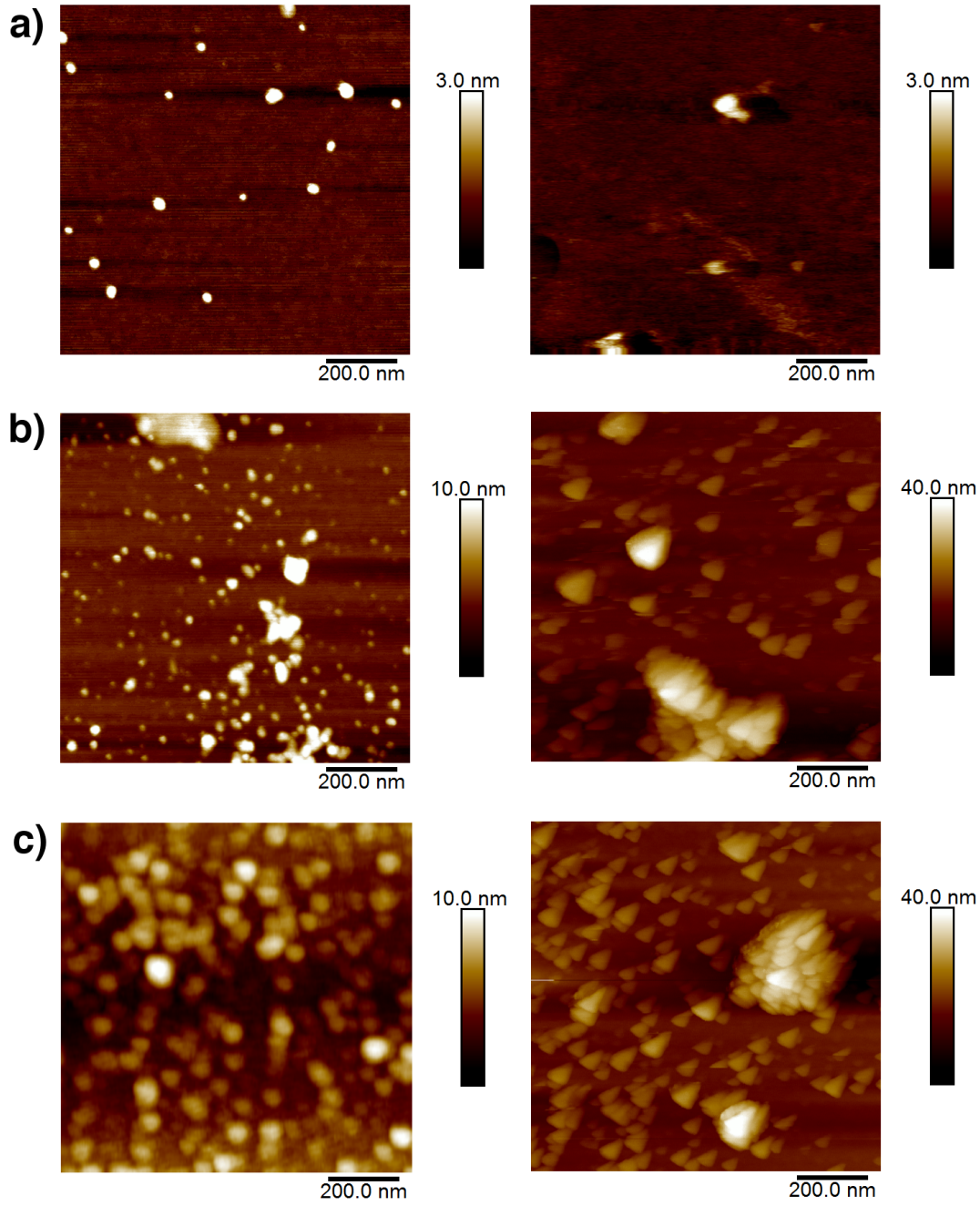

Figure 6-7 - AFM imaging of 10 nm HPHT BNDs at pH=1, and salt (KCl) concentrations of a) 10^{-1}, b) 10^{-2} and c) 10^{-3}. Images on the left were taken using a 10 nm AFM tip, while images on the right were taken using a 5 nm AFM tip. Surface coverage reaches 50% at KCl concentrations of 10^{-3}, the highest recorded using ultra-sonication nucleation.

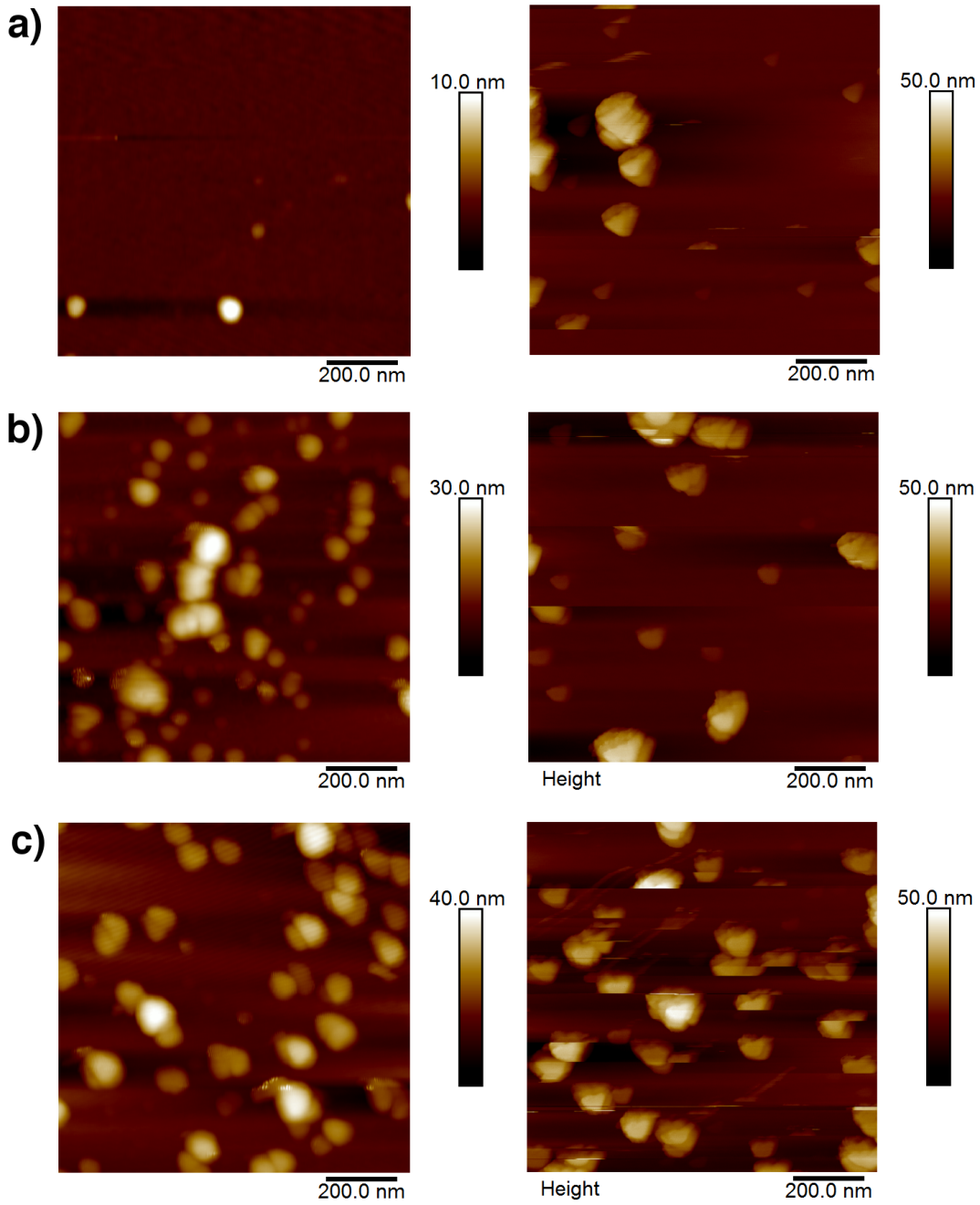

Figure 6-8 - AFM imaging of 20 nm HPHT BNDs at a) pH=1, b) pH=2 and c) pH=3. Images on the left were taken using a 10 nm AFM tip, while images on the right were taken using a 5 nm AFM tip. All images here taken using the 5 nm AFM tip (right column) experienced particle dragging. Images affected by particle dragging were not used to estimate surface coverage.

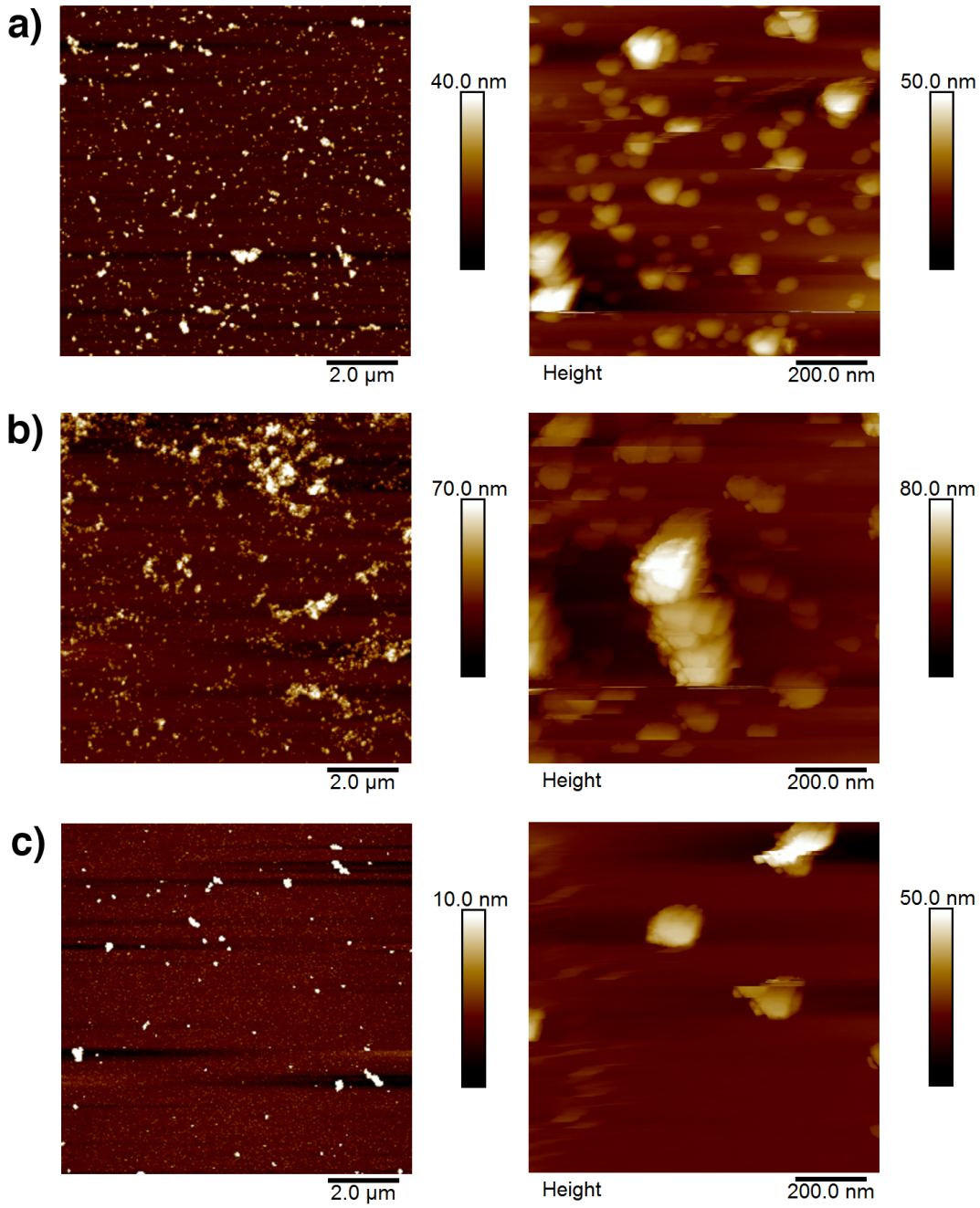

Figure 6-9 - AFM imaging of 45 nm HPHT BNDs at a) pH=1, b) pH=2 and c) pH=3. Images on the left have a 2 µm scale bar, while images on the right have a 200 nm scale bar. Images on the left were taken using a 10 nm AFM tip, while images on the right were taken using a 5 nm AFM tip. Images affected by particle dragging were not used to estimate surface coverage.

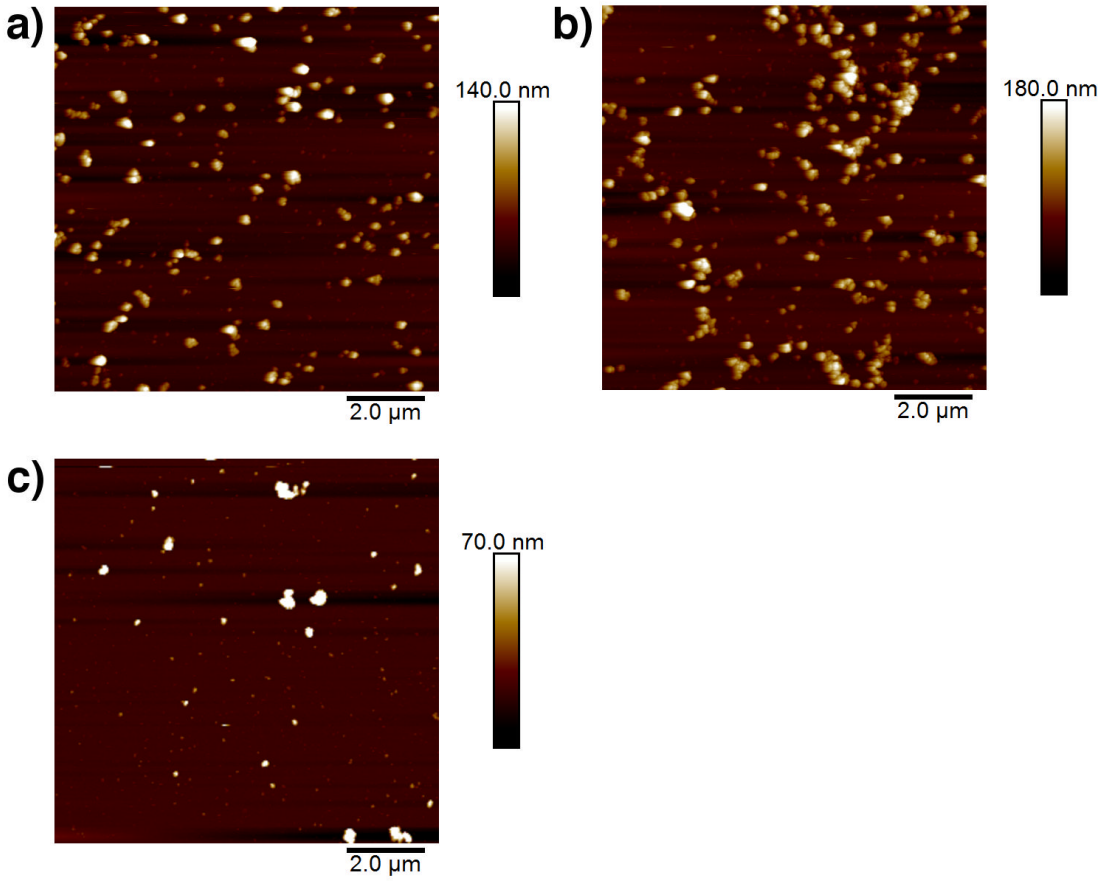

Figure 6-10 - AFM imaging of 100 nm HPHT BNDs at a) pH=1, b) pH=2 and c) pH=3. The nucleation density is highest at pH~2, however it remains very low for complete surface coverage.

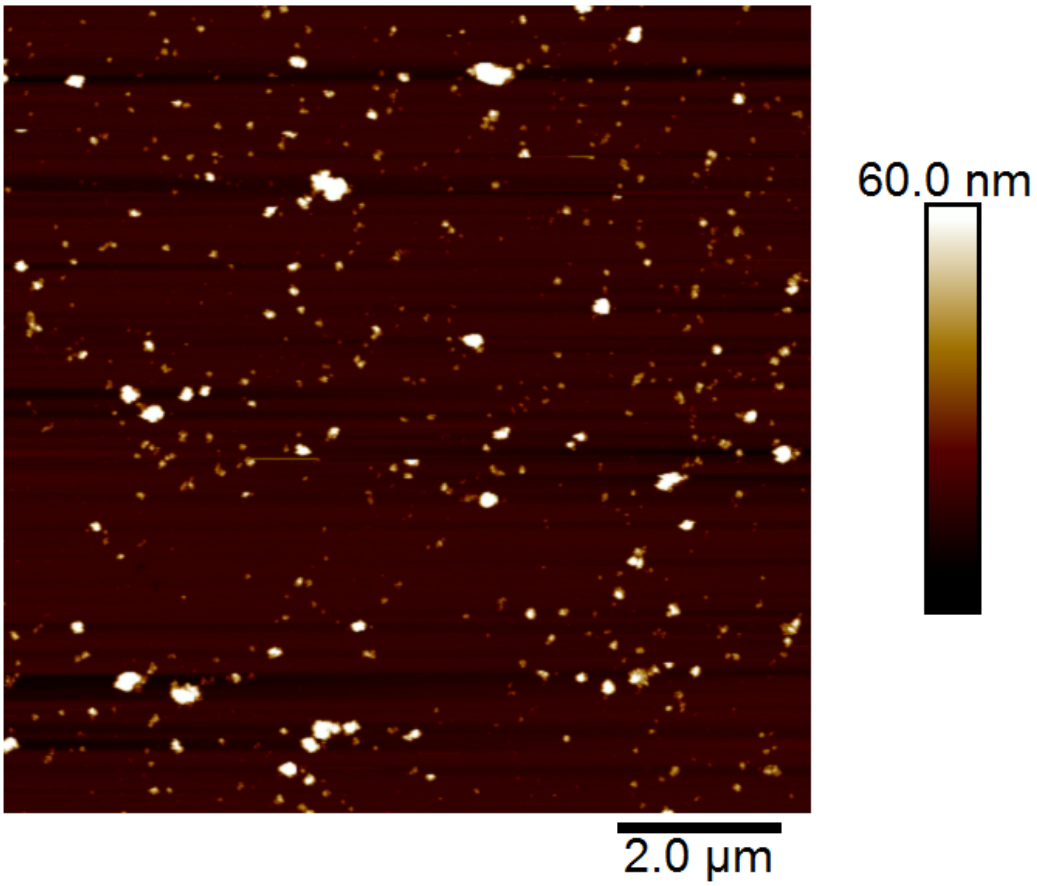

Figure 6-11 – AFM of sample A nucleated at pH ~2.2 without surface modification. This is the highest nucleation density reached by varying pH between 1-8. This image is a good representation of the nucleation density of all samples measured across pH 4-8.

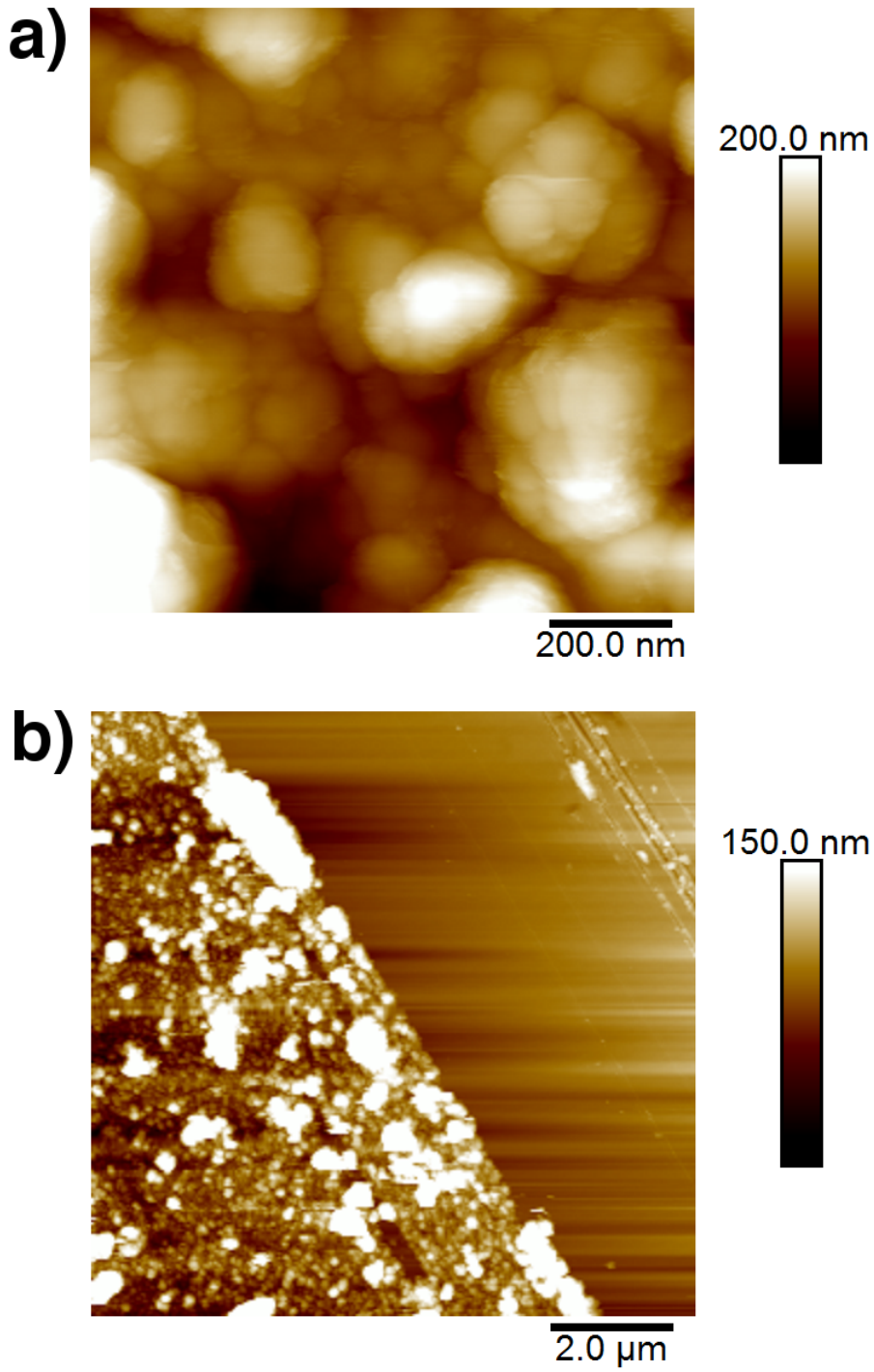

Figure 6-12 – AFM of sample A nucleated at ph~2.2 using PDDAC to reverse the surface charge of silicon. Image a) shows full surface coverage with large aggregates. Image b) shows full surface coverage at a larger scale, also showing a region scratched using metal tweezers to allow measuring total film thickness (~24 nm).

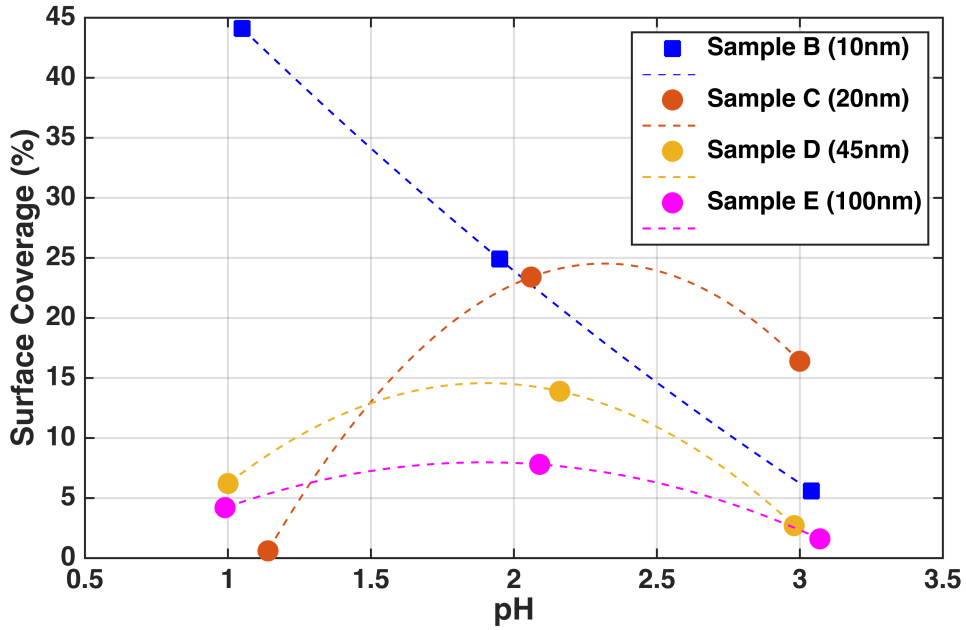

Figure 6-13 - Surface coverage as a function of pH for samples B, C, D and E, between pH 1-3. For sample B, surface coverage is a linear relation between pH 1-3. For samples C, D and E, maximum surface coverage is reached around ph~2.

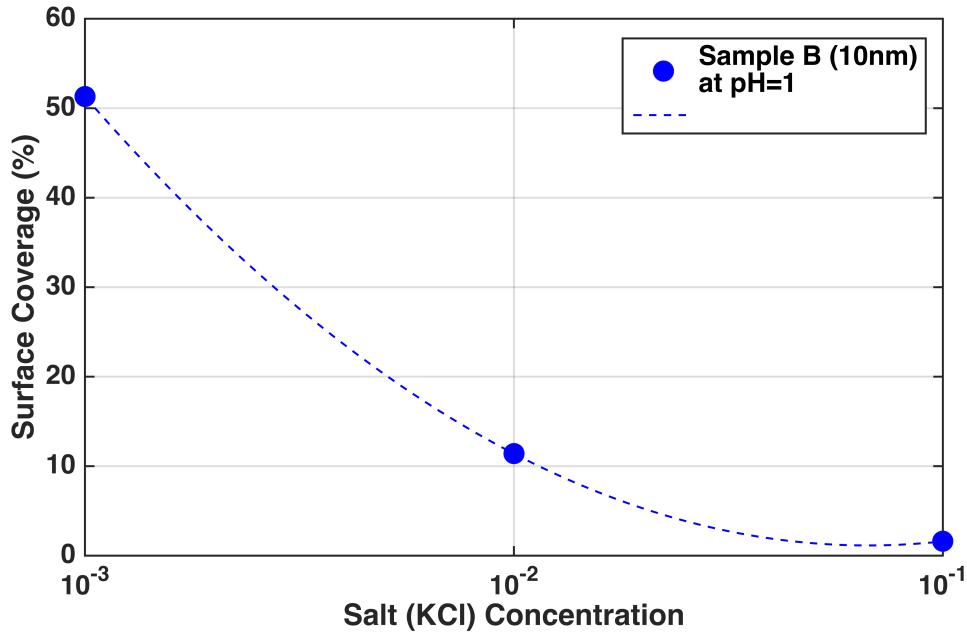

Figure 6-14 – Surface coverage of sample B at pH=1 as a function of salt (KCl) concentration. Adding KCl seems to lower surface coverage and increase aggregation of NDs on the surface.

6.5.4 X-Ray Photoelectron Spectroscopy

Figure 6-15 below shows spectra for C1s and B1s lines for samples under study. Using the CasaXPS software package, background subtraction was performed following fitting of the background using the Tougaard model. After that, peaks were fitted to components using an asymmetric combination of Gaussian and Lorentzian functions (SGL(14)).[141] C1s spectra in figure 6-15(a) are background-subtracted, however B1s spectra in 6-15(b) are shown with backgrounds.

Table 6-2 – Summary of atomic % percentages of boron, carbon, nitrogen and oxygen species from XPS surveys.

Sample	B (At%)	C (At%)	N (At%)	O (At%)
A	11.89±0.74	72.03±0.66	–	16.09±0.27
B	13.05±0.89	49.64±0.45	3.34±0.26	33.98±0.2
C	1.48±0.13	74.47±0.55	–	23.77±0.31
D	–	78.42±0.52	0.9±0.32	20.68±0.27
E	29.74±4.52	16.75±1.59	–	53.5±0.65

A summary of atomic percentages of B, C, N and O species from XPS surveys is presented in table 6-2. In all samples, carbon and oxygen were detected, however boron and nitrogen were not always detected in the survey. Table 6-3 lists all C1s features after fitting. All samples presented with a main carbon peak near ~285 eV (labelled C2) attributed to sp^3 carbon. None of the samples showed any sign of 282~283 eV peaks normally associated with boron carbides.[142] In addition, for samples A, B, C and E no sp^2 peaks were found near ~284 eV (labelled C1), indicating sp^2 carbons were below the detection limit, if present. Sample D, however, has a C1 feature at 284.4 eV which can be associated with sp^2 carbon. Relative errors

are calculated in the CasaXPS® software package using the 'calculate error bars' function under 'quantification parameters'. Errors are <10% for species in most samples, except for nitrogen in sample D and boron in sample E where it is at 15% and 35% respectively. Relatively large errors are attributed to lower signal to noise ratios seen where total counts are lower in survey scans. In samples without a reported at%, an area could not be fitted under the survey graph.

Table 6-3 – Summary of fitted carbon C1s features, showing both binding energies (in eV) and % concentrations.

Sample	C1 BE (eV)	C1 (%)	C2 BE (eV)	C2 (%)	C3 BE (eV)	C3 (%)	C4 BE (eV)	C4 (%)	C5 BE (eV)	C5 (%)	C6 BE (eV)	C6 (%)
A	–	–	284.9	61.86	285.5	14.33	286	15.57	–	–	289.9	8.25
B	–	–	284.9	52.44	285.8	40.99	–	–	–	–	288.6	5.57
C	–	–	285	86.1	–	–	286.8	5.12	288	8.8	–	–
D	284.4	15.1	285.1	48	285.8	31.5	–	–	288.3	5.5	–	–
E	–	–	285	68.9	–	–	286.8	26.4	–	–	289.1	4.7

Features around 285.5 eV, here labelled as C3, represent CH_x groups, while features labelled C4 here are attributed to C–OH and C–O–C bonding.[143] Peaks fitted around ~288 eV (C5) are assigned to –O–C–O– bonding, while those around ~289 eV are assigned to (O=C)–O.[143] Generally, features at or above 286 eV are attributed to oxide states. Table 6-4 lists fitted features from boron (B1s) lines, plotted in figure 6-15(b). Plots feature two main peaks in most samples, which may be associated with clusters of boron (~186.5 eV, labelled B1),[142] while features around ~192 eV (labelled B2) are assigned to Boron oxides or B-C & B-O mixtures.[142]

Table 6-4 – Summary of fitted boron B1s features, showing both binding energies (in eV) and % concentrations.

Sample	B1 BE (eV)	B1 %Conc.	B2 BE (eV)	B2 %Conc.
A	187.3	9.76	191.9	90.24
B	185.4	44.7	190.1	55.3
C	186.6	44.72	191.9	55.28
D	–	–	–	–
E	186.1	88.16	191.7	11.84

No direct evidence of features representing crystalline boron-carbide (hexagonal or cubic) are present. Sample D had no clear boron features near the B1s binding energy range, and was not detected in the survey, possibly due to the acid reduction process (refer to sample definitions in 6.4.1).

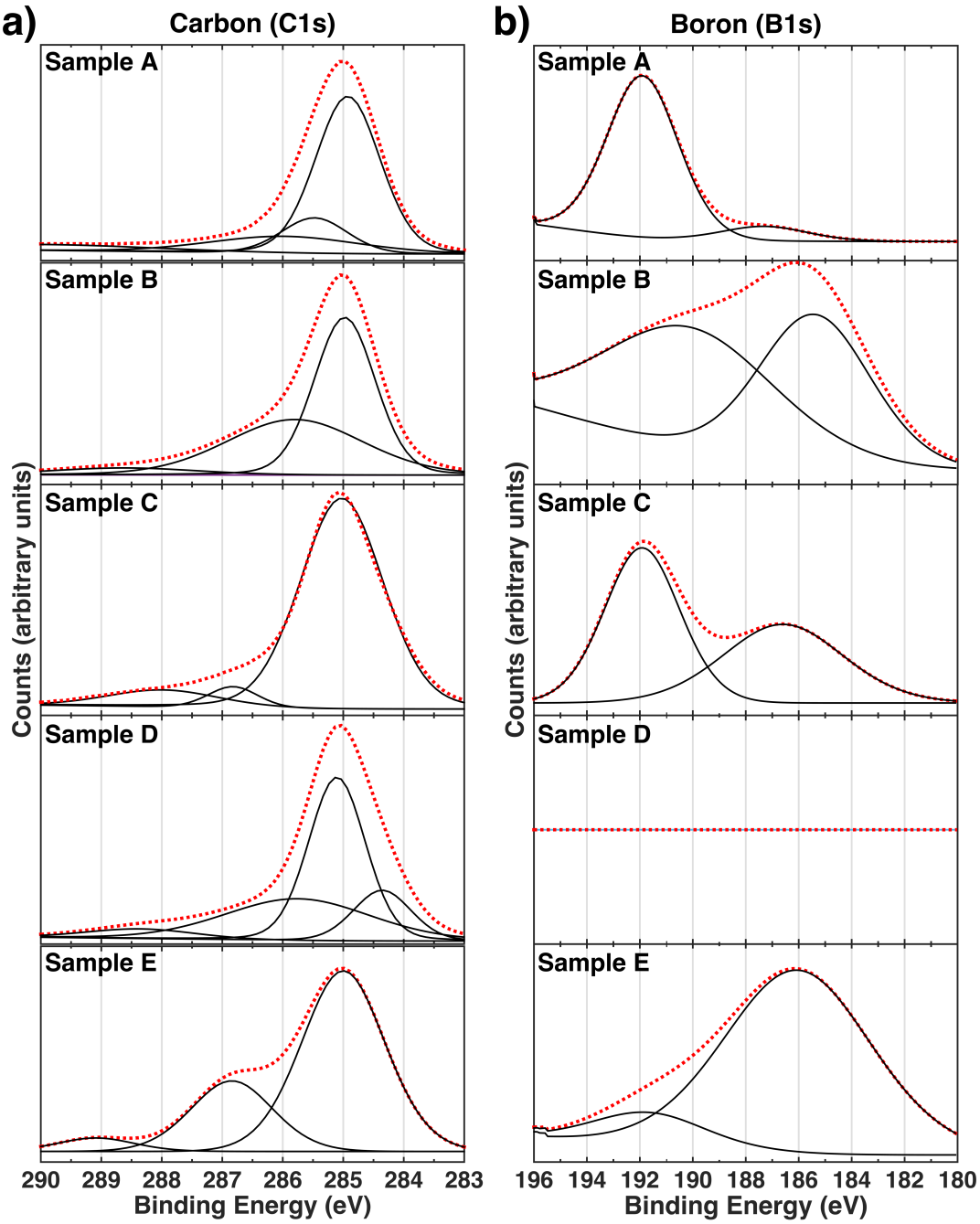

Figure 6-15 – XPS spectra of samples A-E, showing C1s features (a) and corresponding B1s features (b).

6.6 Discussion

Previous studies have discussed the effects of pH on the surface charge and Zeta potential on detonation nanodiamonds in aqueous solutions.[83] It was found that detonation NDs with dominantly oxygen groups on their surfaces maintain negative Zeta potentials across the pH range, while nanodiamonds annealed in a hydrogen atmosphere maintain a positive Zeta potential for the entire pH range studied (3-11). In both cases, the Zeta potential is seen to drop as pH increases. In air-annealed detonation NDs, this behaviour was attributed to de-protonation of hydroxyl and carboxyl surface groups, which are dominant on acid-cleaned ND surfaces[83,144] (refer to sections 4.1 and 4.2). On the other hand, Williams *et al.*[144] attributed the positive Zeta potential in hydrogen annealed DNDs to electronic interactions with hydronium in the aqueous solution. According to those authors, graphitic shells around nanodiamond cores provide the high density of states necessary to facilitate this interaction. Figures 6-13 and 6-14 sum the results of all the variable pH seeding experiments in this work, applied to samples B, C, D and E. Sample A was the topic of discussion earlier in this thesis. As concluded in chapter 5, this sample is composed of detonation nanodiamonds, purposefully boron-doped, and is estimated to have a substitutional boron concentration between 10^{17} and 10^{20} cm^{-3}. For sample B, which is heavily boron-doped, and synthesised by HPHT, the peak nucleation density decreases linearly between pH 1 and 3. The nucleation density reaches 45% of the surface area at pH 1. Further analysis was performed to find whether or not the salt concentration would affect the seeding density; it was found that the seeding

density, at pH 1, is affected by the concentration of potassium chloride in the aqueous solution. The surface coverage rises exponentially with decreasing KCl concentration, between 10^{-1} and 10^{-3}. At a KCl concentration of 10^{-3}, the surface coverage reaches 50%, slightly higher than that with no added salt. The added salt's inability to affect the nucleation density drastically may be explained by the high acidity of the solution used in this work, compared to Yoshikawa's. For samples C, D and E, all of which are heavily boron doped (B~800 ppm), it is clear that the highest nucleation intensity is reached around pH~2. Silicon dioxide is known to have a negative Zeta potential across a wide range of pH, however, a small window below pH~2 opens for positive Zeta potentials.[145] At this low pH, silicon dioxide, as well as silica and quartz surfaces, acquire positive Zeta potentials that have large enough magnitudes to attract negatively charged particles, such as air-annealed detonation nanodiamonds as well as acid treated HPHT nanodiamonds. Error bars on Zeta potential data show a spread of zeta potential as high as ±12 meV, however all error bars remain negative across the pH range. The stability of a nanodiamond suspension in solution is greatly affected at very low pH, as seen in DLS data (figure 6-3). Large agglomerates are seen when the absolute magnitudes of Zeta potentials drop and approach zero, due to the weakening of repulsive electrostatic forces. While the Zeta-potential of silicon becomes more positive below ph~2, the opposite happens to boron-doped nanodiamonds, and their absolute Zeta-potential weakens, which allows them to agglomerate together in solution as they approach the silicon substrates. This has the combined effect of enabling attraction to substrate while causing

thickening of the deposited layer beyond a monolayer, at the cost of limiting surface coverage to about 50% as measured in this work. Seeding time and freshness of prepared solution is expected to have a great effect on the dynamics of nucleation. From the results shown in this work, boron doping is found to have considerable effects on the physics of nanodiamond seeding, especially when compared to intrinsic nanodiamond materials. Heavily boron-doped nanodiamonds were found to affect the strength of hydrogen bonds in water,[58] which is also expected to have an influence on stability and surface nucleation. Williams and Hawn[146] performed pH dependant Zeta-potential measurements on boron-carbide (B_4C) particles of diameters below 3μm in aqueous solutions. They used NaOH and KOH to adjust solution between pH 1-13. Results of their measurements are shown in figure 6-16 below.

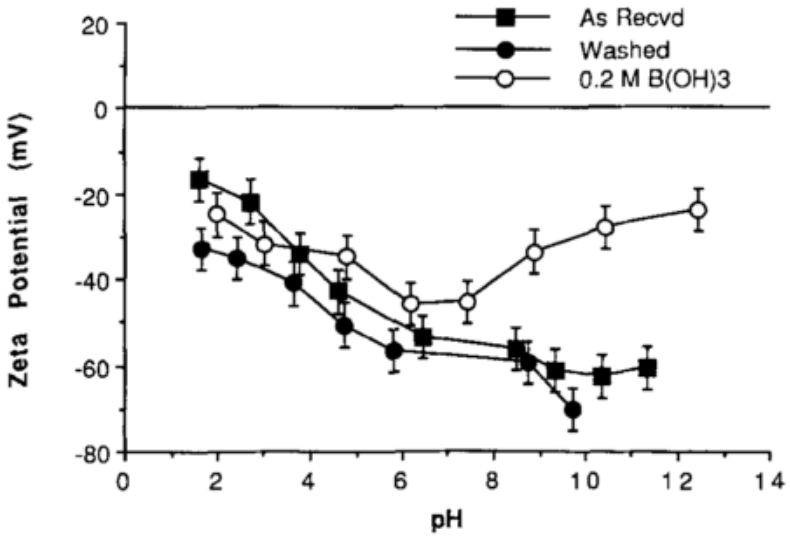

Figure 6-16 – Zeta-potential of boron-carbide (B_4C) powder (<3μm) in aqueous solution as a function of pH. Data points in squares represent an aqueous solution of untreated boron carbide powder, while opaque circles are for powder washed with DI water. Hollow circles represent a solution in which concentrated boric acid was added. Figure taken from Williams & Hawn [1991][146]

Williams and Hawn[146] conclude in their paper that the negative Zeta-potential observed across a wide pH range is caused by the high acidity of boron-carbide surfaces, with iso-electric points (IEP) below pH~1. This high acidity is assumed to be the result of the surface being rich in boron-oxy-carbides and boron oxide states, where the negative charge of this surface is de-localized. Zhang *et al.*[147] have also measured the Zeta-potential of boron carbide powders (particle diameters ~930 nm) as a function of pH. They compared the dispersion of B_4C in DI water with and without added TMAH. Their findings on the relation between Zeta-potential and pH are in line with Williams and Hawn, as shown in figure 6-17. To change pH, they used HNO_3 and NaOH, and the pH range in this study was from 1.7 to 12. According to Zhang *et al.*, TMAH, which acquires a positive charge in water, adheres weakly to the surface of boron-carbide, and mainly acts as a pH modifier. In both cases, B_4C is found to have an IEP at pH<2, again suggesting its surface is highly acidic in water.

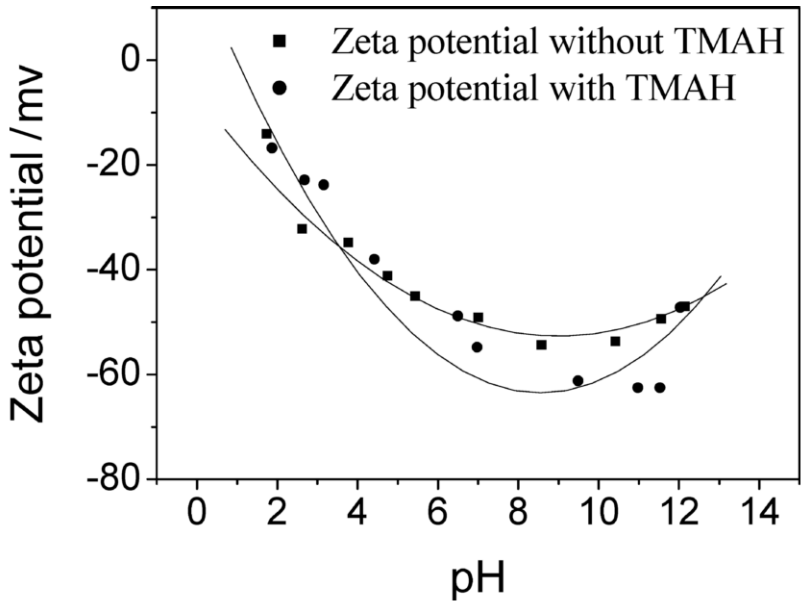

Figure 6-17 – Zeta-potential of boron-carbide (B_4C) powder (<0.93 μm) in aqueous solution as a function of pH, both with (squares) and without added TMAH (circles). Figure taken from Zhang et al. [2008][147]

Although diamond and boron-carbide are two distinct materials, heavy boron doping of NDs can cause their surfaces to be rich in boron states. XPS results in table 6-2 (section 6.5.4) show that B-ND samples have boron content between ~12-30 at.%. More specifically, table 6-4 shows an abundance of boron-oxygen and boron-carbon bonds, as well as boron clusters. This suggests that B-NDs can have surfaces similar to boron-carbides in their high acidity, explaining why B-NDs and B_4C have very similar Zeta-potentials across the pH range. Diamond surfaces can be modified to accept a wide range of chemical bonds. Gribanova *et al.*[148] have performed contact angle measurements of different carbon surfaces, including diamond, at a wide range of pH. They concluded that following acid treatments, an abundance of oxide functional groups dominates on diamond surfaces, making them very acidic, with an IEP at pH<2. The effect of appropriate KCl concentration in

affecting the seeding density of sample B is attributed to the modified separation distance between particles in solution. In a constrained container, or on a surface, an increase in the separation distance forces particles to form agglomerates on surfaces, as found by Yoshikawa *et al.*[86] This effect is clear in figure 6-7, where surface coverage is limited to about 45%, but height measurements confirm the existence of agglomerations in excess of 20nm in height. Since all nanodiamond samples used in this work have different particle diameters, roughness measurements in AFM cannot be used to confirm the quality of seeding. Yoshikawa *et al.*[86] and Hees *et al.*[83] have used roughness to compare seeding quality in nanodiamond samples of the same type, however, for the same reason as above, this does not apply here. In literature, the seeding density is a parameter usually used to compare surface coverage of detonation NDs (~4-5 nm), however different diameters of HPHT ND samples mean a seeding density isn't an appropriate measure of comparison.

Even though 10x10 μm images are relatively large compared to average ND diameters, AFM imaging at this scale does not give an accurate measure of the overall seeding density on silicon substrates. To better assess nucleation densities, stitching of multiple AFM images, up to 100s of microns or even single-millimetres may be required. This, however is time consuming and would require the use of multiple AFM tips per sample due to tip degradation from hard diamond surfaces. Other methods such as SEM or white-light interferometry may be able to scan larger areas, however white-light interferometry does not have the spatial resolution needed here, while SEM

requires the use of conductive substrates, such as highly doped silicon, which would have an effect on seeding dynamics.

6.7 Conclusion

The ultra-sonic assisted nucleation of boron-doped NDs on silicon surfaces was studied by method of pH titration, AFM imaging, Zeta-potential and DLS measurements. To enable explanation of the results in terms of surface chemistry, XPS was also performed on samples. All samples were acid cleaned to get rid of impurities, non-diamond carbon, and metals. No metal species were found in XPS survey measurements. In conclusion, the nucleation behaviour of boron-doped NDs on silicon was found to be highly affected by pH of the solution. Results from pH dependant Zeta-potential measurements and DLS measurements suggest that poor seeding of boron-NDs across pH 3-12 (~5% surface coverage) is due to the electrostatic repulsion between silicon and ND surfaces, as they all have negative Zeta-potentials. This however changes at pH<3, where silicon obtains a positive Zeta-potential while boron-NDs maintain the negative potential. Lack of full coverage can be attributed to the lowered stability of NDs in solution as their absolute Zeta-potentials drop below 30 mV. XPS results confirm the existence of oxygen groups on all samples, and also show presence of boron-oxygen and boron-carbon functional groups, as well as boron-clustering. The errors on XPS fitting should be noted when considering relative concentrations of species; to resolve concentrations with improved accuracy, longer XPS surveys with higher spectral resolution is required. Zeta-potentials of air-annealed NDs measured here and boron carbides are very similar, within measurement error, due to the strong acidity of their surfaces and low iso-

electric points. To improve surface coverage of boron-NDs, surface modification becomes necessary. Hydrogenation of DNDs proved to be an effective way to improve surface coverage, however this can only be applied to ND powders, and is not possible on solutions. Drying of HPHT nanodiamond solutions following acid cleaning proved to be challenging, especially for smaller diameter NDs. Further research into possible surface modification of ND solutions is required, as well as modification of silicon surfaces. It was found that PDDAC significantly improves nucleation of lightly doped B-DNDs, but not heavily doped HPHT B-NDs. This suggests that the boron concentration in the bulk of NDs has an effect on nucleation dynamics. Preparation of HPHT B-NDs at different boron concentrations, but equal diameters, would contribute positively to the discussion. The effect of band structure and band-bending should also be considered in future studies, especially on NDs of smaller diameters, where quantum confinement effects may take place.

7. Electrical Impedance-Spectroscopy of Boron-ND Aggregated Layers

7.1 Introduction

Electrical impedance spectroscopy is a very useful method to study states in the band-gap of a semiconductor, which may be responsible for conductivity.[149] In this chapter, electrical impedance spectroscopy (EIS) is used as a method of obtaining information on conductivity of boron-ND aggregates. Using EIS, AC signals are passed through samples under a constant DC bias, and information about conductivity and conduction mechanisms and their activation energies are obtained. This information is obtained by using equivalent circuit models, which can be compared to measurements using data fitting procedures, where parameters of a proposed model are varied. This technique is of significance for materials with grains and grain boundaries, such as ND materials; it makes it possible to attribute conductivity to crystal grains, grain boundaries, or to electrode carrier injection.[98] In addition, this technique allows for simplified measurement without modification to the material. For example, Hall measurements cannot be directly performed on NDs without modification of the material to improve adhesion with a substrate. Moreover, proper Hall measurements require fabrication of Hall bars, which is not possible without using photolithography or other patterning techniques that would modify the material or its surface groups.

Since diamond has many significant figures of merit,[150] it has been studied and used as an electrode material and in electronic devices. The achievement of diamond thin film growth has made it easier and more economical to work with diamond, however, in grown diamond, including PE-CVD grown films, grain boundaries are almost unavoidable.[151] This has encouraged the study of grain boundaries in diamond films and its effects on conductivity. The understanding of the effects of grain boundaries on conduction paths originates from the fact that they can behave as deep level impurities, such as trap states and recombination centres. Although electrical measurements at variable temperatures can be used to identify dominant impurity levels, it is necessary to use other methods to obtain more information about other, less dominant states.[151] This has led to using spectroscopic methods, AC Hall measurements,[152] as well as C–V[153] measurements and other frequency dependant methods, including impedance spectroscopy.[151] Nath and Wilson[151] have reviewed conductivity of samples reported in the scientific literature, and have found that boron has the most reproducible energy levels among band-gap states. They concluded that grain boundaries are the dominant conduction path in lightly doped samples, regardless of origin. Lee *et al.*[154] have studied undoped, polycrystalline films grown using PE-CVD. They found that the resistance of the film depends on its thickness, and that grain boundaries were again the dominant conductivity path. In their measurement setup, they found that using a metal top electrode and bottom silicon electrode yielded lower resistance, as compared to two lateral top electrodes. They explained this finding as a result of a shorter conduction path

through the material. Lee *et al.* also employed electroplating and electro-etching to find active conduction paths, concluding that grain boundaries are the main conduction path. In a study by Bataineh and Reinhard,[155] impedance spectroscopy between DC and 1 GHz was performed to compare conductivity between thin, PE-CVD grown, and thick, arc-jet deposited freestanding diamond. In this study, several types of Ohmic contacts were used, including p-type silicon and silver paste. It was found that contacts had a small, but non-trivial, effect on conductivity at frequencies of a few-hundred MHz. To fit measurements to an equivalent circuit model, two additional components were added in parallel to the simplified Randles circuit, representing a frequency dependant hopping component, as well as R and C components in series to represent grain interior resistance and inter-grain series caoacitacne.[155] In a recent paper by Paprocki *et al.*,[156] hot-filament CVD diamond films were measured using impedance spectroscopy between 160-290 K. When comparing conduction between grain interiors and grain boundaries, it was found that, in this temperature range, only grain interiors have temperature dependant activation energies. Williams, Lightowlers and Collins[152,157,158] were among the first to research the boron impurity in diamond with detail. At Low boron concentrations ($B \leq 10^{17}$ cm^{-3}), or at low temperatures, single B valence band charge transport is responsible for conductivity, which is contributed by ionised single-B states. Such states have an ionisation energy of ~0.368 eV. At higher B, excited single-B state leads to hopping contribution. As B increases further, overlap of wave-functions leads to an impurity band, which connects with the valence band at some

concentration, making the material semi-metallic via variable-range hopping.[159] According to Mott's theory, the transition point between band and hopping conduction in diamond is at B 2~3x10^{20} cm^{-3} and conduction starts to become of metallic nature.[50] Visser *et al.*[160] have studied conduction mechanisms in Homoepitaxial, CVD boron-doped diamond films using Hall mobility measurements and electrical measurements. They compared samples with different levels of boron concentration, and studied conductivity as a function of temperature. In their work, they found that a transition in activation energy takes place between 225 and 310 K, where a transition from band conduction into hopping starts taking place. The exact temperature depends on the crystal orientation and dopant concentration. The conductivity then can be described as:

$$\sigma = \sigma_1 e^{-E_1/kT} + \sigma_2 e^{-E_2/kT} + \sigma_3 e^{-E_3/kT} \qquad Eqn. 7-1$$

Here E_1 corresponds to the activation energy of band conduction, and E_3 is the activation energy for hopping conduction, and E_2 accounts for impurity band conduction.[50,160]

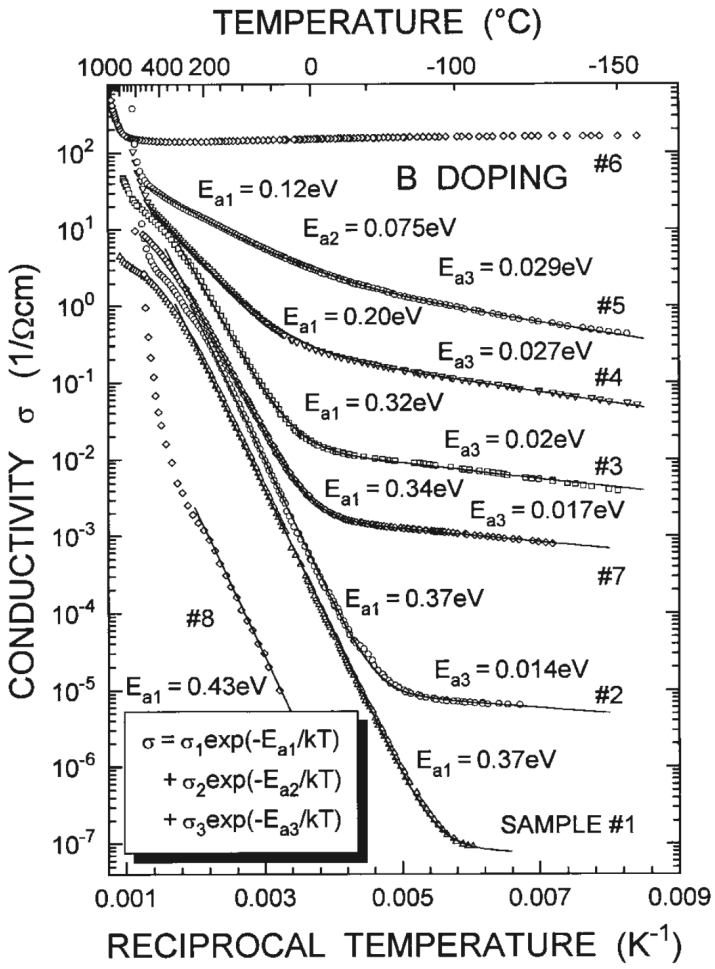

Figure 7-1 – Conductivity as a function of reciprocal temperature for Homoepitaxial boron-doped diamond Hall bars, grown by Borst & Weis.[20,50] *Samples have different levels of boron compensation (from SIMS): sample #1: 7–15 × 10^{17} cm^{-3}, #3: 1.2 × 10^{19} cm^{-3}, #4: 4–5 × 10^{19} cm^{-3}, #5: 1.2 × 10^{20} cm^{-3}, #6: 3 × 10^{20} cm^{-3}, #7: 3–9 × 10^{18} cm^{-3}. Figure taken from Borst & Weis [1996]*[20]

Conductivity paths with activation energies below 150 meV are considered to be in the band conduction regime, and those above this critical value are considered in the hopping regime. In samples where the boron concentration is high, the contribution of band conduction may be ignored.[160] According to Thonke, the terms in the equation above describe valence band conduction (E_1~0.37 eV) at low compensation levels. E_1 diminishes in value as B levels rise above ~10^{19} cm^{-3}, and above the Mott transition point (~2x10^{20} cm^{-3}), its contribution vanishes. According to Thonke, impurity band conduction is

thought to be dominant between room temperature and a few hundred degrees Celsius, when B content is close to the Mott transition concentration, for which E_2 is the activation energy (E_2~75 meV). This is thought to take place where thermal energy allows holes to transport over neutral acceptors.[50] Thonke has also concluded that E_3 is dominated by nearest neighbour hopping when B content is over the Mott transition level.

In n-type (p-type) heterovalent doping, adding an electron (hole) leads to states just at the bottom of conduction band (top of valence band). Confinement makes the added state closer to conduction (valence) band. Also, the lower the hole state energy, the more electrochemically active it will be. In a high dielectric-constant material (5.5 for crystalline diamond, relatively low), carrier states are more localised and are more conductive by being more likely to leak into surroundings. The critical radius for ionization is a measure of carrier state localization in impurity doping, and for higher conductivity, a larger radius is more desirable. Zhang *et al.*[161] found that inter-grain resistance in boron-doped nano-crystalline diamond (B-NCD) is larger than intra-grain resistance. The authors built a resistor-network model, where disorderly sp^2 and sp^3 carbon states form in the grain boundaries during CVD diamond film growth. According to this model, boron behaves as a deep level impurity between diamond grains, meaning it cannot effectively contribute charge carriers at temperature below (<5 K). At higher temperatures, thermal excitation of the deep level boron states, within grain boundaries, gives them mobility and they potentially contribute to conductivity.[161] This leads to an enhancement of the effective boron doping efficiency in the bulk. This then leads to a modification of the resistor-network model by lowering the inter-

grain resistance value. If the resistance becomes very low, the resistor network becomes more complex, and a semiconductor network becomes more fitting of the description; Shottky-barriers can form at grain boundaries, meaning that thermal hopping over barriers, as well as tunnelling through them, becomes possible.[161]

In diamond materials with grain boundaries, many other mechanisms of conductivity have already been suggested, and the occurrence of other phenomena can contribute to impedance measurements. ND materials are known to have a large surface to bulk ratio, and at high temperature, they are subject to graphitisation even under inert gas atmospheres.[162] Diamond grains were also found to decrease in diameter during annealing. This means that under measurement, physical properties of the material can change, and that includes both the bulk and the grain boundaries. Stress or strain in diamond films are also known to affect conductivity. For example, in microcrystalline diamond, stress prevents the direct observation of size-induced Raman shift from 1332 cm^{-1}.[163] This behaviour is expected to be present in aggregated ND films, where stress and re-arrangement of NDs could affect conductivity. Another factor has to do with interfaces with electrodes; when silicon is used, for example, trapped charges at the interface will polarise at higher temperatures, adding to the impedance response. Ye *et al.*[98] suggest that silicon contacts can have an impedance response around 250 ºC due to intrinsic carriers crossing the band gap. They suggest this is related by an unknown mechanism to grain boundary conductivity in nanocrystalline diamond, however this requires further confirmation. The

activation energy they measured for silicon was 670 meV, much higher than activation energies observed in this work.

Zivcova *et al.*[164] have studied polycrystalline boron-doped diamond films using EIS, and have discussed the different equivalent circuit models that can be used to fit data. They concluded in their results that a Randles circuit with a constant phase element (CPE) in place of a capacitor (figure 7–2) best matches their results.

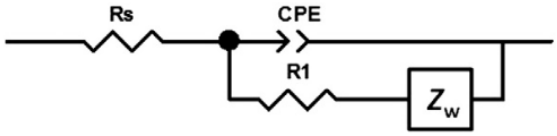

Figure 7-2 – An equivalent circuit used by Zivcova et al.[164] *to fit EIS data to boron-doped diamond films. This circuit is similar to a Randles circuit, but replaces a capacitor with a constant phase element (CPE). Figure is taken from Zivcova et al. [2015]*[164]

A Randles circuit is similar to a parallel R–C circuit, but also includes a Warburg element (Z_W) in series with the resistance in the parallel part. Generally, a simple fitting model includes a series resistance R_S, a parallel plate capacitor C and a second resistance element in parallel with C, which represents resistance due to charge diffusion; this is called a simplified Randles circuit.

Figure 7-3 – The equivalent circuit used in this chapter to fit EIS data to boron-doped ND films. This circuit is similar to a simplified Randles circuit, but replaces a capacitor with a constant phase element (CPE). Figure is adapted from Zivcova et al. [2015][164]

A Randles circuit, however, is generally useful to fit data where a linear portion of the Nyquist plot is measured with a slope of –1/2 (figure 7–4). Since this wasn't observed in our measurements, the simplified Randles circuit with a CPE was used instead. Circuits with CPE elements replacing a parallel plate capacitor C are usually more adequate for fitting or sample results.[165]

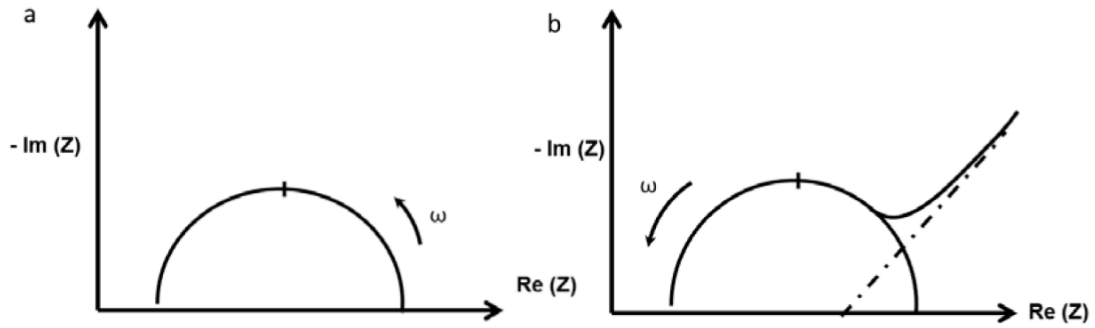

Figure 7-4 – Nyquist plots comparing a Randles circuit (b) and a simplified Randles circuit. A linear portion of the plot, with a 45º angle is indicative of a Warburg element in such circuits. Figure is adapted from Zivcova et al. [2015][164]

7.2 Methods

Samples used in this chapter are A, B, C and E as defined earlier in 6.4.1. Sample A was assumed to have a boron concentration between ~10^{17} and ~10^{20} cm^{-3}. Samples C and E have boron-concentrations of ~800 ppm. Since diamond has atomic density of $1.77x10^{23}$ cm^{-3}, this corresponds to a boron concentration of ~$1.4x10^{20}$ cm^{-3}, which is very close to the Mott transition point in diamond. Sample B is thought to have the highest boron concentration compared to other samples, in excess of ~10^{21} cm^{-3} and well above the Mott transition level.

To perform measurements on nanodiamond aggregates, highly-doped, metallic silicon substrates are used in a 'sandwich' configuration (figure 7–7). Highly n-type arsenic-doped silicon substrates (1×1 cm, 380 μm thick, single side polished, prime grade) of very low resistivity (0.001-0.005 Ω·cm) are used as substrates and Ohmic contacts. Highly conductive silicon substrates are chosen to for two main reasons; the first is to ensure proper physical contact with large surface coverage between the diamond material and the electrode. The second reason is to minimise rectifying effects on the measurement by avoiding p-n or Schottky type junction formation. In addition, having very low resistivity serves to minimise contribution to the skin effect, which is known to arise in high frequency measurement configurations. Nanodiamonds from solution were deposited onto substrates in two steps. Initially, a small volume of nanodiamond solution (~3-5 μl) was deposited onto the polished side of a silicon substrate using a micropipette, and then a second silicon substrate was placed on top of it so the solution is confined between the two polished

surfaces. The two substrates were gently rubbed together while applying pressure until the solution dried, leaving a thin coat of nanodiamond on the substrate. The substrate was then rinsed in DI water. This process can be repeated multiple times. The second step was to drop-coat the substrate using small amounts of the solution, ~50 µl at a time, while the substrate sat on a hotplate (~90 °C). This way a thicker coat of nanodiamond covers the substrate, while ensuring all parts of the substrate are covered. The confined-nucleation step ensures a portion of the nanodiamonds adheres to the whole surface including corners, therefore facilitating further nucleation by reducing the surface tension of solution droplets. In the scientific literature, mechanical abrasion of the surface using diamond grit is known to improve the seeding density.[85] Impedance measurements over a range of temperatures were performed in a vacuum vessel with pressure control and inert gas flow control. The custom designed measurement cell (figure 7–7) allowed precise measurements with very low noise levels. The measurement cell is composed of two ceramic plates separated by 3 cm, and held together by stainless-steel bolts and nuts. The lower substrate is placed on top of a copper contact, while a second copper foil contact is placed on top of the upper substrate. A ceramic plate sits on top of the upper copper foil contact, and the spring is loaded on top of it to keep even pressure. This configuration ensures a uniform, reproducible pressure is applied by using stainless steel springs. A high vacuum environment (2–3x10^{-7} mBar) is used to control adsorption and desorption of humidity, while annealing in Argon gas prior to measurement (1 hour at 30 mBar, 300 sccm) ensures the chamber is properly purged.

Vacuum-compatible, coaxial cables with copper cores were used inside the chamber to improve the signal to noise ratio, while coaxial cables were used between the vacuum feed-through and the measurement apparatus.

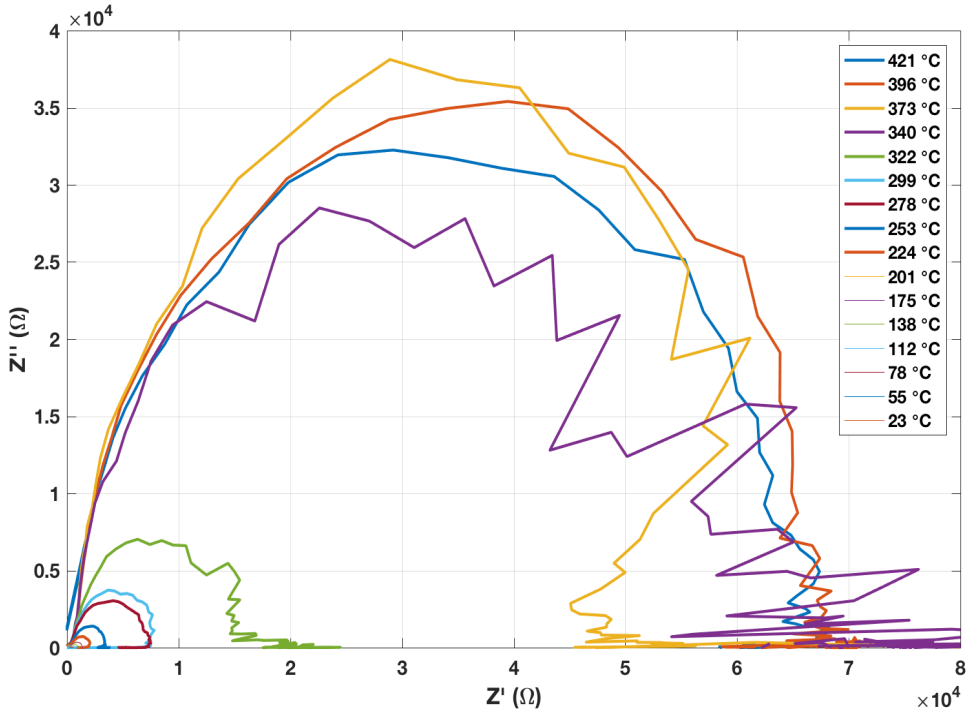

Figure 7-5 – Sample C (20 nm HPHT NDs): Data shown here were obtained using silver paste contacts and tungsten probes, in ambient conditions. Nyquist plots at different temperatures are shown, all showing single semi-circles. The signal to noise ratio is much lower compared to data obtained using the improved test cell. The large difference in magnitude between semi-circles is attributed to the presence of bulk as well as surface conductivity.

Figure 7–5 can be compared to figure 7–10; it shows a significant improvement in signal quality. The first was measured in ambient conditions, using silver paste contacts on conductive silicon substrates, and the latter figure is for measurements done in the vacuum chamber using the purpose-made measurement cell. All measurements are performed at a frequency range between 0.1 Hz and 10 MHz for consistency. An AC bias of 0.01 V is chosen for all samples and measurements on the SMaRT impedance

measurement software, which was interfaced with a programmable DC power supply to automate measurements. At every temperature step, 15 minutes were allowed for the measurement cell to approach thermal equilibrium. Fitting of Nyquist plots using the ZView 2.0 software and equivalent circuit models yields resistance and capacitance values that are used to form Arrhenius plots for activation energy extraction.

7.3 Results

7.3.1 Electrical Measurements

As seen in figures 7–8, 7–10, 7–12 and 7–14, Nyquist plots of real and imaginary impedance, plotted against each other, are semi-circular, with one semi-circle for each temperature step. In chapter 5, figure 5–1, it is clear that more than one conduction mechanism is present at a given temperature (more than one semi-circle), suggesting surface conductivity is present due to humidity. In this chapter, all samples measured in vacuum showed only a single semi-circle at a given temperature. According to the Arrhenius equation, if the natural logarithm of the resistance (in ohms) is plotted as a function of the inverse absolute temperature (1/K), extraction of activation energy E_a values from linear regions in the plot is possible. Each activation energy is potentially corresponding to a conduction mechanism. Figures 7–16 to 7–19 plot the logarithms of R values against reciprocal absolute temperature, showing linear fits and corresponding activation energies, and figure 7–20 is a summary of all the figures together for comparison. Resistivity and conductivity (figure 7–21) are plotted together as a function of reciprocal temperature. Resistivity is calculated from resistance values with the

assumption that average film thickness is 0.5 μm. This average value is obtained from AFM imaging of drop-coated films on silicon substrates (figure7–6). Conductivity is subsequently computed as the inverse of resistivity. Conductivity values range between ~0.4–60 $S \cdot cm^{-1}$. Capacitance values extracted from Nyquist plot fitting is summarised in the appendix (figure 11–8). For samples A, C and E, values of $C=1\sim3x10^{-10}$ F are measured, and remain constant across the temperature range, apart from a slight increase in sample E. For sample B, higher C values across the temperature range are measured, with an abrupt surge above ~180 ºC. Presented measurements for samples B and C are repeated; previous measurement for sample B presented with a measurement software error, which was suspected to be related to sudden change of phase in the diamond material. For sample C, increasing resistance values with increasing temperature below 150 ºC suggest the existence of moisture. Figures of previous attempts (appendix figures 11–1 and 11–2) show an agreement in activation energy (sample B at low temperatures, sample C at T>150 ºC) within calculated error.

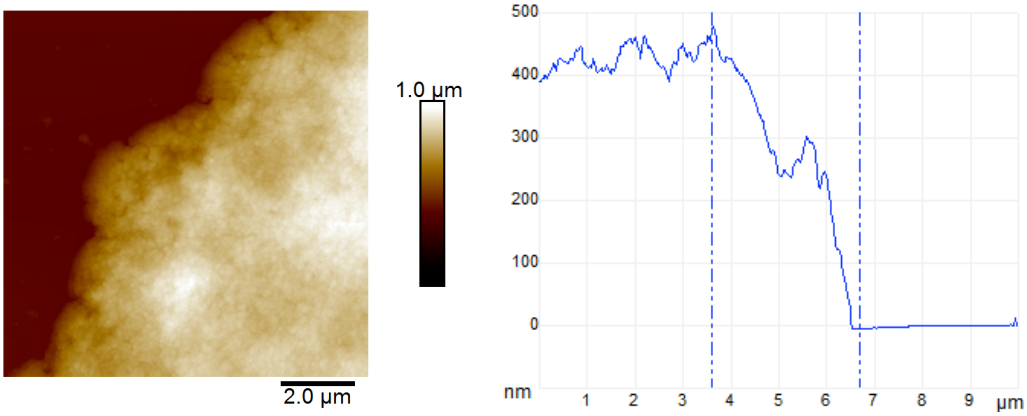

Figure 7-6 – Thickness measurement of Nanodiamond film using AFM imaging (left). A step profile of one horizontal line in the image is also shown (right).

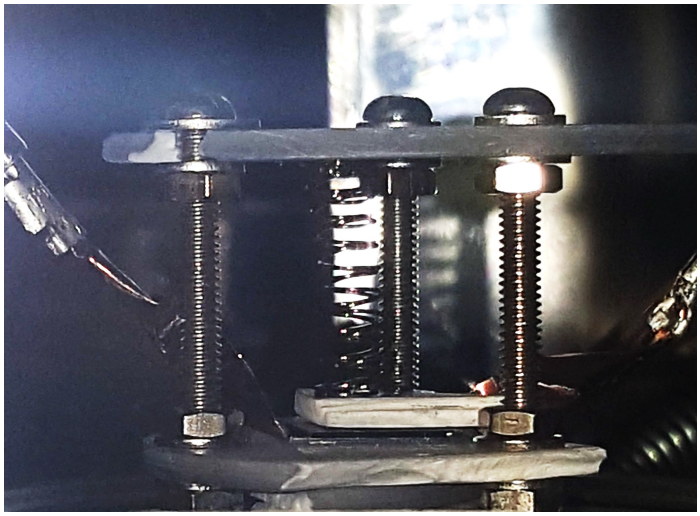

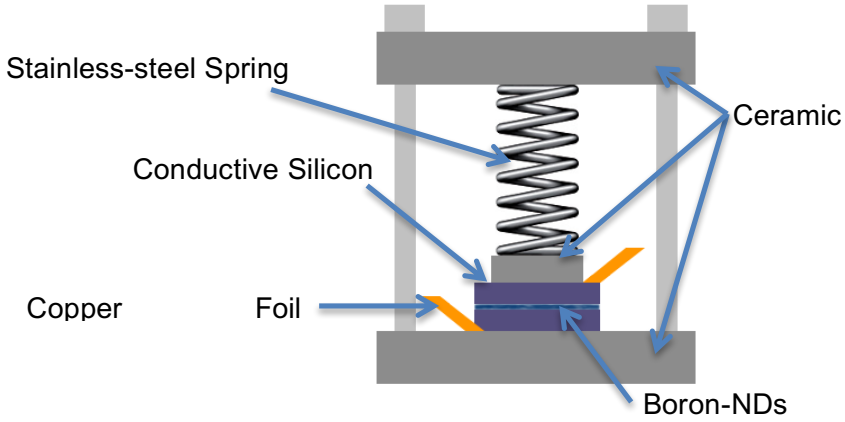

Figure 7-7 - Impedance spectroscopy test cell for nanodiamonds. Image shown on top is for the test cell in vacuum, under measurement. Below a schematic of the test cell is shown.

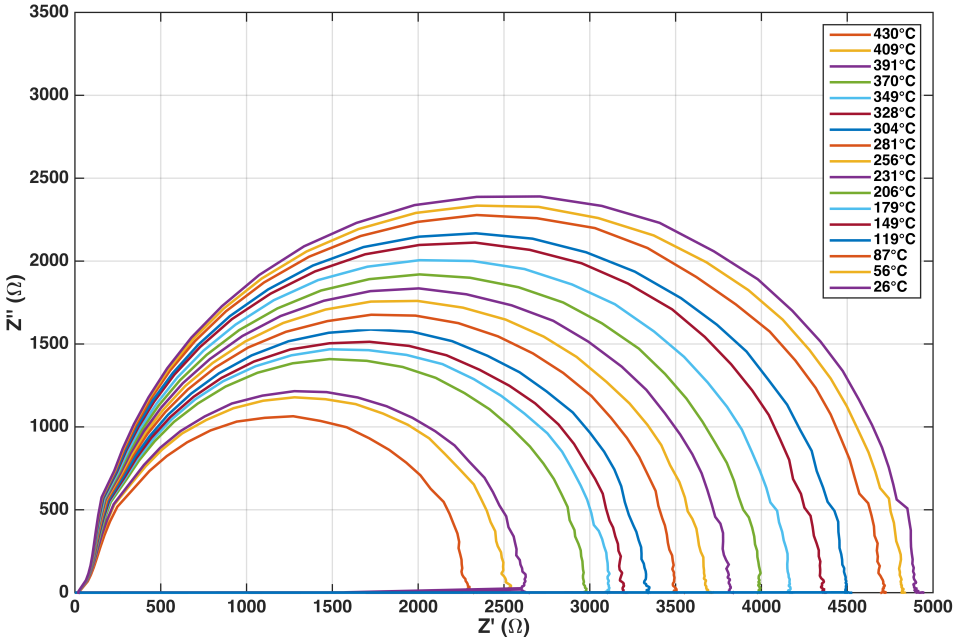

Figure 7-8 – Sample A (DND): Nyquist plot of real vs imaginary impedance components at different temperatures, all showing single semi-circles.

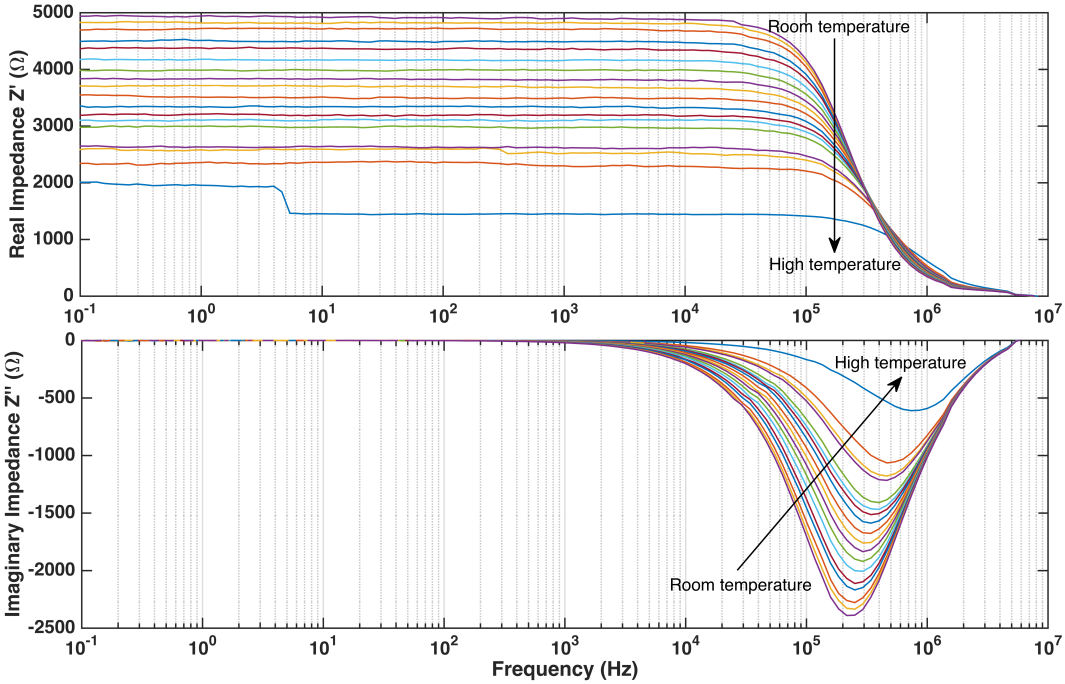

Figure 7-9 – Sample A: Bode plots of real impedance vs frequency (top) and imaginary impedance vs frequency (bottom).

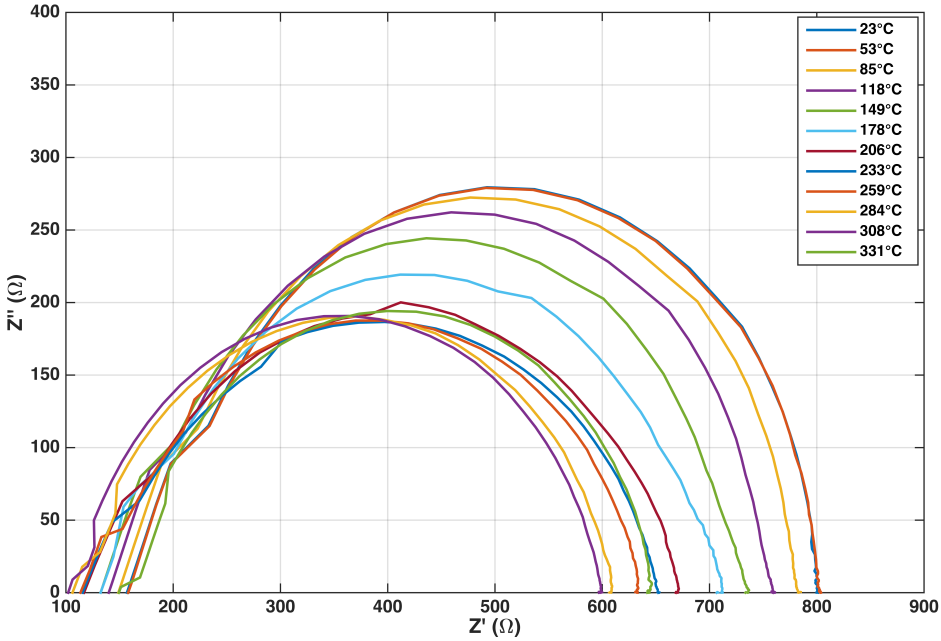

Figure 7-10 – Sample B (10 nm HPHT NDs): Real vs imaginary impedance components at different temperatures, all showing single semi-circles.

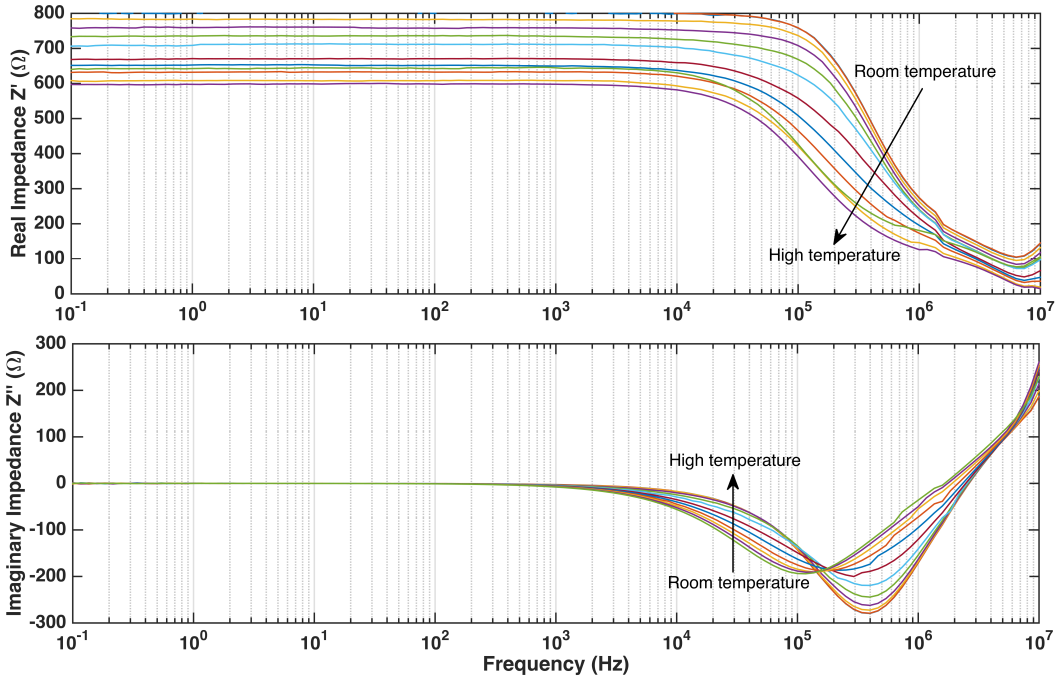

Figure 7-11 – Sample B: Bode plots of real impedance vs frequency (top) and imaginary impedance vs frequency (bottom).

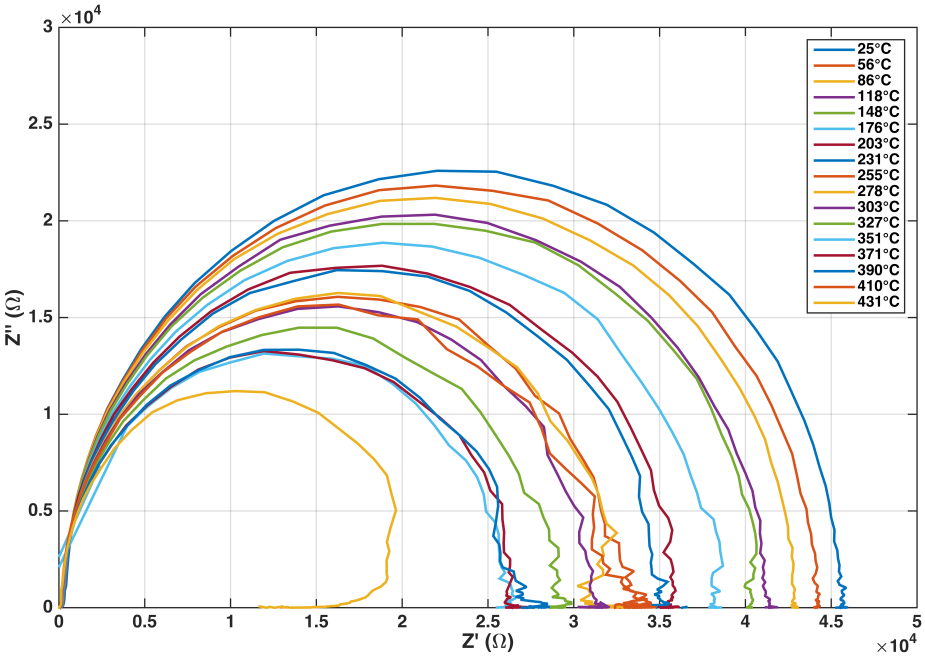

Figure 7-12 – Sample C (20 nm HPHT NDs): Real vs imaginary impedance components at different temperatures, all showing single semi-circles.

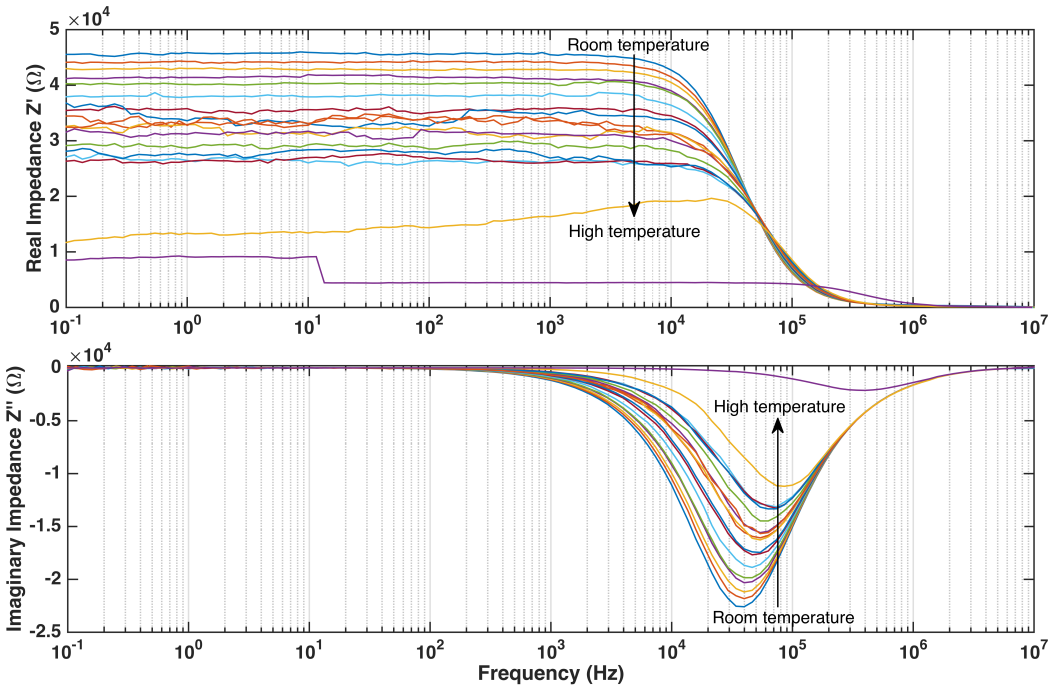

Figure 7-13 – Sample C: Bode plots of real impedance vs frequency (top) and imaginary impedance vs frequency (bottom).

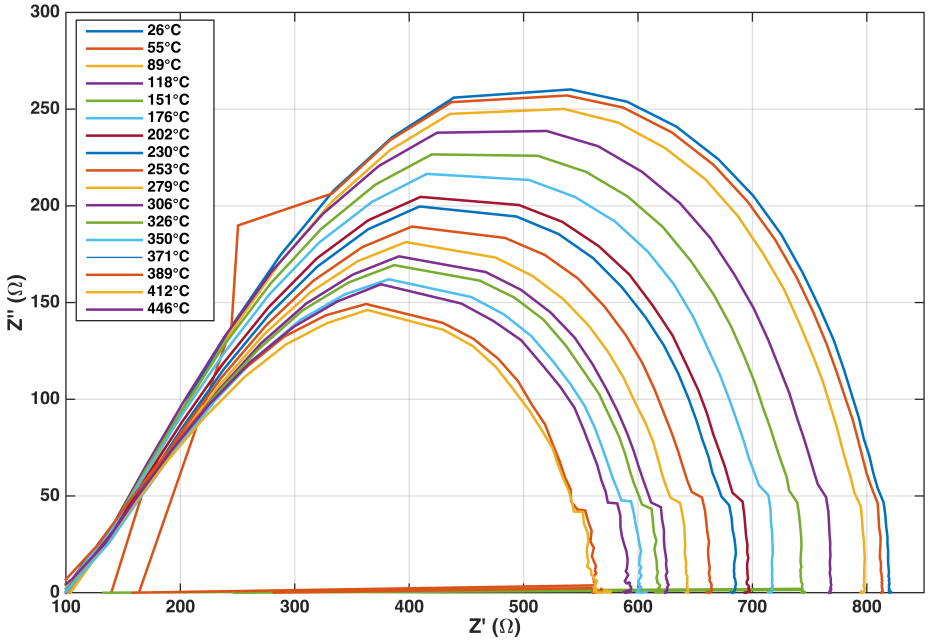

Figure 7-14 – Sample E (100 nm HPHT NDs): Real vs imaginary impedance components at different temperatures, all showing single semi-circles.

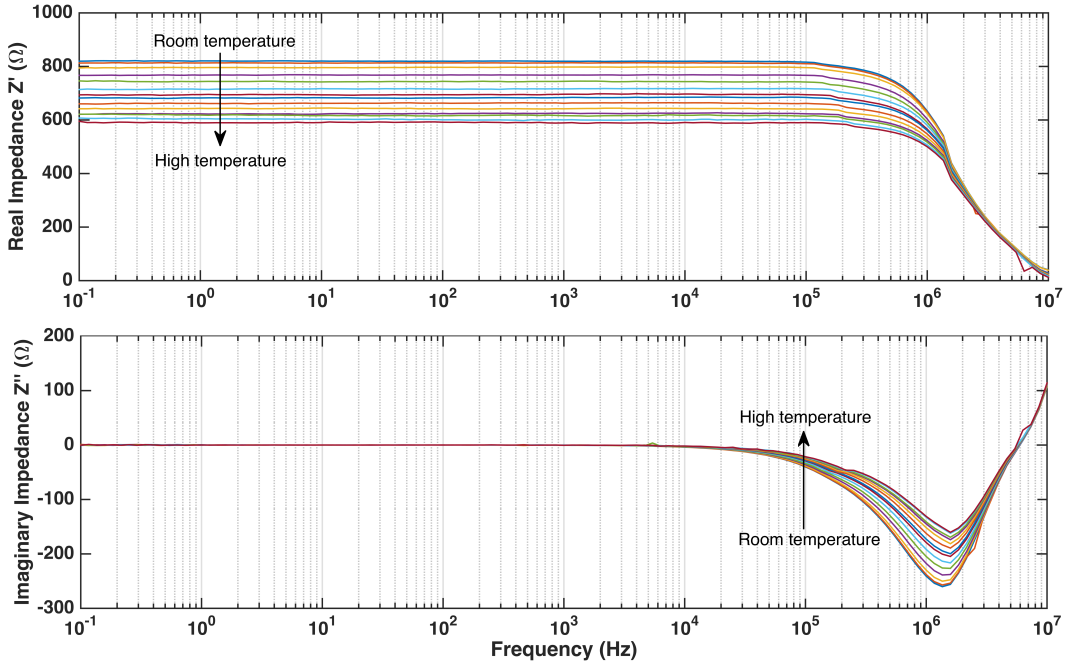

Figure 7-15 – Sample E: Bode plots of real impedance vs frequency (top) and imaginary impedance vs frequency (bottom).

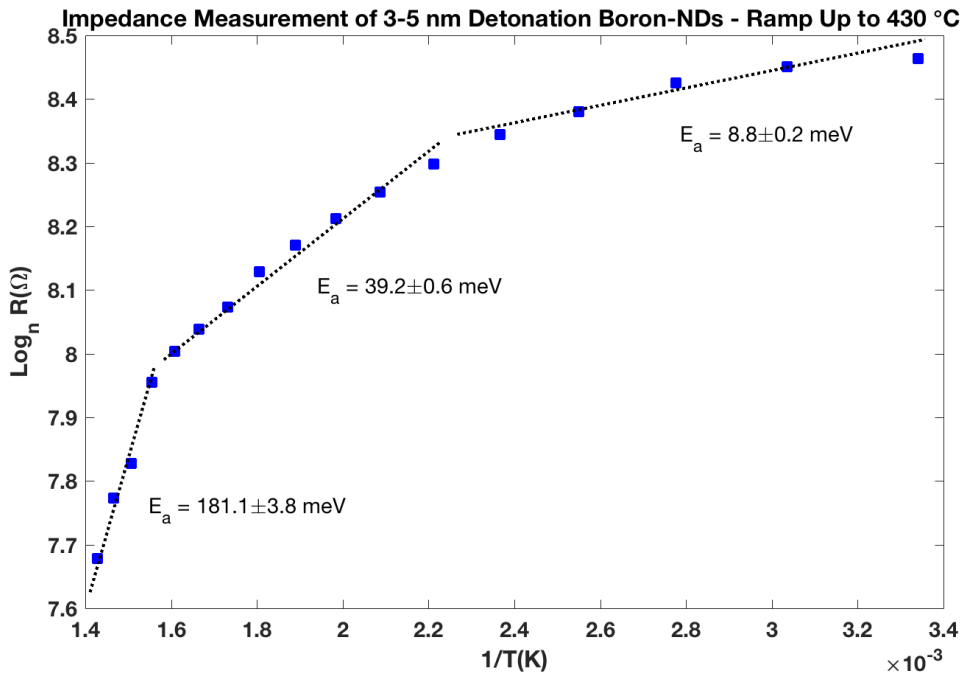

Figure 7-16 – Arrhenius plot of Boron-doped detonation nanodiamond film measured between room temperature and 430 °C.

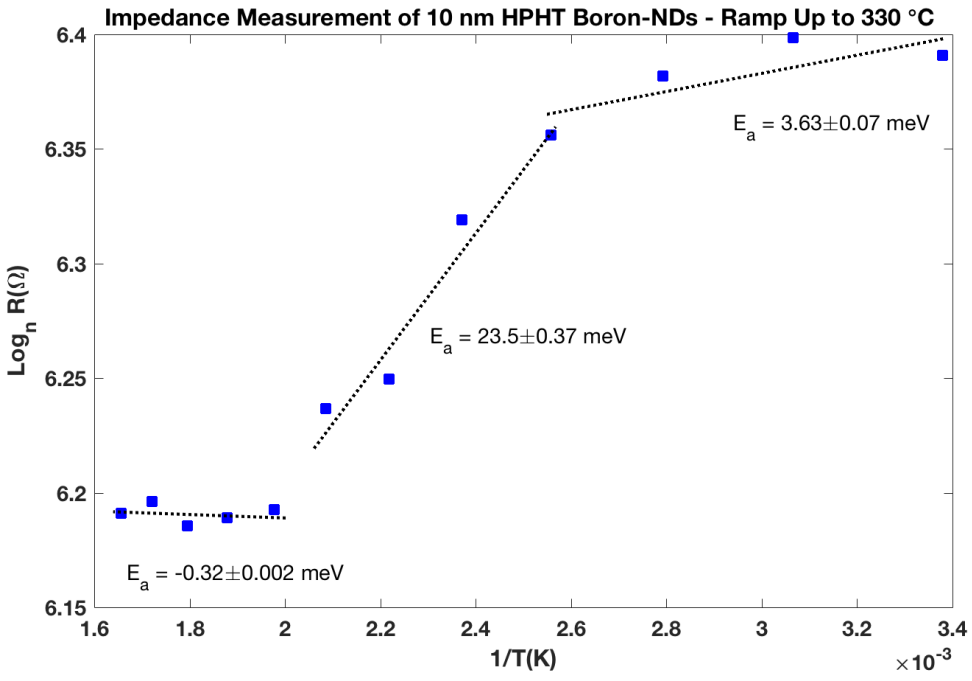

Figure 7-17 - Arrhenius plot of 10 nm Boron-doped HPHT nanodiamond film measured between room temperature and 330 °C.

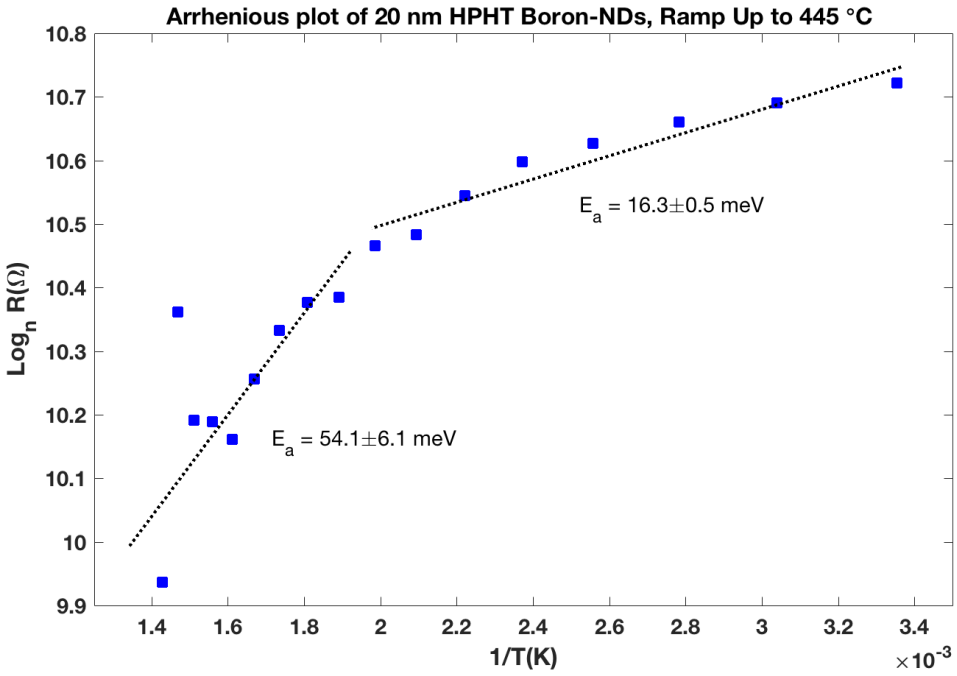

Figure 7-18 - Arrhenius plot of 20 nm Boron-doped HPHT nanodiamond film measured between room temperature and 445 °C.

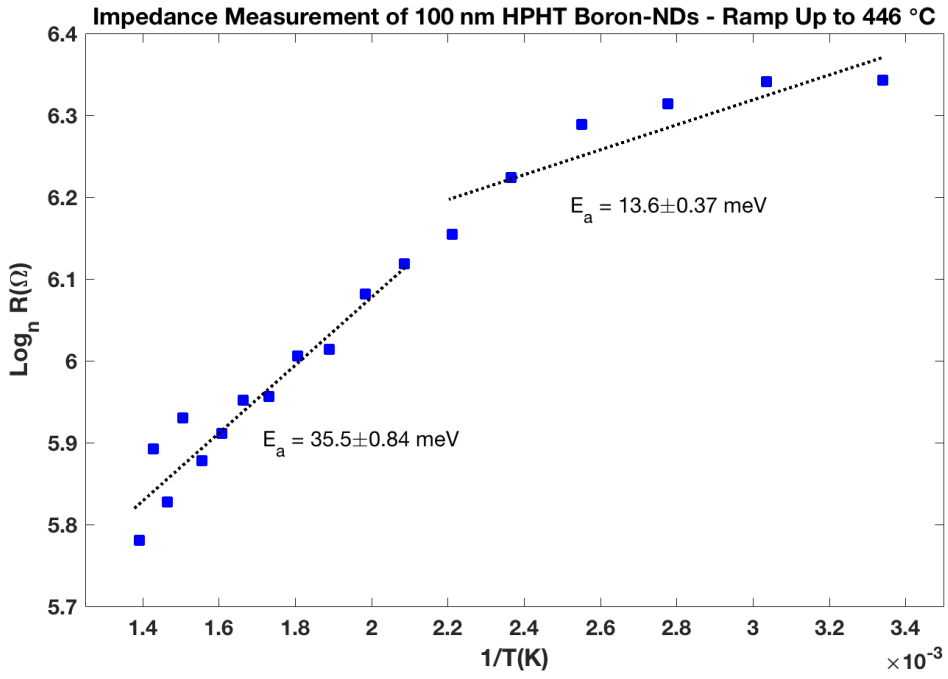

Figure 7-19 - Arrhenius plot of 100 nm Boron-doped HPHT nanodiamond film measured between room temperature and 446 °C.

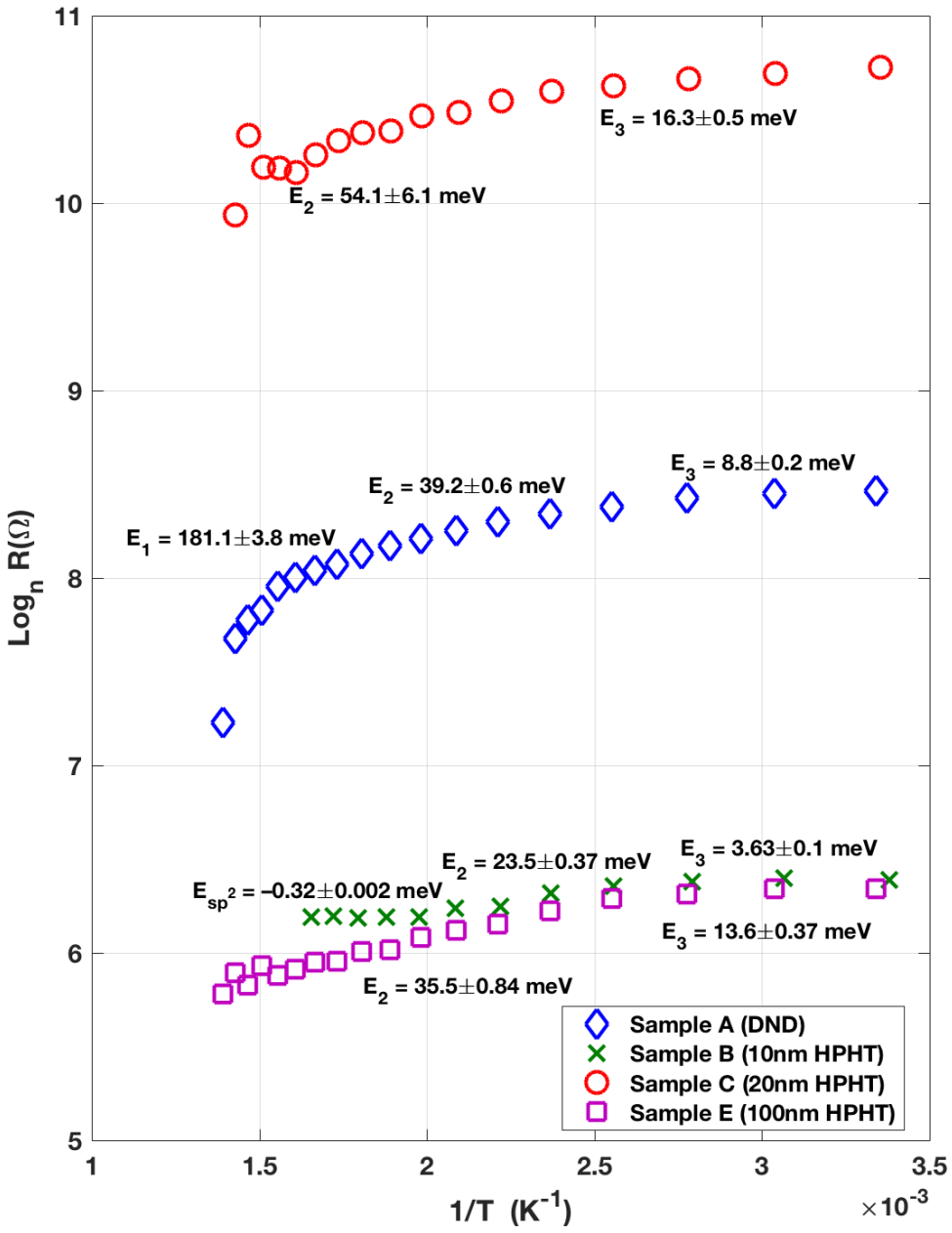

Figure 7-20 – Summary of logarithmic resistance plotted against reciprocal temperature, for all samples. Corresponding activation energies are labelled for comparison.

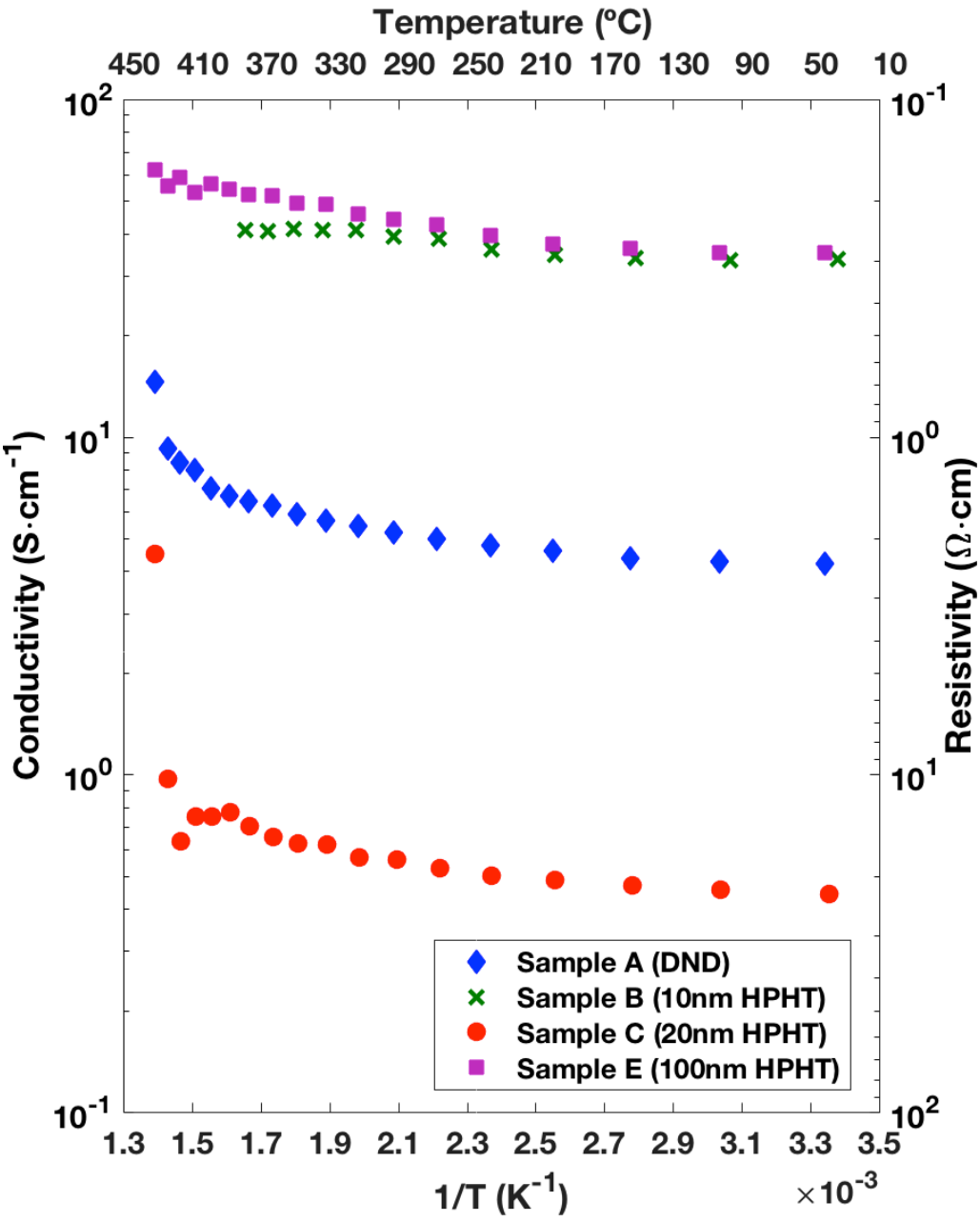

Figure 7-21 - Temperature dependant conductivity and resistivity measurements on Boron-doped nanodiamond films. Data obtained from impedance spectroscopy measurements. Scale on left is for conductivity, and on right is for resistivity.

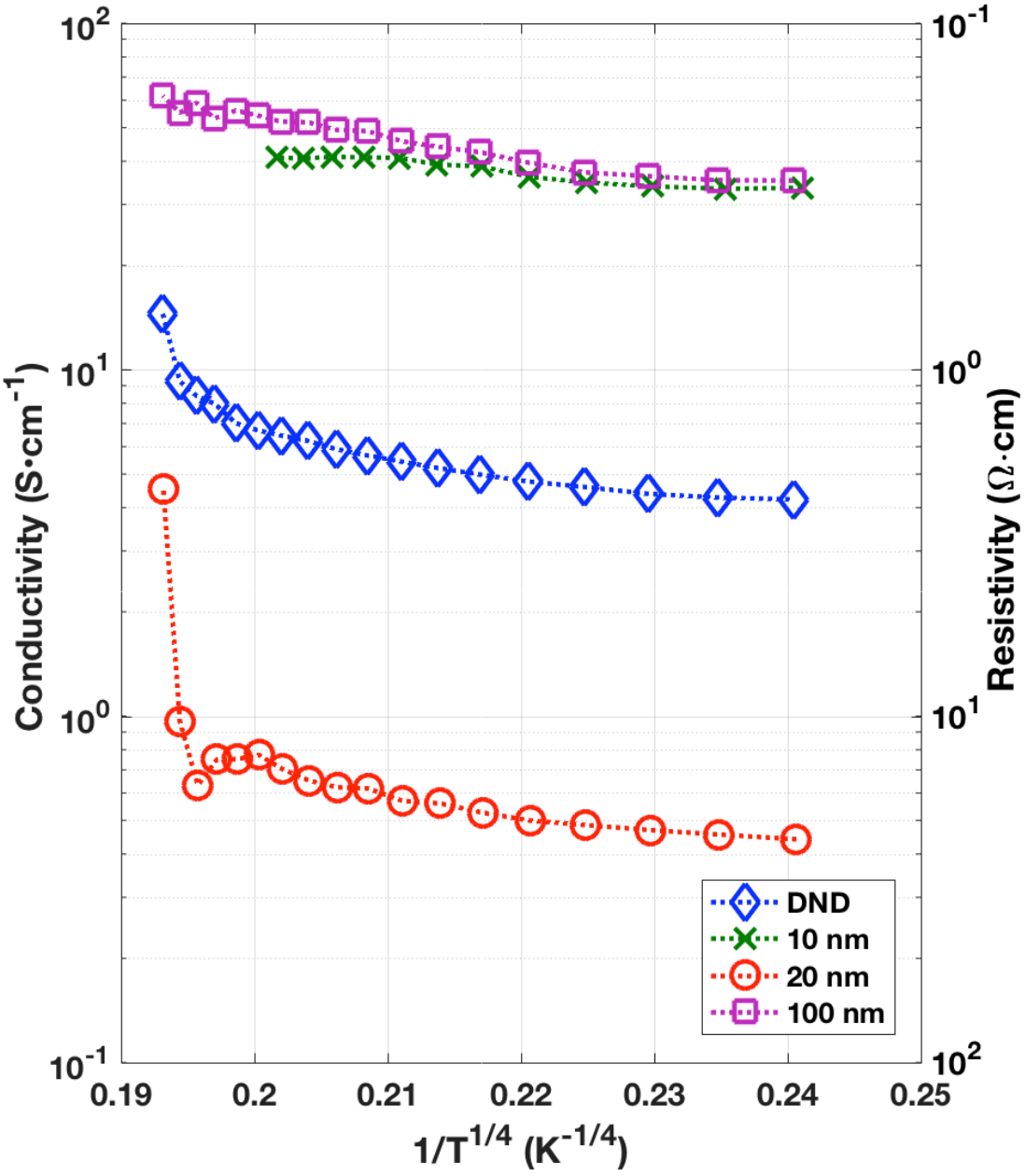

Figure 7-22 – Temperature dependant conductivity measurements on Boron-doped nanodiamond films. Data obtained from impedance spectroscopy measurements. Here the conductivity is plotted against the $1/T^{1/4}$, in order to show variable range hopping trends, which are linear on this scale.

7.3.3 Cut-off Frequency

It is clear that for all samples, the cut-off frequency is shifted up as the temperature rises, which coincides with reduced resistivity of the nanodiamond films at higher temperatures. The cut-off frequency of sample B, on the other hand, takes a rapid step towards a higher frequency when the temperature approaches 200 °C, indicating a potential change of phase. Real impedance plotted against frequency (top portions of figures 7–9, 7–11, 7–13 and 7–15) follows the same pattern for all samples, where the impedance remains constant at low frequency, then drops near the cut-off frequency. For sample B the NDs start to change phase at high temperatures; the ratio of sp^2 to sp^3 carbon phase is increased, as seen in the appearance of sp^2 related peaks in the Raman spectrum (figure 7–26).

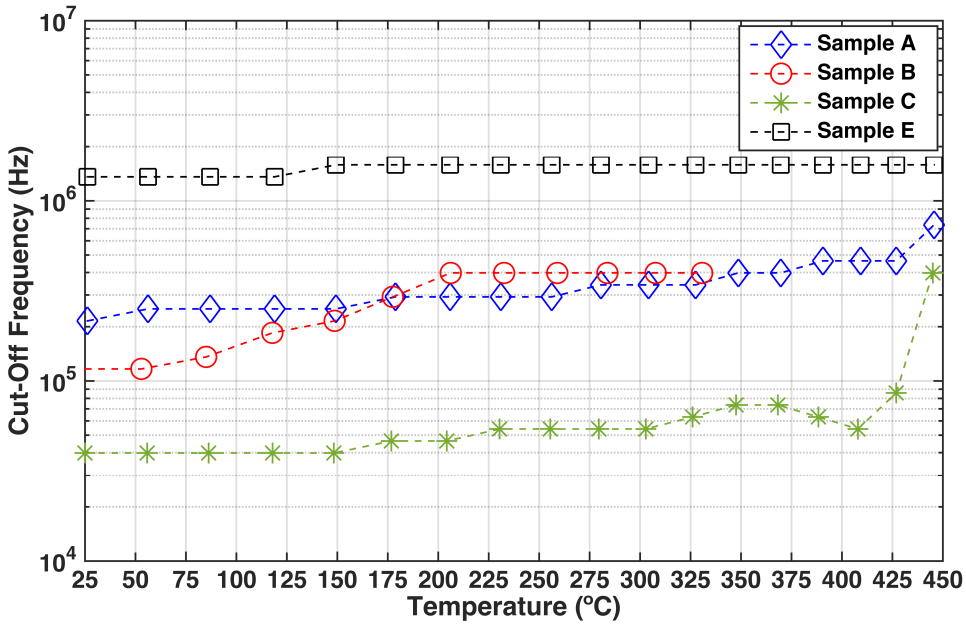

Figure 7-23 – Cut-off frequency as a function of temperature. Cut-off frequencies increase gradually with temperature.

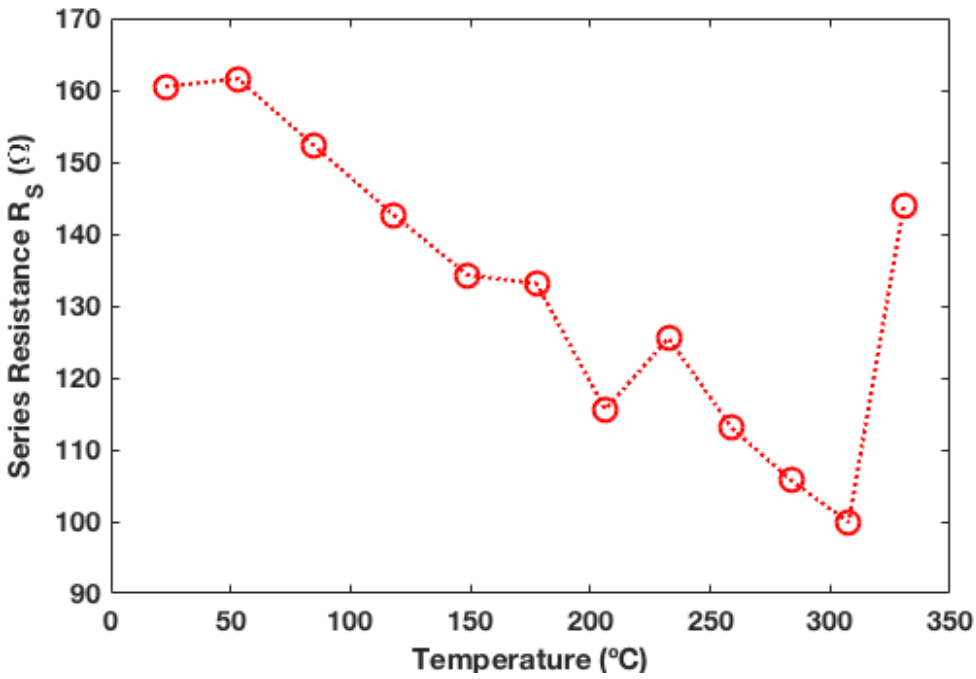

Figure 7-24 – Sample B: series resistance as a function of temperature.

7.3.3 Raman Spectroscopy

In both HPHT and detonation NDs, non-sp^3 phases may be present, however this is dependent on the growth conditions. Raman spectroscopy was used here to get a measure of sample quality. In figure 7–25, Raman spectra for HPHT NDs are all seen to have a diamond first order Raman feature. For sample B, it's located at 1303 cm^{-1}, and for samples C and E it is found at 1327 cm^{-1}. All samples exhibit sp^2 phase peaks (G peak between 1586–1607 cm^{-1} and D peak between 1341–1348 cm^{-1}), except for sample B. For sample B, the sp^2 related features are only observed after annealing, as seen in the comparison in figure 7–26. Narrow diamond peaks in samples C and E are found on top of broader D peak features around ~1340 cm^{-1}. For sample A, a diamond peak isn't clearly distinguishable, but the feature on the lower end of

the spectrum peaks at ~1332 cm^{-1}, which suggests a small diamond peak is again sitting on top of a larger, broader peak around ~1340 cm^{-1}.

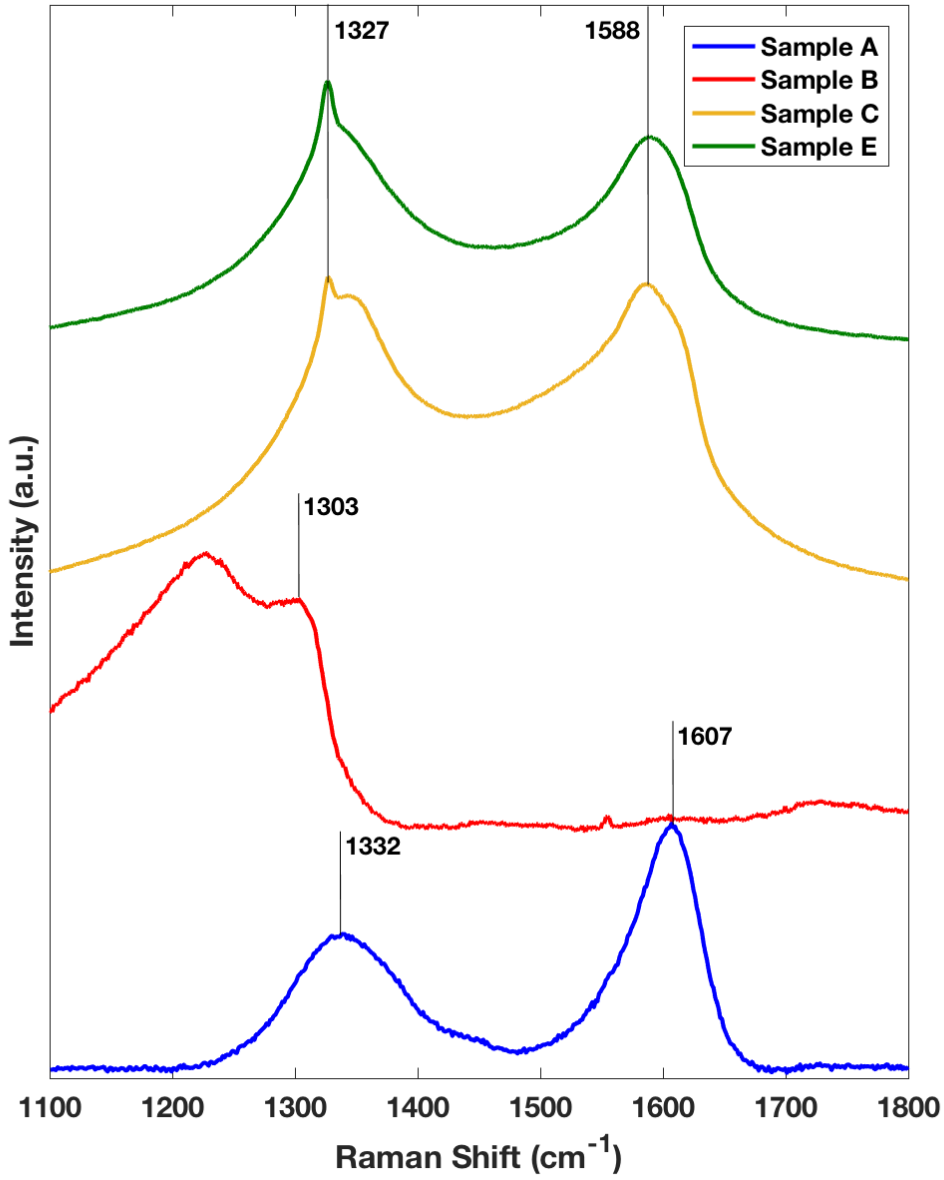

Figure 7-25 – Raman spectra of samples A, B C and E. All spectra are shown after PL background subtraction, and are shifted vertically for easier comparison.

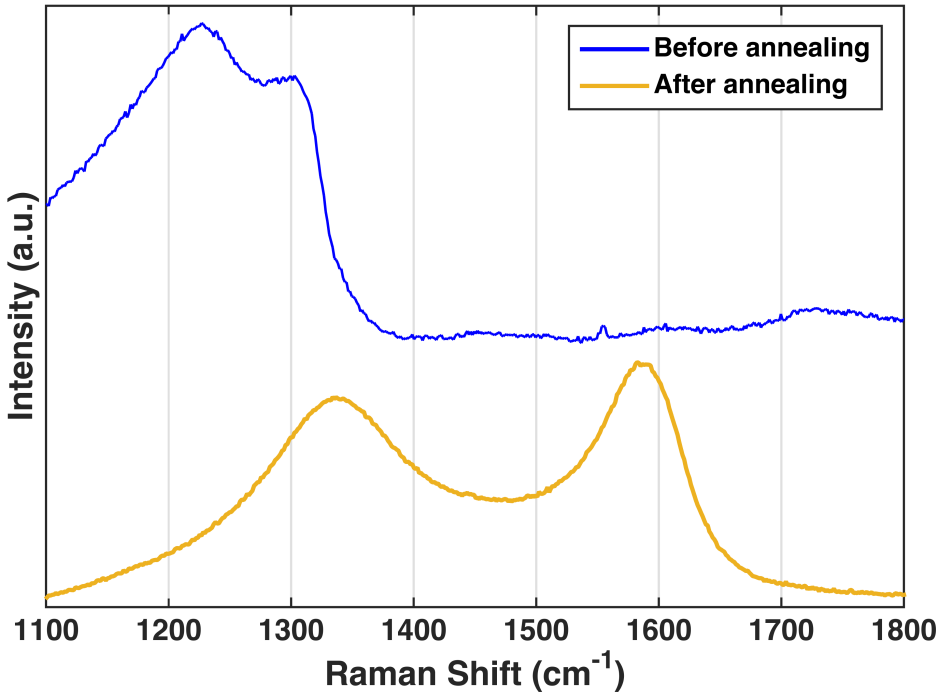

Figure 7-26 – Raman spectroscopy measurements of sample B before annealing (top) and after annealing (bottom) in vacuum while performing impedance measurements in vacuum.

7.4 Discussion

Nyquist plots of all samples studied here, showing a semi-circular response with only a single semi-circle, suggest that at any given temperature, only one conduction mechanism is dominant. The materials' Arrhenius plots are used to obtain activation energies E_A. In all figures (7–16 to 7–19), it is clear that at least two linear regions can be fitted. This suggests that at least two conduction methods are present for each sample, depending on the temperature. In crystalline materials, this is usually interpreted as band conduction within crystal grains, and in grain boundaries surrounding them,[97] however, other conduction methods, such as nearest neighbour hopping[166] and variable range hopping may be present in doped materials.[167] Su *et al.*[168] have shown that in detonation nanodiamonds, grain boundary and grain

interior conductivity are measured. Conductivity in p-type crystalline diamond is related to the concentration of dopants.[157] Another factor that arises in nanodiamonds is the quality of the material, quantified by the Q-factor, the ratio of sp^3 to non-sp^3 carbon phases. In detonation nanodiamonds, the Q-factor is low, as the detonation process causes graphitic shells to form around small diamond cores.[1,16] Figure 7–20 summarises activation energy results for all samples obtained using electrical impedance spectroscopy in vacuum. Boron concentration levels are assumed as given in section 7.2. Here activation energies are compared to epitaxial B-diamond films from literature, which have much higher crystalline quality and very low grain boundary density. It can be inferred that at room temperature and up to ~150 ºC, hopping conduction is the dominant mechanism, with activation energies between E_3=3.63 meV (sample B) and E_3=16.3 meV (sample C). For sample B, an activation energy of 23.5 meV is measured, which could either be attributed to hopping through grain boundaries and/or dielectric barriers, or to impurity band conduction where B content is relatively high. At higher temperatures, and up to ~450 ºC, which is the highest temperature reached in this study, impurity band conduction is assumed to take place with measured activation energies E_2 between ~40–55 meV. Sample A is the only case in which a much higher activation energy (E_1=181.1 eV) is recorded; this can be attributed to valence band conductivity, where B content just below the Mott transition point reduces the value of E_1 from its starting value of ~368 meV (ionisation energy of single B states). In comparison with epitaxial films from literature, this puts the equivalent boron content of sample A in the range $4x10^{19}$~$1x10^{20}$ cm^{-3}. This value, however is obtained from high quality,

epitaxial crystalline diamond films,[50] and in reality, boron content might be higher in the grain interiors of sample A, given that grain boundaries, trap states and dielectric interfaces (in vacuum) will attenuate the flow of free charges across such interfaces.[161,169,170] Between activation energies fitted, there exist, most likely, transitional states with intermediate activation energies, where contributions from different conduction methods might overlap, especially given that materials studied here follow resistor/semiconductor/metal network configurations. In summary, samples A and C show moderate levels of substitutional boron doping making them conductive in the hopping regime, with comparable activation energies to moderately doped diamond thin films (B~$1x10^{20}$ cm^{-3} and B~$5x10^{19}$ cm^{-3} respectively), while samples B and E show higher substitutional boron levels comparable to highly doped films (B~$2x10^{20}$ cm^{-3}).[50] A comparison between figures 7–21 and 7–22, where conductivity was plotted as a function of 1/T and $1/T^{1/4}$ respectively, shows linear regions could be fitted to data points in both cases. This suggests it can be hard to distinguish variable range hopping conductivity from nearest neighbour hopping in polycrystalline diamond films.[171]

In DC circuits, the frequency at which the signal drops by about –3 dB is usually called a cut-off frequency. In a study by Edgington,[26] the cut-off frequency in boron-doped diamond was studied. The author attributed the increase of resistance at high frequencies to the skin effect in contacts. The author also explains that a high cut-off frequency of ~1 MHz is indicative of minimal capacitance and good metallic conductivity.[26] Here an attempt is made to explain the cut-off frequency in boron-NDs. Imaginary impedance

plotted against the frequency (bottom portions of figures 7–9, 7–11, 7–13 and 7–15) is an indicator of the AC cut-off frequency.

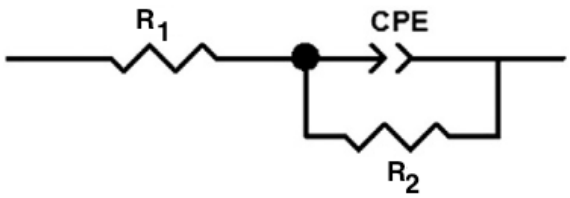

Figure 7-27 – A schematic of the equivalent circuit used in this chapter for Nyquist plot data fitting. This is a simplified Randles circuit with a CPE in place of a capacitor. Figure is adapted from Zivcova et al. [2015][164]

Figure 7–3 shows a schematic of the equivalent circuit used for data fitting of Nyquist plots. For a parallel RC circuit, also known as a low-pass filter, the cut-off frequency is $f_C = 1/2\pi RC$. This however does not apply to the simplified Randles circuit shown above, which has an added series resistance. Although a constant phase element (CPE) is used for fitting, a capacitor is sufficient for qualitative treatment, since deviations from capacitor behaviour is negligible. A more detailed treatment of the circuit, which can be labelled a low pass shelving filter, yields two frequencies, a zero frequency $f_C = 1/2\pi R_2 C$ and a pole frequency $f_P = (R_1 + R_2)/2\pi R_1 R_2 C$. In addition, an approximation of a cut-off frequency, with a –3dB signal drop, yields:

$$f_C \approx \frac{1}{2\pi R_1 C}\sqrt{2 - \left(\frac{R_1}{R_2} - 1\right)^2} \qquad Eqn.\,7\text{–}2$$

At the zero frequency, the capacitor is an open circuit, and the rest of the circuit becomes a voltage divider with a gain of $R_1/(R_2 + R_1)$. At the pole frequency, the capacitor is a short circuit, and the gain is 1. From equation (7–2), the cut-off frequency approximation of this circuit depends on the ratio

R_1/R_2 which is close to zero for samples B and C, hence the approximation $f_C = 1/2\pi R_1 C$ applies where R_1 is the series resistance value of the circuit. This explains why the sample deviates from expected theoretical behaviour above the phase-change temperature. This phase change may also explain the sample's Bode plot behaviour, where at ~100 KHz, the imaginary component of the impedance is seen to have an increased cut-off frequency as the temperature increases.

The reduction of series resistance R_1 is evident in figure 7–24, where the intercept of the semicircle approaches zero as the temperature increases. This clearly indicates that the series resistance is partly responsible for the change in cut-off frequency. The other factor contributing to this effect is the increase seen in capacitance around the same temperature (refer to appendix figure 11–8). Here the change of series resistance (and capacitance) is assigned to the relative increase of sp^2 carbon between diamond grains. This does not affect the response of the circuit significantly at low or high frequencies. When combining results from Raman spectroscopy, series resistance, capacitance and cut-off frequency, it becomes reasonable to attribute the series resistance in the simplified Randles circuit model R_1 to grain boundaries between diamond cores. Here, however, the resistance is relabelled, and this makes for a resistor network where the resistance R_{GB} is the difference between R_1 and contact resistance R_C:

$$R_1 = R_C + R_{GB} \qquad Eqn. 7-3$$

The same reasoning applies to other samples studied here, however sample B is the one strongly affected due to its decreased thermal stability.

Raman spectroscopy results showed a variation in composition between samples, which can be explained by the different conditions for growth. Ratios of sp^2 D to G peak intensities is an indicator of sp^2/sp^3 fraction according to Ferrari & Robertson.[94] This ratio puts sp^2 content in samples C and E at ~1–2%, and for sample A at 0.5–1%. Sample B shown a D/G intensity ratio of zero, suggesting no detectable sp^2 carbon content. Sample A is the most disordered due to the nature of the detonation process. Seemingly, aggregated thin films of NDs from sample B, are closer in structure to heavily doped bulk diamond, as evidenced by 500 cm^{-1} and 1200 cm^{-1} features attributed to heavy boron doping.[172,173] Even though boron incorporation into diamond is known to improve thermal stability,[174] it is found here from comparison of Raman spectra that the heavily doped sample changes phase in absence of oxygen at relatively low temperatures. This may be explained by the presence of protective graphitic layers surrounding the diamond material in other samples, which may be absent in sample B due to high levels of boron clustering on ND surfaces. Sample B, unlike other samples, shows no sign of sp^2 carbon phases. This is unusual for diamond particles of this size; however, it may be explained by a longer acid cleaning procedure. Another explanation might have to do with the very high boron content (~1 at.%) which may be hindering the formation of sp^2 carbon phases at grain boundaries. Computational studies have shown that boron is more likely to be present at grain boundaries,[6,7] and spatially resolved EELS measurements of nanocrystalline boron-doped diamond films have confirmed this.[175] This might also explain the reduced thermal stability of sample B aggregated films, which

may be held together by boron clusters, however it does not explain the appearance of sp^2 carbon related Raman features at increased temperatures. The increased levels of boron doping may explain why sample B, despite having smaller grains compared to others, has a measured conductivity comparable to that of the sample with the largest grain size (sample E). In sample E, the very large grain size results in a reduced sp^2/sp^3, surface to bulk ratio, and hence most of the conductivity at lower temperatures would be due to the bulk of the diamond.

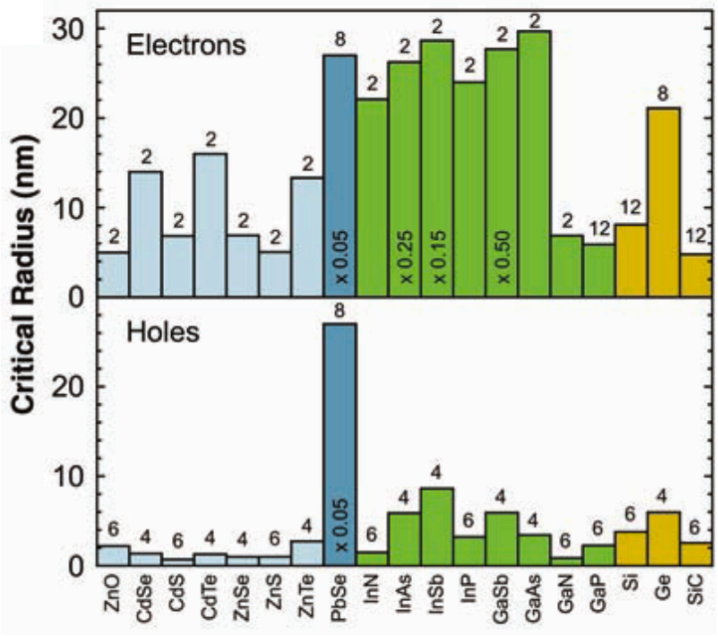

Figure 7-28 – Critical radii in heavily doped semiconductor nanocrystals, adapted from Norris et al. [2008][176]

In a review by Norris *et al.,*[176] the properties of nanoscale doped semiconductors were studied. They inferred from a comparison of different types of doped nanocrystals that below a critical radius, n-type and p-type dopant states can be auto-ionised due to confinement, even without thermal excitation. They attribute this to the fact that confinement energies become larger than Coulombic potentials between carriers and ionized impurity states,

below the critical radius. Critical radii for hole and electron states (figure 7-28) are in the 4-6 nm range for hole carriers in silicon, GaAs, SiC and GaN. Assuming the critical radius for diamond is in the same range, this effect could explain the relatively high conductivity of sample A compared to sample C, which is more heavily doped with boron. Another factor which can potentially contribute to sample A's relatively high conductivity is the presence of sp^2 shells around doped ND cores, which can prevent dopant electrons from being consumed in electrochemical reactions in films.[176]

7.4 Conclusion

It can be concluded from the above discussion that due to the many factors affecting conductivity of doped nanodiamonds, a direct measure of the doping level in any given nanodiamond sample cannot be obtained using electrical and impedance measurements alone, and that direct measurement (such as SIMS) may be necessary. Hall measurements can be used to measure the carrier density and mobility of diamond, however, interfacing nanodiamonds directly with Hall measurement equipment proved to be challenging; patterning of Hall bars and Ohmic contacts, without fixating the nanodiamonds via CVD growth, for example, or lithography, which introduces other chemicals, is yet to be achieved. Other techniques, however, such as STM or conductive AFM, may be used to obtain more information on the electrical properties of single nanodiamond grains. Variable temperature Hall-mobility measurements would be very helpful to this discussion, with van der Paaw contact arrangement or even better, hall bars. This remains technically challenging, since the use of silicon contacts in sandwich configuration is not ideal. Much better understanding of boron content in nanodiamond samples is required using analytical methods like XANES/NEXAFS; understanding the extent of grain boundary and interfacial effects is of utmost importance to the discussion, especially when such materials are considered for micro/nano electronics and photonics applications. A more detailed study of the effects of confinement on doped nanodiamond films, in light of findings by Norris *et al.*, would be greatly supportive to the understanding of conductivity in nanodiamond films.

8. Al-Diamond Schottky Diodes CVD-Grown from Boron-ND Aggregated Films

8.1 Introduction

Schottky-barrier diodes (SBDs) are one of the cornerstones of modern high-power switching electronics, along with the transistor.[80,177,178] In the case of diamond the combination of the two will enable handling of large currents with high efficiency compared to other wide band-gap semiconductor materials, due to the electronic properties of diamond described earlier in this thesis.[76,150] The Schottky barrier, as discussed in chapter 3, brings many advantages when compared to bipolar junctions; having higher frequency operation, lower forward voltage drops, higher breakdown fields and higher mobilities. As a result, diamond SBDs have gained the attention of many researchers, and have been studied widely in recent years.[76,77,79,80,158,177–181] However, currently the fabrication of diamond SBDs, is limited to a small number of laboratories, since it requires p-type doping of diamond films as they are CVD-grown. This means using boron-containing gas precursors, which are known to contaminate growth chambers once introduced, effectively meaning separate growth chambers are required for intrinsic and doped growth, respectively, adding to the cost of development. Recently, several types of boron-doped nanodiamond materials have been developed, which have been studied here and discussed in chapter 5 (detonation NDs), and chapters 6 and 7 (detonation NDs and high-pressure, high-temperature

NDs). Their electronic properties, studied in chapter 7, suggested that if used as seeding materials, they could form Ohmic contacts between CVD grown films and substrates, and the fact that they were highly boron-doped suggested they could also potentially donate boron to the grown film, which could be incorporated in substitutional states. XPS results from chapter 6 suggested relatively large amounts of boron, either as boron oxides or boron clusters, existed between ND grains, which enforced the suggestion they could be incorporated into grown films in low concentrations under growth conditions, which is highly desirable for active layers in diamond SBDs to ensure higher breakdown voltages are achieved.[76] As a proof of concept, boron-ND aggregated layers, similar to the ones used in chapter 7, are deposited onto conductive, n-type silicon substrates and the first diamond SBDs fabricated from B-doped nanodiamonds are reported. SBDs are fabricated in the vertical configuration, where the boron-ND films are used as seeds for PE-CVD diamond growth in our laboratory. The vertical configuration was chosen due to its simplicity in fabrication, and to minimise the length of the conduction path through the active layer, which makes it easier to exclude effects such as surface conductivity and shunt currents. According to Umezawa *et al.*,[177] if the thickness is ~1 μm, conductivity is vertical through the p– layer, minimising conductivity through grain boundaries.

8.1.1 SBD Performance Parameters

In heavily doped semiconductors, quantum tunnelling at energies less than the SBH can act as a limiting mechanism to thermionic emission, effectively

lowering the Schottky barrier. This mechanism is dependent on the temperature, as well as the shape of the barrier. The combined effect is labelled thermionic field emission (TFE).[182] For $N>10^{18}$ cm^{-3}, thermionic emission dominates at room temperature, because of the faster decay of the exponent for tunnelling with increased temperature. Metal-induced gap states (MIGS) are described in the scientific literature as states arising from matching wave-functions in metal-semiconductor interfaces.[72,183] The matching causes what is often referred to as 'pinning' of the semiconductor Fermi level. These states cause a dipole to form at the interface; causing dielectric screening of the barrier, effectively lowering it.[183,184] This effect is called image force lowering, and is known to exist at metal-semiconductor, semiconductor-semiconductor, as well as metal-metal interfaces.[185] Further lowering due to surface states may also be present, depending on the density of such states (see 3.2.2). Tersoff[183] further asserts that MIGS are the dominant factor in causing dielectric screening, contrary to reports[186] attributing the lowering to intrinsic defects in the semiconductor. It is therefore trivial to assume that barrier heights, in experiment, are not simply the difference between the metal work function and semiconductor's electron affinity (refer to equations 3–3 and 3–4), and that deviations in measured barrier heights can arise from more than one potential-lowering mechanism. It follows from the above that measurement of the built-in potential V_{bi} is also affected by the same mechanisms. Tsugawa *et al.*[180] studied the behaviour of Schottky barriers formed between hydrogen-terminated diamond surfaces in contact with several evaporated metals, including aluminium, and have measured a Schottky barrier height ϕ_B of 0.59 eV. Fiori *et al.*[181] have

measured ϕ_B of up to 1.59 eV for Schottky diodes fabricated using CVD with boron doping from diborane gas.

The voltage threshold (V_{TH}), at which current starts to increase exponentially in forward bias, is closely related to the nature of the semiconductor used. Referring to equations 3–1 and 3–2, it can be shown numerically that, at a given temperature, the modified Richardson constant A^* of the semiconductor is the deciding factor of the voltage threshold. Other variables such as the barrier height ϕ_B and ideality factor n have no effect on the voltage threshold. From numerical estimation, diamond SBDs are expected to have V_{TH} ~0.7 V.

Deviation from ideal Schottky-barrier behaviour in devices is commonly observed. The ideality factor *n* in equation 3–1 is very useful in describing barrier heights which have linear dependence on bias. This factor, however, does not provide a physical explanation to the reasons behind such behaviour.[187] Interface states have been suggested as one source of non-ideality, including those arising from trap states and structural defects. In addition, inhomogeneity at the Schottky barrier was also suggested to be a source of non-ideality. Annealing of devices up to certain temperatures has been shown to improve ideality values,[180,181,187] in some cases approaching ideal behaviour, as shown in diamond SBDs by Fiori *et al.*[181] and Tsugawa *et al.*[180] Rhoderick[188] suggests that in absence of interfacial states, only image force lowering may affect the ideality of the barrier. This was shown to be the case for H-terminated diamond SBDs by Monch.[189] It follows from above that measured ideality values largely depend on the nature of the Schottky barrier interface and on the fabrication process.

8.1.2 Current-Limiting Mechanisms

In section 3.2, thermionic emission has been discussed as a conduction mechanism across Schottky barriers, which is described as charge flow due to thermally excited carriers that have energy equal to (or higher than) the barrier potential. According to Cowley & Sze,[190] in addition to thermionic emission, current limiting mechanisms in SBDs include charge diffusion and drift in the semiconductor. Such mechanisms can be visualised as being in series with the metal-semiconductor interface.[191] The Poole-Frenkel mechanism describes how electrons can be thermally excited to the conduction band in insulating materials, even though relatively low thermal energy is present. In this mechanism, prevalent under large electric fields, random thermal fluctuations are thought to provide enough thermal excitation to localised electrons, enabling them to become briefly conductive.[171],[192] These short-live excitations do not last for long, and relaxation takes place shortly after into localised states. This effect is described as lowering of Coulombic barriers under an electric field, specifically, that of a trap state within an insulating bulk material. Positively charged traps, such as present in boron-doped diamond, are required for this effect to manifest itself, although according to Simmons,[193] both donors and acceptors can produce this effect. This mechanism can be thought of as the bulk analogue to the Schottky mechanism, where barriers at semiconductor-metal interfaces are lowered due to dielectric screening.[193] The governing equations for their behaviour are very similar (only differing by a factor of 2). The general equation for current density describing the Poole-Frenkel effect is:

$$J = E\ \sigma_0 exp\left(\beta_{PF}\ E^{1/2}/kT\right) \qquad Eqn.\ 8-1$$

Where β_{PF} is the Poole-Frenkel coefficient of the material (3.23×10^{-4} eV $V^{1/2}$ $cm^{1/2}$ for conductive diamond),[171] E is the applied electric field and σ_0 is the low-field conductivity of the material. This conduction mechanism is known to exist in polycrystalline diamond films under high fields (above ~10^4–10^5 V/cm), which is the case for thin films (~1 μm) under potentials at or above 1 V.

8.3 Methods

Schottky-barrier diodes were fabricated on n-type, highly arsenic-doped silicon substrates (1×1cm, 380 μm thick, single side polished, prime grade) of very low resistivity (0.001-0.005 Ω·cm). High-pressure, high-temperature (HPHT) boron-doped nanodiamonds (samples B, C and D as defined in chapter 6) from DI water solutions were drop-coated onto silicon substrates at a temperature of 90 °C following a process of confinement-nucleation (see 4.12.1), where the nanodiamond solutions are pressed onto the substrate using another flat silicon substrate. It was found that applying pressure between two substrates in the presence of the ND solution, at room temperature, significantly improves nucleation density and uniformity of nanodiamonds onto silicon substrates with a native oxide layer. All silicon substrates were de-greased in an ultrasonic bath using Acetone, followed by Isopropyl alcohol and then DI water. Substrates were dried using a Nitrogen gun. Following drop coating of NDs, samples were loaded into a Seki-AsTex 1.5 kW PE-CVD microwave plasma reactor, and a stable pressure of ~2×10^{-6} mBar was reached using rotary and turbo pumping, before commencing with

growth. PE-CVD growth is performed at a pressure of 50 Torr, using a 99:1 H_2:CH_4 gas ratio (99 sccm and 1 sccm respectively). A hydrogen plasma was ignited and conditions optimised until the substrate temperature, measured using a dual-wavelength pyrometer (Williamson Pro 92-40), reached 700 °C at 1 kW power. At this temperature methane is admitted into the growth chamber, and growth took place for 1 hour, reaching an average temperature of ~815 °C. At the end of a growth cycle, methane flow is stopped, and pressure and power were gradually reduced until the plasma goes off. The sample was left to cool down in hydrogen, and the above process was repeated for a second phase of growth, also for 1 hour. Growth is done in two steps to minimise substrate over-heating, potentially damaging to the sample due to thermal mismatch between diamond and silicon. Following film growth, aluminium contacts are deposited using an Edwards Bell-jar A306 evaporator, using highly pure aluminium wire as the source (Goodfellow, 1 mm diameter, 99.999% purity). This was performed in a clean-room environment, and a total of 200 nm of metal was deposited, using a 2.5 mm circular shadow mask. DekTak profilometer characterisation was performed after film evaporation. Drop coated layers have an average height of ~500 nm (refer to figure 7–6), while PE-CVD grown films are approximately 1 μm in thickness, estimated from growth time and grain size (AFM figures 8–12 to 8–14).

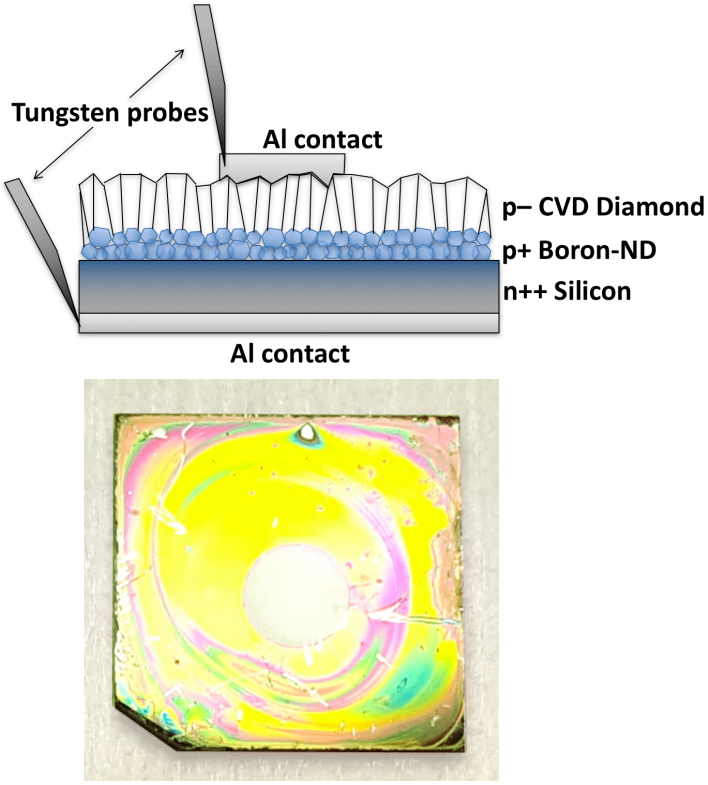

Figure 8-1 – (Top) Schematic of diamond Schottky diode devices layout as grown for this study. (Bottom) a top view of device B with the circular aluminium top contact showing in the middle.

The final device (figure 8–1) is a metallic silicon back contact, with a p+ layer of heavily boron doped diamond layer on top, covered on top by a p– PE-CVD grown, polycrystalline diamond film, where boron is sourced by diffusion from the p+ layer below, as well as potentially residual boron introduced into the growth chamber by drop-coated Boron-NDs. Boron concentrations in HPHT Boron-ND samples are estimated to be in excess of 10^{20} cm^{-3}, as found from electrical impedance measurements in chapter 7. A vertical structure and shadow-mask metal evaporation were implemented to avoid chemical contamination which may arise from photolithography, especially that NDs are used as the boron source in this study. For I-V, C-V and G-V measurements, aluminium contacts on top and bottom of the device were contacted with 15

μm diameter Tungsten probes, as part of the EverBeing Analytical Probe Station used to perform measurements. The probe station was in a metal enclosure to minimise noise. Co-axial (tri-axial) cables and connectors were used between samples and a Keithley 4200-SCS analyser for I-V (C-V) measurements. The instrument was equipped with a CVU capacitance-voltage module. C-V and G-V measurements were performed using the parallel model to allow for correction of measured C and G using serial resistance (R_s) values. All measurements were performed between –5 and +5 V in steps of 0.02 V, with a maximum current tolerance of 0.1 A. In case of C-V measurements, an AC voltage of 100 mV was chosen.

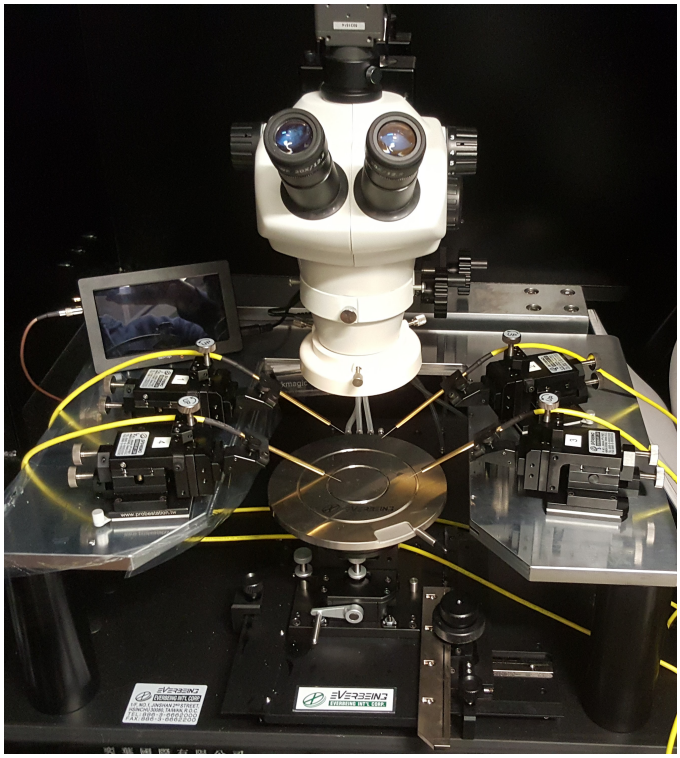

Figure 8-2 – The Everbeing Analytical Probe Station used to perform I-V, C-V and G-V measurements on diodes.

8.4 Results

8.4.1 Electrical I–V Measurements

It can be seen from room-temperature I-V characteristics in figure 8–3 that vertical Schottky diode devices fabricated here using boron-doped nanodiamonds show rectifying behaviour. In samples B, C and D a Schottky barrier is clearly formed. Good fitting of the current density in the linear region between 0 V and 0.8 V using equation 3–1 confirms this behaviour (figure 8–4). A voltage threshold V_{TH}≈0.7 V is measured for devices B, C and D. Ideality factors of the devices as fabricated are n=8.53±0.23, 5.45±0.25 and 7.27±0.37 respectively for devices B, C and D.

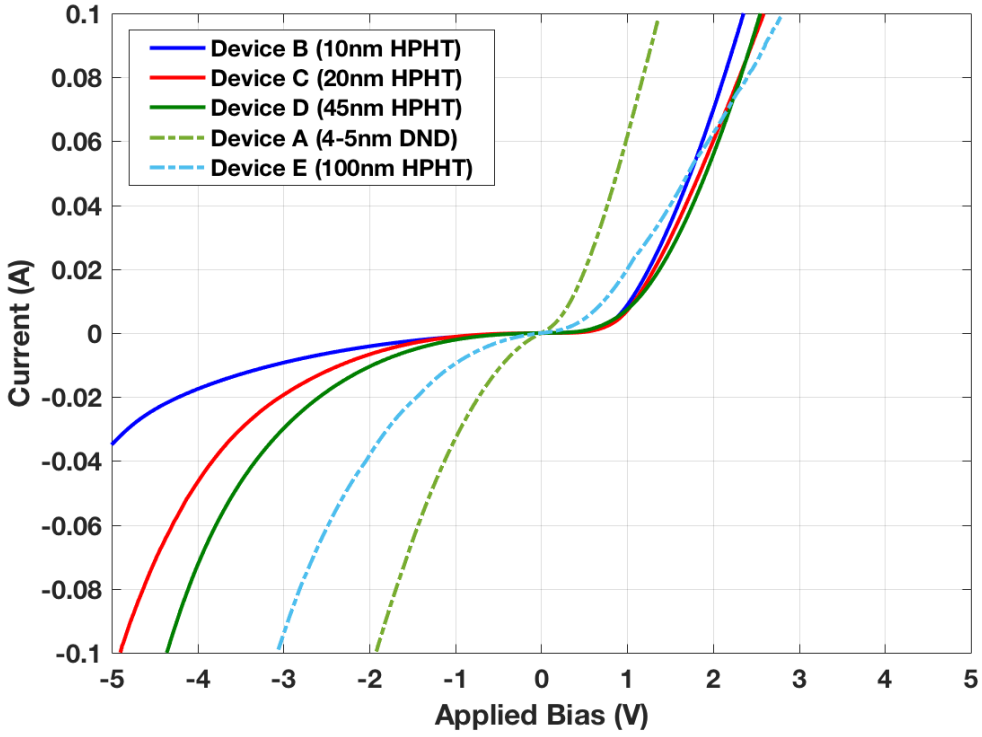

Figure 8-3 – Current-voltage measurements for all devices as measured at room temperature. Devices B, C and D show diode behaviour, while devices A and E are representative of non-ideal resistor behaviour.

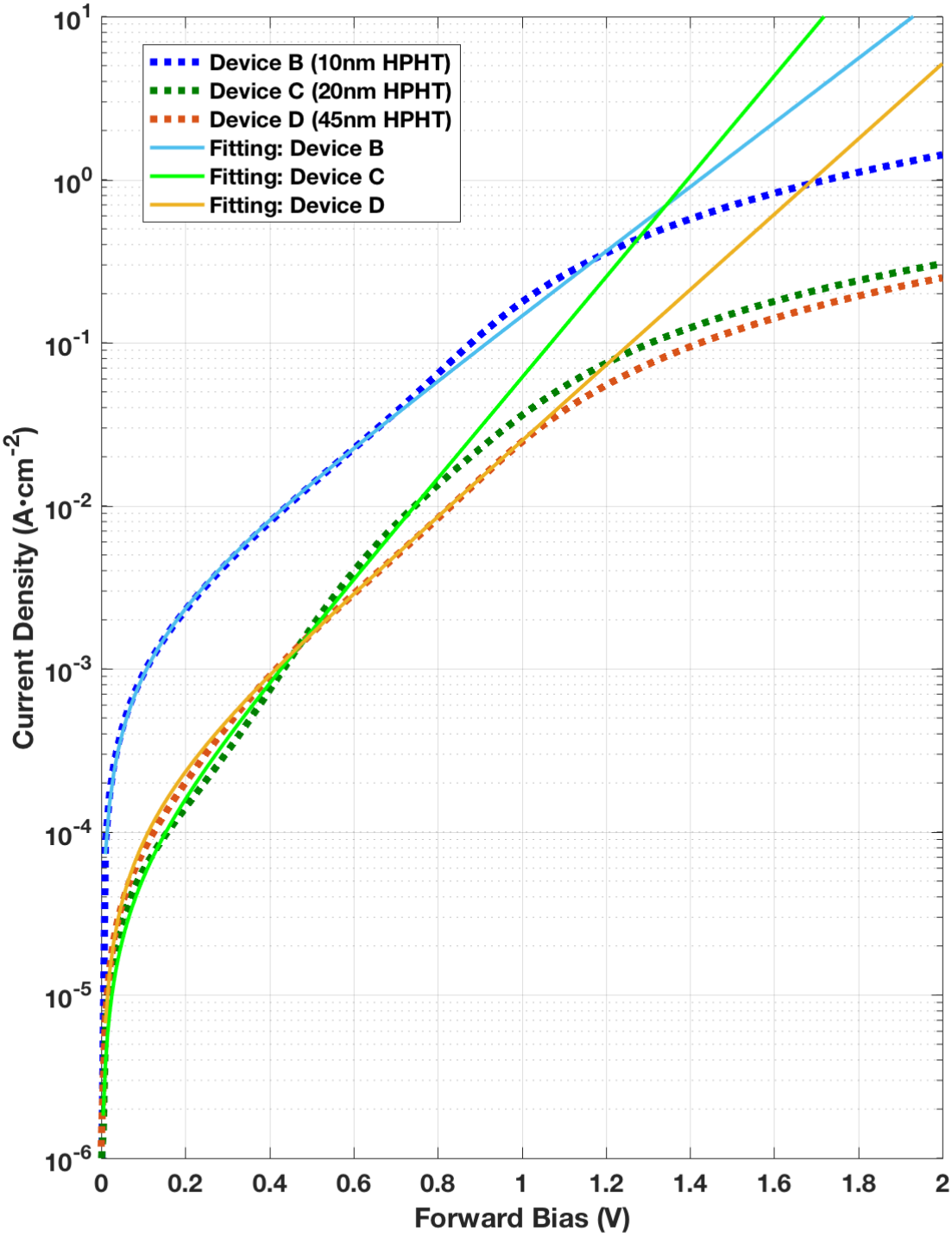

Figure 8-4 –Semi-log plot of Current density against forward bias for devices B, C and D. Dashed lines represent measured data, while solid lines represent fitting using equation 3–1.

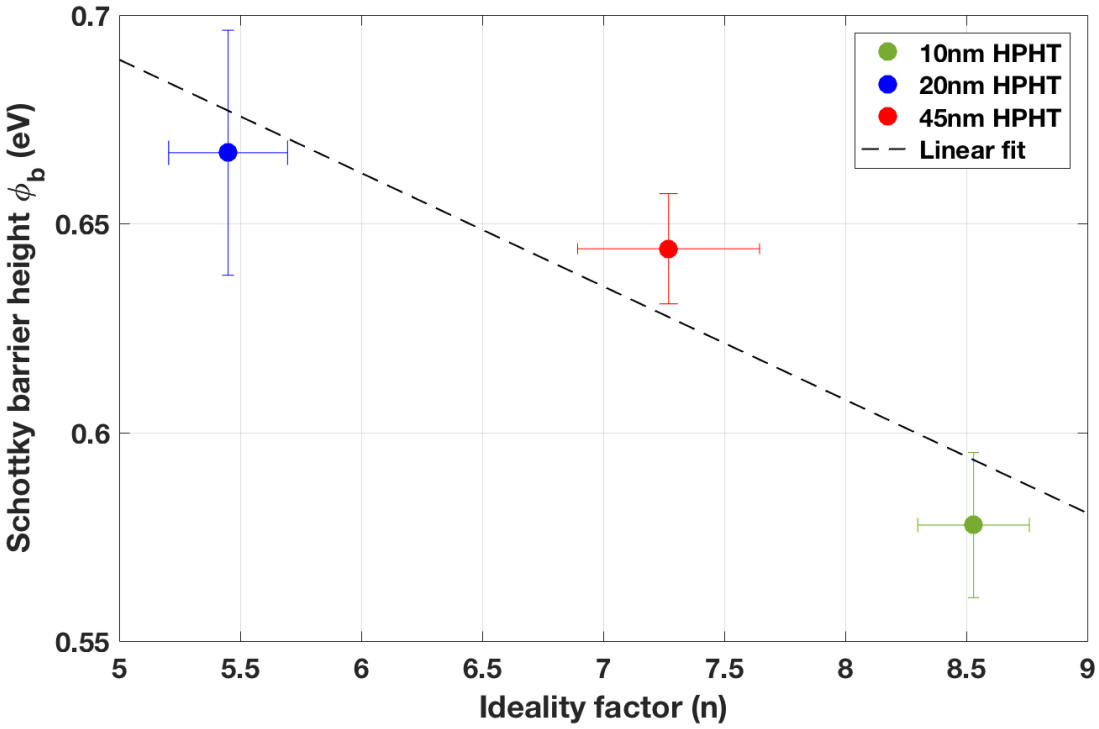

Figure 8-5 – Measured barrier heights for devices B (green), C (blue) and D (red) are plotted as a function of their corresponding ideality factors. The dashed line represents weighted linear fitting of the results. Horizontal error bars are shown for ideality factors, while vertical bars are for Schottky barrier heights.

Samples A and E do not show good rectifying properties. Specifically, sample E shows properties of a poor Schottky diode, with a very low threshold voltage V_{TH} compared to samples B, C and D. This is likely due to shunt currents bypassing the diode. Sample A does not have I-V characteristics of a diode, and fitting of the I-V curve using equation 3–1 was unsuccessful; its I-V characteristic is more representative of a non-ideal resistor. Barrier heights are plotted against Ideality factors in figure 8–5, and they follow a linear trend as expected. Measured barrier heights ϕ_B for samples B, C and D were 0.578±0.017 eV, 0.667±0.029 eV and 0.644±0.013 eV respectively. Horizontal and vertical error bars in the figure represent fitting error of ideality factor and barrier height respectively, in addition to absolute temperature variation and

measurement compliance limits (refer to experimental methods section 4.12.4 for details). The error contribution from fitting was found to be dominant, on the order of a few percent. In all I-V measurements, currents could not exceed 0.1 A due to current compliance limitations on the Keithley 4200 used to take measurements.

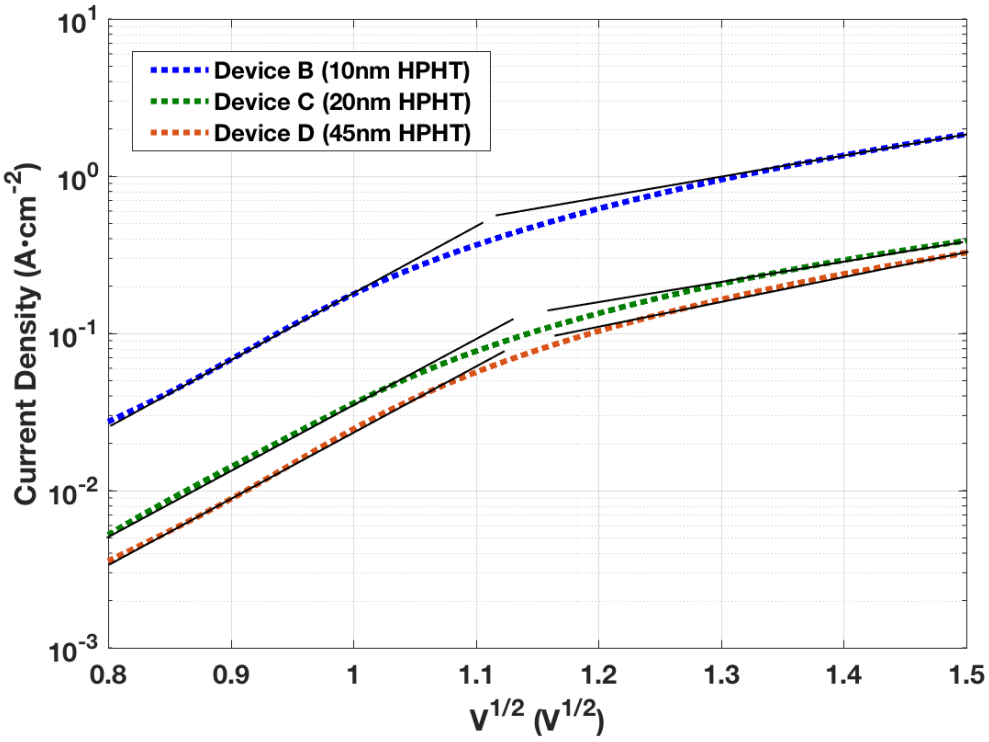

Figure 8-6 – Semi-log plot of current densities against the square root of the forward bias. Dashed lines represent measured data, while solid lines represent linear fitting.

As a result, direct measurement of breakdown fields or saturation currents was not possible. Figure 8–6 plots the current on a logarithmic scale against $V^{1/2}$. The figure was plotted between 0.8 V and 1.5 V, since the square root of the threshold voltage (~0.7 V) is ~0.83, and the Pool-Frenkel mechanism is expected to be effective above ~1 V. Fitting of two linear regions was attempted in the figure, however such trends are not clear here.

8.4.2 C–V Measurements

In addition to the above measurements, capacitance and conductance of devices B, C and D were measured as a function applied bias, in 1 MHz frequency steps between 1-10 MHz. Capacitance and conductance are labelled C and G respectively; plots of C and G are in the appendix (figures 11–9 to 11–14). All samples were measured having negative capacitance values at a certain part of the frequency range. Possible explanations for this behaviour will be provided in the discussion below. Conductance (G) values are all positive for all samples. Measured C and G values were used to obtain series resistance (R_s) values for all three devices, using equation 8–3. Plots of R_s values in the accumulation region against frequency (figure 8–7) show a constant R_s~30 Ω with frequency up to 7 MHz for samples B and C, with sample B having a peak at 9 MHz at 470 Ω. In sample C, the series resistance drops to a negative value of –294 Ω at the same frequency. Sample D has R_s ~60 Ω at 1 MHz, which drops to lower values with increasing frequency. Negative R_s values were only obtained for sample 2 at higher frequencies.

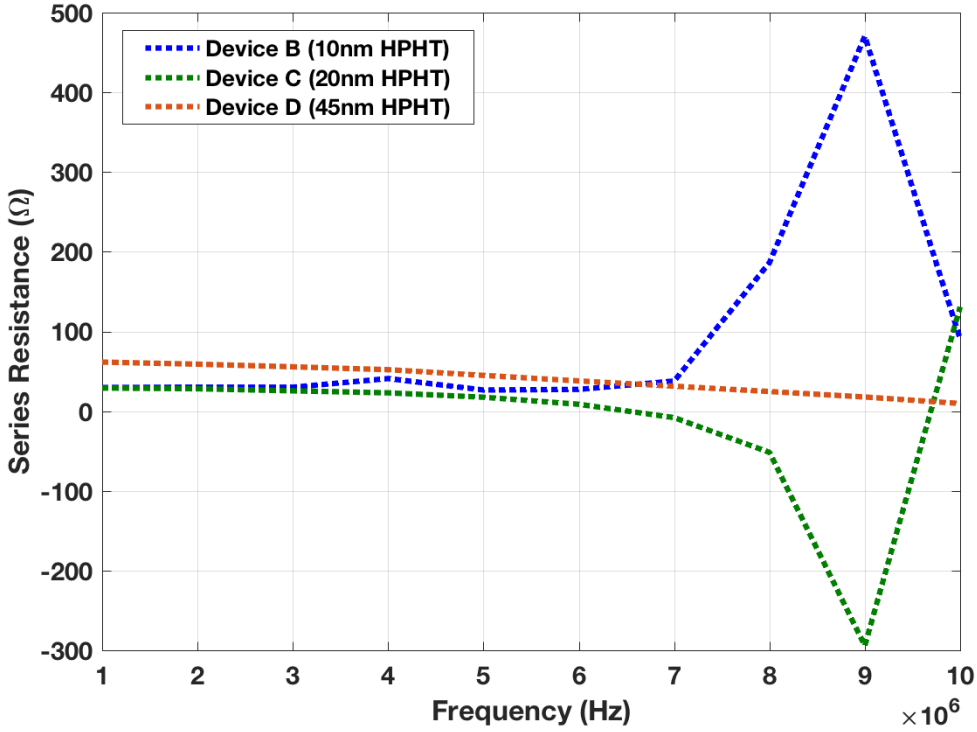

Figure 8-7 – Series resistance (R_S) values in the accumulation region as a function of AC frequency. R_S was calculated from capacitance and conductance measurements according to equation 8–3.

The inverse squared capacitance ($1/C^2$) results can be used to estimate effective acceptor concentrations (N_A–N_D) from the slope of the curve in the reverse bias region.[194] N_A–N_D values in the range of 10^{15}–10^{16} cm^{-3} were obtained for devices B, C and D (figure 8–8).

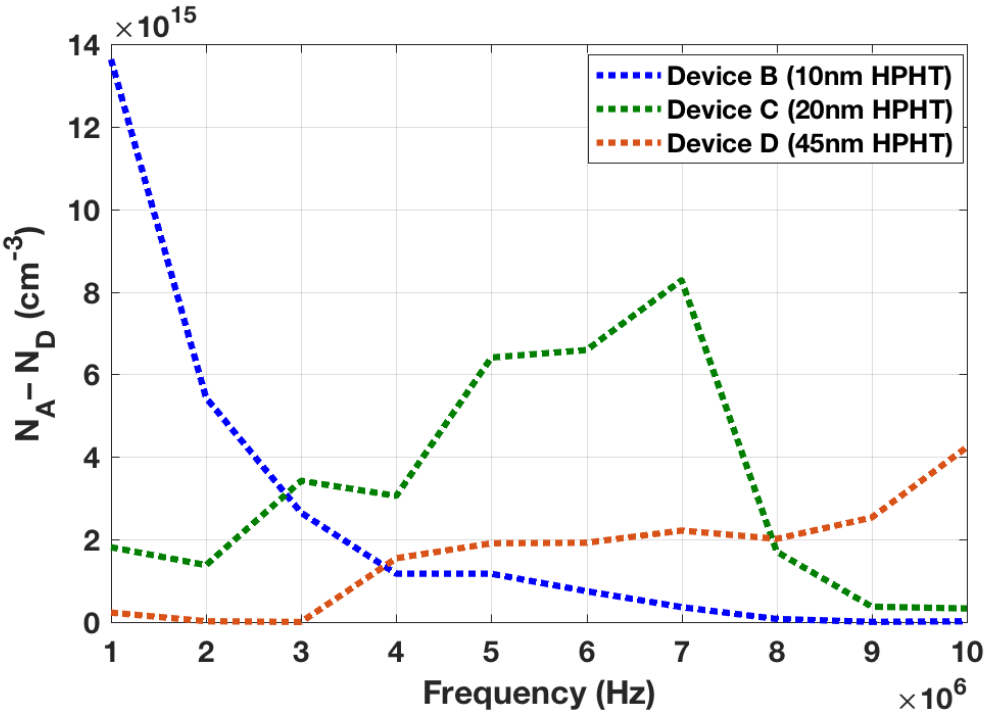

Figure 8-8 – Effective acceptor concertation (N_A–N_D) as a function of AC frequency.

Figure 8–8 shows N_A–N_D plotted against the AC frequency. For sample C, the values obtained for N_A–N_D are rising with increasing frequency up to about 7 MHz, as expected for Schottky barriers,[195] however they drop to lower values at higher frequencies. Sample B behaves differently, where N_A–N_D starts from a higher value then decreases with increasing frequency. Sample D, on the other hand, has very low values at 1 MHz, and increases with increasing frequency. N_A–N_D values obtained above can also be used to estimate V_{bi} using an assumed value for E_F–E_V,[177] however determining this is not straightforward in aggregated ND films.

8.4.3 Raman Spectroscopy

Raman spectra before and after PE-CVD growth were performed for comparison. Figure 8–9 shows Raman spectra before growth, while figure 8–10 shows corresponding Raman spectra after PE-CVD growth. In figure 8–9,

Raman spectra of samples C and D are nearly identical (refer to section 7.4 for discussion). Following PE-CVD growth, figure 8–10 shows diamond peaks at ~1332 cm^{-1}, indicative of crystalline diamond. This value is shifted to higher values compared to those before growth. Samples C and D also have stronger and narrower diamond peaks, indicating larger crystal domains in grown films. Features around 500 and 1200 cm^{-1}, observed for sample B in drop coated nanodiamond films, are suppressed following CVD film growth. In addition, peaks for trans-polyacetylene (1100 cm-1), carbon D and G peaks (~1347 and 1599–1606 cm^{-1}), as well as features associated with amorphous carbon (1470 cm^{-1}) are observed following growth.[95]

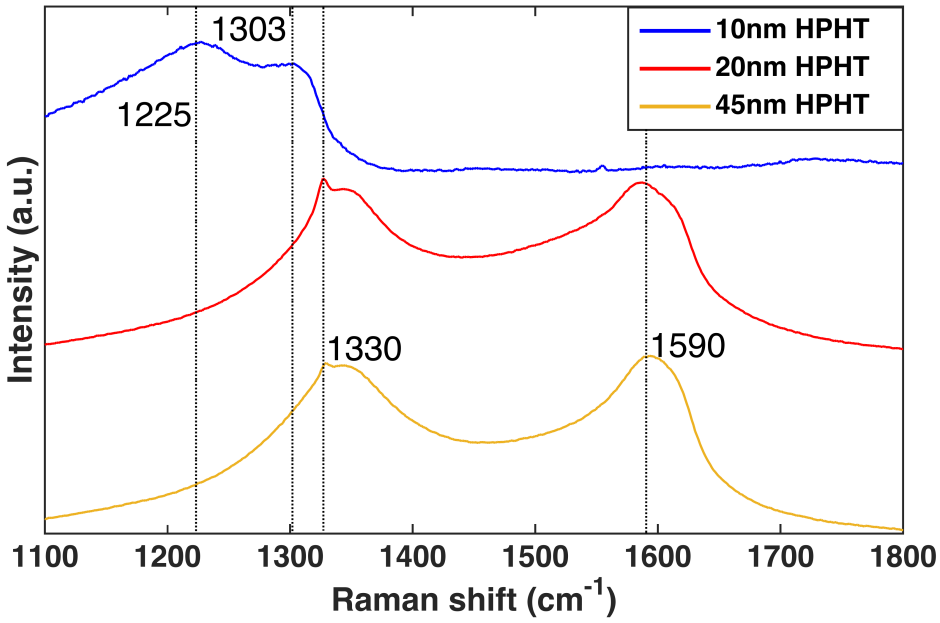

Figure 8-9 – Raman spectra for drop-coated nanodiamond samples used to grow SBD devices. Lines represent sample B (blue), C (red) and D (yellow).

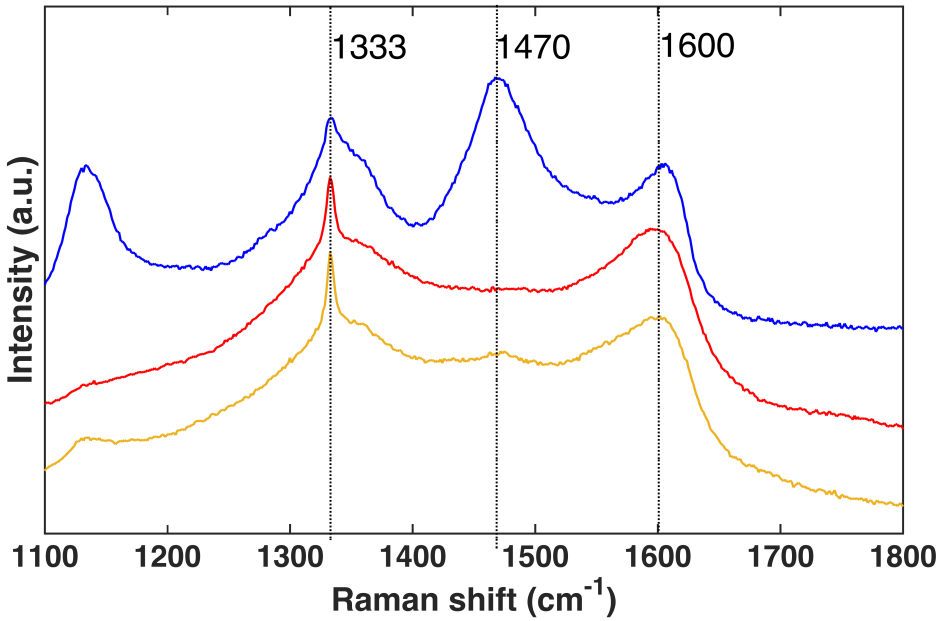

Figure 8-10 – Raman spectra for PE-CVD grown diamond films. Lines represent sample B (blue), C (red) and D (yellow). Strong and narrow diamond features (~1332 cm^{-1}) are observed.

8.4.4 AFM Imaging

Figure 8–11 shows AFM images of samples B, C and D before PE-CVD growth. For sample B, a monolayer was deposited on a silicon substrate as discussed in 7.2. This was only done for AFM imaging purposes. For samples C and D, drop-coating was used. It can be seen that in samples C and D, NDs are agglomerated and are closely packed. From z-axis values, it can be seen that NDs are in the expected height range, however feature dimensions in the x and y-directions are not a good indication of the size of the NDs due to the AFM tip convolution limit. Following the growth, polycrystalline surfaces are observed (figures 8–12 to 8–14). Average crystal grains range in size from ~185 nm (sample B) to ~356 nm (sample D). Details about grain dimensions are given in table 8–1.

Table 8-1 – Average grain diameters (ϕ) and corresponding distributions of PE-CVD grown diamond films, as obtained by AFM image analysis.

Sample	Mean ϕ (nm)	Minimum ϕ (nm)	Maximum ϕ (nm)	Sigma (nm)
Device B	185.1	33.0	675.3	124.7
Device C	330.8	48.2	937.4	169.5
Device D	356.5	56.2	874.6	148.4

Average grain diameters and distributions were obtained using the particle analysis feature of Bruker's NanoScope® software package. Scan areas are 10x10 µm, a minimum diameter threshold of 25 nm and a minimum peak-to-peak threshold of 10 nm is applied. Thresholds ensure grain counts are not underestimated by joining of neighbouring grains.

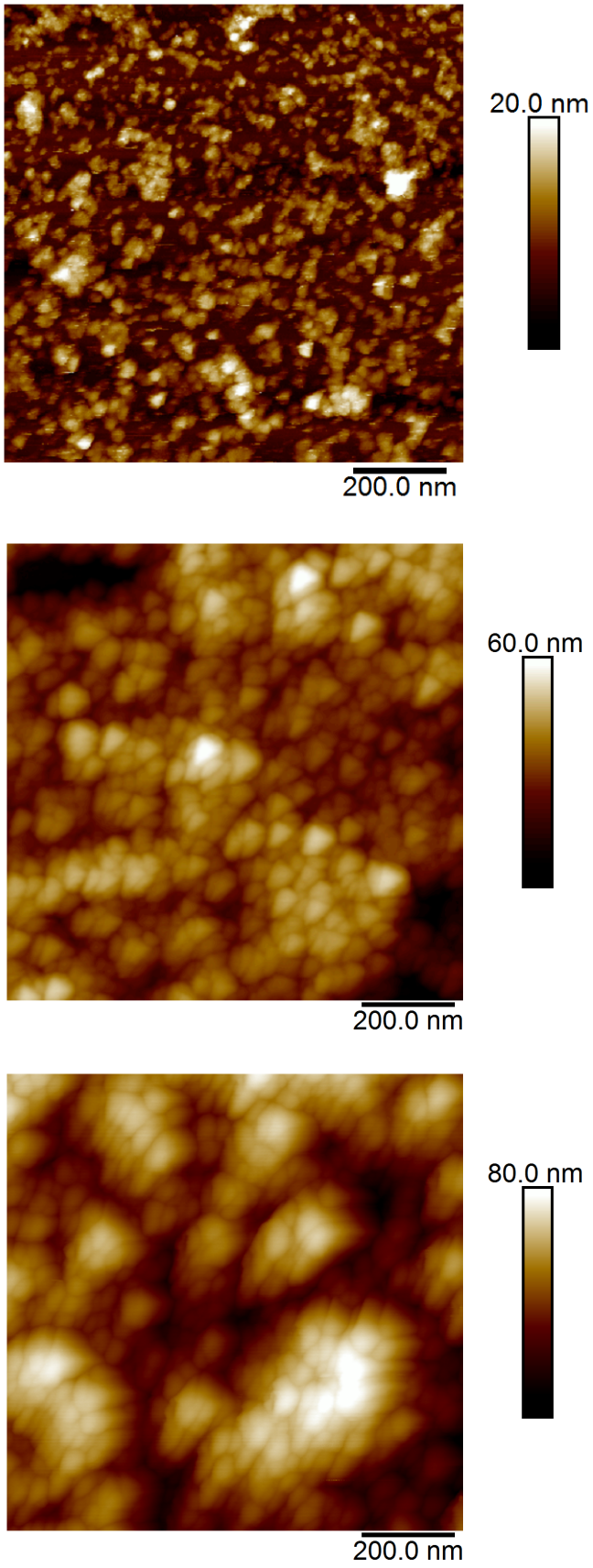

Figure 8-11 – AFM imaging of ND before growths: Sample B (top) as a mono-layer, and samples C (middle) and D (bottom) after drop-coating.

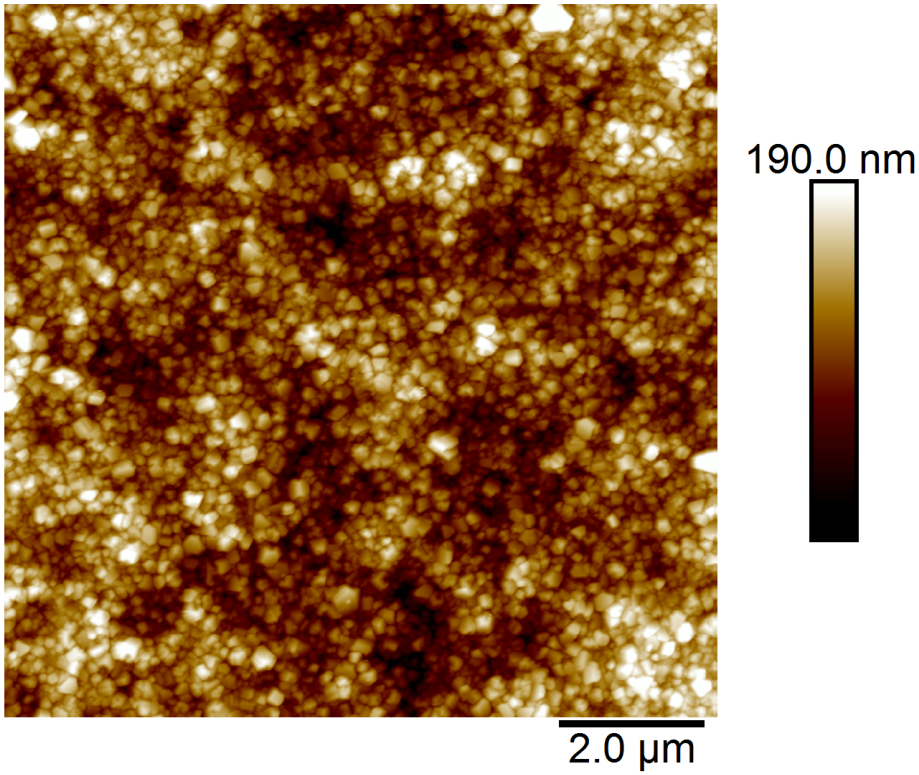

Figure 8-12 – AFM imaging of PE-CVD grown diamond layer of device B. Crystal grains have an average size of ~185 nm.

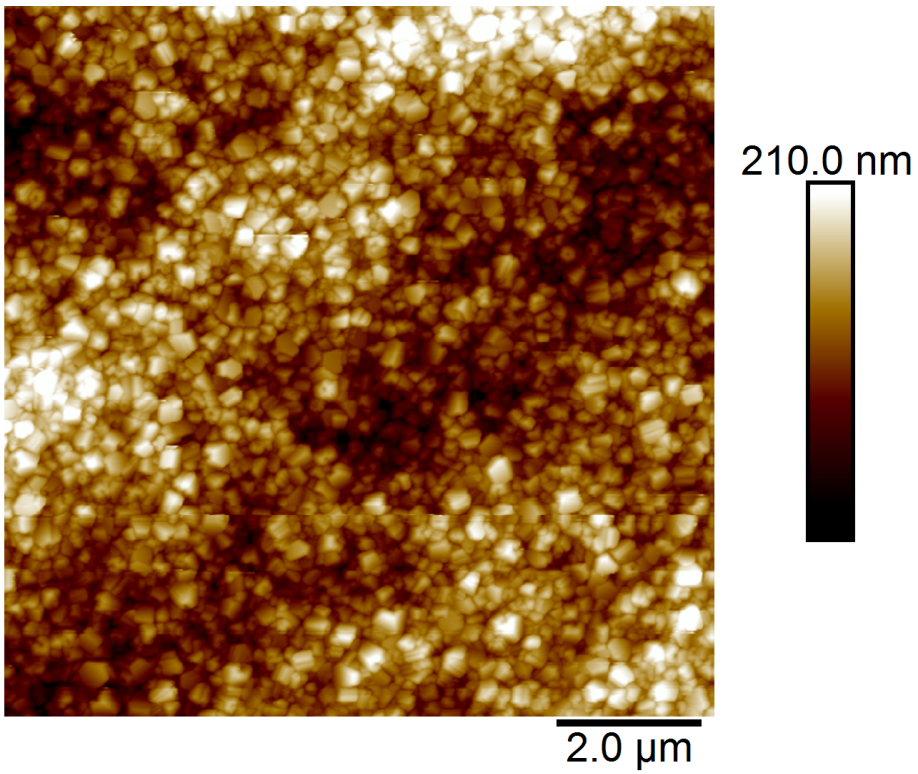

Figure 8-13 – AFM imaging of PE-CVD grown diamond layer of device C. Crystal grains have an average size of ~331 nm.

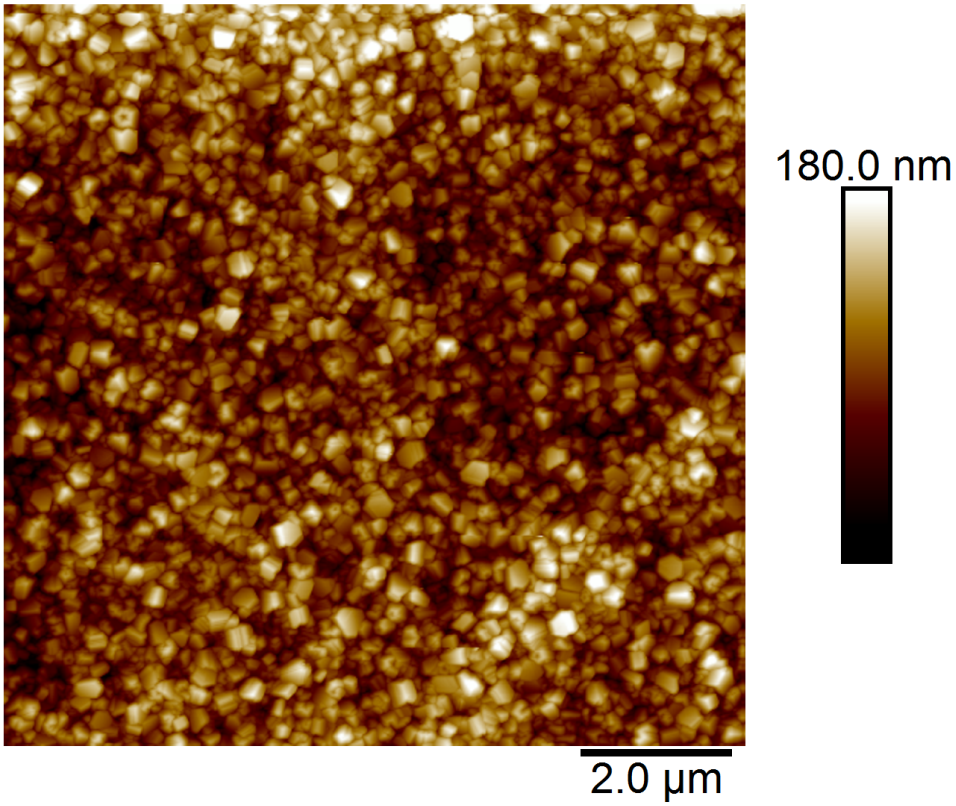

Figure 8-14 – AFM imaging of PE-CVD grown diamond layer of device D. Crystal grains have an average size of ~357 nm.

8.5 Discussion

The I-V figures for devices B, C and D are consistent with Schottky barrier diode behaviour; fitting of current density plots using equation 3–1 indicates all three diodes obey to the expected behaviour of Schottky diodes, where thermionic emission is the main conduction mechanism up to ~1 V. In the active (p–) layers of polycrystalline diamond films, conduction at room temperature is often attributed to thermal ionisation of single-B levels, however other considerations, such as the Poole-Frenkel limiting mechanism, have been found to contribute to conductivity.[171] Figure 8–6 of $V^{1/2}$ against semi-log currents do not clearly show separate linear regions. In figure 8–4, deviation from a linear region below 1 V is attributed to the Poole-Frenkel mechanism. In the Poole-Frenkel regime, the current is related to the square root of the applied voltage as discussed in section 8.1.2. This behaviour is expected for high-voltage conduction in boron-doped diamond.[68,171,192] However, not being able to apply linear fitting in figure 8–6 could indicate another current limiting mechanism may be present. Fitting of the semi-log current density plotted against the applied voltage, between 0 and 0.8 V, yields information about the Ideality factor and the barrier height ϕ_b; this bias range was chosen to avoid current limiting mechanisms for better fitting to thermionic emission behaviour. The Ideality factors in this voltage range are between ~5.5 and ~8.5, suggesting non-ideal behaviour, which is expected given nanodiamond particles were used to fabricate devices. Ideality has been shown to improve with annealing.[180,181,187] Barrier heights are lower than expected for high-quality boron-doped CVD Schottky diodes when compared

to literature, hinting at lowering of Schottky barriers due to image force lowering due to MIGS, as well as potential tunnelling through the barrier. A linear relation between the barrier height and the Ideality factor has been attributed to inhomogeneity in barrier heights in devices of lateral configuration.[181] The equation governing this behaviour is:

$$\phi_b(n) = \phi_b^0 - (n-1)\alpha \qquad Eqn. 8\text{–}2$$

Here ϕ_b^0 is the intrinsic Schottky-barrier height at constant temperature, and α is the slope related to barrier height inhomogeneity.[182,196] In Fiori *et al.*, the slope α is negative, and with annealing, both the barrier height and Ideality factor decrease. The values obtained here are $\phi_b^0 = 0.825 \pm 0.115\ eV$ and $\alpha = -2.71 \pm 0.08 \times 10^{-2}\ eV$, which are different from ideal devices such as in Fiori *et al.*[181] and Tsugawa *et al.*,[180] however the fitting was applied on only 3 devices in this work. In addition, devices with ideality factors further from 1 cannot be used to accurately measure barrier heights.[180] Tsugawa *et al.* have also reported on Schottky barrier height values from Al-oxygenated diamond surfaces, in both (001) and (111) surface configurations, and have measured barrier heights of ~1.2 eV and 0.8~1.0 eV respectively. Although diamond surfaces in this work are expected to have partial hydrogen termination following PE-CVD growth in a hydrogen atmosphere, the relatively high values obtained for currents (up to 0.1 A at ~2 V) in I-V measurements suggest hydrogen surface groups are not actively conductive on un-contacted surfaces of devices. It is assumed that the interface formed between the heavily boron-doped nanodiamond layer and the silicon substrate is acting as the Ohmic contact. Low series resistance values (R_s ~30–60 Ω at low

frequency) measured for devices B, C and D strengthen this assumption. Williams & Jackman[54] have reported surface conductivity values of hydrogen-terminated CVD diamond surfaces around 20 kΩ/sq. Further investigation with better differentiation between surface terminations can be beneficial to the discussion. From C-V results, and specifically from frequency dependant R_s values, it is clear in samples B and C that a mechanism exists where the depletion layer may become thicker with increasing frequency, contrary to behaviour in ideal Schottky barrier devices.[197,198] This mechanism is likely caused by minority carrier injection, tunnelling, or other effects at the metal-semiconductor interface. It is not unusual for Schottky diodes to deviate from ideal behaviour in experiment, especially where an oxide interfacial layer is present. Series resistance was calculated according to:[199]

$$R_S = \frac{\left(\frac{G}{\omega C}\right)^2}{\left(1 + \left(\frac{G}{\omega C}\right)^2\right) G} \qquad Eqn.\,8\text{–}3$$

Negative capacitance was measured for all devices (Appendix, figures 11–9, 11–11 and 11–13). Negative values of series resistance are a direct consequence of negative capacitance measured for device C. Negative capacitance in literature is often attributed to interface states in metal-semiconductor interfaces.[182,195] However, effects from minority carrier injection under small AC bias, which can cause excess capacitance and negative capacitance, are often ignored.[182,200] Such effects cannot be disregarded in low-mobility semiconductors or in interfaces with large Schottky barrier heights.[182] This suggests that device C could be suffering from significant minority carrier injection (from back Ohmic contact) or minority

contact storage. This can be attributed to an imperfect back contact,[200] and is not necessarily a genuine feature of the Schottky interface. Back-contact imperfections can, in this case, originate at the p+ layer (most likely source, due to its aggregated nature), silicon-p+ interface, or the p+–p- interface. No such effect was measured in chapter 7 between silicon and p+ layers, although in chapter 7 nanodiamond layers were not subjected to PE-CVD growth.

Tsigkourakos *et al.*[201] performed an experiment where intrinsic diamond seeds were CVD-grown on a boron-doped diamond substrate, and have concluded that the seeds remain insulating despite reaching high temperatures during growth. They explained their findings by suggesting a lack of boron diffusion into the seeds. This can be further explained by the lack of excess surface boron in form of clusters (see XPS results in chapter 6) or a lack of abundance of boron surface groups, hence a lack of boron diffusion into diamond seeds. Such surface groups and clusters may contribute to boron content in the atmosphere of the growth chamber, due to higher surface-to-bulk ratios in boron-ND materials compared to diamond film or bulk substrates. In chapter 6, it was found that boron-NDs of different origins showed presence of boron clusters and boron surface groups. The doping seen in this chapter may be explained by the large surface area to bulk ratio of NDs, hence their potential ability to contribute enough boron during PE-CVD growth at increased temperatures. To confirm this mechanism, direct measurement of boron content in grown films, such as SIMS, is necessary, while taking growth conditions into consideration. Carrier concentrations estimated from C-V measurements (N_A–N_D) are effective

carrier concentrations, taking into account compensation from donor states which are known to exist, such as nitrogen states.[202] N_A–N_D values can be used to estimate levels of acceptor concentrations from substitutional boron-doping (N_A). Ratios of N_A/N_D is can be as high as two orders of magnitude at the highest,[202,203] suggesting N_A could be at or below ~10^{17} cm^{-3}, which is ideal for p– layers in SBDs. Raman results show an overlap between spectra measured before and after growth, especially for devices C and D. This suggests that PE-CVD growth minimally affected the diamond material in the nanodiamond p+ layers, and resulted in growth of a higher quality diamond film on top, as evidenced in the emergence of a stronger diamond feature (1333 cm^{-1}) when compared to ND films before growth. D/G peak intensity ratios following growth are ~1 for all grown films, putting sp^2 content at ~1–2%.[94] For device B, minimal overlap in the Raman spectrum is seen before and after growth. The emergence of strong peaks at ~1100 and 1470 cm^{-1} suggest the presence of trans-polyacetylene after growth.[94,95,106] AFM imaging of samples before and after growth confirm good quality polycrystalline diamond films were grown in all three devices. Higher boron-levels expected in NDs from sample B, in addition to their lower thermal stability (chapter 7), could explain both the higher carrier concentration (figure 8–8) and the smaller crystal size observed in figure 8–12. Higher levels of boron incorporation are known to affect crystalline quality of CVD grown films.[204] This likely affected the grown film in device B in the initial stage of growth, slowing down grain growth compared to other samples. Devices fabricated using samples A and E did not show good rectifying behaviour. In

sample A, this can be explained by a poor Ohmic back contact. In chapter 7, it was concluded that sample A had relatively high conductivity due to confinement effects, and also due to the presence of sp^2 shells surrounding ND cores. Etching of sp^2 phases during PE-CVD could justify a decrease in conductivity in the seeding layer of device A, leading to a poor back contact. In sample E, geometric considerations could explain reduced conductivity in the Ohmic back contact following PE-CVD growth. Larger ND grains laying on flat silicon will leave significant voids between the ND film and silicon; this is hypothetically filled with intrinsic, or low doped diamond during growth, therefore reducing the effective conductivity of the Ohmic contact. Another explanation would be the reduced surface to bulk ratio of the larger 100 nm NDs, meaning less boron was contributed to the ‘p–‘active layer.

8.7 Conclusion

All three SBD devices exhibit slightly different properties, however they all confirm the possibility of purposeful low-level doping of diamond films using previously doped nanodiamond ‘seeds’. This eliminates the need for using diborane or other boron gas sources during CVD growth, however device performance is expected to be inferior to high quality epitaxial CVD devices grown on single crystal or polycrystalline diamond films. In addition, a current-limiting mechanism is present, potentially attributable to the Pool-Frenkel mechanism, however further investigation is required to determine it. When compared to p-type diamond Schottky diodes found in the scientific literature, it can be seen that devices created for this work are not currently ideal for high-power applications. However, they demonstrate the possibility of using doped seeds for other applications, such as detectors and electrodes in CVD diamond devices, for example. Other potential applications can include lithography on the micron or even the nanoscale, enabling further research and development in the diamond electronics field.

9. Conclusions

In chapter 5 the properties of detonation boron-doped NDs were studied. Prior to this study, no single-digit nm doped diamond materials were reported, and diamond nanoparticles doped with diamond were only obtainable by milling of larger diamond materials.[17] Theoretical studies have not been able to settle the argument about the stability of boron in ND materials, in some cases suggesting that boron aggregates or attaches to edge structures[18-20]. In the present study detonation-derived NDs with purposefully added boron during the detonation process have been measured with a wide range of experimental techniques. The individual DNDs are of 4-5 nm diameters, were studied using Raman and IR spectroscopies, AFM and HR-TEM as well as impedance spectroscopy. When the results from these techniques are combined it is predicted that semiconducting properties of B-DNDs studied here are potentially due to substitutional boron doping. Assuming the above, moderate doping levels are found (~10^{17} B cm^{-3}) alongside the observation that some particles are heavily doped (~10^{20} B cm^{-3}) and likely to be quasi-metallic in character. Whilst further B-DND research is required to generate a more homogeneous distribution of doping concentration, the current study has shown that substitutional boron doping in sub-nm NDs is worthy of further, more detailed investigation, which could open up the path to a whole host of new applications for this interesting class of nano-particles. Applications include, but are not limited to: studies in spintronics, superconductivity, as well as nanomagnetometry and single photon emission[59]. They are also potentially useful as biosensors on the nanoscale[59].

In chapter 6, the ultra-sonic assisted nucleation of boron-doped NDs on silicon surfaces was studied by method of pH titration, AFM imaging, Zeta-potential and DLS measurements. To interpret results in terms of surface chemistry, XPS was also performed on samples. All samples were acid cleaned to get rid of impurities, non-diamond carbon, and metals. No metal species were found in XPS survey measurements. In conclusion, the nucleation behaviour of boron-doped NDs on silicon was found to be highly affected by pH of the solution. Results from pH dependant Zeta-potential measurements and DLS measurements suggest that poor seeding of boron-NDs across pH is due to the electrostatic repulsion between silicon and ND surfaces, as they all have negative Zeta-potentials (within measurement error). This however changes at pH<3, where silicon obtains a positive Zeta-potential while boron-NDs maintain the negative potential. Lack of full coverage can be attributed to the lowered stability of NDs in solution as their absolute Zeta-potentials drop. XPS results confirm the existence of oxygen groups on all samples, however uncertainties in XPS survey require measurements with higher spectral resolution. They also show presence of boron-oxygen and boron-carbon functional groups, as well as boron-clustering. Zeta-potentials of air-annealed NDs and boron carbides are very similar, due to the strong acidity of their surfaces and low iso-electric points. To improve surface coverage of boron-NDs, surface modification becomes necessary. Hydrogenation of DNDs proved to be an effective way to improve surface coverage, however this can only be applied to dry ND samples, and is not possible on solutions. Further research into possible surface modification of ND solutions is required, as well as modification of silicon surfaces. It was

also found that PDDAC significantly improves nucleation of lightly doped B-DNDs, but not heavily doped HPHT B-NDs. This suggests that the boron concentration in the bulk of NDs has an effect on nucleation dynamics. Preparation of HPHT B-NDs at different boron concentrations, but equal diameters, would contribute positively to the discussion. The effect of band structure and band-bending should also be considered in future studies, especially on NDs of smaller diameters, where quantum confinement effects may take place.

For chapter 7, It was concluded from that due to the many factors affecting conductivity of doped nanodiamonds, a direct measure of the doping level in any given nanodiamond sample cannot be obtained using electrical and impedance measurements alone, and that direct measurement (such as SIMS) may be necessary. Hall measurements can be used to measure the carrier density and mobility of diamond, however, interfacing nanodiamonds directly with Hall measurement equipment proved challenging. Other techniques, such as STM or conductive AFM, may be used to obtain more information on the electrical properties of single nanodiamond grains. Variable temperature Hall-mobility measurements would be very helpful to this discussion, with van der Paaw contact arrangement or even better, hall bars. This remains technically challenging, since the use of silicon contacts in sandwich configuration is not ideal. Better understanding of boron content in nanodiamond samples is required using analytical methods like XANES/NEXAFS; understanding the extent of grain boundary and interfacial effects is of utmost importance to the discussion, especially when such materials are considered for micro/nano electronics and photonics

applications. A more detailed study of the effects of confinement on doped nanodiamond films, in light of findings by Norris *et al.*, would be greatly supportive to the understanding of conductivity in nanodiamond films.

In chapter 8, the three SBD devices fabricated exhibited slightly different properties, but confirmed the possibility of purposeful low-level doping of diamond films using previously doped nanodiamond seeds. This eliminates the need for using boron-containing gas sources during CVD growth, however device performance is expected to be inferior to high quality epitaxial CVD devices grown on diamond films. When compared to p-type diamond Schottky diodes found in the scientific literature, it can be seen that devices created for this work are not ideal for high-power applications. However, they demonstrate the potential of using doped seeds for further diamond electronics applications.

10. Future Work

Detailed analysis of the fine structure of substitutional boron states in NDs is essential; this can be obtained using techniques such as XANES/NEXAFS and nanoscale-optimised spectroscopic Cathodoluminescence (CL). In addition, a better understanding of the distribution of different carbon phases (sp^2, sp^3 and amorphous) in and around NDs is of great significance. This can also be obtained using the above techniques. In addition, the ability to perform Hall-mobility measurements on ND materials should be investigated and developed, without significant modification to the materials under study. Chapter 6 concluded without achieving full surface coverage of boron-NDs on silicon substrates using ultra-sonication nucleation, suggesting further surface modification of B-NDs is required to achieve this goal. Surface terminations (such as hydrogen-termination) should be attempted via electrochemical methods (of aggregated NDs on conductive substrates, preferably also diamond). Computational studies of heavily doped NDs, their electronic band structure and surface charges as a function of diameter will should be performed to explain and complement results found in this study. Moreover, temperature dependant electrical measurements of SBD devices would give better insight into intrinsic properties of devices, and hence of PE-CVD grown diamond layers.

11. Appendix

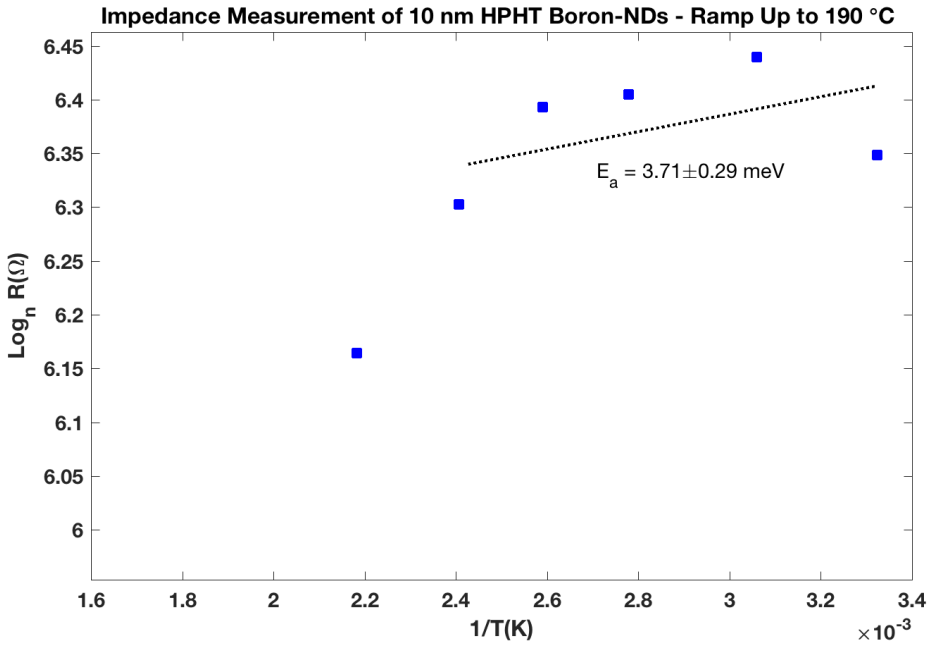

Figure 11-1 – Arrhenius plot of 10 nm Boron-doped HPHT nanodiamond film measured between room temperature and 190 °C. Measurement was discontinued above 190 °C due to overload error in the measurement software, indicating damage to the sample or phase change. The activation energy measured is in agreement with the low temperature activation energy shown in figure 7–17.

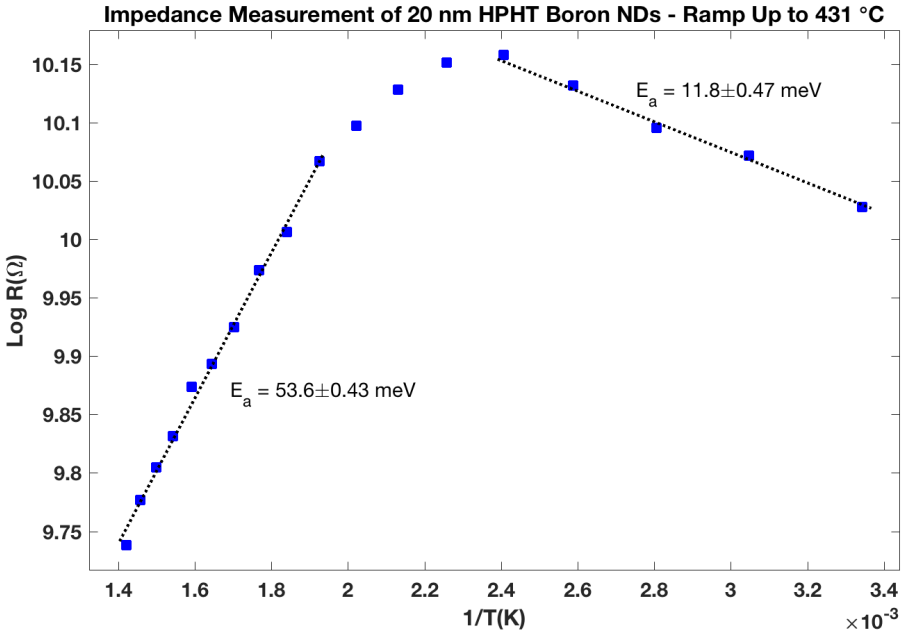

Figure 11-2 – Arrhenius plot of 20 nm Boron-doped HPHT nanodiamond film measured between room temperature and 431 °C. Low temperature activation energy is not accepted as increasing resistance with increasing energy indicates moisture was initially present. The high temperature activation energy is in agreement with that shown in figure 7–18.

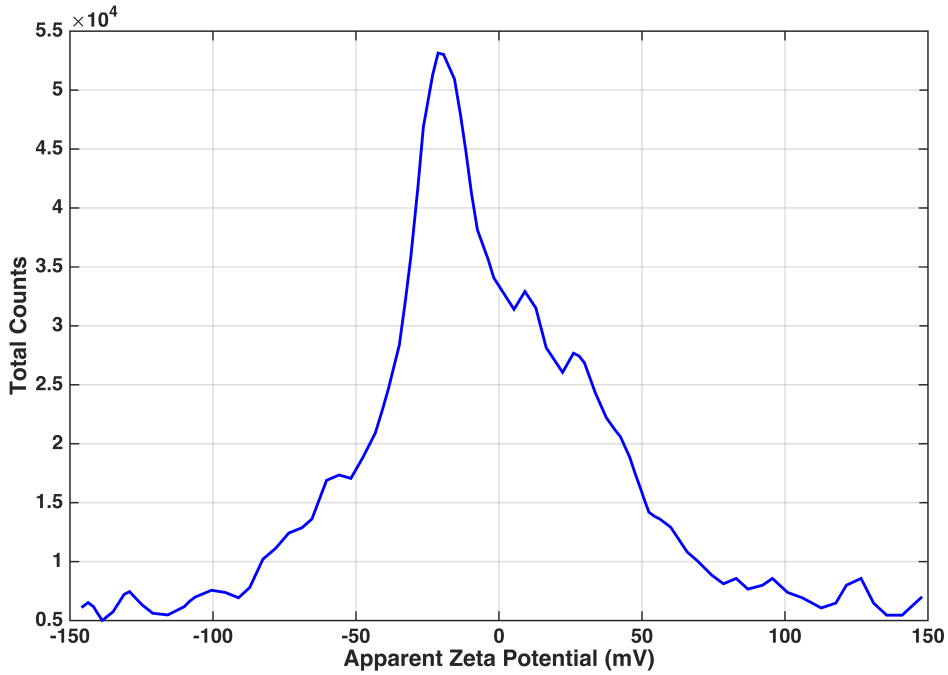

Figure 11-3 – Zeta potential quality report for sample A (5 nm B-DND), showing an overall negative zeta potential, with positive contributions. This is explained by the rich chemical nature of detonation ND surfaces.

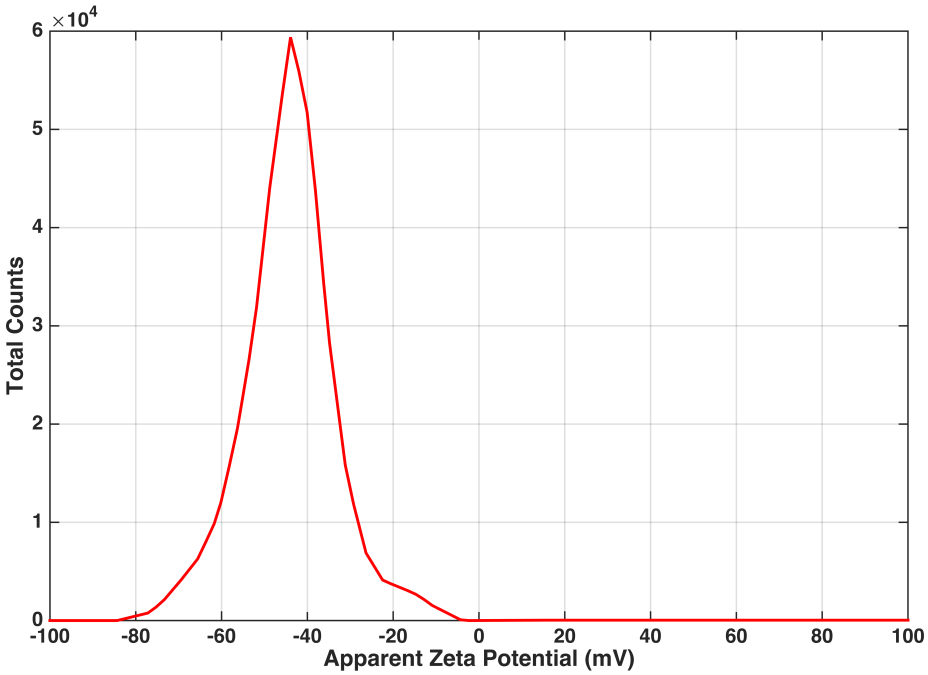

Figure 11-4 – Zeta Potential quality report of sample E (100 nm HPHT Boron-NDs). This shows contributions only in the negative part of the spectrum.

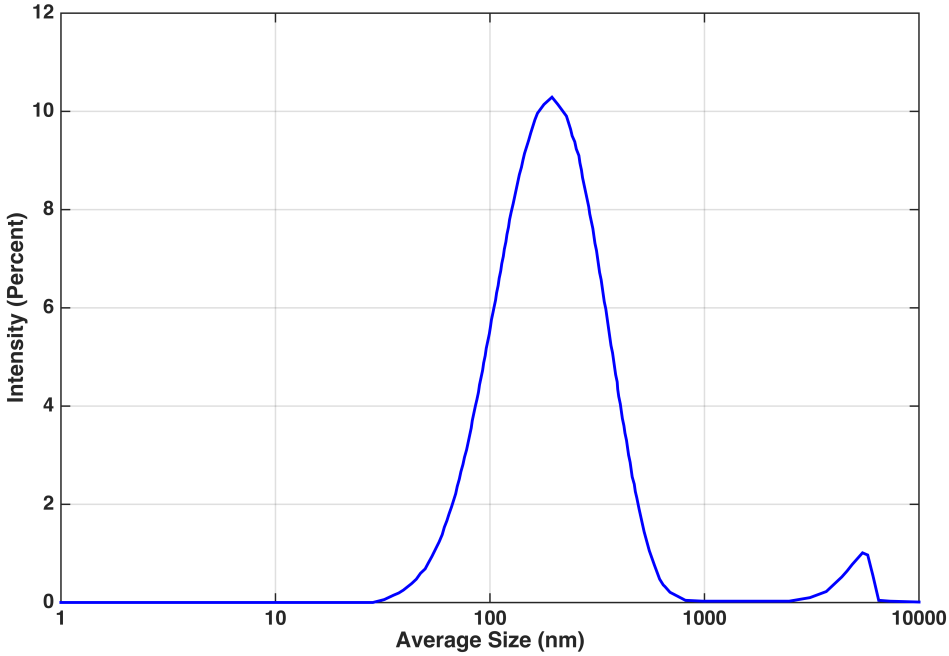

Figure 11-5 – Dynamic Light Scattering results for sample A (5 nm B-DND). This shows major contribution from agglomerates, which have an average diameter of ~100 nm.

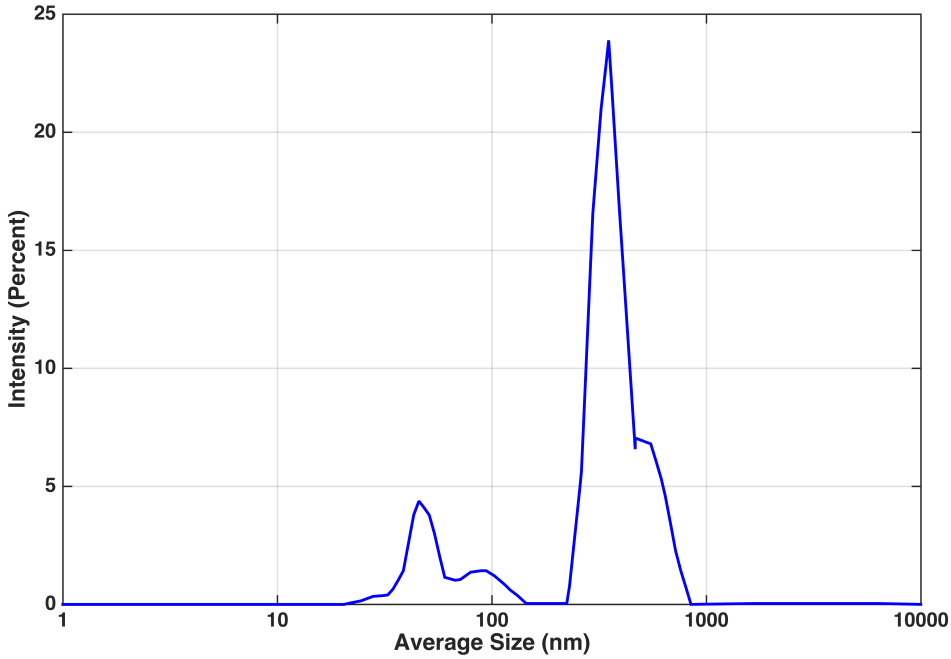

Figure 11-6 – Dynamic Light Scattering results for sample B (10 nm HPHT B-ND). This shows major contribution from agglomerates, which have an average diameter of ~500 nm, however smaller particles of diameters down to ~20 nm are also measured.

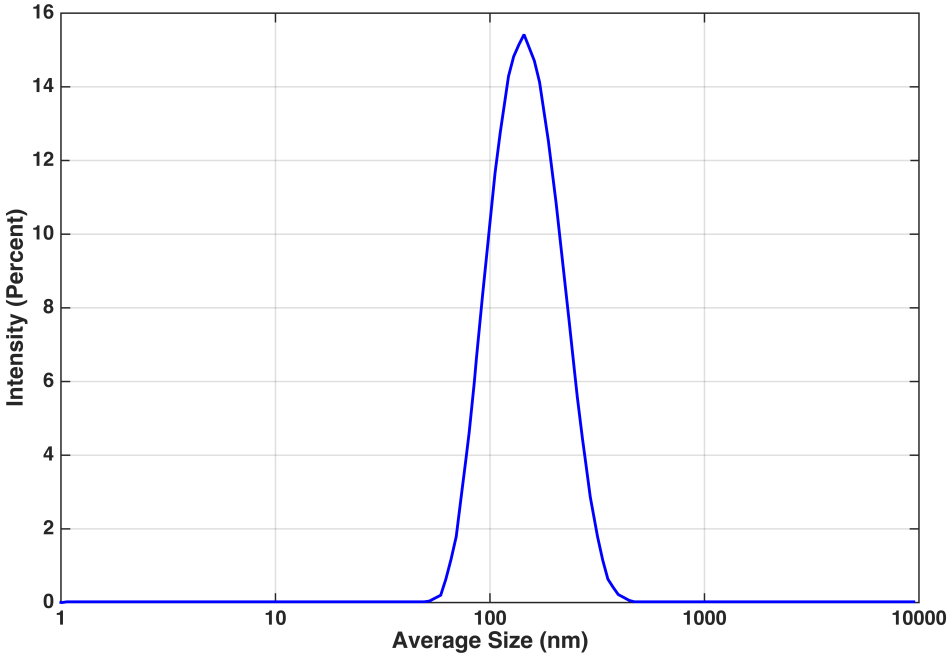

Figure 11-7 – Dynamic Light Scattering results for sample E (100 nm HPHT B-ND). This shows a single peak centred just above 100 nm.

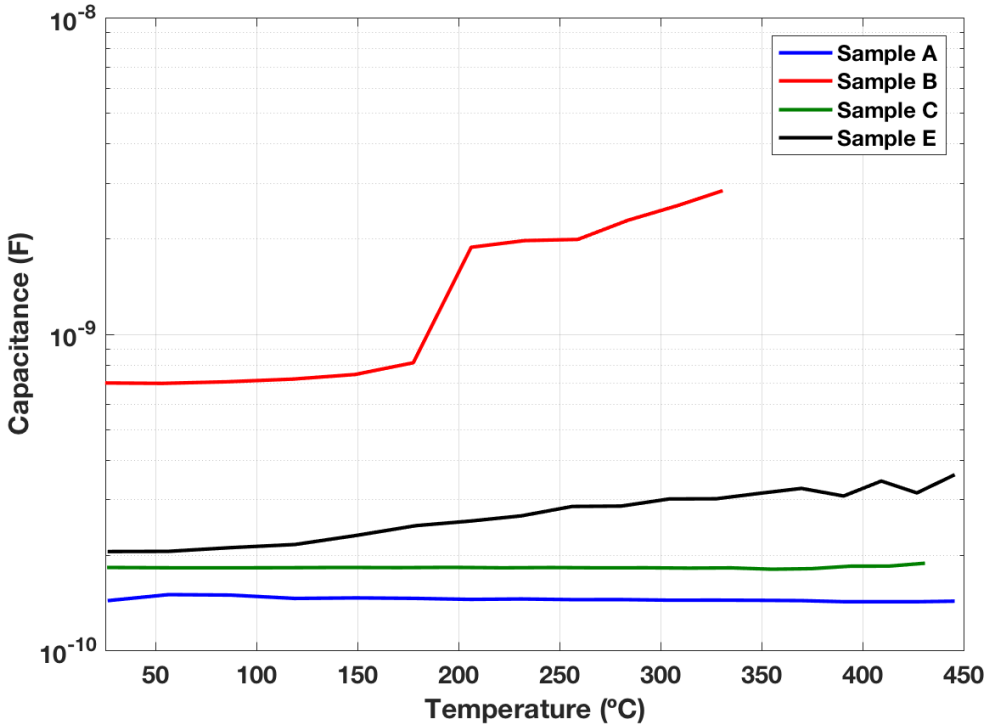

Figure 11-8 –Capacitance from impedance spectroscopy measurements (chapter 7) for samples A, B, C and E. Constant values are measured for samples A and C, with a slightly increasing capacitance in sample E, as temperature increases. Sample B has higher capacitance at room temperature, and shows a sudden increase around ~180 ºC.

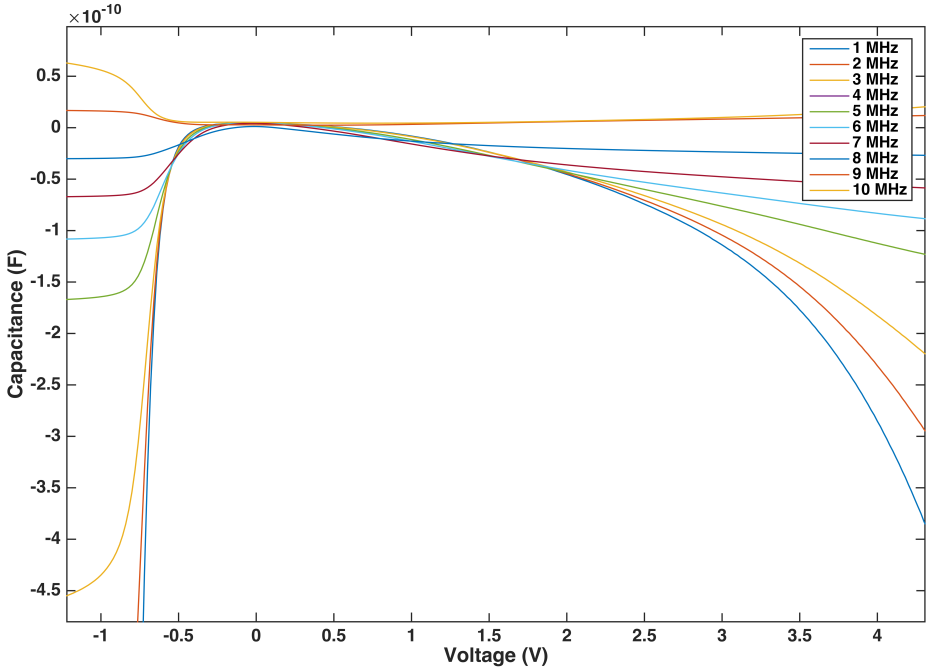

Figure 11-9 –Capacitance measurements (device B, chapter 8) as a function of applied bias, shown for frequencies between 1 MHz and 10 MHz.

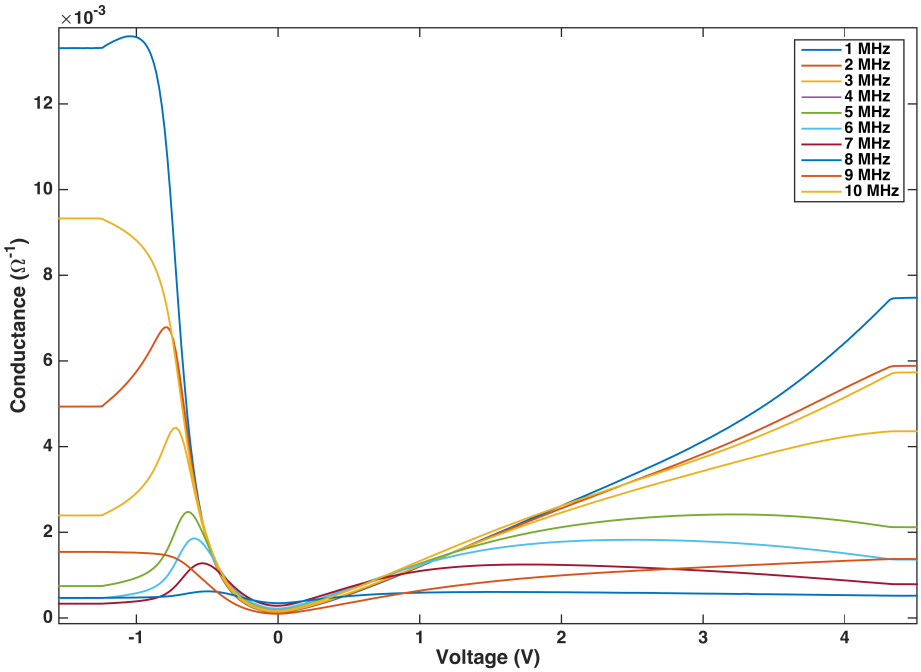

Figure 11-10 – Conductance measurements (device B, chapter 8) as a function of applied bias, shown for frequencies between 1 MHz and 10 MHz.

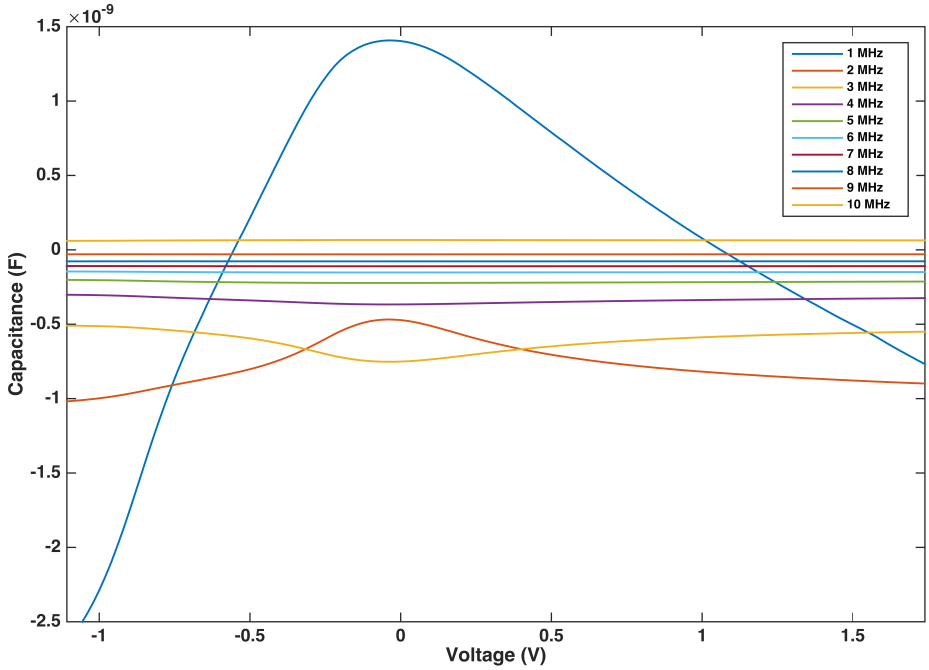

Figure 11-11 – Capacitance measurements (device C, chapter 8) as a function of applied bias, shown for frequencies between 1 MHz and 10 MHz.

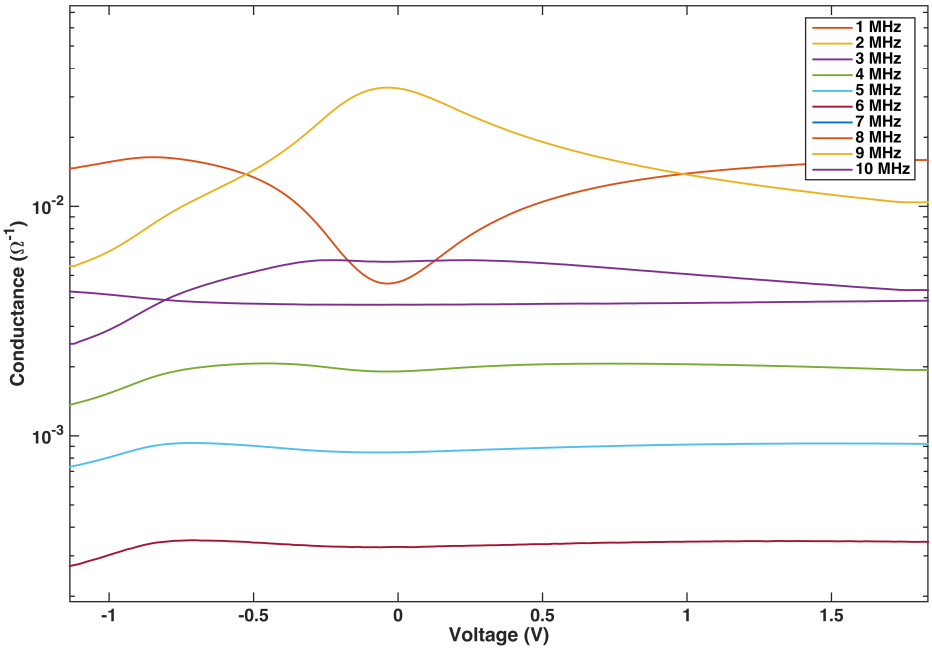

Figure 11-12 – Conductance measurements (device C, chapter 8) as a function of applied bias, shown for frequencies between 1 MHz and 10 MHz.

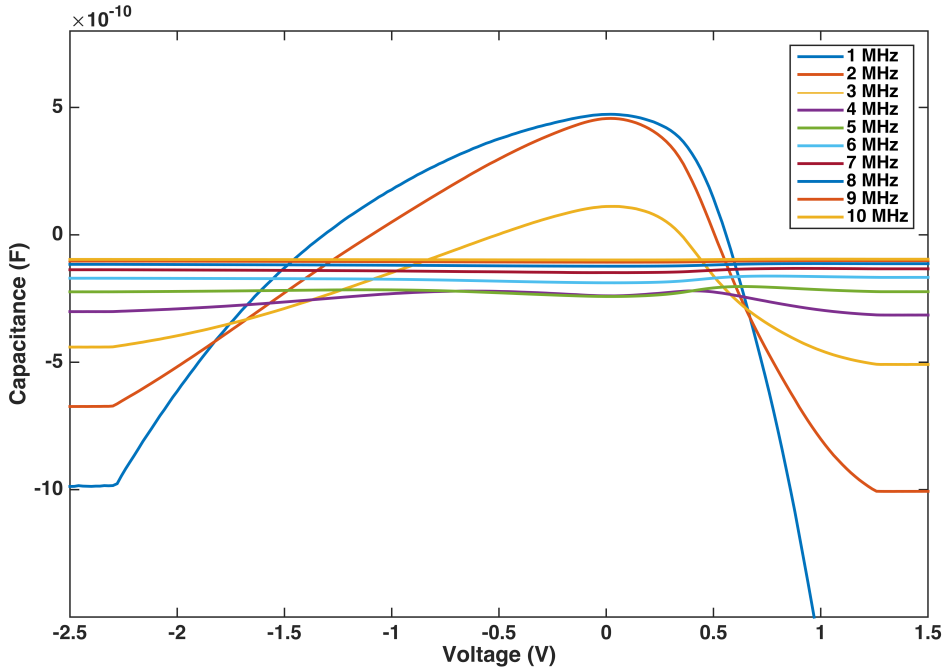

Figure 11-13 – Capacitance measurements (device D, chapter 8) as a function of applied bias, shown for frequencies between 1 MHz and 10 MHz.

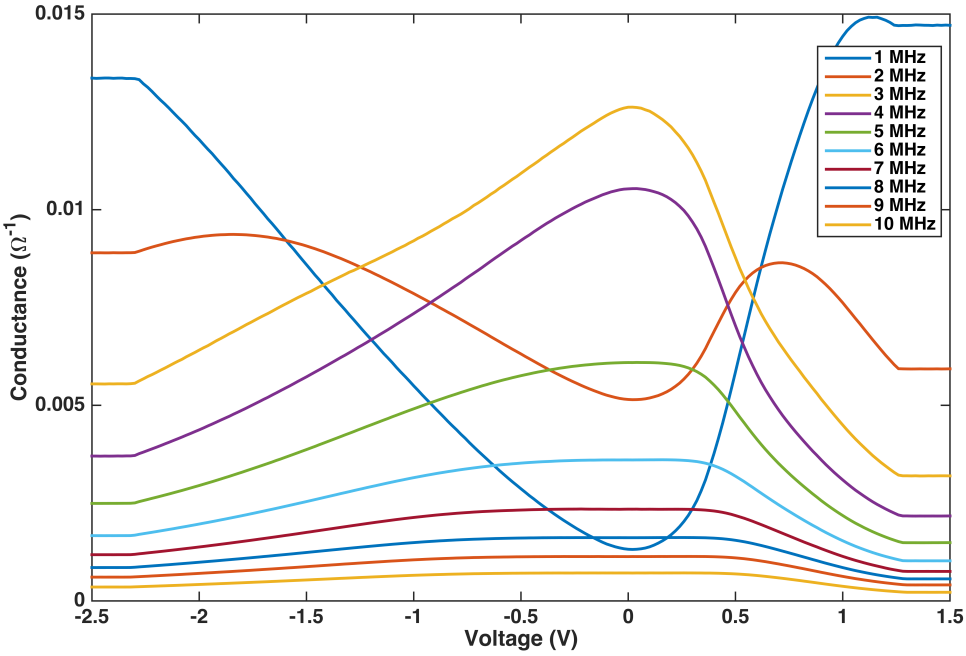

Figure 11-14 – Conductance measurements (device D, chapter 8) as a function of applied bias, shown for frequencies between 1 MHz and 10 MHz.

References

(1) Nunn, N.; Torelli, M.; McGuire, G.; Shenderova, O. Nanodiamond: A High Impact Nanomaterial. *Curr. Opin. Solid State Mater. Sci.* **2017**, *21*, 1–9.

(2) Mochalin, V. N.; Gogotsi, Y. Nanodiamond-Polymer Composites. *Diam. Relat. Mater.* **2015**, *58*, 161–171.

(3) Vaijayanthimala, V.; Lee, D. K.; Kim, S. V; Yen, A.; Tsai, N.; Ho, D.; Chang, H.-C.; Shenderova, O. Nanodiamond-Mediated Drug Delivery and Imaging: Challenges and Opportunities. *Expert Opin. Drug Deliv.* **2015**, *12*, 735–749.

(4) Kirmani, A. R.; Peng, W.; Mahfouz, R.; Amassian, A.; Losovyj, Y.; Idriss, H.; Katsiev, K. On the Relation between Chemical Composition and Optical Properties of Detonation Nanodiamonds. *Carbon N. Y.* **2015**, *94*, 79–84.

(5) Fokin, A. A.; Schreiner, P. R. Band Gap Tuning in Nanodiamonds: First Principle Computational Studies. *Mol. Phys.* **2009**, *107*, 823–830.

(6) Barnard, A. S.; Sternberg, M. Substitutional Boron in Nanodiamond, Bucky-Diamond, and Nanocrystalline Diamond Grain Boundaries. *J. Phys. Chem. B* **2006**, *110*, 19307–19314.

(7) Barnard, A. S.; Sternberg, M. Can We Predict the Location of Impurities in Diamond Nanoparticles? *Diam. Relat. Mater.* **2007**, *16*, 2078–2082.

(8) Afandi, A.; Howkins, A.; Boyd, I. W.; Jackman, R. B. Nanodiamonds for Device Applications: An Investigation of the Properties of Boron-Doped Detonation Nanodiamonds. *Sci. Rep.* **2018**, *8*, 3270.

(9) Holt, K. B. Diamond at the Nanoscale: Applications of Diamond Nanoparticles from Cellular Biomarkers to Quantum Computing. *Philos. Trans. A. Math. Phys. Eng. Sci.* **2007**, *365*, 2845–2861.

(10) Terranova, M. L.; Orlanducci, S.; Rossi, M.; Tamburri, E. Nanodiamonds for Field Emission: State of the Art. *Nanoscale* **2015**, *7*, 5094–5114.

(11) Laraoui, A.; Hodges, J. S.; Meriles, C. A. Nitrogen-Vacancy-Assisted

Magnetometry of Paramagnetic Centers in an Individual Diamond Nanocrystal. *Nano Lett.* **2012**, *12*, 3477–3482.

(12) Holt, K. B.; Caruana, D. J.; Millán-Barrios, E. J. Electrochemistry of Undoped Diamond Nanoparticles: Accessing Surface Redox States. *J. Am. Chem. Soc.* **2009**, *131*, 11272–11273.

(13) Krueger, A. Diamond Nanoparticles: Jewels for Chemistry and Physics. *Adv. Mater.* **2008**, *20*, 2445–2449.

(14) Xing, Y.; Dai, L. Nanodiamonds for Nanomedicine. *Nanomedicine (Lond).* **2009**, *4*, 207–218.

(15) Williams, O. A.; Douhéret, O.; Daenen, M.; Haenen, K.; Osawa, E.; Takahashi, M. Enhanced Diamond Nucleation on Monodispersed Nanocrystalline Diamond. *Chem. Phys. Lett.* **2007**, *445*, 255–258.

(16) Mochalin, V. N.; Shenderova, O.; Ho, D.; Gogotsi, Y. The Properties and Applications of Nanodiamonds. *Nature Nanotechnology*, 2011, *7*, 11–23.

(17) Voznyakovskii, a. P.; Dolmatov, V. Y.; Shumilov, F. a. The Influence of Detonation Synthesis Conditions on Surface Properties of Detonation Nanodiamonds. *J. Superhard Mater.* **2014**, *36*, 165–170.

(18) Danilenko, V. V. On the History of the Discovery of Nanodiamond Synthesis. *Phys. Solid State* **2004**, *46*, 595–599.

(19) Krüger, a.; Kataoka, F.; Ozawa, M.; Fujino, T.; Suzuki, Y.; Aleksenskii, a. E.; Vul', a. Y.; Osawa, E. Unusually Tight Aggregation in Detonation Nanodiamond: Identification and Disintegration. *Carbon N. Y.* **2005**, *43*, 1722–1730.

(20) Borst, T. H.; Weis, O. Boron-Doped Homoepitaxial Diamond Layers: Fabrication, Characterization, and Electronic Applications. *Phys. Status Solidi* **1996**, *154*, 423–444.

(21) Ekimov, E. a; Ekimov, E. a; Sidorov, V. a; Sidorov, V. a; Bauer, E. D.; Bauer, E. D.; Mel'nik, N. N.; Mel'nik, N. N.; Curro, N. J.; Curro, N. J.; *et al.* Superconductivity in Diamond. *Nature* **2004**, *428*, 542–545.

(22) Tsigkourakos, M.; Hantschel, T.; Bangerter, C.; Vandervorst, W. Electrical Probing of B-Doped Diamond Seeds Embedded into the

Interfacial Layer of a Conductive Diamond Film. *Phys. Status Solidi* **2014**, *211*, 2284–2289.

(23) Fischer, A. E.; Swain, G. M. Preparation and Characterization of Boron-Doped Diamond Powder - A Possible Dimensionally Stable Electrocatalyst Support Material. *J. Electrochem. Soc.* **2005**, *152*, B369–B375.

(24) Cunci, L.; Cabrera, C. R. Preparation and Electrochemistry of Boron-Doped Diamond Nanoparticles on Glassy Carbon Electrodes. *Electrochem. Solid-State Lett.* **2011**, *14*, K17.

(25) Heyer, S.; Janssen, W.; Turner, S.; Lu, Y. G.; Yeap, W. S.; Verbeeck, J.; Haenen, K.; Krueger, A. Toward Deep Blue Nano Hope Diamonds: Heavily Boron-Doped Diamond Nanoparticles. *ACS Nano* **2014**, *8*, 5757–5764.

(26) Edgington, R. Diamond at the Brain-Machine Interface. **2012**, 1–218.

(27) Shenderova, O. Production of Conductive Nanodiamond by Dynamic Synthesis Approaches. *United States Patent*, 2014, US 8728429 B2.

(28) Wang, J.; Ma, L.; Zhao, J. First-Principles Study Of Nanodiamond Doped With B And N. *International Journal of Modern Physics B*, 2010, *24*, 6099–6106.

(29) Pan, L. S.; Kania, D. R. *Diamond: Electronic Properties and Applications*; Springer Science & Business Media: New York, 2013.

(30) Carbon - An Amazingly Allotropic Element http://virtuallaboratory.colorado.edu/CLUE-Chemistry/chapters/chapter3txt-3.html (accessed Sep 19, 2016).

(31) Pierson, H. O. Handbook of Carbon, Graphite, Diamond and Fullerenes. *Handb. Carbon, Graph. Diam. Fullerenes* **1993**, 23–36.

(32) Nature of the Chemical Bond http://rjwarren0.tripod.com/OAC_HW/Chem_HW-Chapter4.html (accessed Sep 10, 2016).

(33) Schwander, M.; Partes, K. A Review of Diamond Synthesis by CVD Processes. *Diam. Relat. Mater.* **2011**, *20*, 1287–1301.

(34) May, P. W. Diamond Thin Films: A 21st-Century Material. *Phil. Trans.*

R. Soc. Lond. A **2000**, *358*, 473–495.

(35) Bachmann, P.; Leers, D.; Wiechert, D.; Bachmann, P.; Leers, D.; Diamond, D. W.; Vapour, C. Diamond Chemical Vapour Deposition. *J. Phys. IV Colloq.* **1991**, *2*, pp.C2-907-C2-913.

(36) Synthetic Diamonds http://diamondabrasives.eu/synthetic-diamonds (accessed Oct 2, 2016).

(37) Bundy, F. P.; Hall, H. T.; Strong, H. M.; Wentorf, R. H. Man-Made Diamonds. *Nature* **1955**, *4471*, 51.

(38) Collins, A. T.; Kanda, H.; Kitawaki, H. Colour Changes Produced in Natural Brown Diamonds by High-Pressure, High-Temperature Treatment. *Diam. Relat. Mater.* **2000**, *9*, 113–122.

(39) Fang, L.; Ohfuji, H.; Irifune, T. A Novel Technique for the Synthesis of Nanodiamond Powder. *J. Nanomater.* **2013**, *2013*, 201845.

(40) Dolmatov, V. Y. Detonation-Synthesis Nanodiamonds: Synthesis, Structure, Properties and Applications. *Russ. Chem. Rev.* **2007**, *76*, 339–360.

(41) Danilenko, V. V. Phase Diagram of Nanocarbon. *Fiz. Goreniya i Vzryva* **2005**, *41*, 341-110–116.

(42) Bevilacqua, M.; Patel, S.; Chaudhary, A.; Ye, H.; Jackman, R. B. Electrical Properties of Aggregated Detonation Nanodiamonds. *Appl. Phys. Lett.* **2008**, *93*, 0–3.

(43) Krüger, A.; Liang, Y.; Jarre, G.; Stegk, J. Surface Functionalisation of Detonation Diamond Suitable for Biological Applications. *J. Mater. Chem.* **2006**, *16*, 2322–2328.

(44) Aleksenskiy, A. E.; Eydelman, E. D.; Vul', A. Y. Deagglomeration of Detonation Nanodiamond. *Nanosci. Nanotechnol. Lett.* **2011**, *3*, 68–74.

(45) Dolmatov, V. Y.; Vehanen, a.; Myllymäki, V.; Rudometkin, K. a.; Panova, a. N.; Korolev, K. M.; Shpadkovskaya, T. a. Purification of Detonation Nanodiamond Material Using High-Intensity Processes. *Russ. J. Appl. Chem.* **2013**, *86*, 1036–1045.

(46) Williams, O. A.; O'Brien, P.; Nuzzo, R. *Nanodiamond*; Royal Society of Chemistry 2014, 2014.

(47) Collins, A. T. Diamond Electronic Devices-a Critical Appraisal. *Semicond. Sci. Technol.* **1989**, *4*, 605.

(48) Arnault, J. C. Novel Aspects of Diamond. *Top. Appl. Phys.* **2015**, *121*, 85–122.

(49) Locher, R.; Wagner, J.; Fuchs, F.; Maier, M.; Gonon, P.; Koidl, P. Optical and Electrical Characterization of Boron-Doped Diamond Films. *Diam. Relat. Mater.* **1995**, *4*, 678–683.

(50) Thonke, K. The Boron Acceptor in Diamond. *Semicond. Sci. Technol.* **2003**, *18*, S20–S26.

(51) Massarani, B.; Bourgoin, J. C.; Chrenko, R. M. Hopping Conduction in Semiconducting Diamond. *Phys. Rev. B* **1978**, *17*, 1758–1769.

(52) Mori, M.; Saeki, Y.; Hakamata, M.; Sato, T.; Kabasawa, E.; Nakamura, J. Electronic Structures of Aluminum-Doped Diamond near the Fermi Level. *J. Phys. Soc. Japan* **2015**, *84*, 44704.

(53) Maier, F.; Riedel, M.; Mantel, B.; Ristein, J.; Ley, L. Origin of Surface Conductivity in Diamond. *Phys. Rev. Lett.* **2000**, *85*, 3472–3475.

(54) Williams, O. A.; Jackman, R. B. Surface Conductivity on Hydrogen Terminated Diamond. *Semicond. Sci. Technol.* **2003**, *18*, S34–S40.

(55) Chen, W.; Qi, D.; Gao, X.; Wee, A. T. S. Surface Transfer Doping of Semiconductors. *Prog. Surf. Sci.* **2009**, *84*, 279–321.

(56) Ozawa, M.; Inaguma, M.; Takahashi, M.; Kataoka, F.; Krüger, A.; Osawa, E. Preparation and Behavior of Brownish, Clear Nanodiamond Colloids. *Adv. Mater.* **2007**, *19*, 1201–1206.

(57) Huang, H.; Pierstorff, E.; Osawa, E.; Ho, D. Active Nanodiamond Hydrogels for Chemotherapeutic Delivery. *Nano Lett.* **2007**, *7*, 3305–3314.

(58) Vervald, A. M.; Burikov, S. A.; Vlasov, I. I.; Ekimov, E. A.; Shenderova, O. A.; Dolenko, T. A. Boron-Doped Nanodiamonds as Possible Agents for Local Hyperthermia. *Laser Phys. Lett.* **2017**.

(59) Ekimov, E. A.; Kudryavtsev, O. S.; Khomich, A. A.; Lebedev, O. I.; Dolenko, T. A.; Vlasov, I. I. High-Pressure Synthesis of Boron-Doped Ultrasmall Diamonds from an Organic Compound. *Adv. Mater.* **2015**,

27, 5518–5522.

(60) Ay, A.; Swope, V. M.; Swain, G. M. The Physicochemical and Electrochemical Properties of 100 and 500 Nm Diameter Diamond Powders Coated with Boron-Doped Nanocrystalline Diamond. *J. Electrochem. Soc.* **2008**, *155*, B1013.

(61) Williams, O. a.; Nesladek, M.; Daenen, M.; Michaelson, S.; Hoffman, a.; Osawa, E.; Haenen, K.; Jackman, R. B. Growth, Electronic Properties and Applications of Nanodiamond. *Diam. Relat. Mater.* **2008**, *17*, 1080–1088.

(62) Williams, O. A. Nanocrystalline Diamond. *Diam. Relat. Mater.* **2011**, *20*, 621–640.

(63) Van Der Drift, A. Evolutionary Selection, A Principle Governing Growth Orientation In Vapour-Deposited Layers. *R626 . Philips Res. Repts* **1967**, *22*, 267–288.

(64) Butler, J. E.; Sumant, A. V. The CVD of Nanodiamond Materials. *Chem. Vap. Depos.* **2008**, *14*, 145–160.

(65) Braun, F. Ueber Die Stromleitung Durch Schwefelmetalle. *Ann. Phys.* **1875**, *229*, 556–563.

(66) Wilson, A. H. A Note on the Theory of Rectification. *Proc. R. Soc. A Math. Phys. Eng. Sci.* **1932**, *136*, 487.

(67) Nordheim, L. Zur Theorie Der Detektorwirkung. *Zeitschrift für Phys.* **1932**, *75*, 434–441.

(68) Frenkel, J.; Joffe, A. On the Electric and Photoelectric Properties of Contacts between a Metal and a Semiconductor. *Phys. Rev.* **1932**, *39*, 530–531.

(69) Mott, N. F. The Theory of Crystal Rectifiers. *Proc. R. Soc. A Math. Phys. Eng. Sci.* **1939**, *171*, 27–38.

(70) Mönch, W. On the Present Understanding of Schottky Contacts. *Festkörperprobleme 26* **1986**, *26*, 67–88.

(71) Singh, J. Semiconductor Devices: Basic Principles. In *Semiconductor Devices: Basic Principles*; 2001; pp. 227–240.

(72) Heine, V. Theory of Surface States. *Phys. Rev.* **1965**, *138*, A1689–

A1696.

(73) Tyagi, M. S. Physics of Schottky Barrier Junctions. In *Metal-Semiconductor Schottky Barrier Junctions and Their Applications*; 1984; pp. 1–60.

(74) Bardeen, J. Surface States and Rectification at a Metal Semi-Conductor Contact. *Phys. Rev.* **1947**, *71*, 717–727.

(75) Chicot, G. Field Effect in Boron Doped Diamond Effet de Champ Dans Le Diamant Dopé Au Bore. **2013**.

(76) Traore, A. High Power Diamond Schottky Diode. **2014**.

(77) Makino, T.; Oyama, K.; Kato, H.; Takeuchi, D.; Ogura, M.; Okushi, H.; Yamasaki, S. Diamond Electronic Devices Fabricated Using Heavily Doped Hopping P + and N+ Layers. *Jpn. J. Appl. Phys.* **2014**, *53*.

(78) Grotjohn, T. A.; Tran, D. T.; Yaran, M. K.; Demlow, S. N.; Schuelke, T. Heavy Phosphorus Doping by Epitaxial Growth on the (111) Diamond Surface. *Diam. Relat. Mater.* **2014**, *44*, 129–133.

(79) Traore, A.; Muret, P.; Fiori, A.; Eon, D.; Traore, A.; Muret, P.; Fiori, A.; Eon, D.; Gheeraert, E.; Muret, P.; *et al.* Zr / Oxidized Diamond Interface for High Power Schottky Diodes To Cite This Version : **2014**.

(80) Tatsumi, N.; Ikeda, K.; Umezawa, H.; Shikata, S. Development of Diamond Schottky Barrier Diode. *SEI Tech. Rev.* **2009**, 54–61.

(81) Vul, A. Y.; Aleksenskiy, A. E.; Dideykin, A. T. Detonation Nanodiamonds: Technology, Properties And Applications. **2009**.

(82) Vul', a. Y.; Dideĭkin, a. T.; Tsareva, Z. G.; Korytov, M. N.; Brunkov, P. N.; Zhukov, B. G.; Rozov, S. I. Direct Observation of Isolated Ultrananodimensional Diamond Clusters Using Atomic Force Microscopy. *Tech. Phys. Lett.* **2006**, *32*, 561–563.

(83) Hees, J.; Kriele, A.; Williams, O. A. Electrostatic Self-Assembly of Diamond Nanoparticles. *Chem. Phys. Lett.* **2011**, *509*, 12–15.

(84) Tutorials, E. The Zeta Potential. *Building* **1999**, 1–4.

(85) Ralchenko, V.; Saveliev, A.; Voronina, S.; Dementjev, A.; Maslakov, K.; Salerno, M.; Podesta, A.; Milani, P. Nanodiamond Seeding for Nucleation and Growth of CVD Diamond Films. *Synth. Prop. Appl.*

Ultrananocrystalline Diam. **2005**, 109–124.

(86) Yoshikawa, T.; Zuerbig, V.; Gao, F.; Hoffmann, R.; Nebel, C. E.; Ambacher, O.; Lebedev, V. Appropriate Salt Concentration of Nanodiamond Colloids for Electrostatic Self-Assembly Seeding of Monosized Individual Diamond Nanoparticles on Silicon Dioxide Surfaces. *Langmuir* **2015**, *31*, 5319–5325.

(87) MALVERN. Zetasizer Nano Series. *Malvern Instruments Ltd* **2014**, 20.

(88) Fernández Lahore, M.; Aguilar, O.; Reddy Vennapusa, R.; Aasim, M. Expanded Bed Chromatography, Surface Energetics of Biomass Deposition. *Encycl. Ind. Biotechnol.* **2010**, *4*, 2377–2388.

(89) Sze, A.; Erickson, D.; Ren, L.; Li, D. Zeta-Potential Measurement Using the Smoluchowski Equation and the Slope of the Current-Time Relationship in Electroosmotic Flow. *J. Colloid Interface Sci.* **2003**, *261*, 402–410.

(90) Griffiths, P. R.; De Haseth, J. A. *Fourier Transform Infrared Spectrometry*; 2007.

(91) Fourier Transform Infre Red Spectrometers. http://www.expertsmind.com/topic/instruments-for-ir-spectrometry/fourier-transform-infra-red-spectrometers-913564.aspx (accessed Oct 11, 2016).

(92) Lewis, I. R.; Edwards, H. Handbook of Raman Spectroscopy. From the Research Laboratory to the Process Line, 2001, 1–12.

(93) Surface-Enhanced Raman Spectroscopy for the Study of Surface Chemistry. http://archive.cnx.org/contents/f8a19258-739c-43d6-9b26-cc6b9cf70821@1/surface-enhanced-raman-spectroscopy-for-the-study-of-surface-chemistry (accessed Oct 1, 2016).

(94) Ferrari, A. C.; Robertson, J. Raman Spectroscopy of Amorphous, Nanostructured, Diamond-like Carbon, and Nanodiamond. *Philos. Trans. A. Math. Phys. Eng. Sci.* **2004**, *362*, 2477–2512.

(95) Ferrari, a.; Robertson, J. Interpretation of Raman Spectra of Disordered and Amorphous Carbon. *Phys. Rev. B* **2000**, *61*, 14095–14107.

(96) Eaton, P.; West, P. *Atomic Force Microscopy*; 2010.

(97) Barsoukov, E.; Macdonald, J. R. *Impedance Spectroscopy: Theory, Experiment, and Applications*; 2005.

(98) Ye, H.; Jackman, R. B.; Hing, P. Spectroscopic Impedance Study of Nanocrystalline Diamond Films. *J. Appl. Phys.* **2003**, *94*, 7878–7882.

(99) Reimer, L.; Kohl, H. *Transmission Electron Microscopy Physics of Image Formation*; 2008; Vol. 51.

(100) Haug, H.; Koch, S. W. *Quantum Theory of the Optical and Electronic Properties of Semiconductors*; Fifth Edit.; World Scientific, 2009.

(101) Collins, A. T. The Characterisation of Point Defects in Diamond by Luminescence Spectroscopy. *Diam. Relat. Mater.* **1992**, *1*, 457–469.

(102) Lifespec II Spectrometer. https://www.edinst.com/wp-content/uploads/2015/09/Lifespec-2-Flyer-updtae-070815.pdf (accessed Oct 19, 2016).

(103) Solartron Analytical. 1296 Dielectric Interface Specification. **1994**.

(104) Prawer, S.; Nemanich, R. J. Raman Spectroscopy of Diamond and Doped Diamond. *Philos. Trans. A. Math. Phys. Eng. Sci.* **2004**, *362*, 2537–2565.

(105) May, P. W.; Ludlow, W. J.; Hannaway, M.; Heard, P. J.; Smith, J. a.; Rosser, K. N. Raman and Conductivity Studies of Boron-Doped Microcrystalline Diamond, Facetted Nanocrystalline Diamond and Cauliflower Diamond Films. *Diam. Relat. Mater.* **2008**, *17*, 105–117.

(106) Ferrari, a.; Robertson, J. Origin of the 1150-Cm-1 Raman Mode in Nanocrystalline Diamond. *Phys. Rev. B* **2001**, *63*, 2–5.

(107) Bernard, M.; Deneuville, a.; Muret, P. Non-Destructive Determination of the Boron Concentration of Heavily Doped Metallic Diamond Thin Films from Raman Spectroscopy. *Diam. Relat. Mater.* **2004**, *13*, 282–286.

(108) Linstrom, P. J.; Mallard, W. G. NIST Chemistry WebBook http://webbook.nist.gov/chemistry/.

(109) Hanson, J. IR Absorption. In *http://www2.ups.edu/faculty/hanson/Spectroscopy/IR/IRfrequencies.html* (accessed Sep 10, 2016).

(110) Chung, P. H.; Perevedentseva, E.; Cheng, C. L. The Particle Size-

Dependent Photoluminescence of Nanodiamonds. *Surf. Sci.* **2007**, *601*, 3866–3870.

(111) Freitas, J. A.; Doverspike, K.; Klein, P. B. Luminescence Studies of Nitrogen- and Boron-Doped Diamond Films. **1994**, *3*, 821–824.

(112) Zhao, H.-Q.; Fujiwara, M.; Takeuchi, S. Suppression of Phonon Sidebands in the Spectrum of Nitrogen Vacancy Centers in Diamond Nano-Crystals. **2012**, 82720W.

(113) Jiang, T.; Xu, K.; Jib, S. FTIR Studies on the Spectral Changes of the Surface Functional Groups of Ultradispersed Diamond Powder Synthesized by Explosive Detonation after Treatment in Hydrogen, Nitrogen, Methane and Air at Different Temperatures. *J. Chem. Soc., Faraday Trans.* **1996**, *92*, 3401–3406.

(114) Yoshikawa, M.; Mori, Y.; Maegawa, M.; Katagiri, G.; Ishida, H.; Ishitani, a. Raman Scattering from Diamond Particles. *Appl. Phys. Lett.* **1993**, *62*, 3114–3116.

(115) Wada, N.; Gaczl, P. J.; Solin, S. a. “Diamond-Lik E” 3-Fold Coordinated Amorphous Carbon. *J. Non. Cryst. Solids* **1980**, *36*, 543–548.

(116) Lu, Y. G.; Turner, S.; Verbeeck, J.; Janssens, S. D.; Haenen, K.; Van Tendeloo, G. Local Bond Length Variations in Boron-Doped Nanocrystalline Diamond Measured by Spatially Resolved Electron Energy-Loss Spectroscopy. *Appl. Phys. Lett.* **2013**, *103*.

(117) Karna, S. K.; Vohra, Y. K.; Weir, S. T. Optical and Electrical Characterization of Boron-Doped Diamond. 1–16.

(118) Bevilacqua, M.; Tumilty, N.; Mitra, C.; Ye, H.; Feygelson, T.; Butler, J. E.; Jackman, R. B. Nanocrystalline Diamond as an Electronic Material: An Impedance Spectroscopic and Hall Effect Measurement Study. *J. Appl. Phys.* **2010**, *107*.

(119) Chaudhary, A.; Welch, J. O.; Jackman, R. B. Electrical Properties of Monodispersed Detonation Nanodiamonds. *Appl. Phys. Lett.* **2010**, *96*, 2008–2011.

(120) Aharonovich, I.; Castelletto, S.; Simpson, D. A.; Su, C. H.; Greentree, A. D.; Prawer, S. Diamond-Based Single-Photon Emitters. *Reports Prog.*

Phys. **2011**, *74*, 76501.

(121) Aharonovich, I.; Castelletto, S.; Simpson, D. A.; Greentree, A. D.; Prawer, S. Photophysics of Novel Diamond Based Single Photon Emitters. *Quantum* **2009**, *1296*, 12.

(122) Rabeau, J. R.; Stacey, A.; Rabeau, A.; Prawer, S.; Jelezko, F.; Mirza, I.; Wrachtrup, J. Single Nitrogen Vacancy Centers in Chemical Vapor Deposited Diamond Nanocrystals. *Nano Lett.* **2007**, *7*, 3433–3437.

(123) Hui, Y. Y.; Cheng, C.-L.; Chang, H.-C. Nanodiamonds for Optical Bioimaging. *J. Phys. D. Appl. Phys.* **2010**, *43*, 374021.

(124) Tisler, J.; Balasubramanian, G.; Naydenov, B.; Kolesov, R.; Grotz, B.; Reuter, R.; Boudou, J. P.; Curmi, P. A.; Sennour, M.; Thorel, A.; *et al.* Fluorescence and Spin Properties of Defects in Single Digit Nanodiamonds. *ACS Nano* **2009**, *3*, 1959–1965.

(125) Balasubramanian, G.; Chan, I. Y.; Kolesov, R.; Al-Hmoud, M.; Tisler, J.; Shin, C.; Kim, C.; Wojcik, A.; Hemmer, P. R.; Krueger, A.; *et al.* Nanoscale Imaging Magnetometry with Diamond Spins under Ambient Conditions. *Nature* **2008**, *455*, 648–651.

(126) Schrand, A. M.; Huang, H.; Carlson, C.; Schlager, J. J.; Osawa, E.; Hussain, S. M.; Dai, L. Are Diamond Nanoparticles Cytotoxic? *J. Phys. Chem. B* **2007**, *111*, 2–7.

(127) Yang, W. S.; Auciello, O.; Butler, J. E.; Cai, W.; Carlisle, J. A.; Gerbi, J.; Gruen, D. M.; Knickerbocker, T.; Lasseter, T. L.; Russell, J. N.; *et al.* DNA-Modified Nanocrystalline Diamond Thin-Films as Stable, Biologically Active Substrates. *Nat. Mater.* **2002**, *1*, 253–257.

(128) Yang, W.; Hamers, R. J. Fabrication and Characterization of a Biologically Sensitive Field-Effect Transistor Using a Nanocrystalline Diamond Thin Film. *Appl. Phys. Lett.* **2004**, *85*, 3626–3628.

(129) Chevallier, E.; Scorsone, E.; Bergonzo, P. Modified Diamond Nanoparticles as Sensitive Coatings for Chemical SAW Sensors. In *Procedia Chemistry*; **2009**; Vol. 1, pp. 943–946.

(130) Lukin, M. D.; Hemmer, P. R. Quantum Entanglement via Optical Control of Atom-Atom Interactions. *Phys. Rev. Lett.* **2000**, *84*.

(131) Naydenov, B.; Dolde, F.; Hall, L. T.; Shin, C.; Fedder, H.; Hollenberg, L. C. L.; Jelezko, F.; Wrachtrup, J. Dynamical Decoupling of a Single-Electron Spin at Room Temperature. *Phys. Rev. B - Condens. Matter Mater. Phys.* **2011**, *83*.

(132) Chang, Y.-R.; Lee, H.-Y.; Chen, K.; Chang, C.-C.; Tsai, D.-S.; Fu, C.-C.; Lim, T.-S.; Tzeng, Y.-K.; Fang, C.-Y.; Han, C.-C.; *et al.* Mass Production and Dynamic Imaging of Fluorescent Nanodiamonds. *Nat. Nanotechnol.* **2008**, *3*, 284–288.

(133) Garrett, D. J.; Ganesan, K.; Stacey, A.; Fox, K.; Meffin, H.; Prawer, S. Ultra-Nanocrystalline Diamond Electrodes: Optimization towards Neural Stimulation Applications. *J. Neural Eng.* **2011**, *9*, 16002.

(134) Kim, J. H.; Lee, S. K.; Kwon, O. M.; Lim, D. S. Ultra Thin CVD Diamond Film Deposition by Electrostatic Self-Assembly Seeding Process with Nano-Diamond Particles. *J. Nanosci. Nanotechnol.* **2009**, *9*, 4121–4127.

(135) Lee, S.-K.; Kim, J.-H.; Jeong, M.-G.; Song, M.-J.; Lim, D.-S. Direct Deposition of Patterned Nanocrystalline CVD Diamond Using an Electrostatic Self-Assembly Method with Nanodiamond Particles. *Nanotechnology* **2010**, *21*, 505302.

(136) Taylor, A. C.; Edgington, R.; Jackman, R. B. Patterning of Nanodiamond Tracks and Nanocrystalline Diamond Films Using a Micropipette for Additive Direct-Write Processing. *ACS Appl. Mater. Interfaces* **2015**, *7*, 6490–6495.

(137) Bizi, M. Stability and Flocculation of Nanosilica by Conventional Organic Polymer. *Nat. Sci.* **2012**, *4*, 372–385.

(138) Ohshima, H. A Simple Expression for Henry's Function for the Retardation Effect in Electrophoresis of Spherical Colloidal Particles. *Journal of Colloid and Interface Science*, **1994**, *168*, 269–271.

(139) Bell, R. P. The Reversible Hydration of Carbonyl Compounds. *Adv. Phys. Org. Chem.* **1966**, *4*, 1–29.

(140) Girard, H. A.; Perruchas, S.; Gesset, C.; Chaigneau, M.; Vieille, L.; Arnault, J. C.; Bergonzo, P.; Boilot, J. P.; Gacoin, T. Electrostatic

Grafting of Diamond Nanoparticles: A Versatile Route to Nanocrystalline Diamond Thin Films. *ACS Appl. Mater. Interfaces* **2009**, *1*, 2738–2746.

(141) Axis, K. Peak Fitting in XPS. *Casa XPS* **2006**, 1–29.

(142) Shirasaki, T.; Derré, A.; Ménétrier, M.; Tressaud, A.; Flandrois, S. Synthesis and Characterization of Boron-Substituted Carbons. *Carbon N. Y.* **2000**, *38*, 1461–1467.

(143) Torrengo, S. Surface Functionalization and Characterization of Diamond Thin Films for Sensing Applications. *PhD Thesis, Univ. Trento* **2010**, 135.

(144) Williams, O. A.; Kriele, A.; Hees, J.; Wolfer, M.; Müller-Sebert, W.; Nebel, C. E. High Young's Modulus in Ultra Thin Nanocrystalline Diamond. *Chem. Phys. Lett.* **2010**, *495*, 84–89.

(145) Antonio Alves Júnior, J.; Baptista Baldo, J. The Behavior of Zeta Potential of Silica Suspensions. *New J. Glas. Ceram.* **2014**, *4*, 29–37.

(146) Williams, P. D.; Hawn, D. D. Aqueous Dispersion and Slip Casting of Boron Carbide Powder: Effect of pH and Oxygen Content. *J. Am. Ceram. Soc.* **1991**, *74*, 1614–1618.

(147) ZHANG, J.; JIANG, D.; LIN, Q. Aqueous Processing of Boron Carbide Powders. *J. Ceram. Soc. Japan* **2008**, *116*, 681–684.

(148) Gribanova, E. V; Zhukov, A. N.; Antonyuk, I. E.; Benndorf, C.; Baskova, E. N. Effect of the Acidity of Aqueous Solutions on the Wettability of Diamond, Graphite and Pyrocarbon Surfaces. *Diam. Relat. Mater.* **2000**, *9*, 1–6.

(149) Orazem, M. E. Impedance Response of Semiconductors. *Chem. Eng. Educ.* **1990**, *24*, 48–55.

(150) Hiraiwa, A.; Kawarada, H. Figure of Merit of Diamond Power Devices Based on Accurately Estimated Impact Figure of Merit of Diamond Power Devices Based on Accurately Estimated Impact Ionization Processes. **2013**, *34506*.

(151) Nath, S.; Wilson, J. I. B. Impedance Measurements on CVD Diamond. *Diam. Relat. Mater.* **1996**, *5*, 65–75.

(152) Lightowlers, E. C.; Collins, A. T. Electrical-Transport Measurements on

Synthetic Semiconducting Diamond. *Phys. Rev.* **1966**, *151*, 685–688.

(153) Lightowlers, E.; Collins, A. Determination of Boron in Natural Semiconducting Diamond by Prompt Particle Nuclear Microanalysis and Schottky Barrier Differential-Capacitance Measurements. *j* **1976**, *9*, 951–963.

(154) Lee, B. J.; Ahn, B. T.; Lee, J. K.; Baik, Y. J. A Study on the Conduction Path in Undoped Polycrystalline Diamond Films. *Diam. Relat. Mater.* **2001**, *10*, 2174–2177.

(155) Bataineh, M. M.; Reinhard, D. K. An Impedance Spectroscopy Investigation of Polycrystalline Diamond from Dc to 1 GHz. *Diam. Relat. Mater.* **1997**, *6*, 1689–1696.

(156) Paprocki, K.; Fabisiak, K.; Dychalska, A.; Szybowicz, M.; Dudkowiak, A.; Iskaliyeva, A. Impedance Study of Undoped, Polycrystalline Diamond Layers Obtained by HF CVD. *Appl. Phys. A Mater. Sci. Process.* **2017**, *123*, 1–6.

(157) Williams, a W. S.; Lightowlers, E. C.; Collins, a T. Impurity Conduction in Synthetic Semiconducting Diamond. *J. Phys. C Solid State Phys.* **1970**, *3*, 1727–1735.

(158) Lightowlers, E. C.; Collins, A. T. Determination of Boron in Natural Semiconducting Diamond by Prompt Particle Nuclear Microanalysis and Schottky Barrier Differential-Capacitance Measurements. *J. Phys. D. Appl. Phys.* **1976**, *9*, 951–963.

(159) Ashcheulov, P.; Šebera, J.; Kovalenko, A.; Petrák, V.; Fendrych, F.; Nesládek, M.; Taylor, A.; Živcová, Z. V.; Frank, O.; Kavan, L.; *et al.* Conductivity of Boron-Doped Polycrystalline Diamond Films: Influence of Specific Boron Defects. *Eur. Phys. J. B* **2013**, *86*, 12–18.

(160) Visser, E. P.; Bauhuis, G. J.; Janssen, G.; Vollenberg, W.; Enckevort, J. P. van; Giling, L. J. Electrical Conduction in Homoepitaxial, Boron-Doped Diamond Films. *J. Phys. Condens. Matter* **1992**, *4*, 7365–7376.

(161) Zhang, G.; Janssens, S. D.; Vanacken, J.; Timmermans, M.; Vacík, J.; Ataklti, G. W.; Decelle, W.; Gillijns, W.; Goderis, B.; Haenen, K.; *et al.* Role of Grain Size in Superconducting Boron-Doped Nanocrystalline

Diamond Thin Films Grown by CVD. *Phys. Rev. B* **2011**, *84*, 214517.

(162) Chen, J.; Deng, S. Z.; Chen, J.; Yu, Z. X.; Xu, N. S. Graphitization of Nanodiamond Powder Annealed in Argon Ambient. *Appl. Phys. Lett.* **1999**, *74*, 3651–3653.

(163) Nistor, L. C.; Van Landuyt, J.; Ralchenko, V. G.; Obraztsova, E. D.; Smolin, A. A. Nanocrystalline Diamond Films: Transmission Electron Microscopy and Raman Spectroscopy Characterization. *Diam. Relat. Mater.* **1997**, *6*, 159–168.

(164) Živcová, Z. V.; Petrák, V.; Frank, O.; Kavan, L. Electrochemical Impedance Spectroscopy of Polycrystalline Boron Doped Diamond Layers with Hydrogen and Oxygen Terminated Surface. *Diam. Relat. Mater.* **2015**, *55*, 70–76.

(165) Barsoukov, E.; Macdonald, J. R. *Impedance Spectroscopy: Theory, Experiment, and Applications*; **2005**.

(166) Yu, D.; Wang, C.; Wehrenberg, B. L.; Guyot-Sionnest, P. Variable Range Hopping Conduction in Semiconductor Nanocrystal Solids. *Phys. Rev. Lett.* **2004**, *92*, 216802–1.

(167) Shklovskii, B. Hopping Conduction in Semiconductor Films. *Phys. Lett. A* **1975**, *51*, 289–290.

(168) Su, S.; Li, J.; Kundrát, V.; Abbot, A. M.; Ye, H. Hydrogen-Terminated Detonation Nanodiamond: Impedance Spectroscopy and Thermal Stability Studies. *J. Appl. Phys.* **2013**, *113*, 1–28.

(169) Abeles, B. Effect of Charging Energy on Superconductivity in Granular Metal Films. *Phys. Rev. B* **1977**, *15*, 2828–2829.

(170) Shapira, Y.; Deutscher, G. Semiconductor-Superconductor Transition in Granular Al-Ge. *Phys. Rev. B* **1983**, *27*.

(171) Gonon, P.; Boiko, Y.; Prawer, S.; Jamieson, D.; Gonon, P.; Boiko, Y.; Prawer, S.; Jamieson, D. Poole – Frenkel Conduction in Polycrystalline Diamond Poole – Frenkel Conduction in Polycrystalline Diamond. *J. Appl. Phys.* **1996**, *79*, 1–4.

(172) Vlasov, I. I.; Ekimov, E. a.; Basov, a. a.; Goovaerts, E.; Zoteev, a. V. On the Origin of the Raman Scattering in Heavily Boron-Doped

Diamond. *Arxiv* **2008**, 7.

(173) Mortet, V.; Vlčková Živcová, Z.; Taylor, A.; Frank, O.; Hubík, P.; Trémouilles, D.; Jomard, F.; Barjon, J.; Kavan, L. Insight into Boron-Doped Diamond Raman Spectra Characteristic Features. *Carbon N. Y.* **2017**, *115*, 279–284.

(174) Wang, S.-F.; Hsu, Y.-F.; Ku, F.-C.; Liu, Z.-Y. The Effects of Boron Dopant on the Thermal Stability, Semiconductor Characteristic and Wear Resistance of Diamond Films. *Mater. Res. Innov.* **2017**, *21*, 358–366.

(175) Lu, Y. G.; Turner, S.; Verbeeck, J.; Janssens, S. D.; Wagner, P.; Haenen, K.; Van Tendeloo, G. Direct Visualization of Boron Dopant Distribution and Coordination in Individual Chemical Vapor Deposition Nanocrystalline B-Doped Diamond Grains. *Appl. Phys. Lett.* **2012**, *101*, 10–14.

(176) Norris, D. J.; Efros, A. L.; Erwin, S. C. Doped Nanocrystals. *Science (80-.).* **2008**, *319*, 1776–1779.

(177) Umezawa, H.; Tokuda, N.; Ogura, M.; Ri, S. G.; Shikata, S. ichi. Characterization of Leakage Current on Diamond Schottky Barrier Diodes Using Thermionic-Field Emission Modeling. *Diam. Relat. Mater.* **2006**, *15*, 1949–1953.

(178) Ebert, W.; Vescan, A.; Gluche, P.; Borst, T.; Kohn, E. High-Voltage Schottky Diode on Epitaxial Diamond Layer. *Diam. Relat. Mater.* **1997**, *6*, 329–332.

(179) Brezeanu, M. Diamond Schottky Barrier Diodes. *PhD Thesis, Univ. Cambridge* **2008**.

(180) Tsugawa, K.; Noda, H.; Hirose, K.; Kawarada, H. Schottky Barrier Heights, Carrier Density, and Negative Electron Affinity of Hydrogen-Terminated Diamond. *Phys. Rev. B - Condens. Matter Mater. Phys.* **2010**, *81*, 3–4.

(181) Fiori, A.; Teraji, T.; Koide, Y. Diamond Schottky Diodes with Ideality Factors close to 1. *Appl. Phys. Lett.* **2014**, *105*.

(182) Tung, R. T. Recent Advances in Schottky Barrier Concepts. *Mater. Sci.*

Eng. R Reports **2001**, *35*, 1–138.

(183) Tersoff, J. Theory of Semiconductor Heterojunctions: The Role of Quantum Dipoles. *Phys. Rev. B* **1984**, *30*, 4874–4877.

(184) Tersoff, J. Schottky Barriers and Semiconductor Band Structures. *Phys. Rev. B* **1985**, *32*, 6968–6971.

(185) Ossicini, S.; Bertoni, C. M. Image-Force Effects. **1987**, *35*, 848–850.

(186) Spicer, W. E.; Lindau, I.; Skeath, P.; Su, C. Y.; Chye, P. Unified Mechanism for Schottky-Barrier Formation and III-V Oxide Interface States. *Phys. Rev. Lett.* **1980**, *44*, 420–423.

(187) Omar, S. U. The Role of Interface Effects and Minority Carriers in The Metal-Semiconductor Schottky Junction. *PhD Thesis, Univ. South. Carolina* **2012**.

(188) Rhoderick, E. H. Metal-Semiconductor Contacts. *IEE Proc. I Solid State Electron Devices* **1982**, *129*, 1–14.

(189) Mönch, W. Barrier Heights of Metal Contacts on H-Terminated Diamond: Explanation by Metal-Induced Gap States and Interface Dipoles. *Europhys. Lett.* **1994**, *27*, 479–484.

(190) Cowley, A. M.; Sze, S. M. Surface States and Barrier Height of Metal-Semiconductor Systems. *J. Appl. Phys.* **1965**, *36*, 3212–3220.

(191) Gomila, G.; Bulashenko, O. M.; Rubí, J. M. Local Noise Analysis of a Schottky Contact: Combined Thermionic-Emission–diffusion Theory. *J. Appl. Phys.* **1998**, *83*, 2619–2630.

(192) Frenkel, J. On Pre-Breakdown Phenomena in Insulators and Electronic Semi-Conductors [3]. *Phys. Rev.* **1938**, *54*, 647–648.

(193) Simmons, J. G. Conduction in Thin Dielectric Films. *J. Phys. D. Appl. Phys.* **1971**, *4*, 613–657.

(194) Paoletti, A.; Tucciarone, A. *The Physics of Diamond*; Proceedings of the International School of Physics “Enrico Fermi,” 1997.

(195) Farag, A. A. M.; Farooq, W. A.; Yakuphanoglu, F. Characterization and Performance of Schottky Diode Based on Wide Band Gap Semiconductor ZnO Using a Low-Cost and Simplified Sol-Gel Spin Coating Technique. *Microelectron. Eng.* **2011**, *88*, 2894–2899.

(196) Werner, J. H.; Güttler, H. H. Barrier Inhomogeneities at Schottky Contacts. *J. Appl. Phys.* **1991**, *69*.

(197) Bohlin, K. E. Generalized Norde Plot Including Determination of the Ideality Factor. *J. Appl. Phys.* **1986**, *60*, 1223–1224.

(198) Cheung, S. K.; Cheung, N. W. Extraction of Schottky Diode Parameters from Forward Current - Voltage Characteristics Extraction of Schottky Diode Parameters from Forward Current-Voltage Characteristics. *Appl. Phys. Lett.* **1986**, *49*, 12–15.

(199) Keithley Instruments Inc. Gate Dielectric Capacitance-Voltage Characterization Using the Model 4200 Semiconductor Characterization System. *Appl. Note Ser.* **2006**, 1–8.

(200) Werner, J.; Levi, A. F. J.; Tung, R. T.; Anzlowar, M.; Pinto, M. Origin of the Excess Capacitance at Intimate Schottky Contacts. *Phys. Rev. Lett.* **1988**, *60*, 53–56.

(201) Tsigkourakos, M.; Hantschel, T.; Simon, D. K.; Nuytten, T.; Verhulst, A. S.; Douhard, B.; Vandervorst, W. On the Local Conductivity of Individual Diamond Seeds and Their Impact on the Interfacial Resistance of Boron-Doped Diamond Films. *Carbon N. Y.* **2014**, *79*, 103–112.

(202) Collins, A. T.; Williams, A. W. S. The Nature of the Acceptor Centre in Semiconducting Diamond. *J. Phys. C Solid State Phys.* **1971**, *4*, 1789–1800.

(203) Yamanaka, S.; Takeuchi, D.; Watanabe, H.; Okushi, H.; Kajimura, K. Extraction of Schottky Diode Parameters from Forward Current-Voltage Characteristics. *Phys. Status Solidi* **1999**, *174*.

(204) Gheeraert, E.; Gonon, P.; Deneuville, A.; Abello, L.; Lucazeau, G. Effect of Boron Incorporation on The “quality” of MPCVD Diamond Films. *Diam. Relat. Mater.* **1993**, *2*, 742–745.

(205) Welch, J. O. Nanodiamonds : From Biology to Engineering. *PhD Thesis, Univ. Coll. London* **2014**, 1–273.